FEDERAL UNIVERSITY OF CEARA
TECHNOLOGY CENTER
DEPARTMENT OF METALLURGICAL AND MATERIALS ENGINEERING
POSTGRADUATE PROGRAM IN ENGINEERING AND SCIENCE OF MATERIALS

MSc. MARCOS NATAN DA SILVA LIMA

EFFECT OF DEFORMATION ON THE MECHANICAL BEHAVIOR OF AN ADVANCED STEEL OF HIGH RESISTANCE WITH HIGH MANGANESE CONTENT

FORTALEZA

2023

MARCOS NATAN DA SILVA LIMA

EFFECT OF DEFORMATION ON THE MECHANICAL BEHAVIOR OF AN ADVANCED STEEL OF HIGH RESISTANCE WITH HIGH MANGANESE CONTENT

Thesis presented to the Graduate Program in Engineering and Materials Science at the Federal University of Ceará and Universitat Politècnica de Catalunya as a partial requirement to obtain the title of Phd in Engineering and Materials Science by both universities. Double degree system. Area of Concentration: Processes of Transformation and Degradation of Materials.

This work has been carried out under the direction of:

Prof. Dr. Hamilton Ferreira Gomes de Abreu
Prof. Dr. José María Cabrera Marrero
Prof. Dra. Jessica Calvo Muñoz

FORTALEZA

2023

Dados Internacionais de Catalogação na Publicação
Universidade Federal do Ceará
Sistema de Bibliotecas
Gerada automaticamente pelo módulo Catalog, mediante os dados fornecidos pelo(a) autor(a)

L699e Lima, Marcos Natan da Silva.
Effect of deformation on the mechanical behavior of an advanced steel of high resistance with high manganese content / Marcos Natan da Silva Lima. – 2023.
182 f. : il. color.

Tese (doutorado) – Universidade Federal do Ceará, Centro de Tecnologia, Programa de Pós-Graduação em Engenharia e Ciência de Materiais, Fortaleza, 2023.
Orientação: Prof. Dr. Hamilton Ferreira Gomes de Abreu.
Coorientação: Prof. Dr. José Maria Cabrera Marrero.

1. High manganese steel. 2. Ecap. 3. Plastic deformation. 4. Toughness. 5. Mechanical resistance. I. Titulo.

CDD 620.11

MARCOS NATAN DA SILVA LIMA

EFFECT OF DEFORMATION ON THE MECHANICAL BEHAVIOR OF AN ADVANCED STEEL OF HIGH RESISTANCE WITH HIGH MANGANESE CONTENT

Thesis presented to the Graduate Program in Engineering and Materials Science at the Federal University of Ceará and Universitat Politècnica de Catalunya as a partial requirement to obtain the title of Phd in Engineering and Materials Science by both universities. Double degree system. Area of Concentration: Processes of Transformation and Degradation of Materials.

Approved on: 30/06/2023.

EXAMINING COURT

Prof. Dr. Hamilton Ferreira Gomes de Abreu
Universidade Federal do Ceará (UFC-Brazil)

Prof. Dr. Jairo Alberto Muñoz Bolaños
Universitat Politècnica de Catalunya (UPC-Spain)

Prof. Dr. Juan Manuel Pardal
Universidade Federal Fluminense (UFF-Brazil)

Prof. Dr. Samuel Filgueiras Rodrigues
Instituto Federal do Maranhão (IFMA-Brazil)

Prof. Dr. Sérgio Souto Maior Tavares
Universidade Federal Fluminense (UFF-Brazil)

I want to God.

I want to my parents, Aureliano and Dorismar.

ACKNOWLEDGEMENTS

I want to thank all people involved during all the stages of preparing this work: God, my family, friends, the collaborators at the Federal University of Ceará, and the Universitat Politècnica de Catalunya who made this planning possible. To the supervising professors, Dr. Hamilton Ferreira Gomes de Abreu, Dr. José María Cabrera Marrero, and Dr. Jessica Calvo Muñoz, for all their support, guidance, dedication, disposition, and assistance at all stages of the investigation.

I want to thank all professors Dr. Mauro Andres Cerra Florez, Dr. Samuel Filgueiras Rodrigues, Dr. Mohammad Masoumi, Dr. Montserrat Español, Dr. Emilio Jiménez Piqué, Dr. Luis Flavio Gaspar Herculano, Dr. Francisco José dos Santos Oliveira, Dr. João Rodrigues de Barros Neto, and Dr. Miloslav Béreš. Thanks for all the support and collaboration in all phases of the project that each one could contribute. Without their collaboration, obtaining the results would not have been possible.

I want to thank all Lacam students who, at some point, supported my experiment procedure for this thesis. To all my study and laboratory colleagues at the Federal University of Ceará, MSc. Rodrigo de Carvalho Paes Loureiro, MSc. Pablo Bruno Paiva Leão, MSc. Ursula Cid, Dr. Raphaella Hermont Fonseca Murta, Dr. Jorge Luiz Cardoso, and Dr. Roberta Bastos Vasques for their support, help in the experiments, companionship, and technical teaching.

I want to thank all my study and life colleagues at the Universitat Politècnica de Catalunya, MSc. Milica Zivanic, MSc. Marc Iglesias, MSc. Silvia Gómez Gonzalez, MSc. Laia Ortiz, MSc Nerea Garcia, MSc. Mohammad Rezayat, MSc Kourosh Nasr, Msc. Patricia Lopez Gomez, MSc. Marc Serra, MSc. Pedro Machado, MSc. Laura Cabezas, MSc. Sergio Elizalde, MSc. Ignasi and MSc. Sandra Garcia, for their support, helps to carry out the experiments, companionship, and shared happy moments.

I want to thank all personnel of the laboratories/research groups: Laboratorio de Caracterização de Materiais – LACAM, Laboratório de Pesquisa em Corrosão – LPC, Laboratório de Pesquisa e Tecnologia em Soldagem – LPTS, Central Analítica of the UFC, the Metal Forming Processes – PROCOMAME, Centro de Integridad Estructural, Fiabilidad y

Micromecánica de los Materiales – CIEFMA of the UPC, and the Barcelona Research Center in Multiscale Science and Engineering of the UPC, in particular Irene Lopes Peña.

I want to thank all academic support staff at different levels, both at the Federal University of Ceará and the Universitat Politècnica de Catalunya, Professor Jimmy Robson Rodrigues da Costa, Professor Dr. Jorge Lira, Professor Dr. Casimir Casas Quesada, Professor Dr. Crisanto Jose Vilalobos, and the coordinators of the postgraduate programs in Material Science and Engineering Professor Dr. Walney Silva Araújo from the UFC.

I want to thank the Fundação Cearense de Apoio ao Desenvolvimento Científico e Tecnológico – FUNCAP, Conselho Nacional de Desenvolvimento Científico e Tecnológico (CNPq), Coordenação de Aperfeiçoamento de Pessoal de Nível Superior – CAPES, Brazilian agencies, for all the financial support received during my doctorate studies.

I want to thank Camila Pinheiro Pereira, my fiancé, and my parents, Aureliano Lima da Silva and Maria Dorismar da Silva Lima, for all their understanding, encouragement, unconditional support, and daily contribution to my development personal and professional.

“O SENHOR é o meu pastor, nada me faltará; Deitar-me faz em verdes pastos, guia-me mansamente a águas tranquilas; Refrigera a minha alma, guia-me pelas veredas da justiça, por amor do seu nome. Ainda que eu andasse pelo vale da sombra da morte, não temeria mal algum, porque tu estás comigo; a tua vara e o teu cajado me consolam; Certamente que a bondade e a misericórdia me seguirão todos os dias da minha vida; e habitarei na casa do Senhor por longos dias”.

Psalms 23:1-6 - Holy Bible.

RESUMO

A exploração de petróleo no pré-sal significa um novo rumo de desenvolvimento para o Brasil. Essa atividade estimula investimentos de empresas nacionais e estrangeiras, impulsiona a produção de tecnologia, promove maior qualificação profissional e gera emprego e renda. Os dutos flexíveis (*risers*) utilizados na extração de gás e óleo do fundo do mar possuem um reforço de tração feito de aço que deve suportar diversos esforços como tração axial, fadiga, alta pressão, torção e corrosão quando em serviço. A presente pesquisa realizou um estudo do comportamento mecânico de um aço especial com elevado ter de manganês e médio cromo.

Objetivando melhorias nas suas propriedades mecânicas, foram realizadas deformações plásticas a frio e a quente. O aço em estudo apresentou propriedades similares de resistência mecânica (limites de resistência, limites de escoamento), resiliência e tenacidade em comparação aos aços perlíticos atualmente utilizados em dutos flexíveis (*risers*).

Deformações plásticas comuns e severas (*Severe Plastic Deformation*-SPD) foram aplicadas ao aço com alto teor de manganês. O material investigado possui efeito TWIP (*Twinning Induced Plasticity*), que provocou o aparecimento de maclas mecânicas após a deformação plástica.

Na primeira etapa, foi realizada a laminação a frio. A correlação entre microestrutura, orientação cristalográfica, testes de tração e características de contorno de grão foram sistematicamente investigadas. As amostras como recebidas e laminadas a frio com redução de 50% e 70% foram analisadas utilizando técnicas de Microscopia Eletrônica de Varredura (MEV), Difração de Eletrônicos Retro-espalhados (EBSD) e Difração de Raios-X. Um aumento significativo na fração de contornos de maclas Σ3 de baixa energia, de 16,21% para 24,41%, foram encontrados na amostra 70% deformada. Isso foi obtido com a formação de uma estrutura austenítica {011} e ocorrência de plasticidade induzida por maclagem. O modo de fratura dúctil-frágil observado na amostra laminada a 70%, que pode ser atribuído à formação da alta fração de contornos de maclas Σ3 de baixa energia, minimizou tanto a energia de deformação armazenada localizada quanto o desajuste da rede e promoveu o deslizamento das discordâncias.

Para conseguir melhorar as propriedades de materiais, têm-se utilizado os processos de deformação plástica severa como o ECAP (*equal channel angular pressing* ou extrusão em canal angular. Assim, na segunda etapa, obteve-se um aço de granulometria ultrafina após deformação plástica severa por ECAP em duas temperaturas (350 ºC e 250 ºC) de processamento, utilizando uma matriz com ângulo interno $\Phi=120°$, e um ângulo de $\psi=30°$ que define o arco de curvatura externo onde os dois canais são interceptados. O material foi processado seguindo a rota (Bc) para diferentes números de passes (1, 2, 4 e 8 passes). A

caracterização microestrutural foi realizada utilizando diferentes técnicas de análise microestrutural como: Microscopia Eletrônica de Varredura (MEV), Difração de Eletrônicos Retro-espalhados (EBSD) e Difração de Raios-X. As texturas obtidas após cada passada apresentam orientação predominante com distribuições contínuas ao longo da orientação das fibras com cisalhamento puro. Foram realizados ensaios de dureza mecânica e tração uniaxial. De acordo com estes testes mecânicos, a resistência do material aumenta com a deformação até atingir um aumento de resistência de ~2 vezes em relação ao material recebido.

Na terceira etapa o aço passou por um teste de torção a quente. Amostras do aço com alto teor de manganês, foram submetidas a ensaios de torção isotérmica contínua. Foram utilizadas duas rotas de deformação, $\varepsilon = 2,5$ (rota A) e $\varepsilon = 3,0$ (rota B), com taxa de deformação de 0,05 s^{-1} a uma temperatura de 900ºC. Os resultados mostraram uma competição entre os mecanismos de endurecimento e amolecimento dinâmico (ou seja, recuperação e recristalização). Esta observação também é consequência da variação da energia de falha de empilhamento (EFE) e do efeito da plasticidade induzida por maclagem (TWIP) com a deformação aplicada. Além disso, a influência dos parâmetros de deformação a quente na forma das curvas de escoamento plástico e no refinamento do grão é regida pelo equilíbrio entre esses mecanismos termicamente ativados. A caracterização microestrutural foi realizada utilizando diferentes técnicas de análise microestrutural como: Difração de Eletrônicos Retro-espalhados (EBSD) e Difração de Raios-X e Microscopia Eletrônica de Varredura (MEV). As propriedades mecânicas foram obtidas após ensaios de tração.

Palavras-chave: aço alto manganês; aço twip; deformação plástica; tenacidade; resistência mecânica; ecap; torção.

RESUMEN

La exploración de petróleo en el presal significa un nuevo camino de desarrollo para Brasil. Esta actividad estimula inversiones de empresas nacionales y extranjeras, impulsa la producción de tecnología, promueve una mayor calificación profesional y genera empleo e ingresos. Los ductos flexibles (risers) utilizados en la extracción de gas y petróleo del lecho marino cuentan con un refuerzo de tracción fabricado en acero que debe soportar diversos esfuerzos como tracción axial, fatiga, alta presión, torsión y corrosión cuando está en servicio. La presente investigación realizó un estudio del comportamiento mecánico de un acero especial con alto manganeso y medio cromo, con el objetivo de establecer un grado comparativo de resistencia mecánica, tenacidad y corrosión de este acero con los aceros perlíticos utilizados actualmente en ductos flexibles. Para ello se aplicaron deformaciones plásticas ordinarias y severas (Deformación plástica severa-DPS) al acero con alto contenido de manganeso. El acero utilizado en este trabajo tiene un efecto TWIP (Twinning Induced Plasticity - Plasticidad Inducida por Maclas), lo que provocó la aparición de maclas mecánicas tras la deformación plástica.

Se investigó sistemáticamente la correlación entre la microestructura, la orientación cristalográfica y las características del límite de grano del acero austenítico con alto contenido de manganeso. En la primera etapa se realizó la laminación en frío. Las muestras tal como se recibieron y laminadas en frío con una reducción del 50 % y el 70 % se analizaron mediante microscopía electrónica de barrido (SEM), difracción de electrones retrodispersados (EBSD) y técnicas de difracción de rayos X. Se encontró un aumento significativo en la fracción de límites de macla Σ3 de baja energía, del 16,21 % al 24,41 %, en la muestra deformada un 70 %. Esto se combinó con la formación de una estructura austenítica {011} y la aparición de plasticidad inducida por maclas. El modo de fractura dúctil-frágil observado en la muestra laminada en frío un 70% se puede atribuir a la formación de la alta fracción de límites de macla Σ3 de baja energía, lo que minimizó tanto la energía de deformación almacenada localizada como el desajuste de la red y promovió el deslizamiento de las dislocaciones.

Para mejorar las propiedades del material, se utilizaron procesos de deformación plástica severa como ECAP (presión en canal angular de sección costante). Así, en la segunda etapa se obtuvo un acero con tamaño de grano ultrafino después de una deformación plástica severa por ECAP a dos temperaturas de proceso (350 ºC y 250 ºC), utilizando una matriz con un ángulo interno $\Phi=120°$, y un ángulo $\psi =30°$ que define el arco de curvatura exterior donde se cortan los dos canales. Se procesó siguiendo la ruta (Bc) para diferentes números de pasadas (1, 2, 4 y 8

pasadas). Las texturas obtenidas después de cada pasada muestran una orientación predominante con distribuciones continuas a lo largo de la orientación de las fibras con corte puro. Se realizaron ensayos de dureza mecánica y tracción uniaxial. Según estos ensayos mecánicos, la resistencia del material aumenta con la deformación hasta alcanzar un aumento de resistencia de ~2 veces en relación al material recibido.

En la tercera etapa, el acero se sometió a una prueba de torsión en caliente. Muestras de acero con alto contenido de manganeso fueron sometidas a pruebas continuas de torsión isotérmica. Se utilizó dos rutas de deformación, $\varepsilon = 2,5$ (ruta A) y $\varepsilon = 3,0$ (ruta B), con una velocidad de deformación de 0,05 s^{-1} a una temperatura de 900°C. Los resultados mostraron una competencia entre los mecanismos dinámicos de endurecimiento y ablandamiento (es decir, recuperación y recristalización). Esta observación también es una consecuencia de la variación de la energía de falla de apilamiento (SFE) y el efecto de plasticidad inducida por maclas (TWIP) con la tensión aplicada. Además, la influencia de los parámetros de deformación en caliente sobre la forma de las curvas de fluencia y sobre el afino del grano se rige por el equilibrio entre estos mecanismos térmicamente activados. La caracterización microestructural se realizó utilizando diferentes técnicas de análisis microestructural tales como: Difracción de Electrones Retrodispersados (EBSD) y Difracción de Rayos X y Microscopía Electrónica de Barrido (SEM). Las propiedades mecánicas se obtuvieron después mediante ensayos de tracción.

Palabras clave: acero de alto manganeso; acero twip, deformación plástica; tenacidad; resistencia mecánica; ecap; torsión.

ABSTRACT

Pre-salt oil exploration means a new development path for Brazil. This activity stimulates investments from national and foreign companies, boosts the production of technology, promotes greater professional qualification and generates employment and income. The flexible pipelines (risers) used in the extraction of gas and oil from the seabed have a traction reinforcement made of steel that must withstand various efforts such as axial traction, fatigue, high pressure, torsion and corrosion when in service. The present research carried out a study of the mechanical behavior of a special steel with high manganese and medium chromium.

Ordinary and severe (Severe Plastic Deformation-SPD) plastic deformations were applied to high manganese steel to establish a comparative degree of mechanical strength, tenacity, and corrosion of this steel with pearlitic steels currently used in flexible ducts. The steel used in this work has a TWIP (Twinning Induced Plasticity) effect, which caused the appearance of mechanical twins after plastic deformation.

The correlation between microstructure, crystallographic orientation, and grain boundary characteristics of austenitic high manganese steel was systematically investigated. In the first stage, cold rolling was performed. The as-received and cold-rolled specimens with 50% and 70% reduction were analyzed using Scanning Electron Microscopy (SEM), Electron Back-Scattered Diffraction (EBSD), and X-ray diffraction techniques. A significant increase in the fraction of low-energy Σ3 twin boundaries, from 16.21% to 24.41%, was found in the 70% deformed sample. This was coupled with the formation of {011} austenitic structure and the occurrence of twinning-induced plasticity. The ductile-brittle fracture mode observed in the 70% cold rolled sample, which can be attributed to the formation of the high fraction of low-energy Σ3 twin boundaries, minimized both the localized stored strain energy and lattice misfit, and promoted dislocation glide.

In order to improve material properties, severe plastic deformation processes such as ECAP (Equal Channel Angular Pressing) have been used. Thus, in the second stage, a steel with ultrafine grain size was obtained after severe plastic deformation by ECAP at two processing temperatures (350 ºC and 250 ºC), using a die with an internal angle Φ=120°, and an angle of ψ=30° that defines the external arc of curvature where the two channels intersect. The material was processed following the (Bc) route for different numbers of passes (1, 2, 4 and 8 passes). Microstructural characterization was performed using technologies such as SEM, EBSD and X-ray diffraction. The textures obtained after each pass show predominant orientation with continuous distributions along the fiber orientation with pure shear. Mechanical

characterization by hardness and uniaxial tensile testing was carried out. According to these mechanical tests, the resistance of the material increases with deformation until it reaches an increase of ~2 times in relation to the received material.

In the third stage, the steel underwent a hot torsion test. Steel samples with high manganese content were subjected to continuous isothermal torsion tests. Two strain routes were performed, $\varepsilon = 2.5$ (route A) and $\varepsilon = 3.0$ (route B), was used with a strain rate of 0.05 s^{-1} at a temperature of 900°C. The results showed a competition between dynamic hardening and softening mechanisms (i.e. recovery and recrystallization). This observation is also a consequence of the stacking fault energy (SFE) variation and the twinning-induced plasticity effect (TWIP) with the applied strain. Furthermore, the influence of hot deformation parameters on the shape of plastic flow curves and on grain refinement is governed by the balance between these thermally activated mechanisms. The microstructural characterization was performed using different techniques of microstructural analysis such as: EBSD, SEM and X-Ray Diffraction. The mechanical properties were obtained after tensile tests.

Keywords: high manganese steel; twip steel; plastic deformation; toughness; mechanical resistance; ecap; torsion.

LIST OF ILUSTRATIONS

LIST OF TABLES

LIST OF ABBREVIATIONS

BCC	Body-Centered Cubic
CAPES	Coordination of Superior Level Staff Improvement
CIEFMA	Center for Structural Integrity, Reliability and Micromechanics of Materials
ECAP	Equal Channel Angular Pressing
ED	Extrusion direction
EDS	Energy Dispersive Spectrometry
EBSD	Electron backscatter diffraction
FCC	Face-Centered Cubic
FE-SEM	Field Emission Scanning Electron Microscope
FEG-SEM	Field Emission Gun-scanning Electron Microscope
FUNCAP	Ceará State Foundation to Support Scientific and Technological development
HAGB	High Angle Grain Boudary
HC	Hexagonal Compact
HV	Dureza Vickers
KAM	Kernel Average of Misorientation
LACAM	Materials Characterization Laboratory
LAGB	Low Angle Grain Boudary
LPC	Corrosion Research Laboratory
LPTS	Welding Research and Technology Laboratory.
MPa	Mega Pascal
ND	Normal direction
ODF	Orientation Density Function
SEM	Scanning Electron Microscope
SPD	Deformação Plástica Severa (Severe Plasctic Deformation)
TEM	Transmission Electron Microscopy
UFC	Federal University of Ceará
UPC	Universitat Politècnica of Catalunya
XRD	X-Ray Diffraction

YS Yield Strength

LIST OF SYMBOLS

α′	Martensite
Al	Aluminum element
C	Carbon element
Co	Cobalt element
CO_2	Carbon dioxide gas
Cr	Chromium
Cu	Copper
Fe	Iron element
γ	Austenite
Icorr	Corrosion current density
J	Joule
Mn	Manganese element
Mo	Molybdenum element
N	Nitrogen element
Ni	Nickel element
Si	Silicon
Φ	Angle between channels
ψ	External curvature
ε	Epsilon
Km	kilometers

TABLE OF CONTENTS

1 INTRODUCTION

This chapter briefly introduces flexible ducts (used for oil exploration), steels with high manganese content, deformation by Equal channel angular pressing (ECAP) and torsion processes, as well as the motivation for the thesis.

1.1. Motivation for the thesis

The pre-salt discovery represented Brazil's self-sufficiency concerning oil since, historically, the country has always needed to import it. According to the IBP (Brazilian Institute of Petroleum, Gas, and Biofuels), by 2035, Brazil will stop importing and become an energy exporter. There is an estimation that oil production will increase by around 109%, making Brazil the largest oil producer in South America. In addition to ensuring Brazilian self-sufficiency, the pre-salt discovery also ensures that the country protects itself from possible energy crises (BELTRÃO, 2009).

This takes Brazil to a privileged position economically and geopolitically, as it strengthens the economy due to significant investments, generates new jobs, and expands technological advances. These reserves are located in a region with a water depth of one thousand to two thousand and five hundred meters and between four and six thousand meters deep underground, thus reaching up to eight thousand meters from the surface of the sea, including up to two kilometres of salt (BELTRÃO, 2009).

The reservoirs are at a distance of up to 300km from the Brazilian coast, which requires even greater reliability of oil exploration and production systems, with a much shorter reaction time for a contingency plan. Figure 1 shows the geographic location of the pre-salt

Figure 1 — Brazilian pre-salt reservoirs.

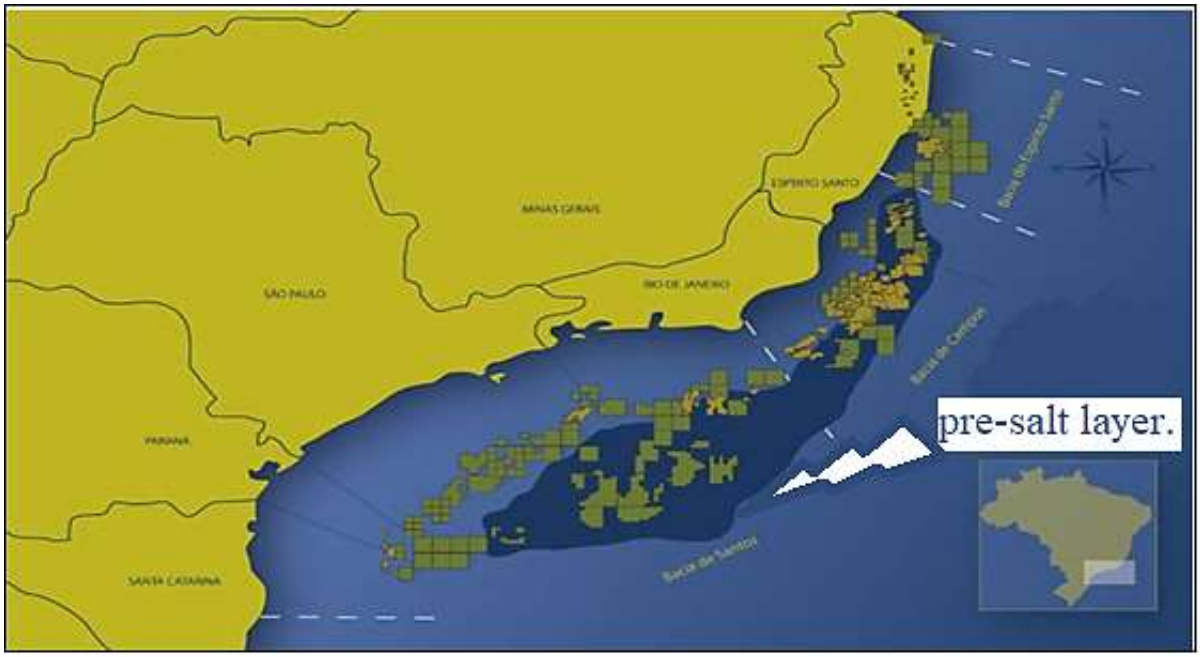

Source: COELHO, (2021).

Extraction in pre-salt fields is significantly more severe than usual, and characteristics such as hydrostatic pressure due to operating depth, reservoir pressure, fluid temperature, and the presence of contaminants such as CO_2 and H_2S in the fluids produced are examples of the main barriers to the development and exploration of these fields. In Brazil, one of the leading production pipeline systems used in the exploration and transportation of oil and gas in offshore production units is flexible pipelines. Flexible pipelines have tubular structures, formed by the superposition of metallic (with a structural function) and polymeric (with a waterproofing function) layers, which provide them with characteristics of resistance to internal fluid pressures, external hydrostatic pressure due to depth and dynamic operating loads due to tidal movement (SANTOS, 2021).

Tensile and pressure reinforcement, whose primary function is to support the axial efforts to which the pipelines are submitted, is the focus of this research. Suppose the material adopted in this structure does not support the residual stresses (from the process of manufacturing the reinforcements of the flexible pipeline and/or from the installation of the pipelines), corrosive process (resulting from the permeation of gases), and service loads (inherent in the operations of oil exploration). In that case, the pipeline could fail, resulting in

substantial financial losses due to the interruption of operation.

FeMnC alloys with high manganese contents (20-30 wt.-%) represent a very recent development of austenitic steels, which, through their differentiated deformation mechanisms (in effect, TWIP (Twinning Induced Plasticity) plastic deformation induced by twins and TRIP (Transformation Induced Plasticity) phase transformation induced by plastic deformation), present an excellent relationship between mechanical strength and toughness. These steels can be considered strategic for the sustainability of the Brazilian economy since Brazil is one of the largest producers of the main alloying element, Manganese (DNPM, 2021).

Currently, many efforts are directed to investigate how to apply improvements or replace pearlitic steels (currently used), with a high failure rate, by steels with better properties (higher yield strength, better toughness) even though they have higher manufacturing costs, which is still considered much less than the loss associate to the stoppage due to the rupture of the pipelines.

During this research, corrosion tests under an atmosphere rich in CO_2 (an essential parameter for materials with application in the petrochemical industry) will be carried out. However, this parameter is not the main focus of the investigation. This work aims to study the mechanical behaviour of high strength steel with high content of Manganese, TWIP steel, before and after plastic deformation for future application in the petrochemical industry in riser reinforcements present in the extraction and injection of oil, water, and gases.

1.2. State of art

1.2.1 Flexible subsea pipes

Flexible pipelines are a fundamental part of the oil exploration arrangement and these influence the design and characteristics of other system components, such as the type of Stationary Production Unit (UEP) used (Semi-Submersible Platforms, Floating, Production, Storage and Offloading Vessels (FPSO), etc.). Figure 2 illustrates a schematic arrangement of an underwater flow system and the interconnections of wells with oil production units.

Figure 2 — Submarine oil exploration arrangement.

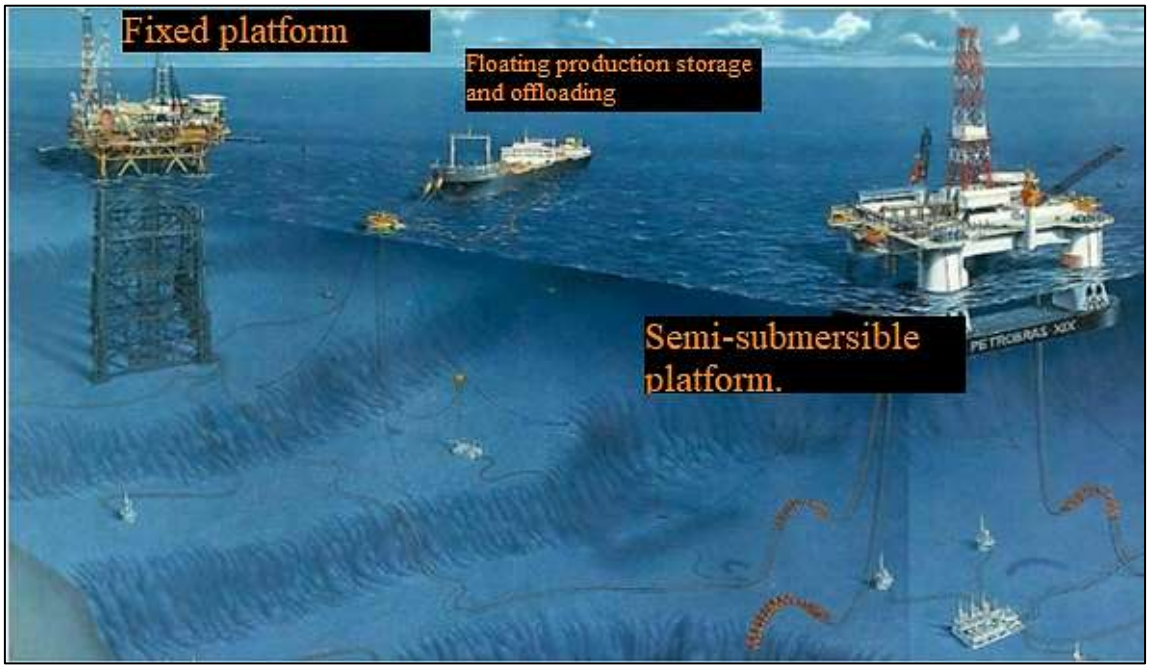

Source: COELHO, (2021).

The flexible pipelines are intended to interconnect oil wells with platforms promoting the transport of fluids such as oil, injection fluids, gas, or water. Compared to rigid pipelines, flexible ones have some advantages, such as the installation process is faster than rigid pipeline systems, using vessels with lower cost, and enabling oil and gas production in a shorter period.

The ideal combination of these ducts should be low bending stiffness and high axial stiffness, and this combination is achieved by constructing a wall composed of layers not adhered to each other (TAMARELLI, 2011). These walls are made up of extruded polymeric cylindrical layers and metal layers with a helical arrangement, each having specific functions and characteristics. One of the main challenges in flexible duct design for ultra-deep-waters applications (more than 2.5 km) is appropriate armor.

For riser applications in which the ducts are connected between the static infrastructure on the seabed and the floating vessel, the duct will be subjected to many variable amplitudes bending cycles caused by movements of the vessels. The most noticeable harmful effect is at the upper end, where the duct is connected to the moving vessel since this region of the duct experiences the most extensive bending curvature cycles.

The precise design and proven durability of traction and compression wires are crucial to ensure the integrity of the service and ensure safe, leak-free operation for more than 25 years of service life. Flexible ducts are long tubular structures made of concentric layers of

metal and polymer, as shown in Figure 3 (SANTOS, 2021).

Figure 3 — Typical construction of a flexible duct.

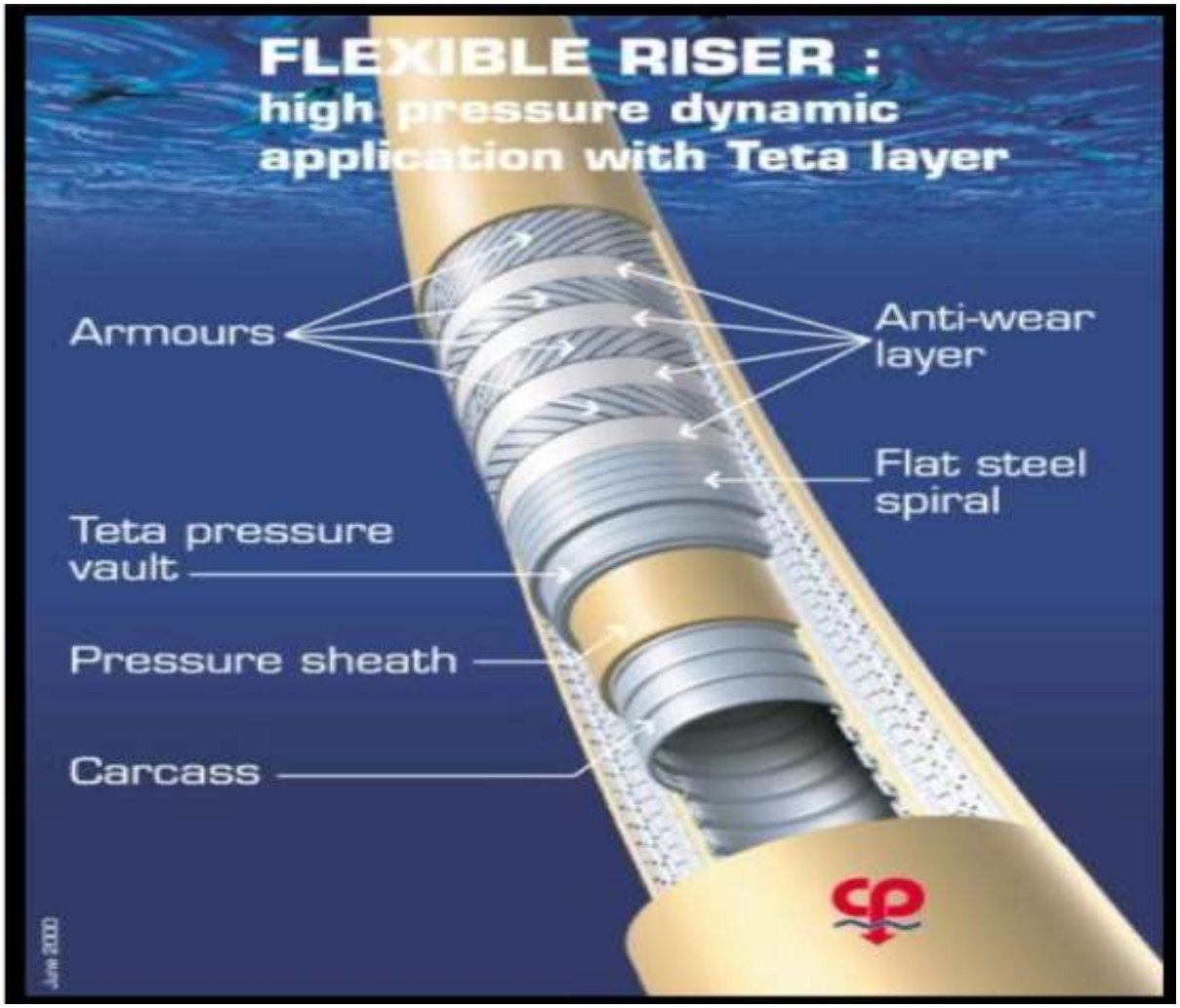

Source: SANTOS, (2021).

The tensile reinforcement layers are constructed by parallel winding several rectangular-shaped wires using a low helix angle between 30° and 50°. They are adding multiple pairs of tensile reinforcement wires rolled in opposite helical directions. This route is used to obtain the necessary axial force, torsion balance, and bending so that the duct moves and bends during service. These reinforcements have the primary function of resistance to axial loads. They consist of high-strength pearlitic carbon steel wire, with resistance limits ranging from 850 MPa to 1500 MPa, flat and rectangular cross-section, applied helically to the duct, and may have several sizes according to the design need. They are used in pairs of wires applied in opposite directions to avoid twisting the structure through the actuation of tensile stresses (COELHO, 2021).

1.2.2. AHSS (Advanced High-Strength Steels)

The increase in the search for lighter structures for the automotive industry and competition with other materials, such as aluminum, magnesium, and composites, has conditioned steel producers to develop new compositions. Thus, they presented the advanced high-strength steels (AHSS), which are usually classified into three generations (TAMARELLI, 2011).

DP (Dual Phase), CP (Complex Phase), TRIP (Transformation Induced Plasticity), FB (Ferritic bainitic), and MS (Martensitic Steel) steels are the first generation and have Ultimate Tensile Strength (UTS) ranging from 600 to 1,700 MPa, with decreasing elongation as the strength is increased. Among the applications of these steels in the automotive industry is the manufacture of bumpers and side protection bars due to the capacity of energy absorption in collisions, a typical characteristic of these materials (TAMARELLI, 2011). The second generation consists of TWIP (Twinning Induced Plasticity), L-IP (Lightweight Induced Plasticity) steels, and austenitic stainless steels, which have a UTS of 900 to 1,500 MPa and elongation of 55 to 80% (BHARGAVA, 2015.).

The third generation of AHSS steels, which includes Q&P (quench and partitioning steels), Nano Steel, and TBF (TRIP-aided bainitic ferrite), has intermediate mechanical properties (between the first and second-generation (BHARGAVA, 2015.). Figure 4(a) illustrates the three generations of AHSS in a tensile strength versus deformation boundary diagram. Figure 4(b) illustrates the exceptional combination of resistance and ductility of a TWIP steel compared to steels of the other generations of AHSS. It can be observed that the TWIP steel exhibits a behavior that combines high strength and ductility (CEES, 2012, BALUCH, 2014, CEES, 2012).

Figure 4 — (a) Steels can be classified as carbon steel, conventional high strength steel (HSS), and advanced high strength steel (AHSS). The latter has three generations. (b) The formability of the second-generation AHSS is significantly higher than the first-generation AHSS with a tensile strength of 980 MPa (140 KSI).

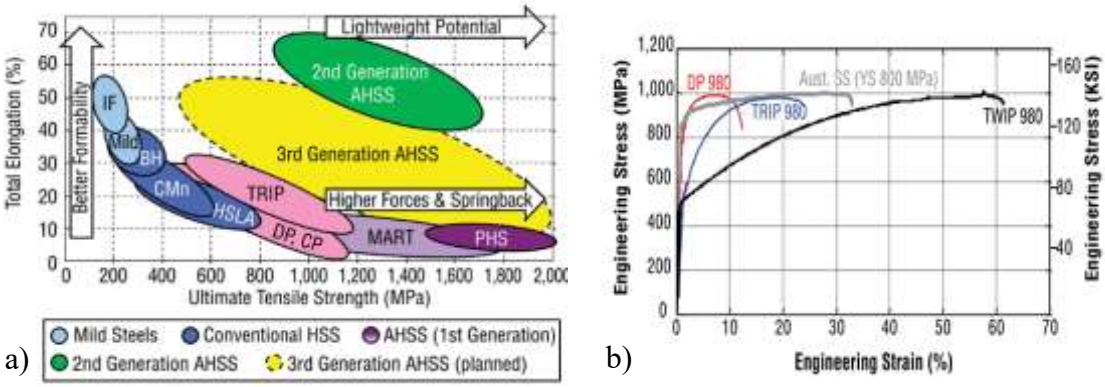

Source: CEES, (2014).

1.2.3. Fe-Mn and Fe-Mn-C System Phase Diagrams

The steels with high Manganese are Fe alloys with Mn contents higher than 12% by weight. This makes the FeMn equilibrium phase diagram an excellent starting point for understanding their behavior. Figure 5 presents the phase diagram of the Fe-Mn system in equilibrium.

Figure 5 — Fe-Mn phase diagram in equilibrium.

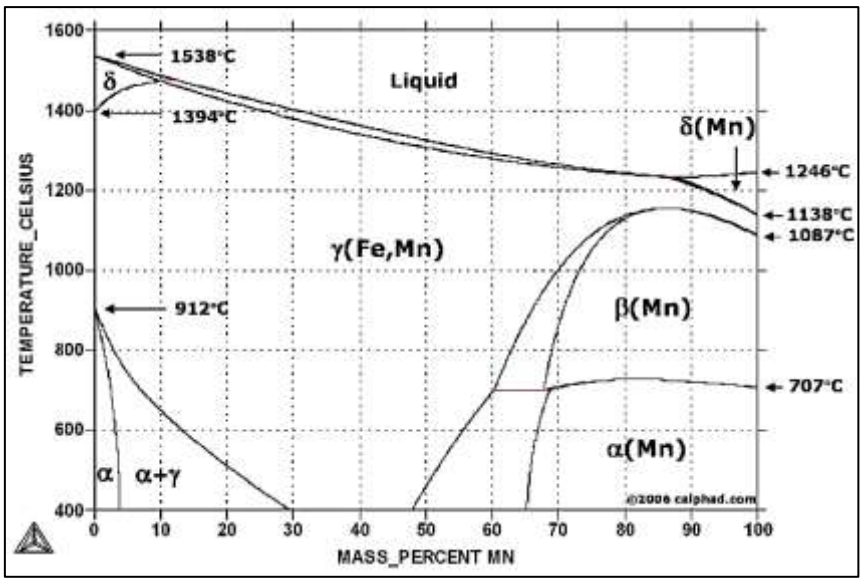

Source: LIMA, (2018).

As shown in Figure 5, the increase in Mn content significantly expands the austenite phase field (γ-FCC). At high temperatures, ferrite (δ-BCC) formation is suppressed by an addition of about (12-13 wt.-%) Mn, indicating that the alloys, with this amount of Manganese or more, will solidify as austenite (SUTTON, 2013). Another characteristic of interest in the Fe-Mn system is that the region of two phases of liquid separation (L) and austenite (γ-FCC) is relatively narrow. In addition to Mn, C is often used to stabilize the austenite and provide interstitial reinforcement in Manganese steels.

However, there are two martensitic products for the Fe-Mn-C system that can form as a result of cooling conditions from an austenitic field. These products are known as martensite-α', a metastable phase which is body-centered cubic (BCC) or tetragonal centered body (TCC) depending on the C content, and martensite-ε, which is hexagonal compact (HC). Schumann created a metastable phase diagram for the Fe-Mn-C system, using samples that were fully austenitized at 950°C and cooled to room temperature (SCHUMANN, 2008).

Figure 6 presents the metastable phase diagram containing both martensites (α' and ε) and austenite (γ-FCC). Figure 6 also shows the approximate levels of onset of both Martensite (α' and ε) in the Fe-Mn-C (SCHUMANN, 2008).

Figure 6 — Diagram of metastable phases of the Fe-Mn-C system, for alloys cooled to room temperature after heating at 950°C.

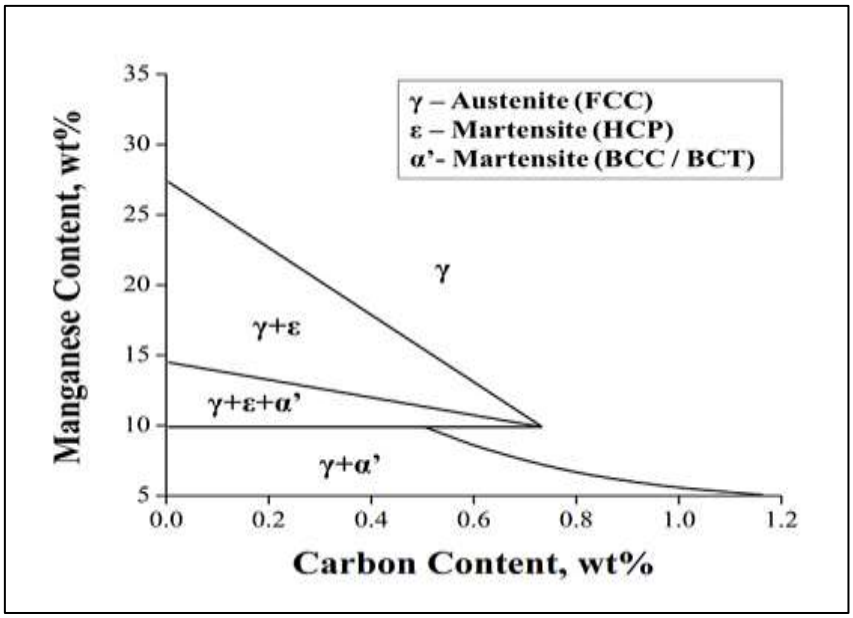

Source: SCHUMANN, (2008).

1.2.4. Stacking Fault Energy (SFE)

Depending on the composition on Manganese and Carbon, different microstructures can appear, as seen in the previous section. The reaction to deformation of the microstructures depends on the defects which are prone to form. These defects are obstacles to the sliding of disagreements responsible for plastic deformation and the spread of cracks. For example, the more grain boundaries, the more resistant to deformation and the tougher the metallic material becomes. Therefore, grain refining is an efficient mechanism to increase the mechanical strength of the material. The movement of atoms (diffusion) through grain boundaries is faster due to the high density of gaps (CALLISTER, 2008).

Stacking faults are a relatively common crystalline defect in cubic materials of centered faces (FCCs). They occur when, in a small region of the material, there is a failure in the stacking sequence of the compact planes. In FCC crystals, this sequence is ABCABCABC type. In compact hexagonal crystals (HC), it is ABABAB. An ABCABABCABC sequence, in a region of the FCC crystal, characterizes a stacking fault, which comes to be a small HC region within the FCC crystal (HULL, 1984), as shown in Figure 7.

Figure 7 — Stacking drawing of planes. (FCC—HC).

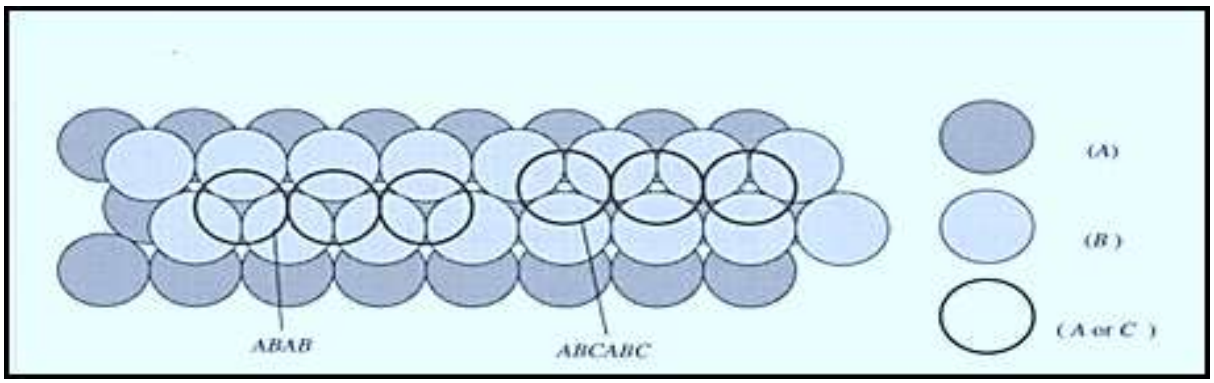

Source: LIMA, (2018).

An FCC metal will have more or less stacking faults according to its stacking fault energy (SFE), a parameter sensitive to the chemical composition evaluated in the transmission electron microscope or by thermodynamic calculations. The chemical composition and temperature are the main factors in the control of SFE, consequently determining the primary mechanism of deformation, as shown in Figure 8 (VERCAMMEN, 2004). If the value of SFE

is too low (≤ 18 mJ/m^2), the formation of ε-Martensite is favored (KRÜGER, 2003). For SFE of the order between (12-35 mJ/m^2) the transformation of the martensitic phase is suppressed and the formation of mechanical twins is favored up to values ≤ 60 mJ/m^2 of SFE (FROMMEYER, 2003).

It is interesting to note that the deformation twin and the induced deformation of the martensitic transformation are microstructurally similar. Both involve a diffusion less shear of a region in the form of a restricted plate in the crystal. Both slips and twins are similar macroscopic shear mechanisms and occur on a distinct plane, and need a deformation force to be activated. However, twinning is a shear process that produces a significant reorientation of the network by deformation. The transformation to ε-Martensite on the other hand, can also be formed by shear due to thermal stresses (HAMADA, 2007). There are several thermodynamic calculation models of SFE (Stacking Failure Energy) proposed by (ALLAIN, 2004) for the Fe-Mn system.

Figure 8 — Influence of SFE (temperature and composition) on the characteristics of the deformation of austenite.

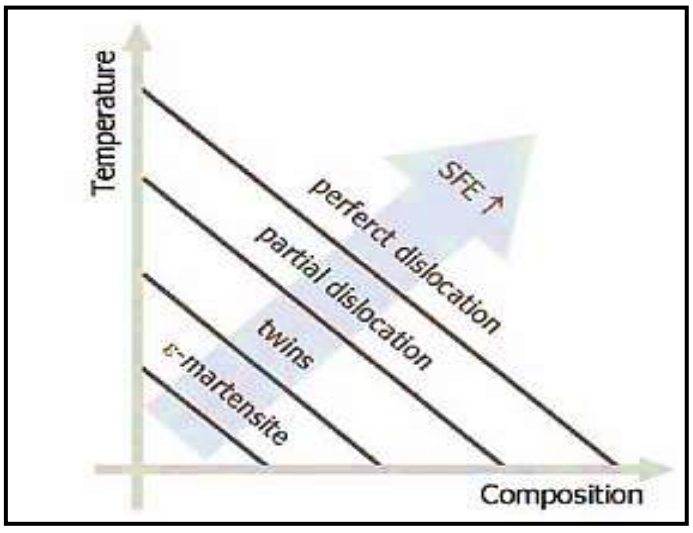

Source: VERCAMMEN, (2004).

1.2.5 TWIP and TRIP mechanisms

TWIP steels have high tensile strength, of the order of 800 MPa, accompanied by high ductility, with elongations in the range above 50%, (ALLAIN, 2004) (BOUAZIZ, 2011). It has an austenitic structure (FCC and non-ferromagnetic) maintained throughout the plastic

deformation process. The high ductility is a consequence of the formation of mechanical twins inside the grains, which, analogous to the grain boundaries, prevent the movement of dislocations. In addition, the austenite does not suffer cleavage, as occurs with the ferrite (BCC and ferromagnetic).

Twinning refines austenitic grain size, resulting in high total elongation, tensile strength, and energy absorption capacity. One of the advantages of TWIP steels is that they maintain the austenitic structure and its attractive properties even at cryogenic temperatures (-196°C) even when subjected to high deformation rates in impact requests (KRÜGER, 2003) (BOUAZIZ, 2011) (QIN, 2008). In TRIP steels, the formation of the metastable phase ε-martensite takes place, which is less harmful than α'-martensite formation, but also reduces ductility and increases the surface hardness of the material. A low SFE is a necessary condition for the activation of the mechanical twin, but obviously, it is not enough on its own.

For example, (BOUAZIZ et al., 2008) reported that only Fe-30Mn deforms by sliding of dislocation while Fe-22Mn-0.6C, Fe-17Mn-0.9C, Fe-12Mn-1.2C (wt.-%) deform both in the sliding of dislocations and by mechanical twinning. The carbon content appears to be a critical parameter that triggers twins and possibly all other deformation mechanisms, as shown in Figure 9. The role of Mn in tensile properties was investigated by (BOUAZIZ, 2011), demonstrating, using statistical analysis techniques, that the direct contribution to hardening is negligible, directly interfering with TRIP or TWIP mechanisms.

Figure 9 — Mn and C effects on TWIP and TRIP mechanisms in four high Mn steel based on the Schumann diagram.

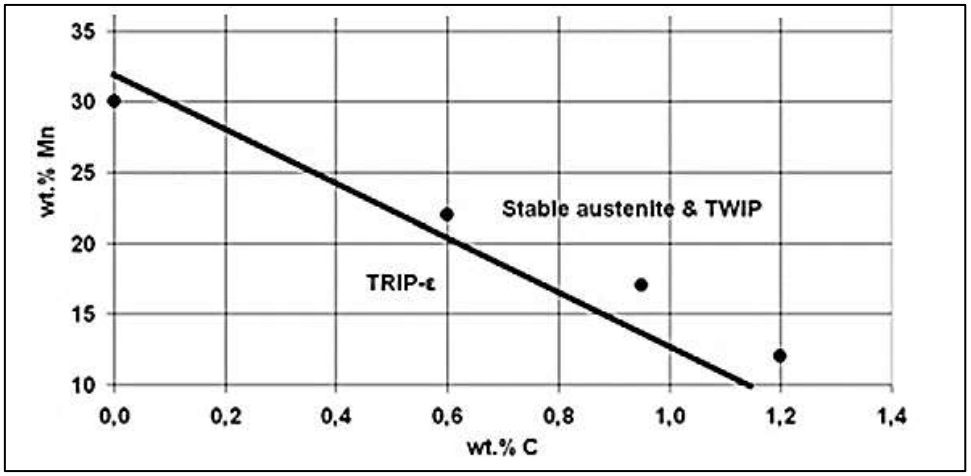

Source: BOUAZIZ, (2011).

1.2.6. Use of Mn, Cr, and Cu in TWIP steels

The primary influence of Mn on TWIP/TRIP steels is to control the SFE according to some experimental data from two studies that investigated the effect of Mn on the Fe-Mn-C system (LEE, 2000). Accordingly, with an increase in Mn content, SFE decreases to a minimum value and then increases again. With increased Mn and/or C content, the mode of deformation changes from TRIP to TWIP due to increased SFE (MENDONÇA, 2014).

For very significant increases in chromium contents above 2% and Carbon, the ductility is reduced due to an increased volume fraction of carbides in the microstructure (HIGUERA-COBOS, 2013). Chromium is a protective element to corrosion in steel and as the chromium content increases, the steel becomes practically indestructible by corrosion. Chromium is, in fact, the essential element, and when used at high levels – above 10% – it is the most efficient of all for corrosion protection, in most conditions. For levels below 1%, it hardly slows corrosion, but Copper, already at 0.2% slows atmospheric corrosion by improving the resistance of steels to atmospheric corrosion three to five times compared to unprotected steels (COSTAESILVA, 2011).

Adding 1-2Cu (wt.-%) in high-content Manganese austenitic steels increases stacking fault energy (SFE) and acts as an austenite stabilizer to explore a transition from TRIP to TWIP. The yield and tensile strength decrease with increased Cu content, while elongation increases in steel with 1% Cu (CHOI, 2012). Some authors (SANGWON, 2011) have reported an increase in total elongation resulting from a more gradual decrease in the work hardening rate in a TWIP Cu-alloyed steel. The kinetics of twins' formation is suppressed, and the increase in Cu content delays the critical deformation related to the evident change in the hardening rate. Meanwhile, it has been reported that TWIP steels with Cu additions had a higher resistance to delayed fracture compared to TWIP Fe-Mn-C steels.

1.2.7. Cold Rolling and Torsion in High Mn steel with TWIP effect

In addition to alloys that have been established for wear resistance, such as Hadfield steels, Mn high steel concepts have been explored for applications that require exceptional resistance and ductility during plastic deformation (GRÄSSEL, 2000) and low magnetic permeability (YAN, 2002). Of these examples, most of the attention has been paid to steels with

high Mn content that exhibit high strength and ductility for applications in automobiles (GRÄSSEL, 2000) (FROMMEYER, 2003).

In these steels and at room temperature, twinning generates a small-scale substructure in the microstructure where the twin limits act to prevent disagreements. In general, in deformed metals and alloys, the average free path of dislocations decreases, as proposed in Taylor's theory, in 1934 (SMALLMAN, 1999) (HUMPHREYS, 2012). After sliding over a distance, dislocations become "immovable" when their density reaches a specific value. This results in a hardening while the excellent ductility is promoted by the formation of twins (VERCAMMEN (2004) (BOUAZIZ, 2001) (SHIEKHELSOUK, 2007) (DE COOMAN, 2011).

(HAUPT et al., 2019) showed the effects of plastic deformation in high Mn TWIP steel in their research. Figure 10 shows image quality maps (Image Quality) obtained by Electron backscatter diffraction-EBSD of the microstructure resulting from Fe-23Mn-0.3C-1Al (wt.-%), high Manganese steel, after cold rolling and rolling at low temperatures (below the recrystallization temperature) ranging from 200 °C to 500 °C, respectively. Limits of deformation twins were identified (60° <111>) and indicated with blue color. However, the fraction of the limits of deformation twins detected decreases significantly in rolling at higher temperatures (HAUPT, 2019).

The material rolled at 200 °C and 300 °C shows a high fraction of the deformation twins limits. Therefore, it is comparable to the cold-rolled sample. In the rolled material at 400 °C, the limits of deformation twins decreased dramatically compared to the material rolled at lower temperatures. Despite the drastic drop, the material still shows a significant fraction of twins' limits. The rolled material at 450 °C exhibited lower deformation twins, while virtually no twin limit was identified in the rolled material at 500 °C (HAUPT, 2019).

Figure 10 — EBSD-IQ maps of deformed Fe-23Mn-0.3C-1Al steel for 50% thickness reduction by (a) cold rolling and rolling a (b) 200°C, (c) 300°C, (d) 400°C, (e) 450°C and (f) 500°C. Blue lines indicate deformation twins' limits (60°<111>).

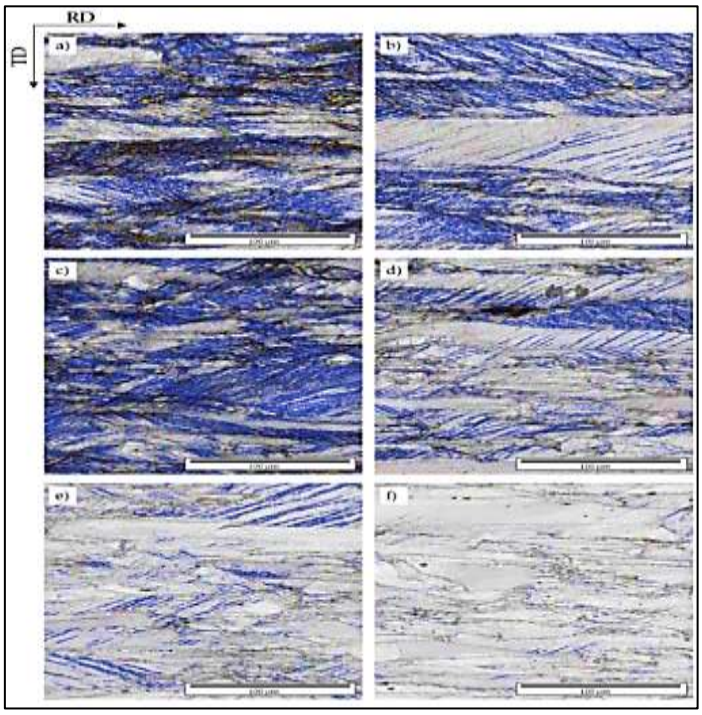

Source: HAUPT, (2019).

Also, according to the same authors (HAUPT, 2019), this correlation between rolling temperature and detected deformation twins' limits indicates a change in the predominant deformation mechanism during rolling from twinning to slip in the temperature range of 400 °C to 500 °C. In the hot rolling of the high Manganese steel 23Mn, 0.3C, 1Al, balance Fe (wt.-%), at 500 °C, it was possible to achieve a thickness reduction of 50%, having slip as the primary deformation mechanism (HAUPT, 2019).

In a study with high-Mn TWIP steel with 26.34Mn, 0.018C, 4.84Al and 3.56Si, balance Fe (wt.-%), the same authors performed torsion tests and compared it with the results obtained by tensile tests. The torsion tests were performed with deformation rates of =0.0125 and 0.0033 s^{-1}, and the tensile tests were performed with strain rates of 0.012, 0.006, and 0.0002 s^{-1}. The post-processing techniques used are described in (KHODDAM, 2004, 2010, 2014), for the conversion of torque-torsion data to effective stress-strain.

Figure 11 shows the gage section of the torsion sample and the radius dependence of plastic strain in the specimen twisted through the θ torsion angle. When a particle in a torsion sample is deformed by twinning, its position changes. Since the effective strain increases linearly with radius, ε is proportional to r (Figure 11c), radial work hardening increases, so the

twin does not move easily towards the measurement surface. This confinement encourages the formation of "tangential twinning" under torsional loading and prevents bifurcation effects, and heterogeneous twinning. This is because the initial one-dimensional (tangential) vector field in the measured section of the deformed torsional sample is not perturbed by the non-tangential strain component. The samples were deformed until the fracture. The torsional behavior of the TWIP steel samples overlapped with the tensile results is shown in Figure 12.

Figure 11 — Torsion sample before deformation(a), deformed by a twist angle of θ (b) and radius dependent strain distribution in the radial a longitudinal directions (c).

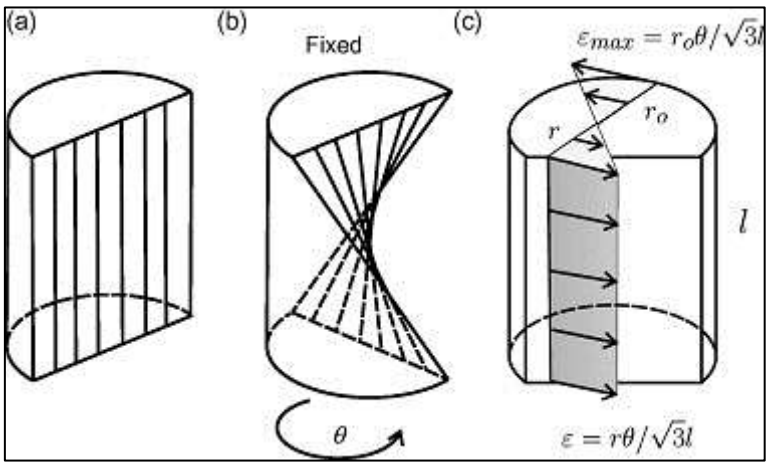

Source: KHODDAM, (2014).

According to the authors, visual inspection of the tensile samples showed that the surfaces were wrinkled (crumpled) at the beginning of the plastic deformation (yielding). The material has twice as many shear stresses without producing such surface changes during twisting than in traction. It was also noted that the tensile effort altered the cross-section of the TWIP steel sample from round to an ellipse, while the pure shear deformation, the circular cross-section remained unchanged (KHODDAM, 2014).

Figure 12 — Hardening by deformation of TWIP steel under three different deformation rates in torsion and tensile test modes.

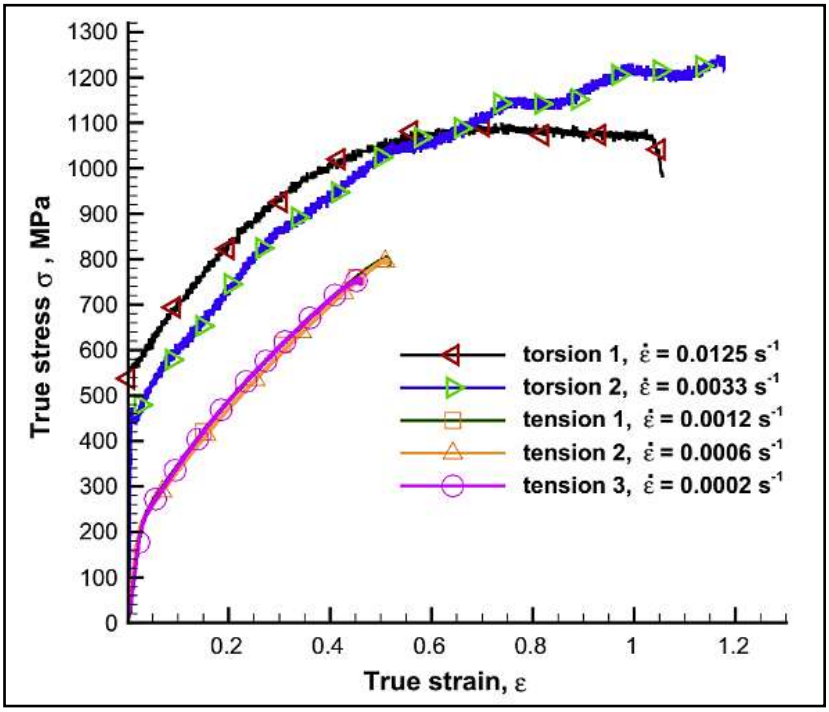

Source: KHODDAM, (2014).

Microhardness distribution data in the samples after tensile and torsion tests presented heterogeneous deformation in the traction sample of TWIP steel. Regarding the microstructure analysis, the torsion samples' deformation twin was distributed more evenly than the traction samples. This indicates that shear deformation can effectively prevent heterogeneous twinning compared to uniaxial deformation and allow the accumulation of more deformation without developing visual marks on the sample surface. Therefore, the torsion test was shown to suffer less from this effect (KHODDAM, 2014).

According to the literature, steels with high Mn content may have different effects on chemical composition and mechanical processing. Therefore, it is necessary to study the mechanical behavior of these steels. Thus, these effects can be sought through the mechanisms of conventional or severe plastic deformation (Severe Plastic Deformation). Of this last type, one can mention the ECAP (Equal Channel Angular Pressing) applied in the material under study (ZUOGUI, (2006) (VALIEV, 2006).

1.2.8. Severe Plastic Deformation (SPD)

Severe Plastic Deformation (SPD) (VALIEV, 2006) (VALIEV, 2006), is a method

of plastic deformation, which can introduce large deformations into the material (traditional plastic deformation processes rarely reach such high strains). It can be affirmed that conventional forming methods (rolling, extrusion, and compression, for example) are limited when applying total deformations due to the reduction in the dimensions of the cross-section of the material and the low conformability of some metal alloys at room temperature.

The technique of severe plastic deformation as a way to generate fine-grained metallic materials has undergone three stages of development (VALIEV, 1999):
I. 1980s, the main methods of severe plastic deformation were proposed. Thus, several preliminary studies began. In 1981, (SEGAL et al. 1941) proposed extrusion in Equal Angular Channels (ECAP - Equal Channel Angular Pressing); and in, (JIANG et al., 2000) proposed torsion deformation under high pressure (HPT - High-Pressure Torsion).
II. 1990s, the work on the subject was done mainly by (R. Z. VALIEV, T. G. LANGDON et al., 2006). In the early 1990s, this research gradually gained notoriety from several academics, and work on severe plastic deformation gradually spread around the world.
III. At the end of the 90s, the group of researchers working on severe plastic deformation had gradually grown to a high number, and several documents and patents emerged. The topic became one of the most sought-after in Materials Science and Engineering (VALIEV, 2006).

After nearly ten years of intensive research, much knowledge was generated about the methods of preparation, materials, microstructural characterization (VALIEV, 2006), which is a solid base for industrial applications in the near future. Actually, the main techniques of SPD to obtain fine-grained materials are: Extrusion in Equal Angular Channels (ECAP) (VALIEV, 2006) (SEGAL, 1995), Accumulative Roll-Bonding (ARB) (SAITO, 1998) (SAITO, 1998), High Pressure Torsion (HPT) (VALIEV, 1997) (VALIEV, 1991), Ball grinding (BM) (BENJAMIN, 1970) (KOCH, 1996), Cyclic compression and extrusion (CEC) (RICHERT, 1998) (RICHERT, 1986), Super Short interval Multi-pass Rolling (ETOU, 2008). The principles of some of these techniques may be seen in Figure 13. Among them, the ECAP (in Figure 13, a technique that will be commented on below) one of the most common and developed nowadays.

Figure 13 — Main techniques of SPD.

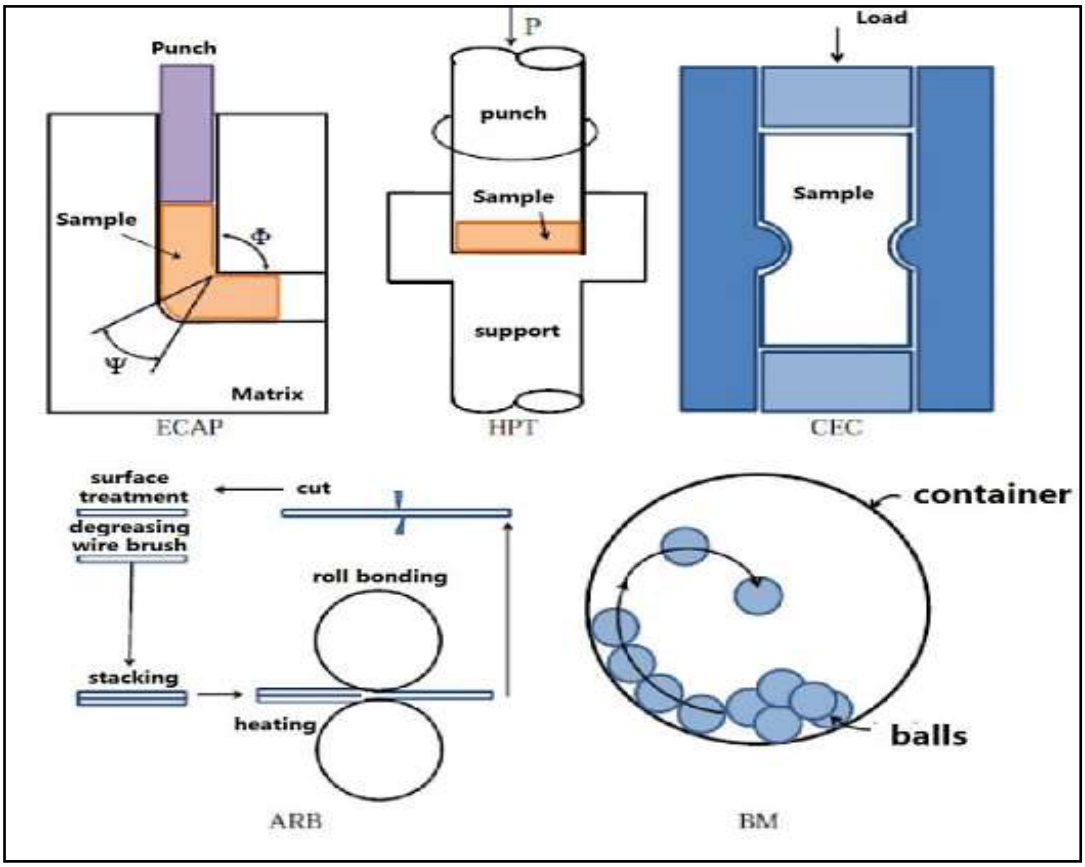

Source: VALIEV, (2000).

A distinct characteristic of materials submitted to SPD methods is the structure of ultrafine or nanometric grains and the presence of a high volume of high angle grain boundaries (HAGB) (LEI, 2017) (VALIEV, 2000), which can be achieved by three mechanisms (SEVILLANO, 1980). The first is the elongation of the existing grains during plastic deformation, causing an increase in the HAGB area; the second implies the subdivision of the grains, and finally, the shear bands that divide the elongated grains can also be considered a source of HAGB. Many references prove that ECAP can generate ultrafine grains in materials (VALIEV, 2000) (MEYERS, 2006), which opens the door to its application in engineering structures. This thesis will use the ECAP process to refine the grain of a high- Mn TWIP steel.

1.2.9. ECAP

ECAP processing is a Soviet technology developed by (SEGAL, 1941). He was trying to obtain pure shear during deformation to study the texture and microstructure of the steels subjected to this mode of deformation. In the 1990s, (VALIEV, 1997) realized that ECAP

could produce suitable fine-grained materials with excellent performance. ECAP technology can refine the microstructure of metallic materials, improve mechanical properties, and achieve superplasticity at low temperatures and high deformation rates.

Currently, ECAP technology has been used in the plastic deformation of copper (WANG, 2002) (SUO, 2010), iron (HOHEMWARTER, 2000), titanium and its alloys (STOLYAROV, 2001), magnesium and its alloys (NETO, 2020), and steel (LEI, 2017). The deformation mechanism and the evolution of the microstructure have been well studied for these metallic materials. Figure 14 shows the main parameters that define the ECAP molds and the geometry of the sample before and after pressing. The mold for ECAP consists of two channels with equal sections that intersect. The geometry of the two channels is the same, and they are fully connected according to an angle. Usually, the internal angle is denoted by Φ (may be between 60º and 160º), and the external angle is denoted by ψ.

Figure 14 — Macroscopic deformation during ECAP.

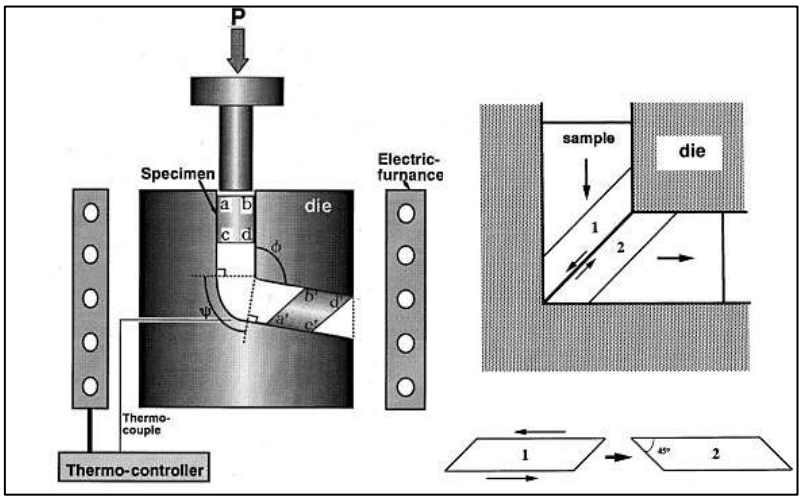

Source: LEI, (2016).

Iwahashi (1996) believe that, during the ECAP process, the cross section will not change if the material completely fills the intersection angle of the two channels. So, there is only one plane, the X plane, which is perpendicular to the X axis, where the deformation occurs. The coordinates, represented in Figure 15, the Y and Z planes are perpendicular to the Y and Z axes, respectively. Disregarding the friction between the inner wall of the channel and the sample, then each sample point would flow at the same distance because each material point passes the same route during the ECAP process. Shear deformation can be expressed as a function of the intersection and external arc of the bend angles as follows:

Figure 15 — Macroscopic deformation scheme of ECAP.

$$\gamma_{YZ} = \frac{d'p}{c'p} = 2ctg\left(\frac{\Phi+\Psi}{2}\right) + \Psi\,\mathrm{csc}\left(\frac{\Phi+\Psi}{2}\right)$$

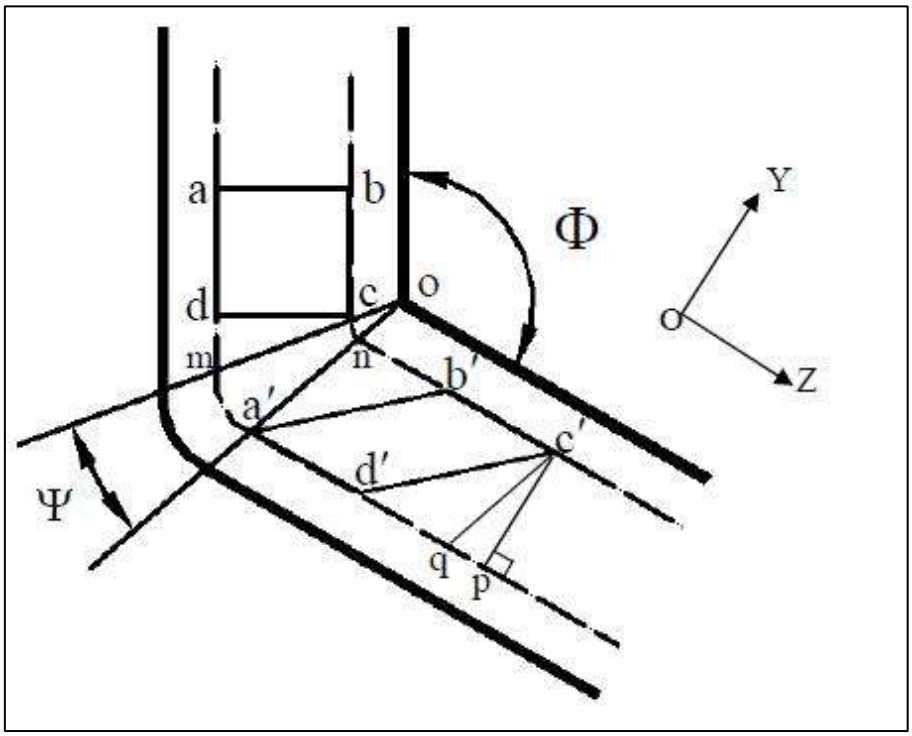

Source: VALIEV, (2000).

Using equivalent plastic strain to describe the amount of deformation of the material, so:

$$\varepsilon_{eq}^{p} = \frac{1}{\sqrt{3}}\gamma_{YZ}$$

The equivalent plastic strain of the material after one pass of ECAP process can be expressed as:

$$\varepsilon_{eq}^{p} = \frac{1}{\sqrt{3}}[2\mathrm{ctg}(\frac{\Phi+\Psi}{2}) + \Psi\,\mathrm{csc}(\frac{\Phi+\Psi}{2})]$$

When the sample is extruded N times, the accumulated equivalent plastic strain can be expressed by:

$$\varepsilon_{eq}^{p} = \frac{N}{\sqrt{3}}[2\mathrm{ctg}(\frac{\Phi+\Psi}{2}) + \Psi\,\mathrm{csc}(\frac{\Phi+\Psi}{2})]$$

The main factors affecting ECAP are: number of passes, processing routes,

extrusion temperature, and extrusion mold geometry.

Plastic deformation will increase with increasing number of extrusions passes. By intuition, the degree of grain refinement should also be higher, but in practice this effect does not occur (CHANG, 2001) (SHIH, 2001) (FERRASSE, 1997) (VALIEV, 1993) (ZUGHAER, 2013). After N passes, the proliferation and annihilation of dislocations are dynamically balanced, the dislocations density is saturated, and the grain size and aspect ratio do not change effectively, as can be seen in Figure 16. However, misorientation between grains continues due to interactions between adjacent grains, as shown in Figure 17.

Figure 16 — The grain size and aspect ratio after number of extrusion passes for pure Al.

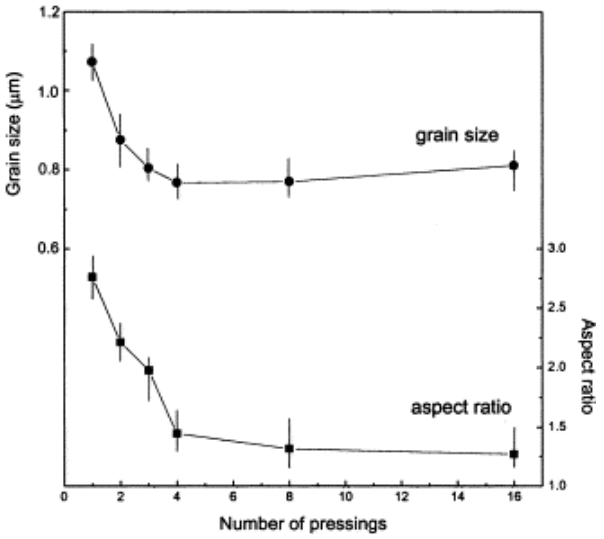

Source: CHANG, (2001).

Figure 17 — The effects of the number of extrusions passes on small-angle and large-angle grain boundary.

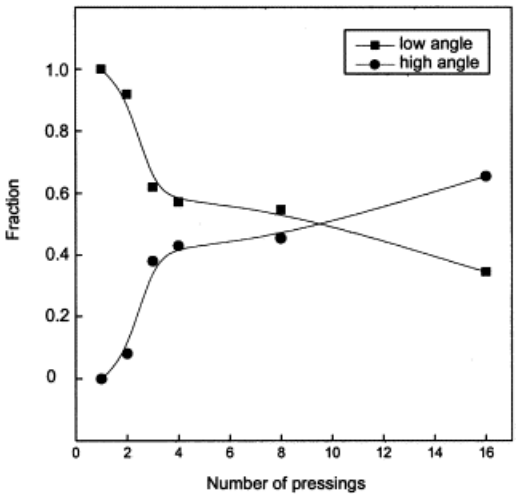

Source: CHANG, (2001).

Segal (1977), observed that by repeating the process, but turning the sample between consecutive passes, there would be a modification of the planes, shear directions and microstructure. The various rotations of the sample between each pass are known as processing routes. The possible routes are A, B_A, B_C and C (Figure 18 and Figure 19). In route A the specimen does not rotate in relation to its longitudinal axis, in Route B_A the sample is rotated 90º clockwise or counterclockwise with the inversion of the direction of rotation, in route B_C the sample is rotated 90º between the passes clockwise or counterclockwise without the inversion of the direction as occurs in route B_A and route C the material is rotated in 180º (NAKASHIMA, 2000).

Figure 18 — Four different extrusion routes.

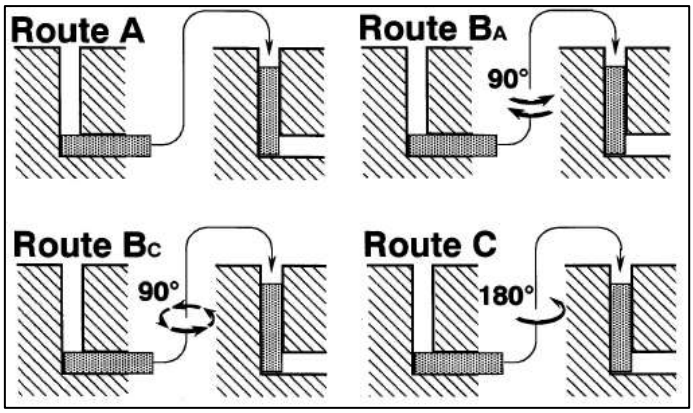

Source: HUANG, (2001).

Figure 19 — Shear plane of A, B_A, B_C, C routes.

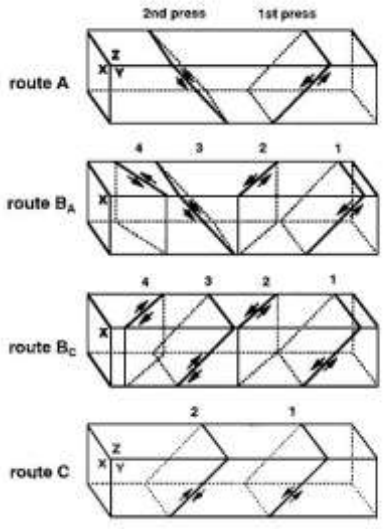

Source: HUANG, (2001).

The ECAP process is generally applied at room temperature because at this temperature the grain refinement potential is better. If the plastic deformation temperature is increased, deformed metals are in an unstable state of high free energy, and prone to a low-energy state, so that recovery can easily occur, leading to low-angle grain limits and grain size is relatively large (YAMASHITA, 2000) (DONG, 2002). In addition, the deformation mechanisms, in some metals, are also temperature dependent (KIM, 2003), for example, metals that would deform by twinning at room temperature will deform by dislocation glide if the temperature is increased.

But it is worth mentioning, even though the high extrusion temperature is not beneficial for the formation of equiaxial fine grains, for some poor toughness high strength metals and hexagonal materials that have limited slip plane systems, such as magnesium alloys, titanium alloys or tungsten alloys, high temperature extrusion can avoid problems to the sample during intense shear deformation (HORITA, 2001).

Many studies (VALIEV, 2006) (KAMACHI, 2003) (LEE, 2002) (NAKASHIMA, 1998) (BERBON, 1999), show that the ECAP extrusion speed has a small effect on grain refinement, as seen in Figure 20, which shows the impact of extrusion speed on yield stress. But if the temperature is increased, using a low extrusion speed, the recovery time would be longer and more dislocations could be absorbed at grain boundaries, leading to a more equiaxial microstructure.

Figure 20 — Impact of extrusion speed on yield strength.

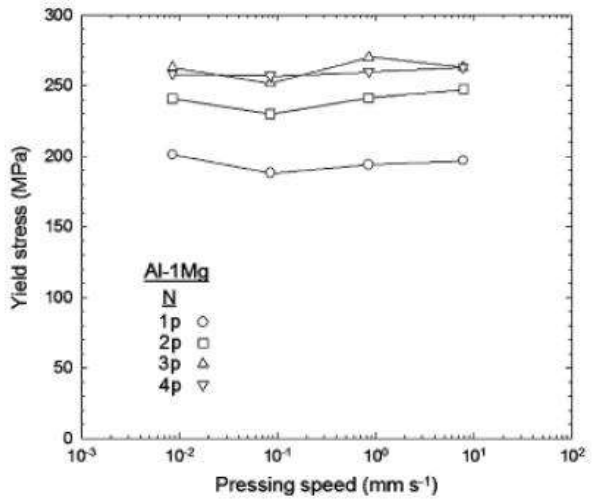

Source: BERBON, (1999).

The most important experimental factor is the internal angle of the canal, Φ, as it causes a great effect on the deformation imposed on each ECAP pass, unlike the outer angle, ψ, as shown in Figure 21. The value of ψ becomes more importance when the inner angle Φ is reduced. At first, the ECAP matrix could be designed with inner angles between 60° and 160°, the smaller the angle Φ, the greater deformation produced by each pass. In practice, the smaller the angle Φ, the greater the force imposed for each pass, and therefore, it requires more resistance of materials. Although the fundamental importance of this angle, most experiments use values from 90° to 120° (VALIEV, 2006).

Nakashima et al., (1998) used four different inner angles and the results showed that to obtain a distribution of equiaxial grains, high angle grain boundaries, the sample must have undergone strong plastic deformation during each pass. Even with an accumulated tension approximately equal by pressing, the grain refinement effect was different.

Figure 21 — Variation of the equivalent strain with the inner angle of channel: the deformations are shown for one pass where N = 1.

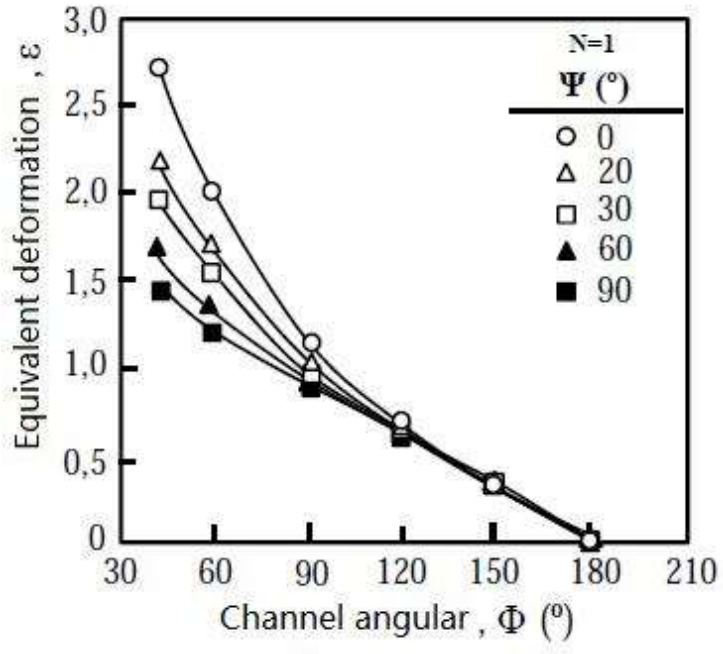

Source: VALIEV, (2006).

Although the 90° angle is the most effective condition for the production of ultrafine grains during the ECAP process, catastrophic fragile fractures can occur. Figure 22 summarizes the relationship between equivalent deformation with outer angle Ψ to four different inner

angles (90°, 105°, 120° and 135°) (EIVANI, 2007).

It is noted that the deformation decreases with the increase of the angle Φ, as well as Ψ. Therefore, the equivalent deformation is non-sensitive to Ψ when at the internal angle Φ is big. However, if Φ is reduced, the effect of the equivalent deformation becomes larger. In practice, using a die with a small angle Φ and an outer angle Ψ with high curvature is the optimal configuration, as it not only allows large deformations, but also extrudes low ductility materials (IWAHASHI, (1997).

Figure 22 — The relationship between equivalent deformation with outer angle.

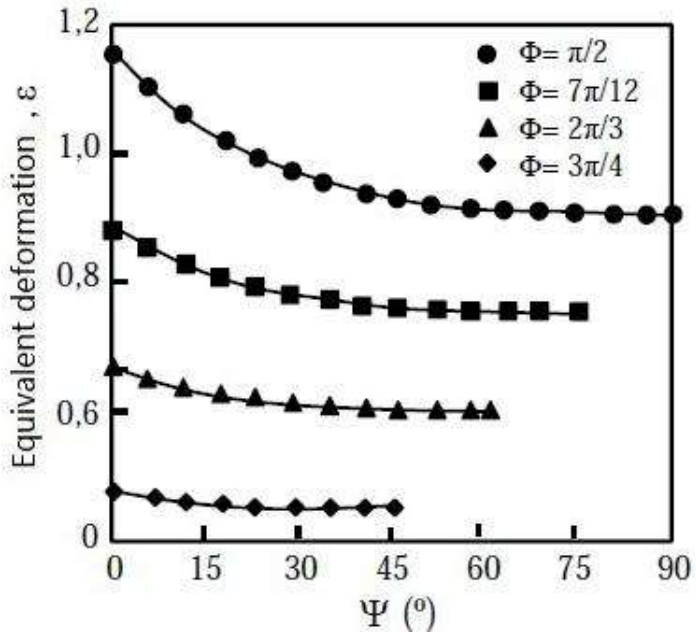

Source: EIVANI, (2007).

Lei et al., (2017) performed four ECAP passes on a Fe-20.1Mn-1.23Si-1.72Al-0.5C (wt.-%), steel with TWIP effect. The development of the microstructure after one and two ECAP passes showed that the grains were elongated in the shear direction and that there was a large increase in the number of sub grains. At the same time, mechanical twins were created with smaller thickness as the deformation proceeded. Secondary twinning was not active after the first and second ECAP passes.

During the third and fourth passes, dislocations and activation of deformation twins led to a more terrific refinement of the microstructure, preventing further deformation and resulting in the low hardening rate obtained during the tensile test of the sample tested four

times in ECAP. Figure 23 shows the tensile results for the samples of ECAP passes performed by the authors. In the investigation done by Lei et al., (2017), the authors also analyzed the microstructure by EBSD, before and after severe plastic deformation by ECAP. Figures 24a and 24b and 25 the deformation of the grains and the production of deformation twins after extrusion can be observed.

Figure 23 — True stress vs true strain curves for TWIP steel (Fe–20.1Mn–1.23Si–1.72Al–0.5C, (wt.-%)) samples before and after ECAP.

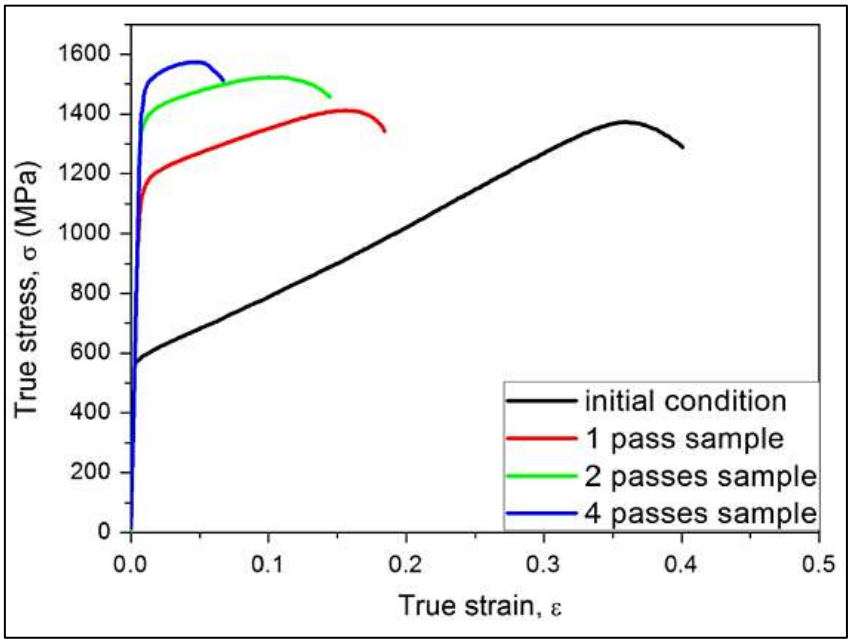

Source: LEI, (2017).

Figure 24 — EBSD grain map (a) IPF and grain contour (b) of initial TWIP steel (Fe–20.1Mn–1.23Si–1.72Al–0.5C, (wt.-%)) samples (grain contour map: black line — high angle grain boundary, green line - low angle grain boundary, white line – twins.

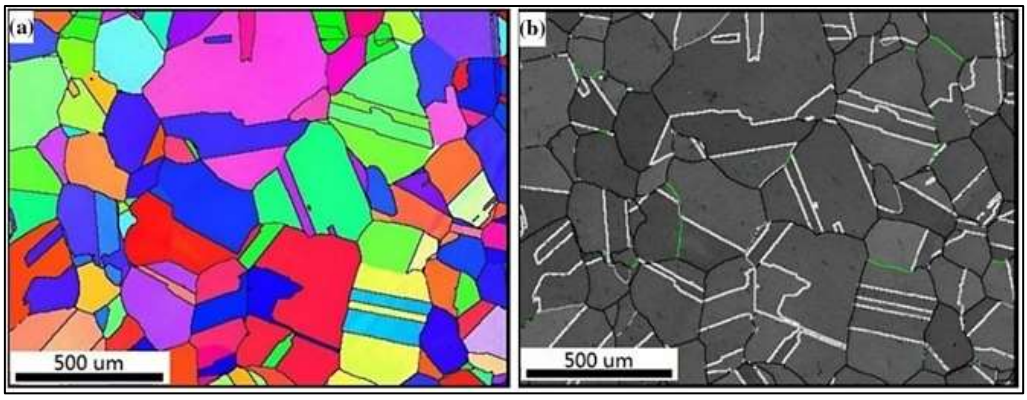

Source: LEI, (2017).

Figure 25 — Grain map EBSD for the TWIP steel (Fe–20.1Mn–1.23Si–1.72Al–0.5C, (wt.-%)): sample with 1 pass (a, b), sample with 2 passes (c, d) and sample with 4 passes (e, f) (grain limit map: line in black-limit color of high-angle grain, line in green color - grain limit of low angle, white line - twins).

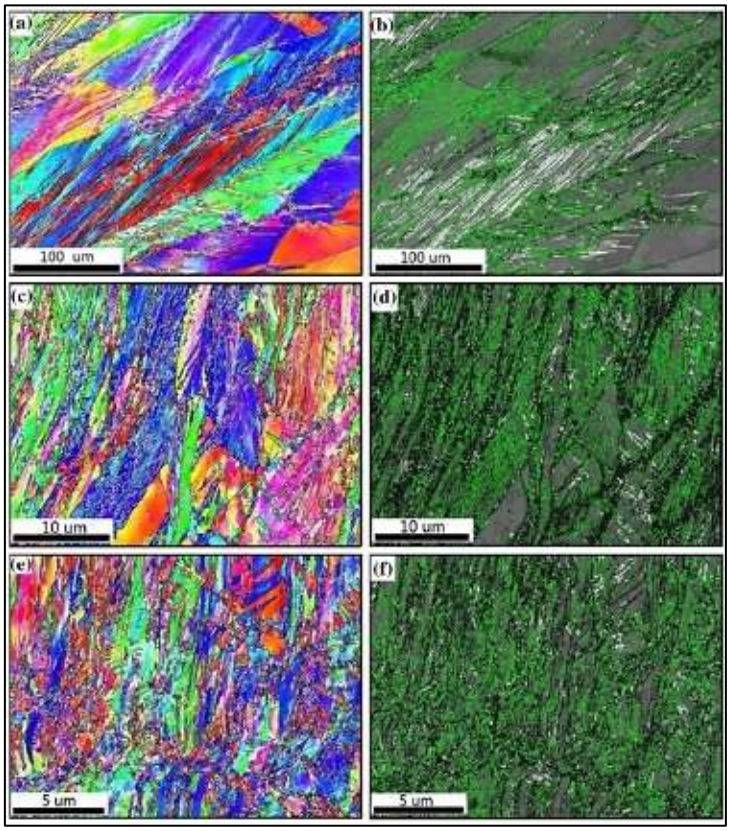

Source: LEI, (2017).

The same authors analyzed the texture of TWIP steel (0.3wt.-%) C and (25wt.-%) Mn after the ECAP procedure. Standard Triclinical Symmetry (0° <φ1 <360) was analyzed. Figure 26 presents the corresponding ODF of TWIP steel. First, monoclinic symmetry can be observed for one pass, two passes and four passes, because the components are repeated every 180°, as confirmed by Li et al., (2005), Suwas et al., (2006), and Haldar et al., (2009), following B_C route.

Figure 26 — (a): Ideal components in triclinic symmetry of FCC materials deformed by simple shear (ZHANG, 2016), (b)-(d):Texture components of investigated TWIP steel (Fe–20.1Mn–1.23Si–1.72Al–0.5C (wt.-%)) after (b) 1 pass of ECAP, (c) 2 passed of ECAP, and (d) 4 passes of ECAP.

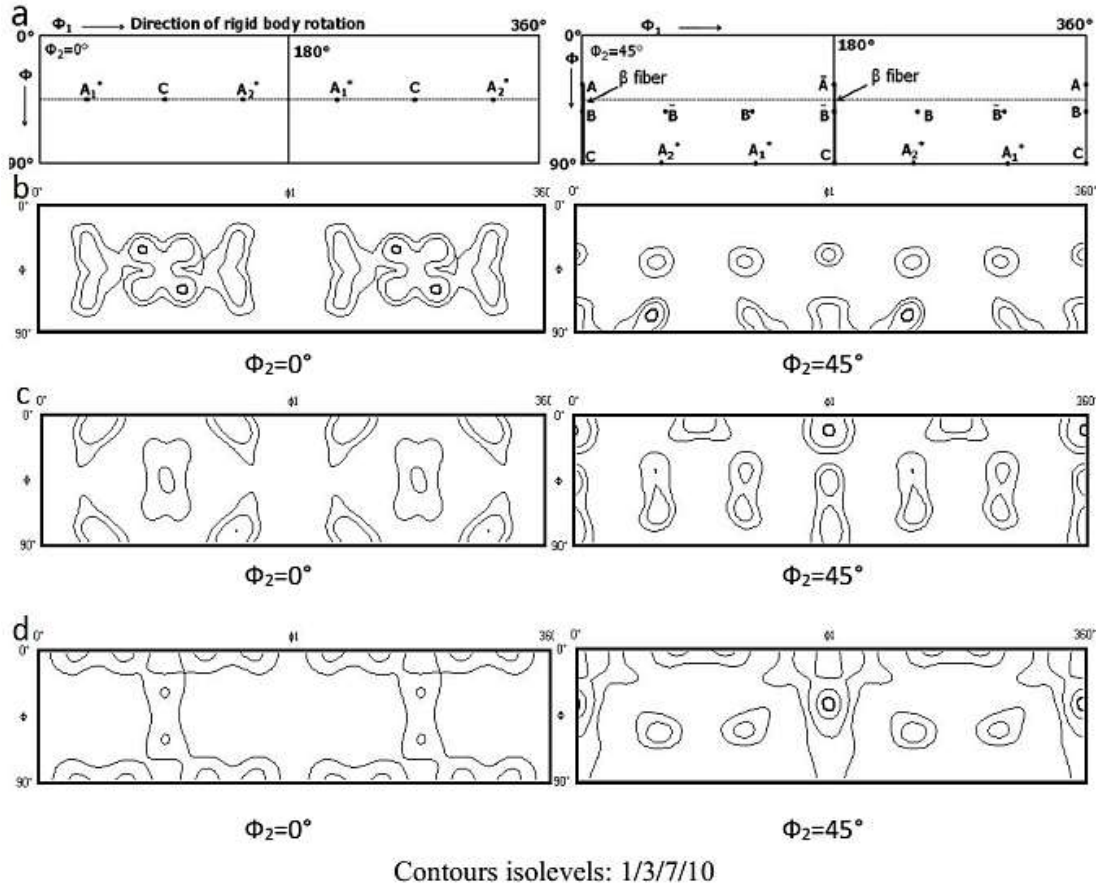

Source: LEI, (2017).

However, after one pass a relatively strong component of A_1*, A_2*, and C can be noticed, while component B shows a lower intensity concerning the preferable texture component. This is probably due to the low SFE value of steel. As for samples that have passed through two passes and four passes, b/b orientations are gradually intensified, as shown in Figure 26.

Abramova et al., (2021), performed ECAP passes on Fe-17Mn-2Al-0.6C (wt.-%), steel with TWIP effect. Using a matrix with an intersection angle from 120° to 400 °C by the Bc route (the piece was rotated 90° between passes) with the number of passes increasing from n = 1 until the fracture that happened after n = 11. Figure 19 summarizes the TWIP steel tensile tests submitted to ECAP for different numbers of passes. Also, in Figure 27, the authors (LEI, 2017) show tensile test results for samples processed by ECAP + rolling. This approach is often

used in the literature to characterize the compensation "force-plasticity" (HAASE, 2016). The hot rolling of coarse grain TWIP steel at 375 °C and 500 °C entails microstructural changes and the corresponding modification of mechanical properties that are well consistent with the values reported in the literature (BELYAKOV, 2016) (HAUPT, 2019).

Figure 27 a) Engineering “stress–strain” curves of the TWIP steel (Fe-17Mn-2Al-0.6C (wt.-%)) before and after multi-pass ECAP. b) Engineering “stress–strain” curves for the TWIP steel (Fe-17Mn-2Al-0.6C (wt.-%)) processed by warm rolling, ECAP to 11 passes (denoted as ECAP 11p), and ECAP 11p + rolling at two temperatures. Note that the elongation to failure of the rolled and ECAP 11p + rolled samples cannot be directly compared to the elongation to failure of the ECAP 11p samples due to different designs of the tensile specimens.

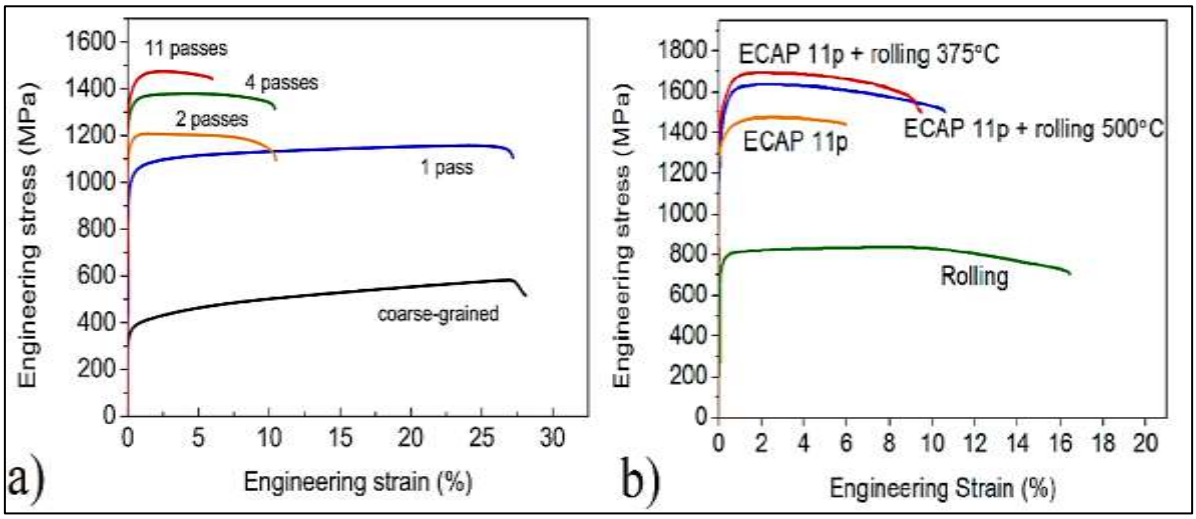

Source: ABRAMOVA, (2021).

2 OBJECTIVES

2.1 General Objective

Evaluate the mechanical behavior of advanced high-strength steel with high manganese content before and after plastic deformation through rolling, torsion, and severe plastic deformation processes. To analyze the microstructure, crystallographic texture, and mechanical properties to apply in risers in the petrochemical industry.

2.2 Specific Objectives

1. Make a thermodynamic study using Thermo-Calc commercial software® of the phases in the composition under study.
2. Determine the effect of applying plastic deformation through cold rolling on the microstructure and mechanical properties of a high manganese steel.
3. Determine the effect of applying plastic deformation through severe plastic deformation by ECAP (Equal Channel Angular Pressing) on the microstructure and mechanical properties of a high manganese steel.
4. Determine the effect of applying plastic deformation through torsional plastic deformation in advanced high-strength steel with high manganese content.
5. Determine the macrotexture, microtexture, and crystallographic microstructure for advanced high-strength steel with high manganese content before and after conventional and severe plastic deformation.
6. Analyze the fracture surface in advanced high-strength steel with high manganese content after tensile test.
7. Compare the effect of plastic deformation applied by rolling, ECAP and by torsion on the evolution of the microstructure and mechanical properties of a high manganese steel.

3 THESIS ORGANIZATION

This chapter describes the thesis organization used to achieve the research objectives. For a better understanding and aiming to fulfill the objectives mentioned, the results of this thesis were organized into chapters based on the transcription of articles (published and/or in the process of being published). Each chapter contains a review, methodology, and results with a discussion. Chapter 4 presents the material used in this investigation. This chapter also contains the first objectives obtained. The chemical composition analysis, application of the software Thermo-Calc® thermodynamic analysis, and presentation of the phases present in the material, as well as the quantification of stacking fault energy are reported.

Chapter 5 is an experimental study about cold rolling including the influence of cold deformation on microstructure, crystallographic orientation, and tensile properties of an experimental austenitic Fe-26Mn-0.4C (wt.-%) steel.

In chapter 6, the ECAP process was applied to and experimental austenitic TWIP steel with chromium and the microstructure, crystallographic orientation, and mechanical properties were analyzed two temperatures and different deformation passes were applied, namely eight passes/ECAP/350 ºC and four passes/ECAP/250 ºC.

In chapter 7, the hot torsion deformed samples of the experimental austenitic Fe-26Mn-0.4C (wt.-%) steel was evaluated. Two deformation routes were performed. The results obtained after strain were of ε=2.5 (route A) and ε=3.0 (route B). All the results of this chapter were performed at a temperature of 900 ºC and with a strain rate of 0.05 s^{-1}. Strain of 0.6, 0.75, 2.2 and 2.6 were considered from calculated regions inside (radius from center to the surface) of the strained specimens. Microstructure, texture, and mechanical properties were analyzed.

In chapter 8 one analysis of deformation processes and mechanical properties was analyzed. A correlation between the mechanical properties and the density of dislocation was commented. The conclusions are listed in chapter 9. Finally, in chapter 10 proposals for future work are presented using high manganese TWIP steel.

4 RESULTS: MATERIAL AND THERMODYNAMIC SIMULATION

4.1 Material

The material of this work is a commercial alloy Fe-Mn-C-Cr-Cu. It has a high manganese content (around 26 wt.-%), with significant contents of chromium and copper, as shown in Table 1. The steel investigated was manufactured by blast furnace steelmaking process, and hot rolled to final thickness of 20 mm.

Chemical analysis was performed using the Energy Dispersive Spectrometry (EDS) technique under a Quanta 450 Field Emission Gun (FEI) microscope and through the Optical Emission Spectroscopy (OES) technique performed in the Shimadzu Optical Emission Spectrometer, model PDA 7000.

Table 1— Chemical composition of the high-Mn TWIP steel investigated.

High Steel Mn	Mn	C	Cr	Cu	Fe		SFE (mJ/m^2)
	26,05	0,45	3,4	0,45	Bal.	(wt.-%)	21

Source: Elaborated by the author.

The SFE was calculated using the thermodynamic mathematical model proposed by Allain, (2004) for the Fe-Mn and Fe-Mn-C systems (HAUPT, 2019). The model needs the values of free energy, chemical composition, temperature, and ASTM grain size of the current high Mn steel. The calculation of the SFE was performed using a program developed especially in Microsoft Excel by (MEDEIROS, 2017), adapting it to the alloy under study.

4.2 Thermodynamic Simulation

A thermodynamic simulation is an essential tool for determining the equilibrium state of systems, mainly benefiting the development of new alloys. Thermodynamic analysis was performed using the commercial computer program Thermo-Calc®. A simulation of the possible phases present in the material was performed, varying temperature and manganese composition. For this analysis, the TCFE6 database was constructed according to the CALPHAD (Computer Coupling of Phase Diagrams and Thermochemistry) protocol, which allows calculations of thermodynamic equilibrium with the elaboration of phase diagrams and

evaluation of thermodynamic data (MEDEIROS, 2017) (SANTOS, 2006).

4.3 Results and discussion

Two diagrams of the high Mn steel TWIP were constructed, one varying the Mn weight percent and the temperature, and the other is the mass fraction phases. Based on previous studies (QIN, 2008) (UMANTSEV, 2012) (ALLAIN, 2004) (LIMA, 2018) (PETROV, 2005), there will be no phase transformations under conventional processing conditions in this TWIP steel, and according to the SFE for this composition, twinning will be the active deformation mechanism (FROMMEYER, 2003).

The chemical composition (Table 1) of the high manganese TWIP steel was used to plot the phase diagrams for the system in equilibrium using the THERMO-CALC® program. Figure 28 shows the phase equilibrium diagram for the Fe-Mn system with the addition of C, Cr and Cu. The diagram presents a vast austenitic field. There is only the austenitic phase in the material for compositions of Mn between 20 and 50 wt.-% and temperature ranging from 500-1380 ºC. Using the chemical composition (Table 1) of the high manganese steel under study, it was also possible to plot the mass fraction diagram of phases present in the equilibrium, as presented in Figure 29.

Through the mass fraction phase diagram obtained with the Thermo-Calc® illustrated in Figure 29 it can be observed that the steel presents a large austenitic field, because above 480ºC approximately, there is only the FCC austenitic phase. No mass fraction of other phases is present. It can then be confirmed that the effect is caused by the high Mn content of the steel, according to the literature.

Figure 28 — Phase Diagram of the Fe-Mn-0.45C-3.4Cr-0.45Cu.

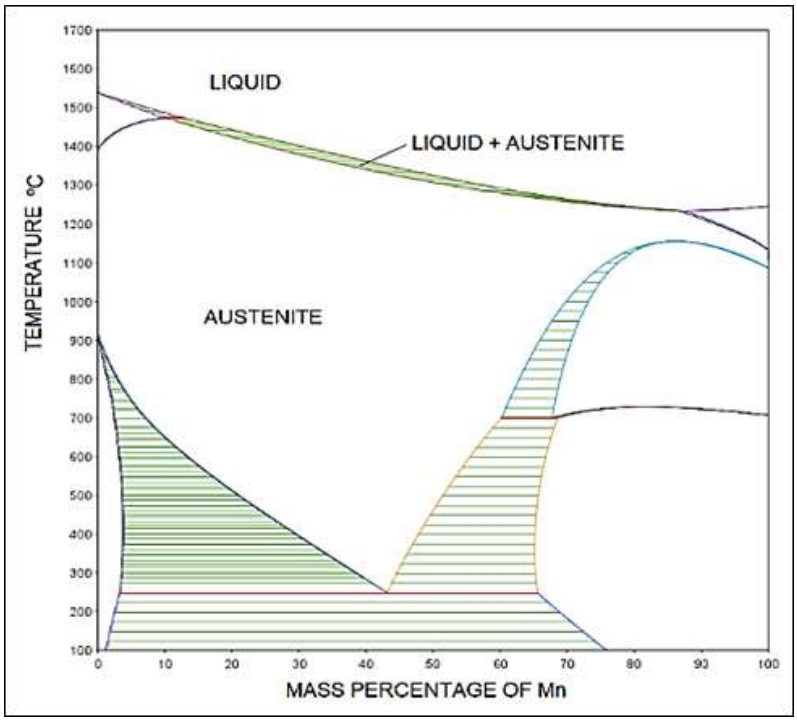

Source: Elaborated by the author.

Figure 29 — Diagram of thermodynamic calculations of the Fe-0.45C-26.05Mn-3.4Cr-0.45Cu (wt.-%) investigated.

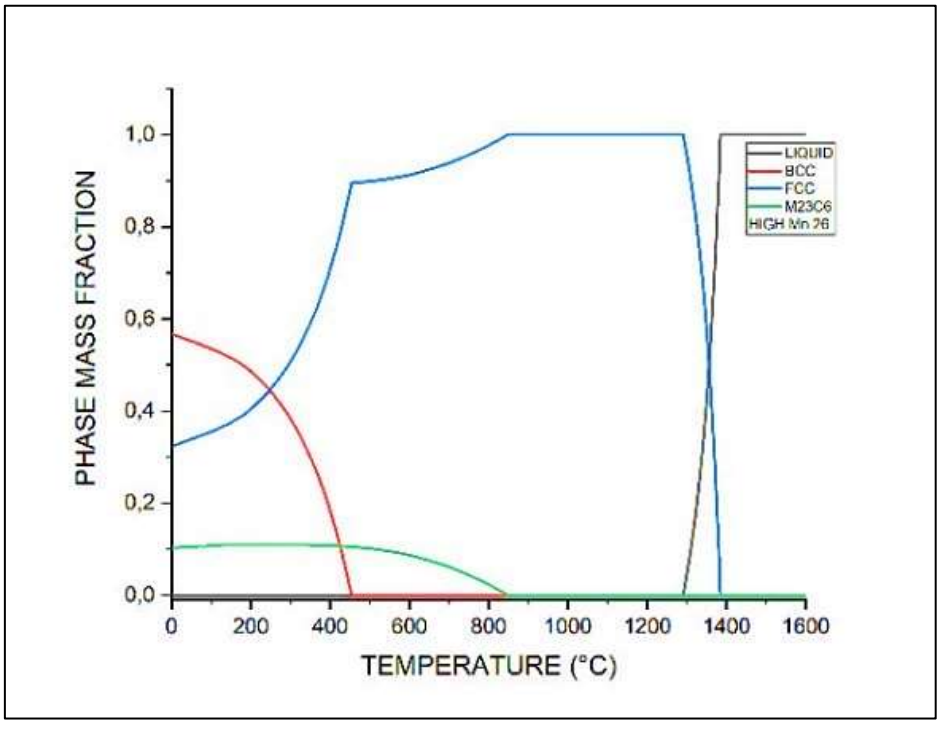

Source: Elaborated by the author.

5 RESULTS: COLD ROLLING

INFLUENCE OF COLD DEFORMATION ON MICROSTRUCTURE, CRYSTALLOGRAPHIC ORIENTATION AND TENSILE PROPERTIES OF AN EXPERIMENTAL AUSTENITIC FE-26MN-0.4C STEEL

5.1 Review

A cold working process is suggested to increase both the yield and ultimate tensile strength of high-Mn austenitic steels. Although cold working increases the tensile strength, it also increases the notch sensitivity and promotes early crack initiation and propagation at grain boundaries and/or at inclusions (FLOREZ, 2020). Although the influence of cold-deformation on microstructure and mechanical properties has been well investigated, a limited research has been conducted on the role of crystallographic orientation changes during cold-rolling. Therefore, it is extremely important to understand the distribution of local strain along particular crystallographic planes and directions in the FCC structure. Such knowledge can provide information about the nature of anisotropy in strain attributed to crystal orientation and action can be taken in order to avoid the formation of crack initiation site and crack propagation when the material is under services (FLOREZ, 2020).

Additionally, another differential point of this work is related to the chemical composition of the TWIP steel evaluated. It is a steel without aluminum, with a high chromium content, to increase corrosion protection and the presence of copper, since this element improves the resistance of steels to atmospheric corrosion three to five times compared to unalloyed steels (WEON, 2016). Moreover, an increase in total elongation resulting from a more gradual decrease in the rate of strain hardening was reported for the TWIP steel with Cu added (WEON, 2016). It was also reported that TWIP steels with Cu additions presented higher resistance to delayed fracture compared to TWIP without Cu steels. All these properties favor the application of TWIP steels containing Cu in the petroleum industry (WEON, 2016). To the best of our knowledge, little attention has been devoted to investigating the role of crystallography of the high-Mn austenitic steel studied in this work. This investigation thus aimed to assess the detailed parameters which govern the microstructure features of the metal as received and under cold rolling process.

All this chapter was published on May/11/2022 with DOI:

https://doi.org/10.1016/j.jmrt.2022.05.020.

5.2 Methodology

Samples with dimensions 20×12×12 mm^3 were extracted from the sheets and studied in the as-received condition and after cold rolling. The chemical composition of steel is listed in Table 1. The cold rolling was conducted at room temperature using a laboratory rolling mill (Coelho Machines Manufacturer/ Model LE-200B) at a rotational speed of 8 m/min. Seven passes were required to obtain a 50% total reduction, whereas with ten passes a 70% total reduction was achieved. Then, the samples were prepared using standard metallographic procedures, including grinding (#120 to #1200 SiC papers) followed by mechanical polishing using 6, 3, and 1 μm diamond paste and finally 0.4 mm colloidal silica suspension. A chemical etching with (40% HNO_3 + 60% H_2O) solution was used for a time of 3 seconds.

Microstructural studies were carried out along the rolling direction (RD)–normal direction (ND) plane in the received and deformed specimens using Optical Microscopy (OM) and Field Emission Gun Scanning Electron Microscopy (FEGSEM) FEI Quanta FEG 450. X-ray diffraction (XRD) method was used to characterize the phase structure in the investigated samples. XRD was performed using a Panalytical X'Pert Pro diffractometer equipped with Co ($K\alpha_1$=1.78897 Å) radiation source. The plane distance of interfered atomic planes was calculated by Bragg's Law $(2 \cdot d \cdot sin\theta = n \cdot \lambda)$ where d is the spacing between atomic planes, 2θ is the diffraction angle, n is an integer and λ is the wavelength. The position of the diffraction peak can be affected by homogeneous and inhomogeneous local strains, which can be calculated by the Sherrer formula below (SANGWON, 2011):

$$D = \frac{C \cdot \lambda}{\beta \cdot cos\theta}$$

where, D is the crystallite size, C is a constant related to crystallite and normally equals to 0.91, λ is the incidence wavelength, β is the full width at half maximum (FWHM) of diffraction peak and θ is the half of diffraction angle.

Macrotexture measurements were conducted using a Panalytical X'Pert Pro diffractometer equipped with a texture goniometer, using Co radiation. The measurements were performed in the reflection mode on a 5° grid at a sample tilt of up to 85°. Orientation Distribution Functions (ODFs) of each sample were calculated from the measured pole figures using the MTEX open-source software toolbox (RANDALL, 2008) (CHEN, 2021). The $\varphi_2 = 0°$ and $45°$ section of Euler space was used to display the computed ODFs.

Samples for Electron Backscatter (EBSD) measurements were prepared by grinding using #120 to #1200 SiC papers. This was followed by electrolytic polishing solution (60% ethanol + 34% n-butanol + 6% perchloric acid), with a voltage of 20 V and current ranging from 0-2 A for 1-3 minutes. Finally, the specimens were polished with 0.05 μm colloidal silica slurry for 15 min.

FEI Quanta FEG 450 and FEI Quanta FEG 650 FEGSEM microscopes operated at 20 kV were used to collect the EBSD data. The working distance was set to about 17 mm with a tilt angle of 70°. Microtexture analyses were conducted using the Channel 5 and ATEX data processing software package. ODFs were determined from EBSD maps through the statistical Kernel density estimation method and plotted at constant Euler angles of $\varphi_2 = 45°$.

Tensile tests were performed at room temperature on samples with a gauge length of 16 mm and overall length of 55 mm using MTS 370 universal testing machine. The strain rate applied was 2×10^{-2} s^{-1}. Six specimens were tested for each condition including as-received and cold-rolled samples submitted to 50% and 70% reduction. The fractured surfaces of tensile samples were subjected to fractographic analysis using FEGSEM.

5.3 Results and discussion

5.3.1 Microscopy analysis

The OM and SEM micrographs at cross-section of the as-received specimen, 50% and 70% reduced under cold-rolled samples are shown in Figure 30. The as-received sample, Figure 30a, exhibited a fully recrystallized refined austenitic microstructure, with mostly equiaxed grains containing abundant thermal twins originated from the hot-rolling process, and few mechanical twins originated from the sample preparation. This is consistent with observation reported by Florez et al., (2019).

The determined micro-hardness value was 202±5 HV. Mechanical twins (red arrow) gradually increased in the 50% cold-rolled sample, Figure 30b. The formation of mechanical twins is associated with low Stacking Fault Energy (SFE) of this alloy system. The micro-hardness values also increased to 420±8 HV by applying a 50% rolling reduction. In samples subjected to a 70% cold rolling reduction, the mechanical induced-twinning occurred on deformation shear bands, resulting in an increase of the micro-hardness to about 502±7 HV.

Austenitic grains showed a heterogeneous morphology structure due to the formation of shear bands resulting from the rolling process. The shear bands intersection formed

a spatial network, which is shown in Figure 30c (depicted with yellow). The gradual development of shear bands occurs with the progressing degree of the cold rolling reduction, and comprised ultrafine grains coupled with dislocation tangles structure as reported by Kowalska and Kowalski (2020).

Figure 30 — Optical micrographs of samples (a) as-received, cold-rolled to (b) 50% and (c) 70% reduction. FEGSEM secondary electron micrographs of specimens (d) as-received, cold-rolled to (e) 50% and (f) 70% reduction. (Mechanical twins are depicted with red and shear bands are depicted with yellow).

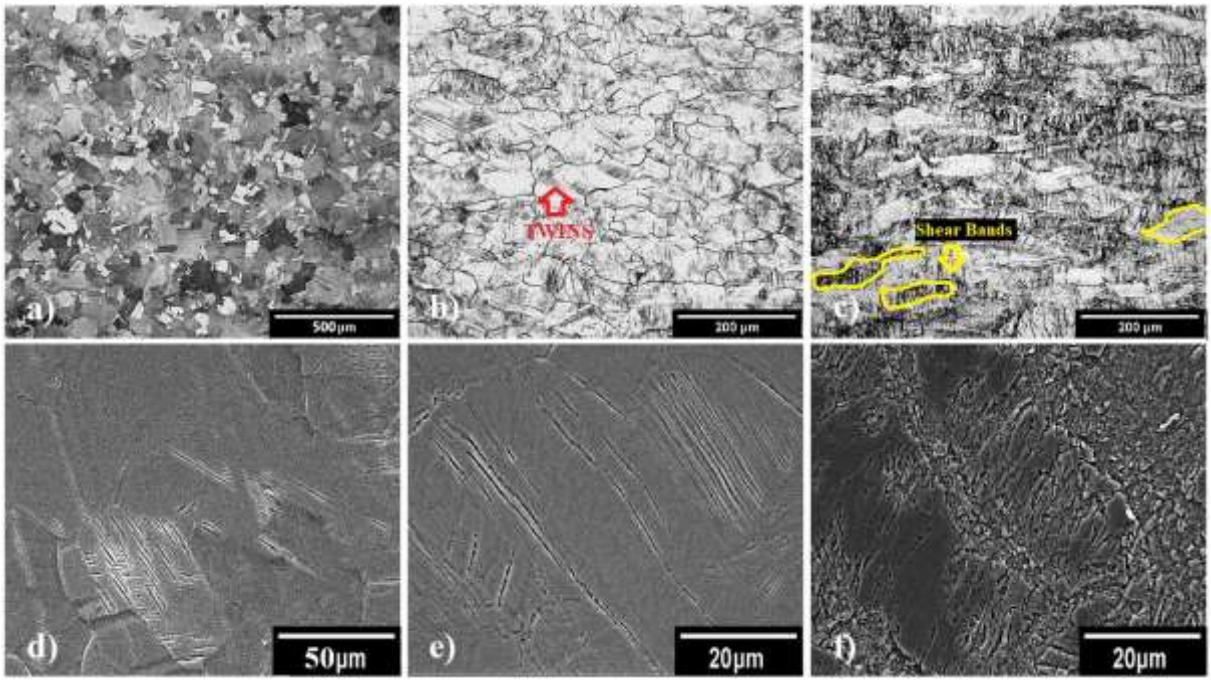

Source: Elaborated by the author.

5.3.2 XRD investigation

Figure 31 presents the XRD patterns of all investigated specimens. The single austenite phase was observed in the as-received sample. The XRD patterns of cold rolled specimens confirmed the absence of any other phases (including α' and/or ε martensite). Therefore, deformation-induced martensitic transformation did not occur even in samples subjected to a 70% cold rolling reduction. The high Mn-content (26.05 wt.%) as austenite stabilizer suppress the deformation-induced martensitic phase transformation. Diffraction peaks shifted towards higher diffraction angles and peak broadening was observed in the cold

deformed specimens. According to Berkum et al., (1996), single-dimensional defects such as dislocations can cause peak broadening, and planar defects, such as twins, can cause peak position displacement diffraction angles. This can be attributed to an increase in dislocation density in addition to a lattice distortion induced by plastic deformation (YE, 2021). The asymmetric diffraction peak is another consequence of the lattice distortion, and is an indication of formation of Coincidence Site Lattice (CSL) boundaries, including twinning (UNGAR, 1996).

The high dislocation density due to cold rolling causes a localized lattice distortion that altered the peak shape of diffracted peak patterns. Notably, peak broadening value can represent an indirect evidence of dislocation density in metallic materials. Thereby, the dislocation densities of investigated as-received and cold-rolled specimens to 50% and 70% reduction were estimated by the method proposed by Ungar (1996) and the modified Williamson-Hall method and were determined to be 2.23×10^{13} m^{-2}, 5.13×10^{14} m^{-2}, and 1.51×10^{15} m^{-2}, respectively. The increase in dislocation density generated during cold rolling causes greater distortion of the crystal lattice, increasing the energy stored in the material. As a consequence, there is an elongation of the grains, formation of shear bands and twin contours, which agrees with hardness results reported before.

Figure 31 — XRD patterns of all samples.

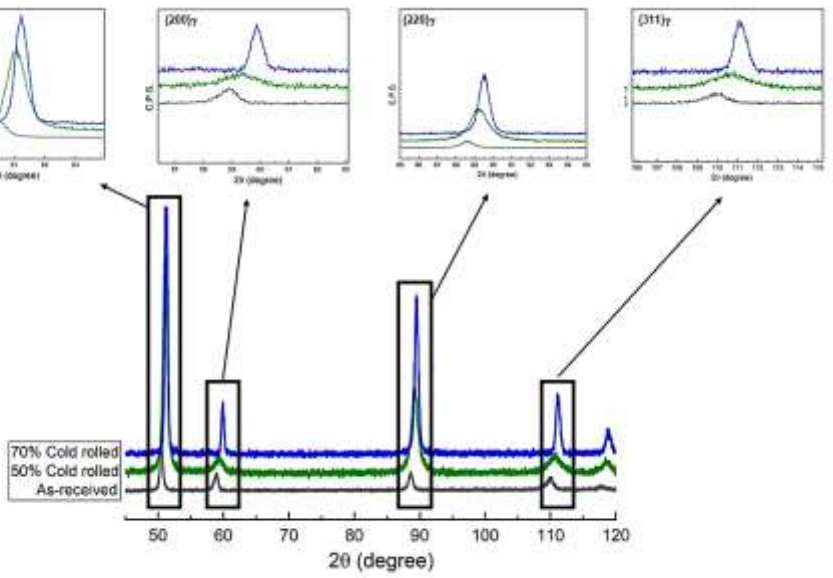

Source: Elaborated by the author.

5.3.3 Electron backscatter diffraction (EBSD) and Orientation distribution function (ODF) analysis

Inverse Pole Figure (IPF) map and ODFs at $\varphi_2 = 0°$ and $45°$ sections in the Euler $(\varphi_1, \phi, \varphi_2)$ space of investigated samples are presented in Figure 32. For rolled strips, the crystallographic orientations are represented by the Miller index (hkl)[uvw] combining of crystallographic plane and direction. In this case, (hkl) is the plane parallel to the rolling plane (RP), and [uww] is the direction parallel to the rolling direction (RD). The results revealed that mainly {001}//RP crystallographic orientations were predominant in the as-received sample. This was attributed to the recrystallized grains which were formed during the hot rolling process. At the same time, sharp orientation change to {110}//RP textures were found in samples subjected to cold-rolling. A remarkable texture re-orientation took place during cold-rolling to 50% reduction, where Goss (110)[001], Brass (110)[2 $\bar{2}$ 1], and {110}<112> texture components were dominant by increasing the cold rolling reduction (KESTENS, 2016).

Although the development of Brass to Goss texture components due to the lattice shear invariant (KESTENS, 2016), the development of sharp {110}<112> crystallographic texture is commonly observed in FCC metals with low SFE, i.e.<25 mJm^{-2} (DE COOMAN, 2018). In austenitic high-Mn steel, slip and twinning is the predominant plastic deformation mechanism and the deformation mode is governed by the value of the SFE. The slip takes place on the most dense-packed planes and directions as a function of the crystal structure. For instance, the {111}<110> is the main slip system in the FCC materials.

With decreasing the SFE values, the ability of plastic deformation by slip decreases, thereby, deformation occurs mainly by twinning mechanism. In this scenario, the twinning mainly takes places on {111} twinning planes and <112> twinning direction (. Moreover, the development of τ-fiber corresponds to orientations having a <110> direction along the line, in the section, i.e., {110}<001> orientation, as reported by Hirsch et al., (1988). The drastic reduction of cleavage (001) planes accompanied by a high fraction of denser atomic (110) planes may facilitate slip under external load application.

Shear deformation induced by the friction between the sample and the rolls is the main reason of crystallographic texture formation especially at the surface. In order to demonstrate the influence of shear stress caused by rolling deformation, skeleton plots for main texture fiber including (001), (111), and (101) crystallographic planes oriented along rolling plane were plotted from their ODFs and are presented in Figure 33. The as-received hot-rolled austenitic steels had predominant (001) and (111) crystallographic texture parallel to the rolling

plane due to the dynamic recrystallization during hot deformation (MASOUMI, 2017).

Meanwhile, the intensity (i.e., normalized number of grains) of these fibers reduced by increasing the cold rolled reduction. On the other hand, the (101) grains oriented along rolling plane were developed gradually with increasing the cold deformation. The formation of shear bands in austenitic grains caused a rotation of in-band crystal into the <110> crystal axis to increase the fraction of softened austenite phase by reducing the stored-energy by means of the mechanism known as strain induced boundary migration (MOURA, 2021) (BRUNA, 2011). Recently, Kamali et al., (2021), reported that the (110) oriented austenitic grains encompass a higher fraction of deformation due to the slip activity.

Figure 32 — Inverse Pole Figure map and Orientation Distribution Function at φ_2=0° and 45° sections of samples (a) as-received, cold-rolled to (b) 50% and (c) 70% reduction.

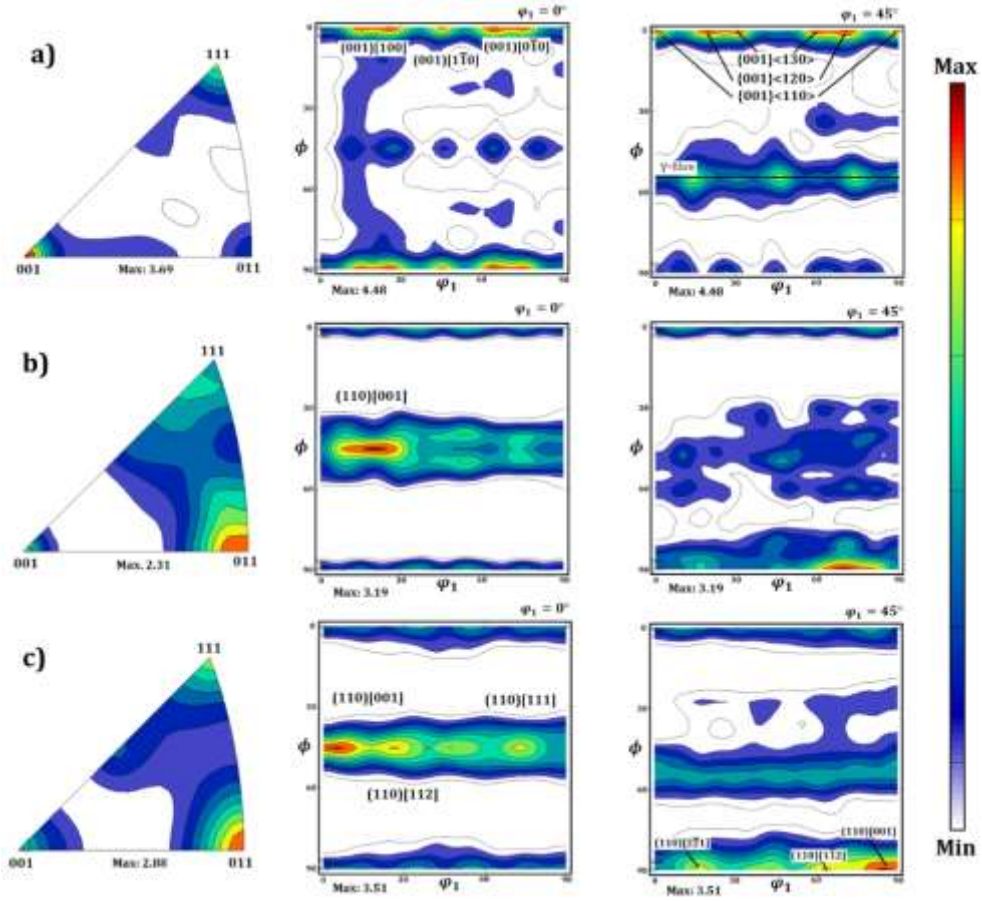

Source: Elaborated by the author.

Figure 33 — Skeleton plots of main fibres crystallographic texture (i.e., (001)//RP, (111)//RP, and (101)//RP) – RP: rolling plane of all investigated sample.

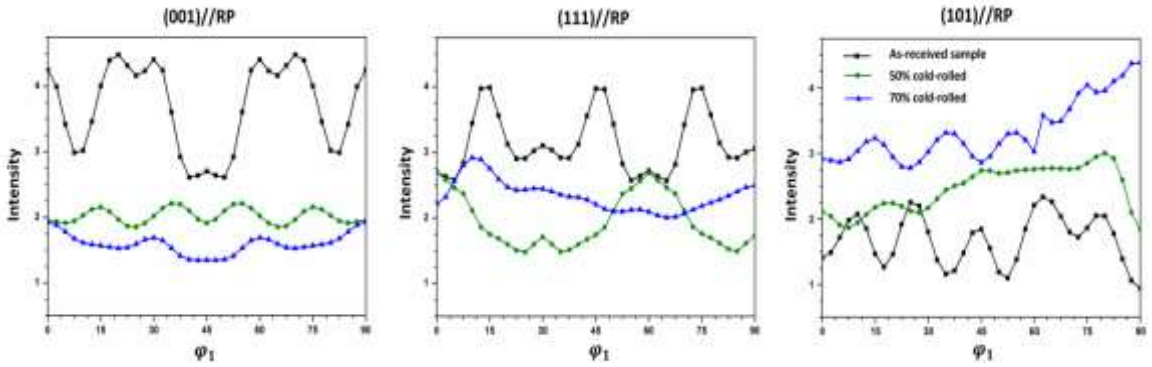

Source: Elaborated by the author.

The orientation image maps (OIMs) of as-received and cold-rolled samples to 50% and 70% reduction obtained by EBSD technique are depicted in Figures 34. These figures revealed that by increasing the amount of deformation, a gradual orientation gradient develops within the grains. The as-received sample had (001)[100] and (001)[120] preferred crystallographic orientations. The presence of cleavage cube (001)[100] component could be related to the fine columnar grains developed during solidification in the direction of the maximum heat conduction accompanied with dynamic recrystallization during hot deformation (ZINOVIEVA, 2020).

Zhang et al., (2016), reported that the {001}<120> components mainly originate during recrystallization of {001} columnar grains and exhibits a low mechanical and corrosion resistance. The results of the present investigation showed that (011)[0$\bar{1}$1] and (221)[1$\bar{1}$0] texture components were developed during cold-rolling to a 50% reduction. Rotated Goss (011)[0 $\bar{1}$ 1] texture component relate to α-fiber (<011>//RD) forms parallel to stress promoting the formation of slip bands during strain. The formation of deformation bands could be attributed to the activation of the different slip systems inside the grain. Thereby, it leads to the different sets of rotation associated with strain accommodation and crystallographic orientation (FENG, 2021). Shamanian et al., (2014), reported the presence of (221)[1$\bar{1}$0] texture components in austenitic stainless steel by the reorientation of (001) grains toward loading direction under high strain due to the twinning deformation mechanism.

With increasing the rolling reduction to 70%, (011)[0 $\bar{1}$ 1] and (331)[1 $\bar{1}$ 0] components were predominant. This can be attributed to the formation of subgrains and substructures in the austenite. Strong rotated Goss (011)[0$\bar{1}$1] and (331)[1$\bar{1}$0] components

aligned <011>//RD fibre correlates well with the peak broadening in the (220)γ planes. No phase transformation occurred during cold rolling and it is notable a formation of sharp texture (FENG, 2021).

Point-to-point misorientation between two adjacent crystals represents the local plastic strain originated from the lattice distortion (DESPRÉS, 2020). In contrast to transmission electron microscopy, the conventional EBSD technique is not able to visualize the spatial resolution below 100 nm. Thereby, the boundary misorientations of less than 2.0° cannot be reliable resolved (SCHWARTZ, 2000). Table 2 provides the fraction of low angle boundaries (LABs, 2° < Θ < 5°) medium angle boundaries (MABs, 5° < Θ < 15°), high angle boundaries (HABs, 15 ° < Θ), and coincidence site lattice (CSL) boundaries. The as-received hot rolled sample contains lowest fraction of low and medium angle misorientations due to dynamic recovery and recrystallization during the strip fabrication, allowing significant dislocation annihilation in this sample. The fraction of LABs and MABs is gradually increased by progressing degree of rolling reduction. High amount of dislocations and crystallographic defects are generated during cold deformation-rolling. Dislocation cell boundaries are first formed, and then deformation-induced boundaries are developed by increased the amount of rolling reduction. Results showed that a gradual increase in misorientation inside the grain with progressing the rolling reduction led to grain fragmentation and re-oriented texture components.

Figure 34 — Orientation Image Maps and corresponding ODFs at constant φ_2=0° and 45° sections of samples (a) as-received, cold-rolled to (b) 50% and (c) 70% reduction.

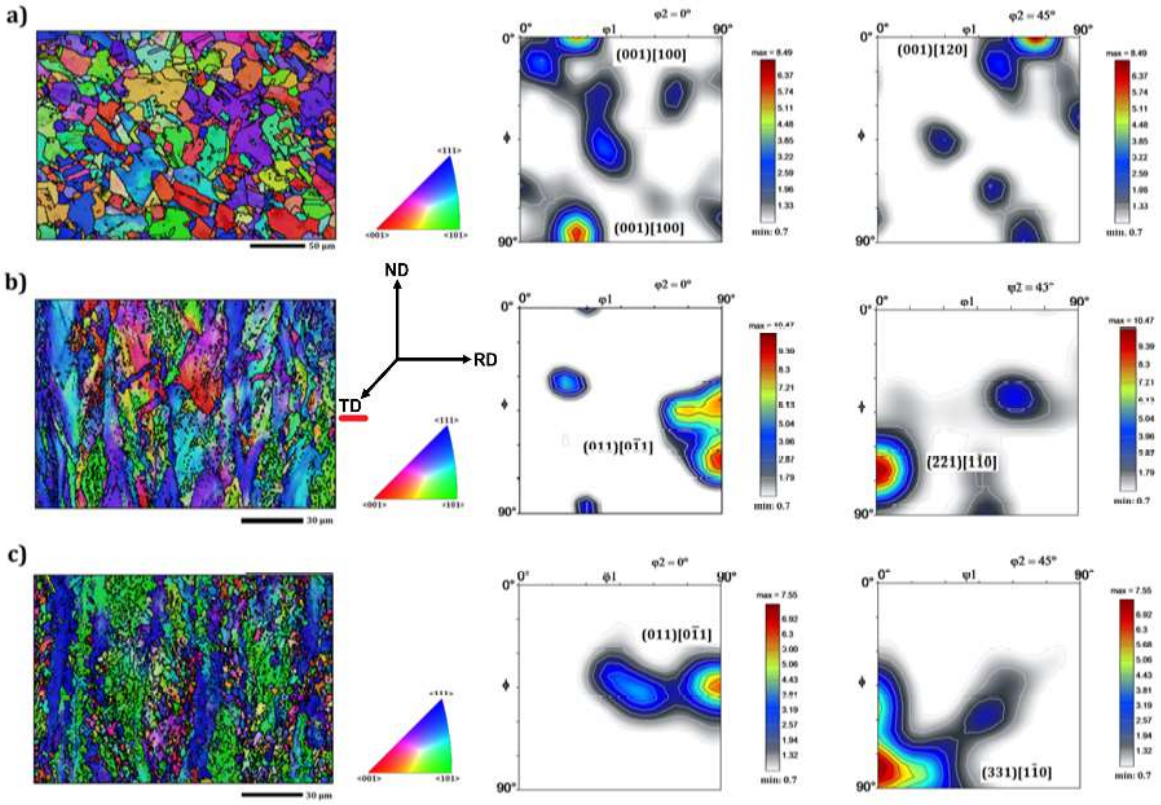

Source: Elaborated by the author.

Table 2 — Grain boundaries characteristics in investigated specimens (% of boundaries).

Type of grain boundaries	As-received	50% cold-rolled	70% cold-rolled
LABs (2° < Θ < 5°)	0.31	0.43	0.49
MABs (5° < Θ < 15°)	0.01	0.25	0.29
HABs (15 ° < Θ)	0.68	0.32	0.22
CSLs	0.10	0.15	0.23

Source: Elaborated by the author.

The development of low-energy CSL boundaries including $\sum 3^n$ twinning boundaries is commonly observed in austenitic steels (BELADI, 2013). The results of the present study also revealed that the highest portion of CSLs belongs to the 70% of cold rolled sample due to the formation of slip bands and deformation twins. Deformation-induced twinning in the cold-rolled samples could be associated with the planar slip bands as proposed by Guan et al., (2020). They suggested that planar-slip dislocation contains many Shockley partial dislocations that generate massive deformation twins by absorbing the planar-slip

dislocations. Notably, the fraction of CSL boundaries increases with progressing the amount of deformation. The crystallographic anisotropy also plays a significant role in the development of lattice distortion including misorientation and this should be discussed on a grain-to-grain level. However, this is not the object of this study.

Although point-to-point misorientation refers to the relative orientation changes between two adjacent crystal orientations due to relative lattice rotation, the Kernel Average Misorientation (KAM) analysis evaluates misorientation between reference points with defined numbers of neighboring points within the grain. It is well known that the KAM analysis with a threshold of 5° has the purpose of eliminate the effect of subgrains (FUJII, 2021). Therefore, the strain distribution within the crystal grains can be estimated using the local change in orientation between third neighboring pixels following the KAM analyses. The quantitative results are shown in Figure 35. The highest portion of low KAM values (KAM < 1°) was found in the as-received sample. This could be attributed to the dynamic recrystallization with strain-free grains developed during hot deformation. With increased degree of cold-rolling reduction, a significant fraction of deformed grains with high medium (1° < KAM < 3°) and high (KAM > 3°) was developed. High values of KAM's could be associated with high local lattice distortion and dislocation density resulting in increasing of internal energy (VICENTIS, 2017).

The as-received sample with recrystallized austenitic grains exhibited the lowest inter-granular misorientation within the microstructure. The formation of dislocation cells and dislocation tangles during cold-rolling increases the lattice distortion within the grain detected by KAM analyses. The kernel average misorientation distribution presented in Figure 35 and Table 3 exhibits the variation of KAM values due to the misfit strains induced during deformation. Crystallographic defects (i.e., dislocations and grain boundaries) that were generated during plastic deformation were absorbed and united to developing the dislocation cells, low-angle boundaries and micro-twins. Thereby, the localized stored strain energy due to lattice misfit acts as a barrier against dislocation glide, resulting in the increased strength accompanied by deterioration in ductility (VICENTIS, 2017).

Figure 35 — Kernel average misorientation distribution of all investigated specimens.

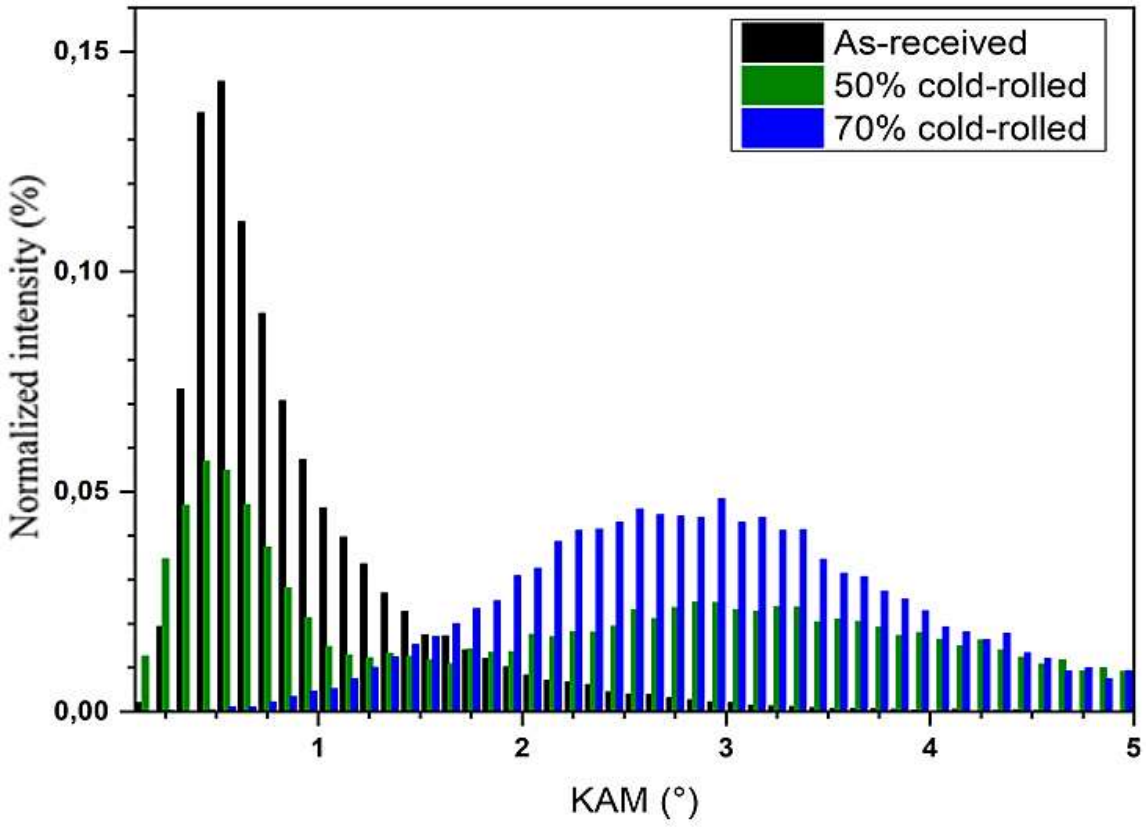

Source: Elaborated by the author.

Table 3 — Variation of volume fractions of KAM values of investigated specimens.

KAM value	As-received	50% cold-rolled	70% cold-rolled
Low	0.70	0.34	0.01
Medium	0.29	0.33	0.55
High	0.01	0.33	0.44

Source: Elaborated by the author.

The EBSD analysis was carried out to determine the volumetric fraction of CSL boundaries and quantify the increase in the probability of <111>formation and boundaries associated the mechanical twins. Although a gradual increase in the volume fraction of CSL boundaries was observed by increasing degree of the rolling reduction, more than 90% of CSL boundaries were attributed to the Σ3 deformation-induced twin boundaries. Figure 36 shows the correlation with local slip bands formed under cold deformation with special boundaries identified by EBSD technique. Also, the volumetric fraction of low Σ CSL boundaries is listed in Table 4. In general, mechanical twins contribute to the superior mechanical properties of

TWIP steels.

Tokita et al., (2017), reported enhanced mechanical properties by forming of the low-energy Σ3 twin boundaries during the thermomechanical processing which reduces the total boundary energy in a triple junction. Shimada et al., (2002), indicated that events and reactions of active twins increase the frequency of CSL boundaries. Well-distributed low-angle boundaries in the grain contour network create a discontinuous chain that can disrupt the percolation of intergranular surface corrosion, which is of interest to petroleum industry.

Figure 36 — SEM and (b) CSL boundaries map of 50% cold rolled sample.

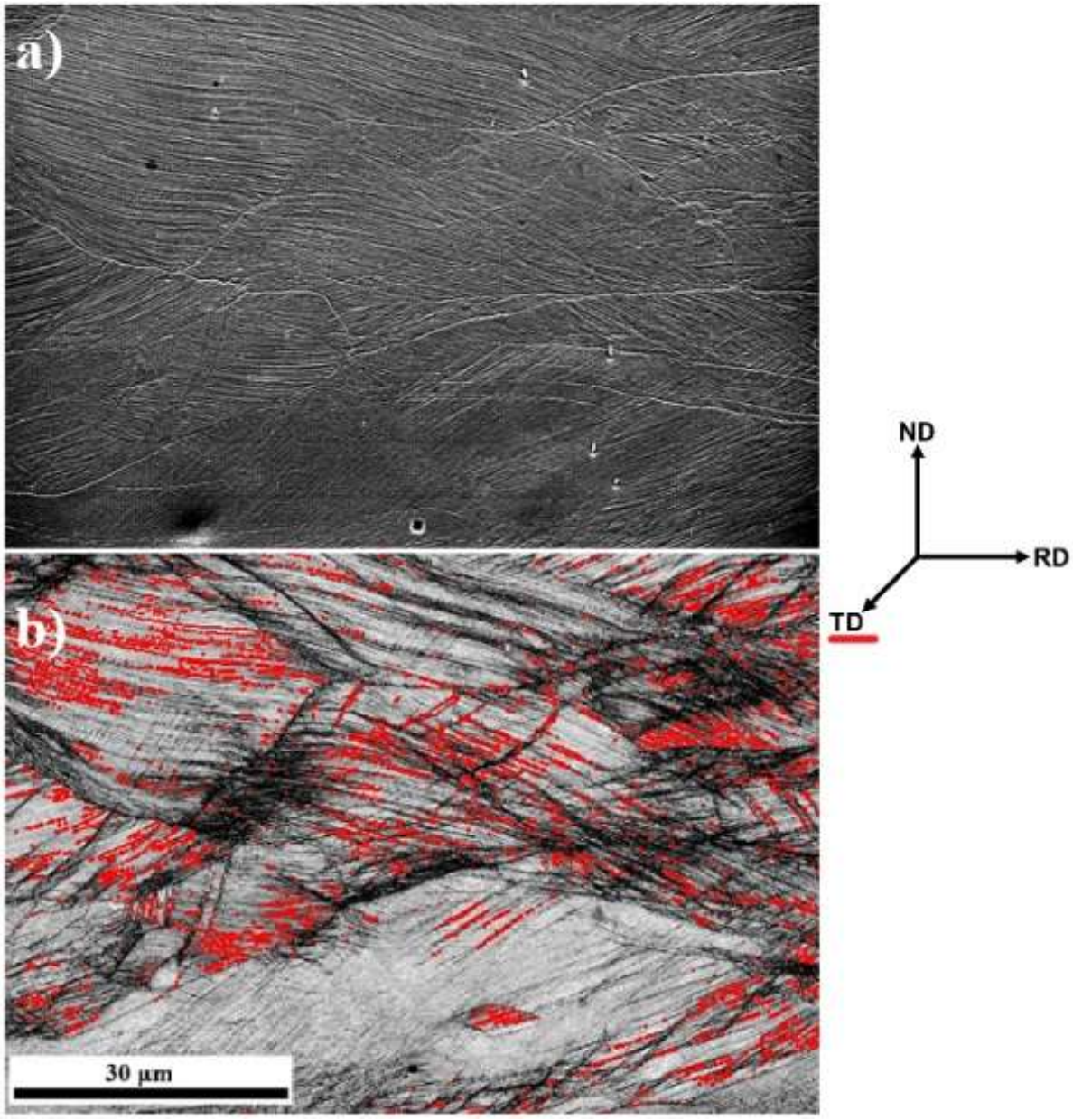

Source: Elaborated by the author.

The activated slip systems of grains associated with the rolling direction were examined in terms of Schmid factor. The maximum value of Schmid factor during rolling was estimated to be 0.7, Figure 37. The soft grains with high Schmid factor values tends to slip easily, while the hard grains (low Schmid factor) required higher shear stress to provide adequate slip systems required for deformation. Figure 37 revealed that most of the grains in the 50% cold-rolled sample exhibited the Schmid factor values higher than 0.4, thereby, tend to deform easily. The fraction of grains with low Schmid factor values increased after 70% cold rolling reduction, indicating more resistance against plastic deformation.

Table 4 — Volumetric fraction of Σ CSL orientation relationships of investigated specimens.

Σ	Angle	Axis	Volumetric fraction (%)		
			as-received	50% cold rolled	70% cold rolled
3	60.0000	<111>	16.213	18.589	24.412
5	36.8699	<100>	0.172	0.211	0.298
7	38.2132	<111>	0.144	0.215	0.238
9	38.9424	<110>	1.653	0.653	0.943
11	50.4788	<110>	0.131	0.312	0.460
13a	22.6199	<100>	0.009	0.023	0.029
13b	27.7958	<111>	0	0.049	0.045
15	48.1897	<210>	0.115	0.098	0.208
17a	28.0725	<100>	0.034	0.025	0.020
17b	61.9275	<221>	0.087	0.193	0.250
19a	26.5254	<110>	0.034	0.041	0.051
19b	46.8264	<111>	0.062	0.066	0.087
21a	21.7868	<111>	0	0.006	0.012
21b	44.4153	<211>	0.065	0.210	0.193
23	40.4591	<311>	0.021	0.118	0.149
25a	16.2602	<100>	0.003	0.016	0.014
25b	51.6839	<331>	0.087	0.119	0.209
27a	31.5863	<110>	0.306	0.048	0.098
27b	35.4309	<210>	0.187	0.046	0.117
29a	43.6028	<100>	0.046	0.066	0.057
29b	46.3972	<221>	0.046	0.041	0.153
	sum		19.427	21.154	28.052

Source: Elaborated by the author.

The FCC crystal structure contains 12 slip systems, considering four octahedral {111} planes with three close-packed <110> directions on each plane. The calculation of slip systems and their corresponding volume fractions in austenitic high-Mn steel according to (Lin,

1965) were carried out using the ATEX analysis software and results are listed in Table 5. Results showed that the same active slip systems, including $(1\bar{1}\bar{1})[101]$, $(1\bar{1}\bar{1})[110]$, $(1\bar{1}1)[011]$, $(1\bar{1}1)[110]$, $(111)[01\bar{1}]$, and $(111)[10\bar{1}]$, are common in all investigated specimens. According to the Von-Mises theory, at least five active slip systems are required for plastic deformation; thereby, the six mentioned activated slip systems prevent dislocation accumulation (LIN, 1965) (GIRARD, 2021).

Figure 37 — Schmid factor maps of samples (a) as-received, cold-rolled to (b) 50% and (c) 70% reduction.

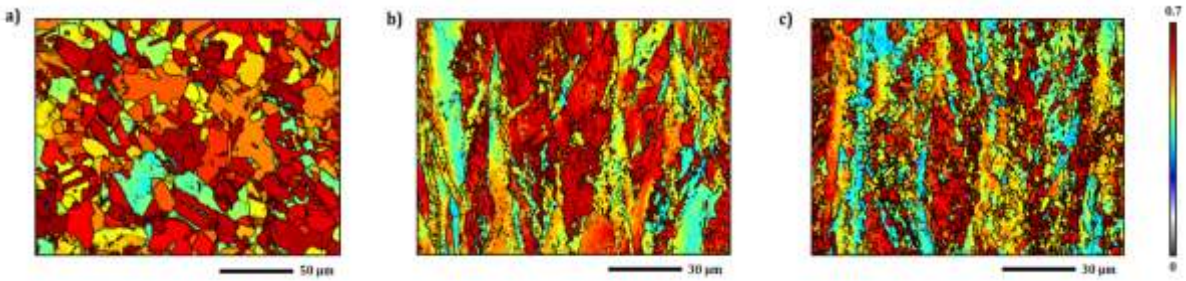

Source: Elaborated by the author.

Table 5 — Slip systems and their corresponding volume fractions.

Slip system	As-received	50% cold-rolled	70% cold-rolled
(1 1 $\bar{1}$) [0 1 1]	0.364	0.705	0.865
(1 1 $\bar{1}$) [1 0 1]	0.020	0.943	0.787
(1 1 $\bar{1}$) [1 $\bar{1}$ 0]	0.007	0.020	0.149
(1 $\bar{1}$ $\bar{1}$) [0 1 $\bar{1}$]	0.382	0.248	0.154
(1 $\bar{1}$ $\bar{1}$) [1 0 1]	23.145	13.828	19.034
(1 $\bar{1}$ $\bar{1}$) [1 1 0]	16.669	18.466	22.455
(1 $\bar{1}$ 1) [0 1 1]	16.003	16.261	16.416
(1 $\bar{1}$ 1) [1 0 $\bar{1}$]	0.544	0.346	0.250
(1 $\bar{1}$ 1) [1 1 0]	9.518	33.425	23.237
(1 1 1) [0 1 $\bar{1}$]	18.194	5.898	8.355
(1 1 1) [1 0 $\bar{1}$]	15.155	9.775	8.050
(1 1 1) [1 $\bar{1}$ 0]	0.002	0.084	0.250

Source: Elaborated by the author.

5.3.4 Mechanical tensile tests

Tensile tests were carried out to determine mechanical properties and these are presented in Figure 38. Please note some serrated flows in tensile test curves of the as-received sample caused by the dynamic strain aging induced from interactions between partial dislocations and C-Mn clusters (JO, 2021).

On the one hand, the yield stress and ultimate tensile strength significantly increased by increment in deformation degree. On the other hand, the total elongation drastically decreased from ~89% to 17% in the 70% cold-rolled sample. In the as-received sample the high elongation was associated with high glide planarity of dislocations in the austenitic matrix that enhances the TWIP effect during the tensile test. In addition, in the sample submitted to 70% cold-rolling a high level of lattice distortion was evidenced by XRD analysis, Figure 31. This leads to both the highest tensile strength (1.7 GPa) and the highest strain hardening beside fine grain strengthening effect. Moreover, the XRD and microstructure results revealed, that a fully austenitic structure is present in the 70% cold rolled samples. The toughness decreased proportionally the deformation applied. Still remained high even with the refinement of the grain and highest tensile strength. It is noteworthy that the values reported by Skilbred et al., (2020), yield tensile strength, ultimate tensile strength and toughness for conventional Fe-C-Mn steels currently used in the petroleum industry are lower than those of cold-deformed samples of high-Mn steel investigated in this work. Thereby, a considerable mechanical and corrosion resistance (by the Cr and Cu contents) can be expected in these samples, for being purely austenitic, favoring application in petroleum industry (CHENG, 2021) (WANG, 2020) (LI, 2020).

Figure 38 — Engineering stress-strain curves.

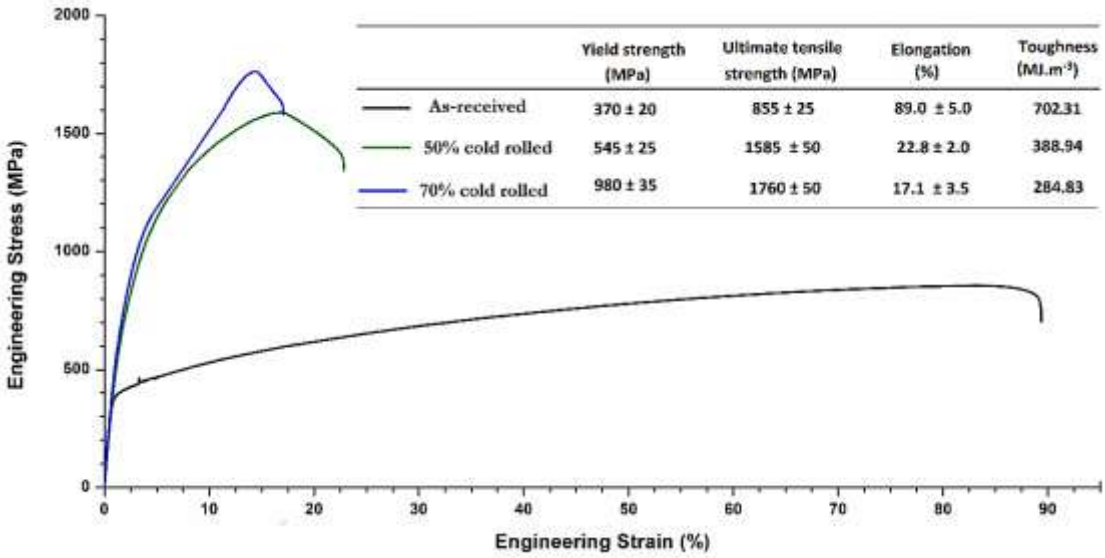

Source: Elaborated by the author.

Figure 39 illustrates the true tensile stress, σ, and strain hardening rate curves (dσ/dε) versus strain plots for the as-received specimen in addition to samples subjected to cold rolling. It is possible to verify that the samples tested obeyed the Considère criterion, which establishes that the maximum load is the point of the beginning of the formation of the "neck" in the test body (reduction of the cross-sectional area), where the strain hardening rate is equal to the tension. Specimens present strain hardening rate curves with three defined stages (RENARD, 2012) (KUSAKIN, 2016).

The plot of the as-received sample shows that the plastic deformation can be divided into three stages: first, a dramatic decrease in the strain range of 0–0.028 (Stage A) that corresponds to the elastic-plastic transition; second, a slight decrease until 0.12 strain (Stage B), which may be associated with plastic deformation governed by the slip of the dislocations, and finally, above 0.13 strain an decrease in hardening rate is observed by deformation (stage C). It interrupts the linear decline of the deformation hardening rate observed in stage B and delays the asymptotic approach for zero deformation hardening (constant state). This behavior is similar to the one found for TWIP steels, with no increase in the strain hardening rate during stage B and with its marginal decrease during stage C. The SFE values for the studied steel favored the mechanical twinning. This decrease is even more pronounced during secondary twinning since secondary twinning systems are less active and this is reflected in lower strain hardening rates during stage B and especially in stage C when compared to other TWIP steels

such as FeMnC TWIP steels (BARBIER, 2009) (JIN, 2009) (JAE, 2012) (GUTIERREZ-URRUTIA, 2011) (MIN, 2017).

Figure 39 — Strain hardening rate (dσ/dε)-true strain curve.

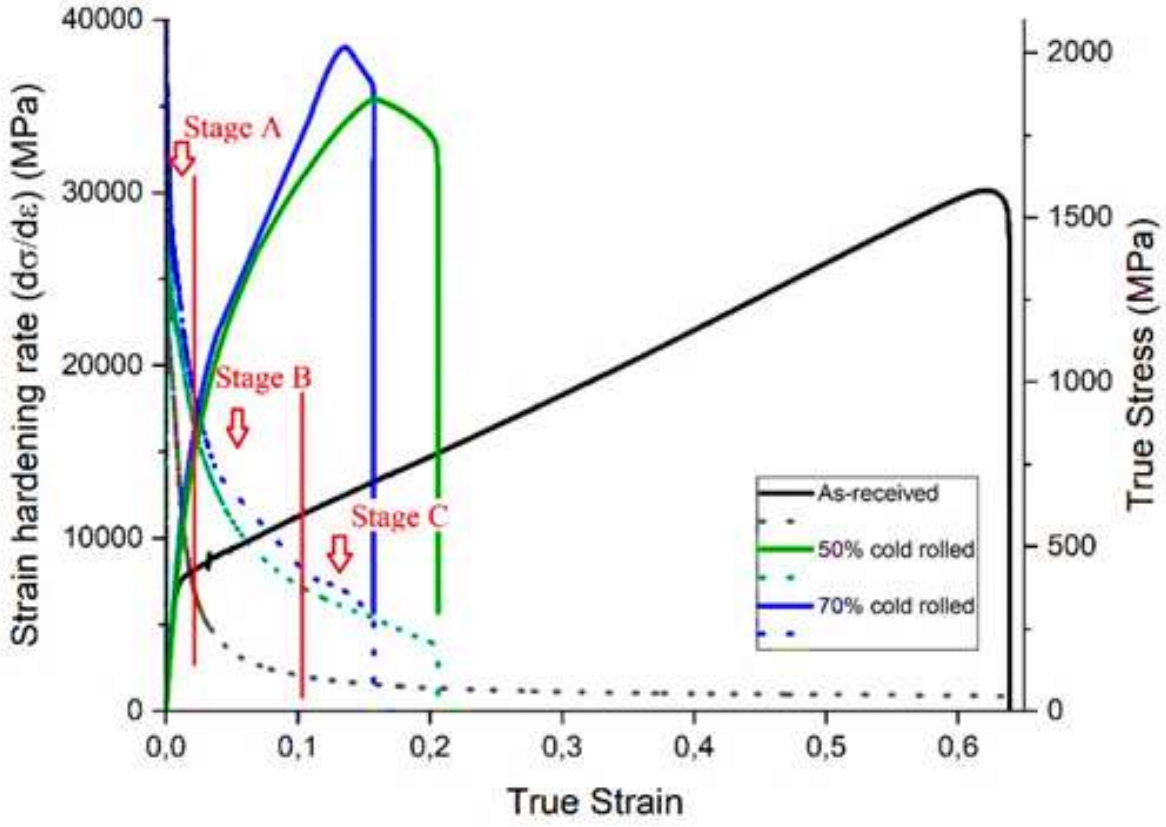

Source: Elaborated by the author.

5.3.5 Fracture analysis

The fracture surfaces samples were investigated, and are presented in Figure 40. The fractography of as-received sample mainly contains the fibrous zone with some dimples with different sizes and depths and shear lip zone, indicating the good plastic deformation capacity. Dimple fracture mode corresponds to the nucleation and growth of micro-cracks originating at the intersection of slip bands and grain boundaries.

Ren et al., (2021), reported that the larger and deeper dimple improves the plastic deformation capacity. At the same time, some noticeable differences in fracture morphology between the as-received and cold-rolled samples are observed. Although typical ductile fracture features were observed in the as-received sample, the brittle fracture facets were found in the cold-rolled specimens. Shear bands intersection shown in the deformed microstructure acts as

favorable sites for micro-crack initiation due to the stress concentration. In addition, the induced misfit strains revealed by the Schmid factor analysis facilitate crack propagation by providing a low-energy transgranular crack trajectory, which is consistent with the low tensile ductility presented in Figure 40. Notably, the ductile-brittle fracture mode observed in the 70% cold-rolled sample could be associated with formation of the high fraction of low-energy Σ3 twin boundaries, which minimized the localized stored strain energy and lattice misfit to promote dislocation glide.

Figure 40 — Fracture surfaces of the fractured tensile test specimens (a) as-received, (b) 50%, and (c) 70% cold-rolled.

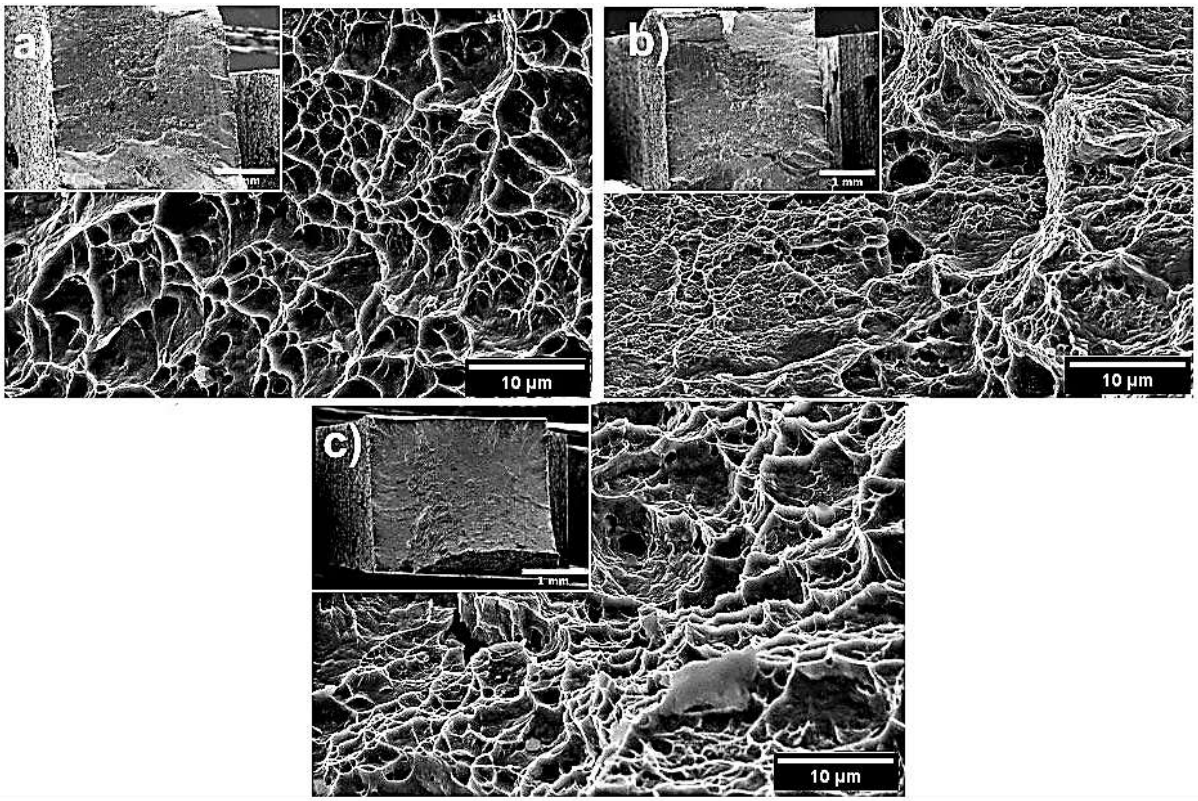

Source: Elaborated by the author.

6 RESULTS: EQUAL CHANNEL ANGULAR PRESSING

EQUAL CHANNEL ANGULAR PRESSING OF AN EXPERIMENTAL TWIP STEEL WITH THE ADDITION OF CHROMIUM: MICROSTRUCTURE, CRYSTALLOGRAPHIC ORIENTATION AND MECHANICAL PROPERTIES.

6.1 Review

The Severe Plastic Deformation (SPD) technology, based on the application of considerable shear stresses at high pressures, is a promising technique to significantly upgrade the grain refinement of metallic materials beyond the limitations of conventional metal forming processes (VALIEV, 2004). Few researchers have focused on the SPD of high-Mn TWIP steels (MATOSO, 2012) (ABRAMOVA, 2016). Both used high-pressure torsion (HPT) on different TWIP steels, and both set up significant improvements in microstructure, hardness, and yield stress.

Equal-channel angular pressing (ECAP), another SPD technique, can produce bulk nanostructured workpieces of much larger size. The first investigations of TWIP steels subjected to ECAP showed that the microstructure was significantly modified after one ECAP pass (BAGHERPOUR, 2012) (TIMOKHINA, 2014) (VALIEV, 2013). Many researchers reported (LEI, 2017) (ABRAMOVA, 2021) (HAASE, 2016) (TIMOKHINA, 2014), a complex microstructure composed of a mixed substructure (deformation microbands, dislocation tangles and cells, nano and micro-twins, fragments and subgrains, stacking faults) in TWIP steels submitted to multi-pass ECAP. Nucleation of nano twins inside micro-twins/microbands was also observed (TIMOKHINA, 2014). Timokhina et al., (2014), reached a high-strength state (yield stress of 1480 MPa and ultimate tensile stress of 1624 MPa) in the alloyed Fe–0.61C–22.3Mn–0.19Si–0.14Ni–0.27Cr TWIP steel. Nevertheless, the accumulated strains are usually applied not to exceed four ECAP passes because TWIP steels are tough to process by ECAP, i.e. the specimen can sometimes undergo fracture even after a single ECAP pass (HAASE,

2016).

Some authors claim that the temperature to modify the dominant deformation mode for dislocation slip is approximately 300 °C, however, there are authors who observed twinning activity even after ECAP at 400 °C (LEI, 2017) (HAASE, 2016) (BAGHERPOUR, 2012) (TIMOKHINA, 2014). A recent review states that the highest yield stress and ultimate tensile strength values for a TWIP steel processed by ECAP are 1480 MPa and 1675 MPa, respectively. These values have not yet been overcome. It is noteworthy that when comparing the absolute values of mechanical properties reported in the literature, the content of alloy elements also needs to be considered because the chemical composition of high-Mn TWIP steel can vary significantly (TIMOKHINA, 2014) (HAASE, 2016) (YANG, 2021).

An important point of this work is related to the chemical composition of the evaluated TWIP steel. It is an aluminum-free steel with a high chromium content and presence of copper (SANGWON, 2011). The addition of copper retards the kinetics of twin formation and influences the type of serrations on the stress–strain curve. The copper additions also resulted in a remarkable increase in total elongation without a loss of strength (SANGWON, 2011). There are few reports about consequences regarding the application of severe plastic deformation in steels with high levels of Mn and medium C with TWIP effect. To the best of our knowledge, little attention has been devoted to investigating the mechanical behavior of the novel proposed TWIP of this research processed by ECAP. This study thus aimed to assess the detailed parameters used during SPD and describe the microstructural evolution by means of electron back-scattered diffraction (EBSD), scanning electron microscopy (SEM), texture, and their influences on final mechanical properties.

6.2 Methodology

Cylindrical specimens of 8 mm in diameter and 55 mm in length were machined from the supplied material. The chemical composition of steel is listed in Table 1. The samples were subjected to ECAP process. This technique consists of a repetitive process of pressing the billet through the die-set, which consists of channels with the same periphery bisected at a certain angle. The geometry of the process performed simple shear. The layout of the apparatus allows for high stresses on bulk parts of different metallic materials. ECAP principles and their effect on the microstructure refinement and improvement of the multifunctional properties of other steels and alloys have been reported elsewhere (VALIEV, 2006).

The die used for ECAP experiments was manufactured with tool steel, and inside,

contains an insert die of two channels intersecting at an internal angle Φ = 120° (see Figure 41). The specimens were submitted to severe plastic deformation by the route Bc (specimen rotation of 90° along its longitudinal axis in the same direction after each pass (RAAB, 2022). Experiments were conducted at 350 ºC and a maximum of 8 passes using a hydraulic press with a maximum capacity of 80 tons and a punch speed of 2 mm/s were employed. According to Iwahashi's relationship, these angles promote approximately a true strain of 0.6 approximately after each pass (IWAHASHI 1997). The calculated SFE value was ~21 mJ/m^2, for the composition of Table 1, at room temperature, and 69 mJ/m^2 and 53 mJ/m^2 at 350 °C and 250 °C, respectively (ALLAIN, 2004) (DUMAY, 2008). A mixed lubricant of molybdenum disulfide (MoS_2) and graphite powder was used to reduce friction between the die wall and the punch and specimen.

Figure 41 — (a) Route Bc and ECAP die configuration and the corresponding coordinates system used in current research; ND normal direction, ED extrusion direction, TD transverse direction. (b) selected zones to analyzing the microstructure, microtexture and (c) micro-tensile specimens.

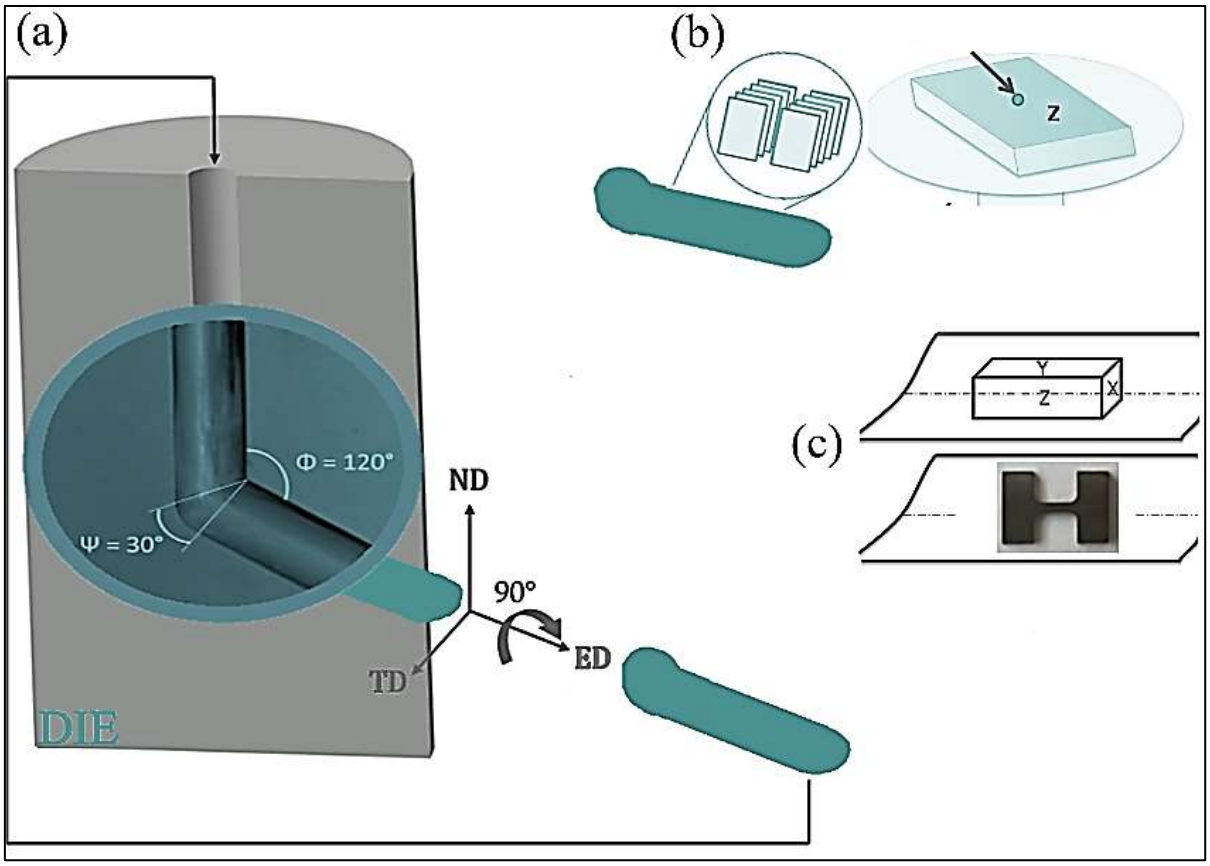

Source: Elaborated by the author.

The samples were prepared using standard metallographic procedures, including grinding (#400 to #1200 SiC papers) followed by mechanical polishing using 6, 3, and 1 μm diamond paste and, finally, 0.05 μm colloidal silica suspension. A chemical etching with (40% HNO_3 + 60% H_2O) solution was used for 3 seconds. Microstructural studies were carried out along the transverse plane in the received and deformed specimens using Optical Microscopy (OM) and Electron Microscopy in a FEI Quanta FEG 450 (Fortaleza, Ceará, Brazil).

Before and after the ECAP process, phase identification was analyzed using an X-ray diffractometer (XRD, Panalytical X'Pert Pro, Fortaleza, Ceará, Brazil) equipped with Co (Kα1=1.78897 Å) radiation source. The scanning rate and range of XRD analysis were 0.5°/min and 45° ~ 120°, respectively. The plane distance of interfered atomic planes was calculated by Bragg's Law $(2 \cdot d \cdot sin\theta = n \cdot \lambda)$ where d is the spacing between atomic planes, 2θ is the diffraction angle, n is an integer, and λ is the wavelength. The position of the diffraction peak can be affected by homogeneous and inhomogeneous local strains, which can be calculated by the Sherrer methodology (MASOUMI, 2017).

EBSD samples were prepared by grinding using #400 to #2000 SiC papers. This was followed by an electrolytic polishing solution (60% ethanol + 34% n-butanol + 6% perchloric acid), with a voltage of 20 V and current ranging from 0-2 A for 1-3 minutes at temperature of 10 °C. Lastly, the samples were polished with 0.05 μm colloidal silica slurry for 45 min. EBSD scans were run over FEI Quanta FEG 450 (Fortaleza, Ceará, Brazil) and JEOL JSM-7001F (FE-SEM, Barcelona, Spain) microscopes operated at 20 kV. The working distance was set to about 13 mm with a tilt angle of 70°. Figure 41 shows the extrusion direction (ED), the normal direction (ND), and the transverse direction (TD) and are parallel to 'x', 'y', and 'z', respectively. Different scan step sizes were used: 0.3 mm for the annealed condition, 0.1/0.05 mm for the sample with 2 ECAP passes, and 0.03 mm for the sample with 4 and 8 passes. The indexation rate was above 95% for the initial condition sample and was maintained at 70% for the samples after the ECAP procedure. The results were post-processed utilizing the HKL Channel 5 software. The grain boundaries were identified as high-angle boundaries in which misorientation was above 15º, while subgrain boundaries were low-angle boundaries with a misorientation between 2º and 15º. For the twin boundaries, a specific misorientation was chosen. Microtexture images were performed using the ATEX data processing software. ODFs were determined from EBSD maps through the statistical Kernel density estimation method.

The micro-tensile specimens, with the shape specified in Figure 41, were machined from the middle of the longitudinal section of the samples processed by ECAP. Tensile testing was carried out using a micro-test (DEBEN, Barcelona, Catalunya, Spain) machine at a cross-

head speed of 3.3 x 10^{-3} mm/s (quasi-static loading conditions). The fracture surfaces were examined under a scanning electron microscope with a field emission gun JEOL JSM-7001F (FE-SEM, Barcelona, Catalunya, Spain) operated at 20 kV. High-resolution fracture graphs were obtained for discussion.

6.3 Results and discussion

6.3.1 Microscopy analysis

The micrographs were taken at the cross sections, i.e., normal direction parallel to the 'z' axis, for all samples, i.e., as received and after 1, 2, 4 and 8 ECAP passes. Figure 42(a) exhibits a refined austenitic microstructure, with mostly equiaxed grains containing abundant thermal twins originated from the hot-rolling process and a few mechanical twins arising from the sample preparation. The measured micro-hardness value was 202±5 HV. The as-received sample is consistent with the observation reported by Lima et al., (2022) and (HAASE, 2016). Figure 42 (b, c, d, e) depicts the microstructure after 1, 2, 4, and 8 ECAP passes, respectively. Mechanical twins (green arrow) gradually increased with increasing the number of ECAP passes. After 1 ECAP pass, grains were elongated along the shear direction. Plastically deformed and longitudinally elongated grains were observed, see Figure 42(b). The formation of mechanical twins is associated with low Stacking Fault Energy (SFE). Despite the increased SFE of the material due to the deformation temperature at 350 °C, suitably oriented grains exhibited high reactions of deformation twin bundles, as exemplified by the inset in Figure 42. The longitudinal deformation features were identified to be dislocation slips, bands, deformation twins, and grain-scale micro shear bands. After two, four, and eight passes, plastic deformation of the grains along the shear direction was also observed in continuous shearing in the planes after sample rotation between each pass (Fig 42(c), (d), and (e)).

This analysis agrees with other research published elsewhere (ABRAMOVA, 2021) (HAASE, 2016). Micro-hardness values increased to 441±8 HV (Figure 43) after 1 ECAP pass. In samples subjected to 8 ECAP passes, the mechanically induced twinning occurred on deformation micro shear bands, increasing the micro-hardness to about 566±11 HV.

Figure 42 — FEG-SEM secondary electron micrographs of specimens (a) as-received, (b) after 1 ECAP pass, (c) after 2 ECAP pass, (d) after 4 ECAP pass, and after 8 ECAP pass (e). Mechanical twins are highlighted with white arrows while annealing twins are marked in red.

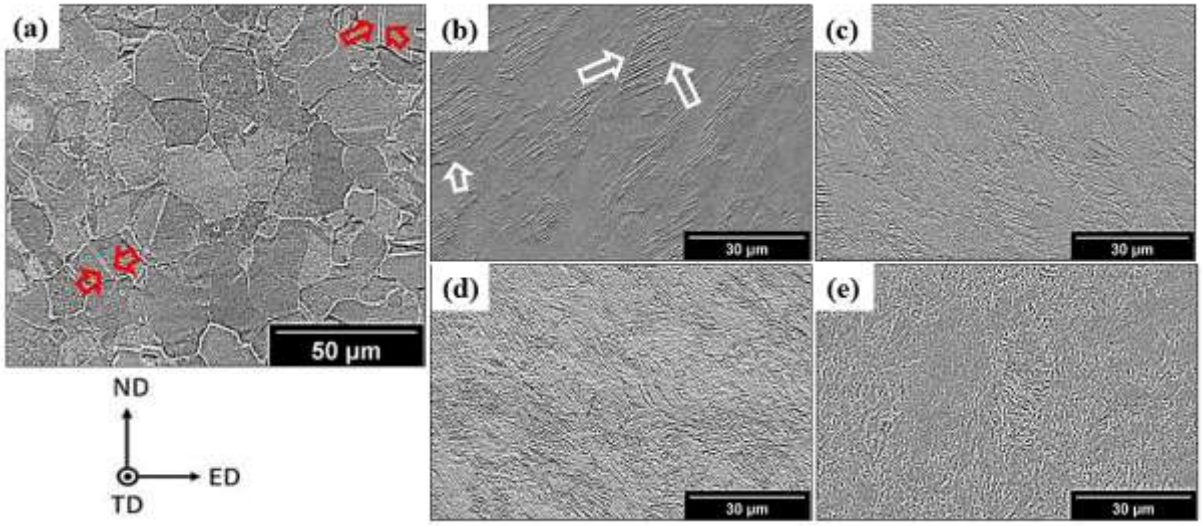

Source: Elaborated by the author.

Figure 43 illustrates the evolution of the micro-hardness as the ECAP passes increased. Austenitic grains showed a heterogeneous morphology structure due to the formation of micro shear bands resulting from the shear process. The gradual development of micro shear bands occurs with the progressing degree of the ECAP passes and comprises ultrafine grains coupled with dislocation tangles structure as reported by (LEI, (2017).

Figure 43 — Microhardness of all samples.

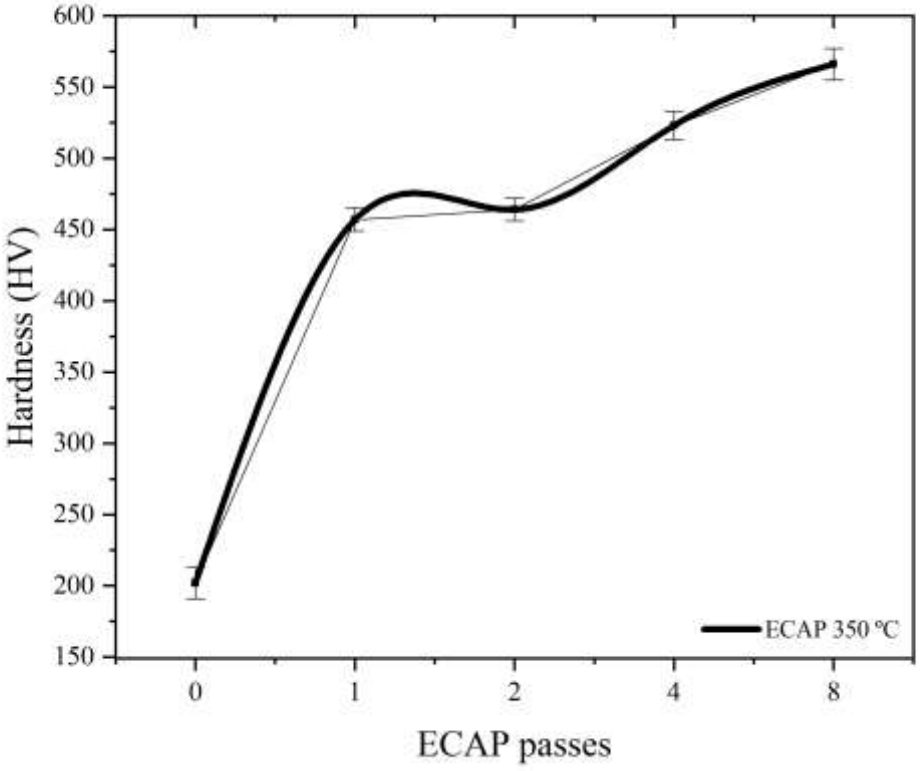

Source: Elaborated by the author.

6.3.2 XRD investigation

XRD patterns of all investigated samples are displayed in Figure 44. The single austenite phase was observed in the as-received sample. The XRD patterns of ECAP specimens confirmed the absence of any other phases (including α' and ε martensite). The high Mn-content (26.05 wt.%) as austenite stabilizer displays only the TWIP effect. Diffraction peaks shifted towards higher diffraction angles, and peak broadening was also observed in the ECAP-deformed samples.

The high dislocation density due to the ECAP process causes a localized lattice distortion that alters the peak shape of diffracted patterns. The peak broadening value can indicate indirect evidence of dislocation density change in metallic materials. Thereby, the dislocation densities of investigated as-received and after ECAP specimens were estimated by the method proposed by (UNGAR, 1996) and the modified Williamson-Hall method and were determined to be 2.23×10^{13} m^{-2} (as-received) and 8×10^{15} m^{-2} after 8 ECAP passes. The increase

in dislocation density for all samples is illustrated in Figure 45. Materials which present low-SFE twin and this mechanism normally create partial dislocations instead of screw dislocations. Screw dislocations that are still present do not cross slip, so dislocation movement is restricted. Hence, pile-up and proliferation of dislocations occur, promoting the drastic increase in the density. A significant increment in the dislocation density is also noticed after the second pass. This is present in microstructures shown in Figures 42 and 47, in which a considerable refinement was observed.

Further refining of the microstructure is also present after four and eight passes, but at a slower rate due to the large deformation already applied to the material. Consequently, the calculated dislocation density has a lower increase, showing a deceleration trend in the rate of dislocation formation. The increased dislocation density generated during ECAP causes more significant distortion of the crystal lattice, increasing the energy stored in the material. Consequently, the material presented an elongation of the grains, formation of shear bands, and twin contours, which agrees with the hardness results reported before (VAN, 1996).

Figure 44 — XRD patterns of all samples.

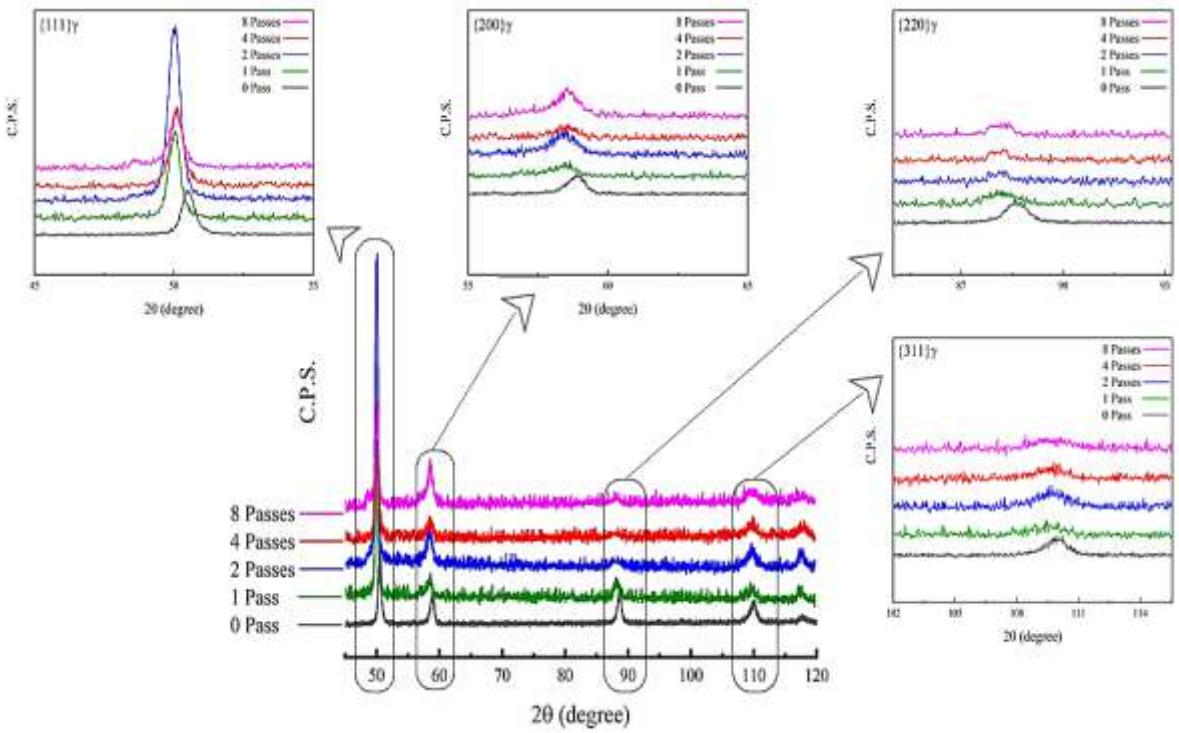

Source: Elaborated by the author.

Figure 45 — Dislocation density of all samples.

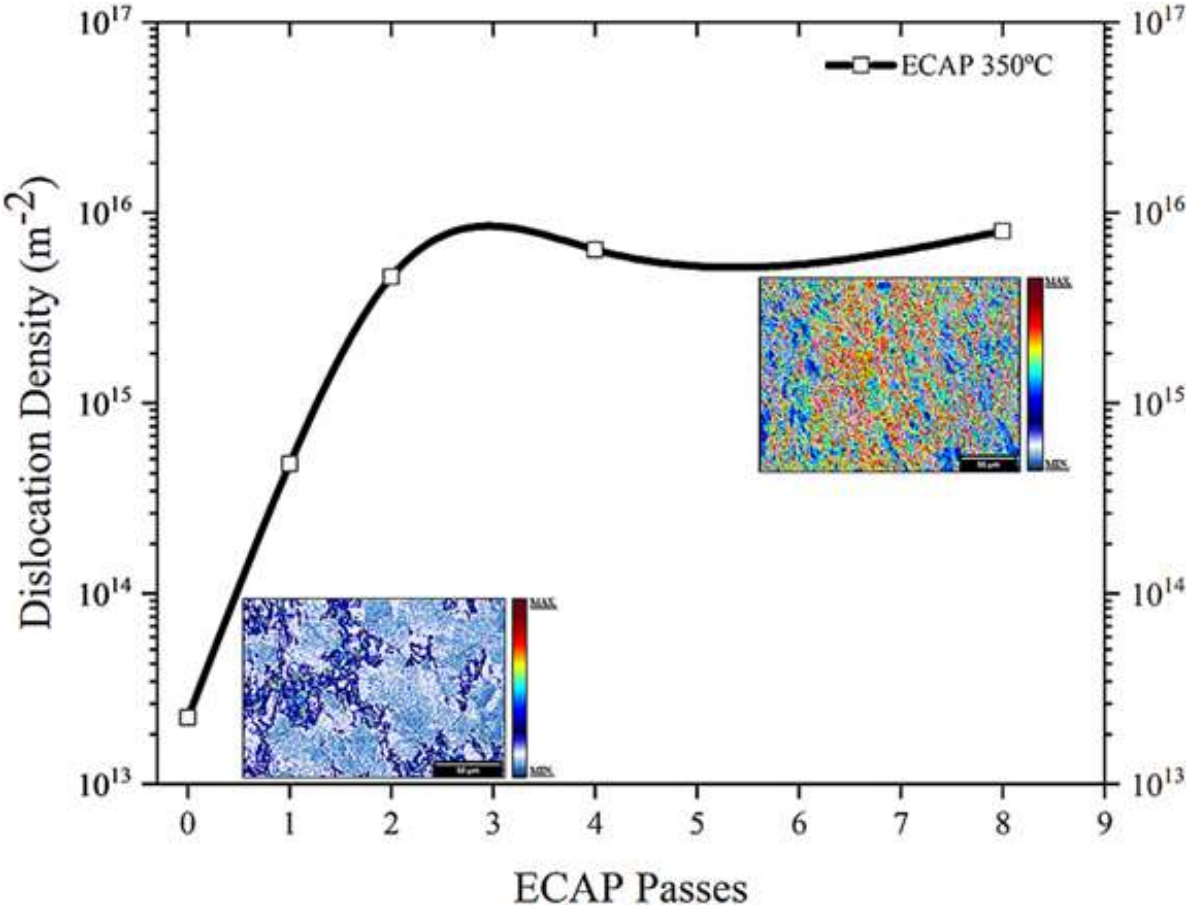

Source: Elaborated by the author.

6.3.3 Electron backscatter diffraction (EBSD) and Orientation distribution function (ODF) analysis

The orientation image maps (OIMs) and grain boundary maps of the as-received samples and after ECAP passes obtained by the EBSD technique are shown in Figures 46 and 47, respectively. Figures revealed that a texture gradient developed inside the grains as the amount of deformation increased. Figure 46 shows that the material exhibits a relatively homogeneous microstructure composed of equiaxed grains with an average grain size of 7 μm ± 1 μm (twins not considered). The grain boundaries indicate almost no subgrains (illustrated in green), and several annealing and mechanical twins (plotted in white) are present. The as-received sample had (001)[100] and (001)[120] preferred crystallographic orientations. The presence of the (001)[100] cleavage cube component could be related to the refinement of columnar grains developed during solidification in the direction of the maximum heat conduction, together with dynamic recrystallization during hot deformation (ZINOVIEVA,

2020). Zhang et al., (2016), reported that the {001}<120> components, mainly originated during the recrystallization of {001} columnar grains, which lead to low mechanical and corrosion resistance. The ODFs for the as-received samples were plotted using orthorhombic symmetry. These results agree with the values reported in the literature (LIMA, 2022).

Figure 46 — EBSD grain map, grain boundary of sample as-received, ((a) IQ mapping), (b) IPF mapping) (grains boundary map: black line ─ high-angle grain boundary, green line ─ low-angle grain boundary, and white line ─ twin boundary), and corresponding ODFs at constant (c) $\varphi_2 = 0°$ and (d) $\varphi_2 = 45°$ sections.

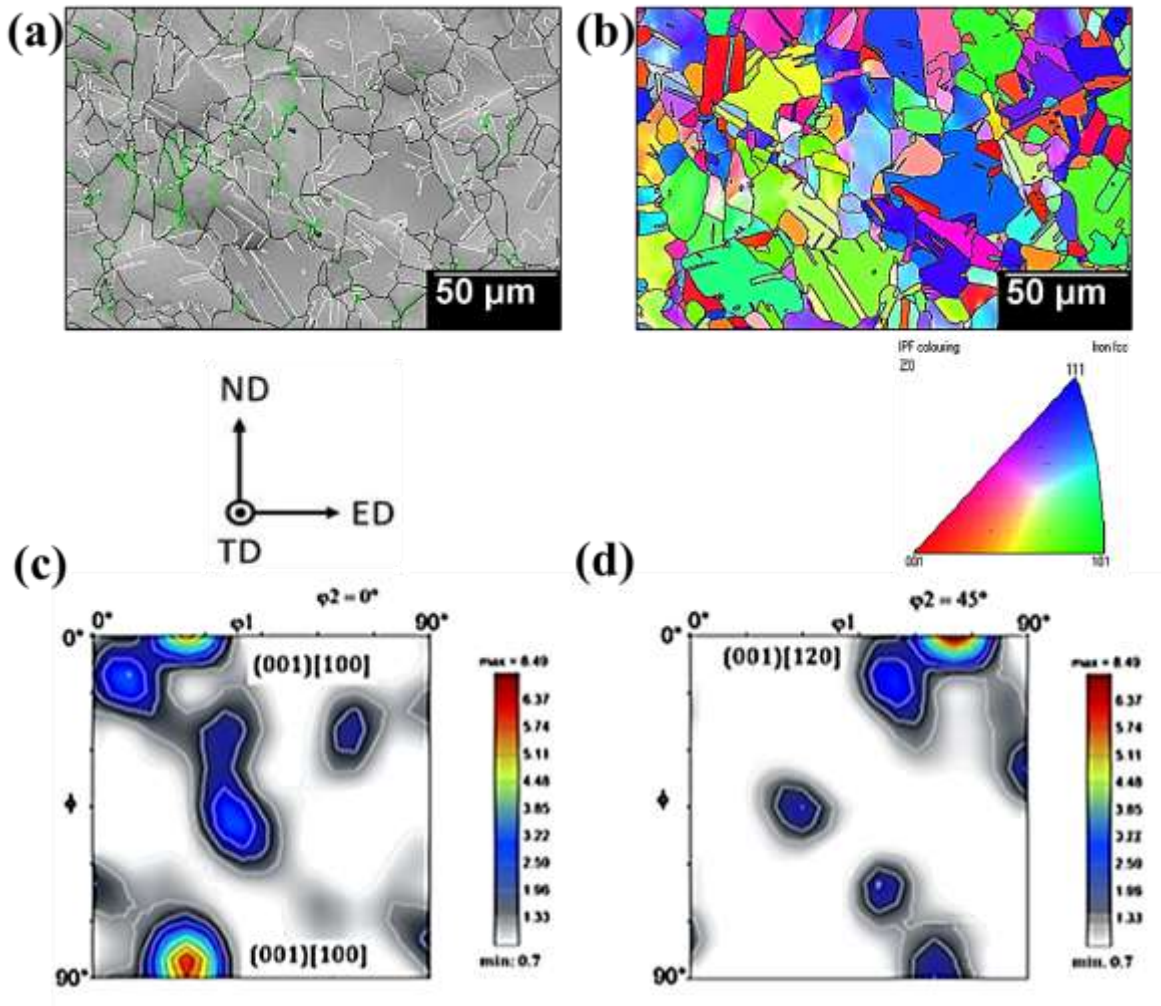

Source: Elaborated by the author.

Figure 47 depicts the essential features of the microstructure after 1, 2, 4, and 8 passes, and the evolution profile of the average grain size can be seen in Figure 48. The grains appear elongated in the shear direction, and in some areas, very fine equiaxed grains are noticed after ECAP passes. After the first pass, in addition to the elongated grains (see Figure 47b), a

large quantity of low-angle grain boundaries has been generated during the ECAP process, and concurrently in other regions, mechanical twins are observed (Figure 47a). Even though the grain size is heterogeneous, the grain size of the new grains formed after 1 ECAP pass is 1μm ± 0.6 μm. The average grain size is further reduced after 2 ECAP passes. While the microstructure is still quite heterogeneous, there is an increase in newly refined grains. The presence of large and elongated grains slowly vanishes with refined microstructure (Figure 47c, 47d). Figures (47e and 47f) represent observations on the microstructure of the TWIP steel subjected to 4 ECAP passes. It comprises deformation bands inhabited with fine twins (plotted in white) and progressive microstructure refinement.

Refinement is realized by the intersection of different families of these deformation bands forming misaligned and disoriented structures (VALIEV, 2013). Finally, eight passes led to new qualitative changes to the microstructure, expressed as a transformation of the deformation bands into subgrains. The microstructure has been refined and detecting areas without a large concentration of defects is challenging, especially subgrain boundaries (illustrated in green). There is also a clear trend towards equiaxed grains in some regions of the sample (Figures 47f and 47g). The average grain size after eight passes is 0.20 μm ± 0.05 μm. The dependence of the average grain size (misorientation >15º) on the number of ECAP passes is displayed in Figure 48. Still, no regular grain size of 0.20 μm after eight passes is observed. This behavior indicates the formation of a partially stable microstructure with an increasing number of passes. The eighth pass and the fourth pass present similar distributions suggesting that a steady state is still not achieved after eight passes (see Figure 47) (HIGUERA-COBOS, 2013).

All fragments are highly defective and subdivided by twinned colonies, forming a complicated hierarchical defect structure. The deformation is localized in the zone of deformation formed by the channels that intersect. Depending on the geometry of the ECAP array, an inevitable heterogeneity in the macroscopic strain distribution along the height of the processed parts can be observed after a few first passes of ECAP. However, this macroscopic heterogeneity disappears with the increase in the number of passes. These trends are not pronounced in the case of a round cross-section of the specimen (VALIEV, 2013) (RAAB, 2022). Deformation twins are noticed at all deformation stages by ECAP. However, it should be taken into account the step sizes used in EBSD analysis and the lowest indexation rate in the most deformed samples. Accordingly, this technique is not suitable to calculate the fraction of twins accurately, and also, many fine twins need to be visible. The microstructural evolution of

the TWIP steel during multi-pass ECAP at 350°C up to four passes agrees with the data published in the literature for processing the material using similar dies and temperatures (ABRAMOVA, 2016) (TIMOKHINA, 2014) (ABRAMOVA, 2021).

Figure 47 — EBSD grain map, grain boundary map, IQ mapping, and IPF mapping of the samples: (a, b) 1 pass, (c, d) 2 passes, (e, f) 4 passes, and (g, h) 8 passes (grains boundary map: black line ─ high-angle grain boundary, green line ─ low angle grain boundary, and white line ─ twin boundary).

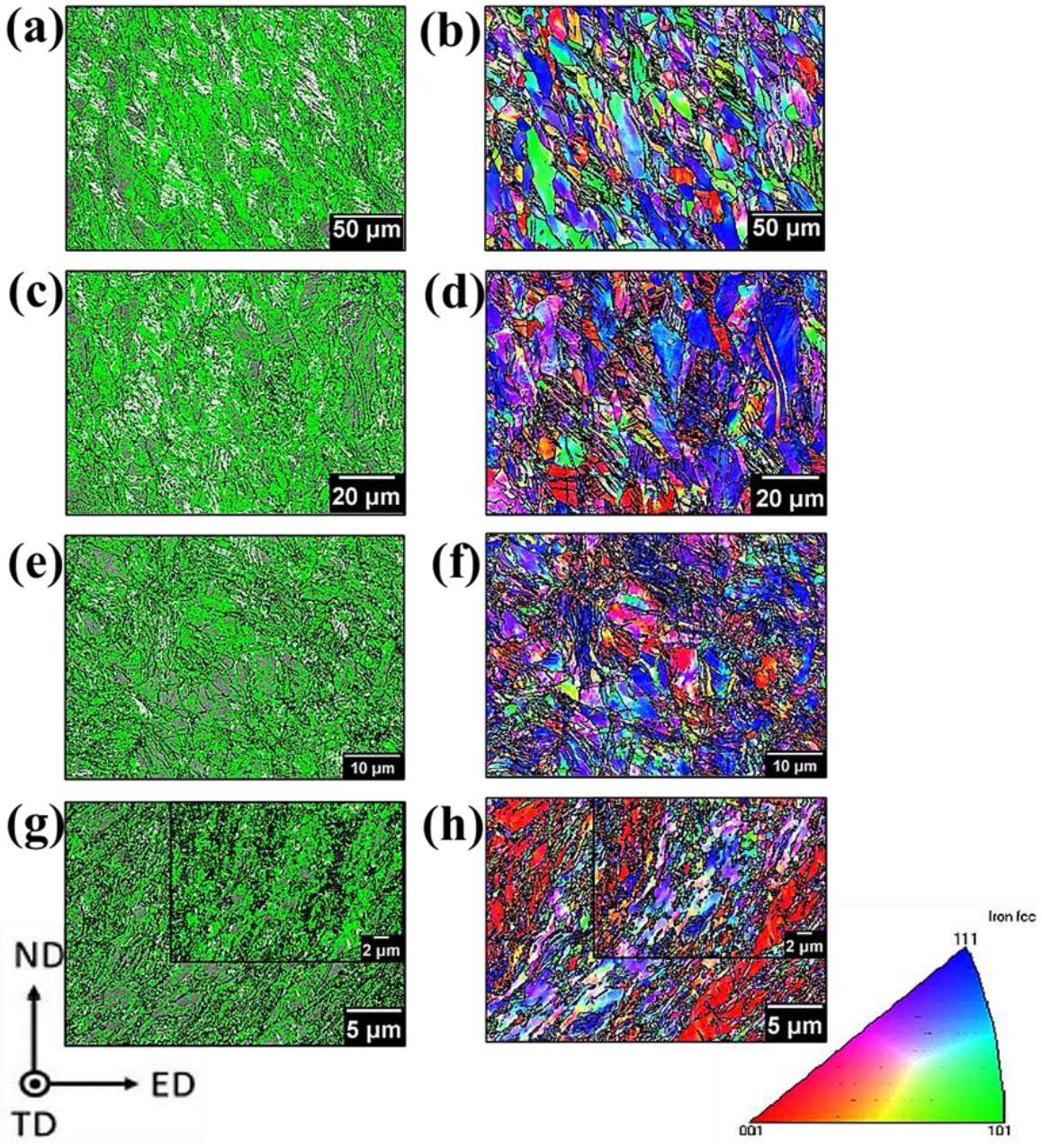

Source: Elaborated by the author.

Figure 48 — Average grain size with the number of ECAP passes.

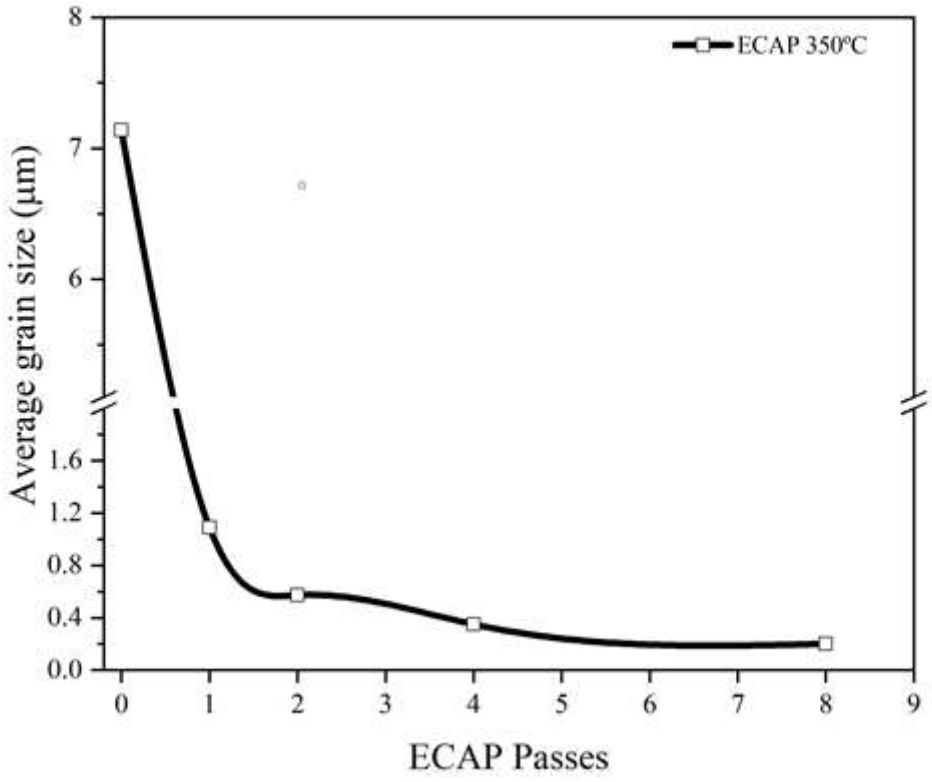

Source: Elaborated by the author.

The nature of the grain boundaries (see Figure 49) can provide the fraction of low angle grain boundaries (LAGBs, $2° < \Theta < 5°$), high angle grain boundaries (HAGBs, $15 ° < \Theta$), and coincidence site lattice (CSL) boundaries. The nucleation of new grains occurs mainly within the shear bands, in the grain boundaries, and because of the rearrangement of dislocations. Dislocation tangles form subgrains and gradually lead to the development of new grain boundaries (DESPRÉS, 2020). Figure 49 shows that after 8 ECAP passes, the microstructure seems to have started a dynamic recrystallization process.

When analyzing the as-received sample, it was found that it had the lowest fraction of low-angle misorientations due to dynamic recrystallization and recovery during the steel production. The initial material contains approximately 30% of the total CSL. After ECAP passes, one can show a large number of subgrains generated in the first pass, which decreases progressively with increasing pass number (Figure 48). However, after the second pass, the deformation introduced into the material promotes a new increase in the HAGBs fraction, which since the fourth pass can be partially attributed to particular misorientation fractions with twin

character CSLs. The misorientation distribution functions were similar from the fourth to the eighth pass. However, they showed a slight continuous increase in the HAGBs fractions (from 22% to 35%, respectively) with a consequent decrease in the low misorientation fractions (from 65% to 55%). A high amount of dislocations and crystallographic defects are generated during ECAP passes. Dislocation cell boundaries are formed first, and deformation-induced boundaries are developed by increasing the number of passes (SCHWARTZ, 2000).

The results indicated that a gradual increase in misorientation of the grain with progressing the ECAP passes led to grain fragmentation and re-oriented texture components. The development of low-energy CSL boundaries, including $\sum 3,9,27^{n}$ twinning boundaries, is commonly observed in austenitic steels (HIGUERA-COBOS, 2013) (BELADI, 2013). The results of the present study also revealed that the highest portion of CSLs is due to the formation of slip bands and deformation twins. Deformation-induced twinning is also associated with the planar slip bands, as proposed by (YE, 2021) (YANG, 2021). The authors suggested that planar-slip dislocation contains many Shockley partial dislocations that produce deformation twins massively by acquiring the planar-slip dislocations. Notably, the fraction of CSL boundaries decreases with the progressing amount of deformation (see Figure 49). However, that is only partially true. What occurs is a limitation of the EBSD technique.

Crystallographic anisotropy also plays a significant role in the evolution of lattice distortion, including misorientation, and this should be analyzed on a grain-to-grain level. However, this is not the object of this study. The results of HAGB and LAGB fractions are similar to those reported by (LEI, 2017) in TWIP steel processed by ECAP after passing the route Bc. These values are lower than those obtained in this work. Anyway, and based on other investigations (ABRAMOVA, 2021) (HAASE, 2016) (MURR, 2004), there is evidence of a saturation in the proportions of HAGB and LAGB with the increase in the number of ECAP passes.

Figure 49 — Misorientation grade of the grain boundaries with the number ECAP passes.

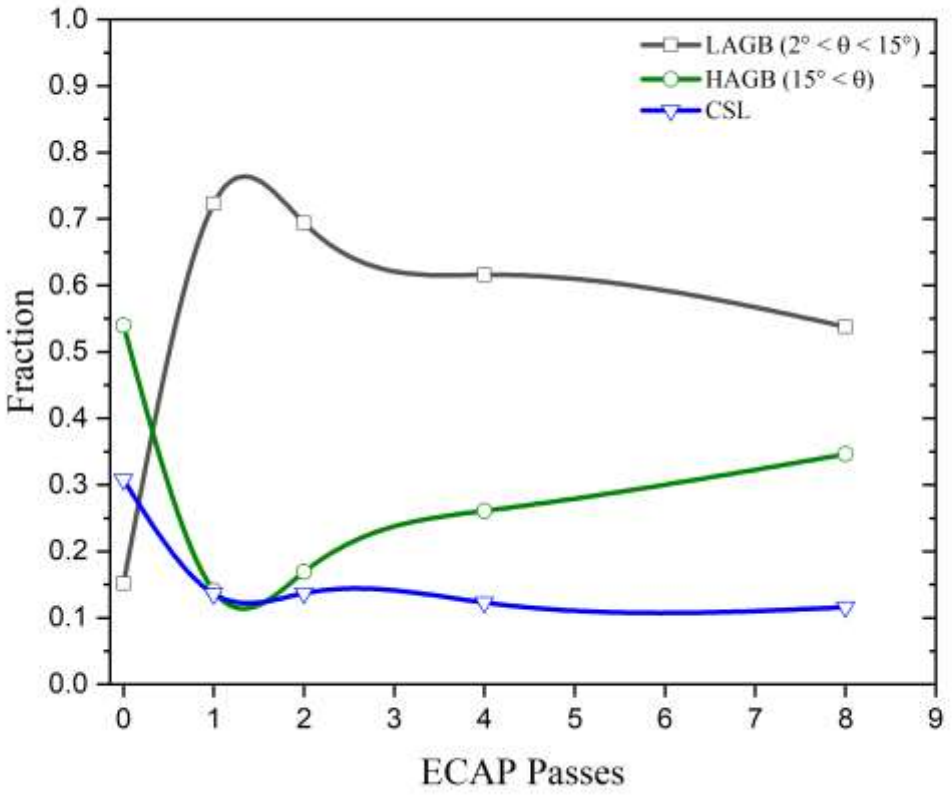

Source: Elaborated by the author.

The texture of the current TWIP steel during the ECAP process was analyzed in triclinic symmetry (0º <<360º). Following the suggestions of (BEYERLEIN, 2009), where they defined the ideal orientations of deformation by simple shear. The texture evolution of the strained material by one, two, four, and eight ECAP passes and the ideal position for texture components for FCC materials deformed by simple shear are presented in Figure 50 and defined in Table 6. The intensities of the $B/\overline{B}$ and $A/\overline{A}$ texture components are almost similar. Monoclinic symmetry can be observed in some cases since the components are symmetrical every 180º. After two and four passes, the existence of monoclinic symmetry following Bc route has not been noticed (BEYERLEIN, 2009). Monoclinic symmetry was observed in another research by (SUWAS, 2006) (HIGUERA-COBOS, 2014) that used a die with a configuration like the one used in this work.

The textures present predominant orientations with continuous distributions along the fibers with a simple shear texture that happens when the die presents an external angle $\psi >$ 0º, and two symmetrical areas are observed (SUWAS, 2006). Figure 50b shows the texture after

1 ECAP pass, all shear texture components, as listed in Table 6, were immediately formed, and developed a complete fiber at (0-360°, 45°, 0°) with ideal components of the simple shear model shown in Figure 50(a) with some deviations. This effect, often observed in variances in Euler space from ideal orientations, is usual in ECAP processes, which are related to different processing factors (HAASE, 2016) (BEYERLEIN, 2009). This effect was found in all conditions after the ECAP process. After one ECAP pass, the presence of A_1* and A_2*, part of α fiber, can be noticed in the TWIP steels. This phenomenon indicates twinning, which is consistent with the observations in Figures 46 and 47. The components showed similar intensities in the FeMnCAl TWIP steel studied by other researchers (LEI, 2017) (HAASE, 2016). The trend to build the B fiber orientations with increasing strain in low-SFE metals has been observed before. The increase of the fiber B is related to the strengthening of component B (BEYERLEIN, 2009) (HIGUERA-COBOS, 2014) mainly due to the replacement of orientations of component C by orientations B ({112}\<110>) (KHODDAM, 2014), which is in accordance with the results found in the present research.

The texture component normally changes from C over A_1* to B with decreasing SFE (SKROTZKI, 2003) (BEYERLEIN, 2007). Other authors (SAEED-AKBARI, 2012) (SUWAS, 2003), have suggested that the effect of SFE on texture evolution during ECAP is similar to that of texture development during cold rolling. The following correspondence was proposed: S => A_1*, Cu => C, Brass => B/$\overline{B}$. In the cold rolling texture, the texture components {112}<111> Cu and {123}<634> S decrease with decreasing SFE, while the texture component {110}<112> Brass increases. So, as SFE decreases, texture component C is expected to decrease, while texture components B//$\overline{B}$ are expected to strengthen. The C texture component was weakened after 4 ECAP passes in the investigated TWIP steel. A significant decrease in A_2* and A_1* components has not been reported for other low-SFE studied materials (HAASE, 2016), (SANDIP, 2011), although, for a FeMnCAl TWIP steel (LEI, 2017) (HAASE, 2016), A_2* and A_1* intensities decrease. It could be that the drop in the signal of these components might be related to the difficulties of EBSD analysis to detect all the new twins formed at high deformations, as reported in the literature (LEI, 2017).

The increase in B/$\overline{B}$ components with increasing strain in low- SFE metals has been previously reported (BEYERLEIN, 2009). This increase has been related basically to the strengthening of the B component, mainly due to the replacement of C component orientations by B orientations ({112}\[110]) (HIGUERA-COBOS, 2014). This line of reasoning partially coincides with the evolution of the current texture since there was a decrease in the C component after four ECAP passes.

Table 6 — Definition of the ideal texture components for an ECAP die with 120° angle.

Crystal Structure	Texture components	φ1(°)	Φ(°)	φ2 (°)
FCC	A_1*	95.26/275.26	45	0
		5.26/185.26	90	45
	A_2*	24.74/204.74	45	0
		114.74/294.74	90	45
	A	60	36.26	45
	$\overline{A}$	240	35.26	45
	B	60/180/300	54.74	45
	$\overline{B}$	120/240/360	54.74	45
	C	150/330	45	0
		60/240	90	45
	{111}-/A-fiber	{111}<uvw>		
	<111>-/B-fiber	{hkl}<110>		

Source: BEYERLEIN, (2009).

Compared with the texture after one ECAP pass, the texture after two ECAP passes (see Figure 50(c)) showed some texture modifications with a decreased A_1*, A_2*, and C texture component and increased A/$\overline{A}$, B/$\overline{B}$ components. Some authors reported texture embrittlement or saturation between 2 and 4 ECAP passes following route Bc (MOLODOVA, 2007) (SAIYI, 2005) (GAZDER, 2006) (FERRASSE, 2004), and texture strengthening was also observed (SANDIP, 2011). After 4 ECAP passes (Figure 50(d)), the texture became more pronounced, as indicated by an increased texture index and a decreased volume fraction of randomly oriented grains. It is worth noticing that the B/$\overline{B}$ and A/$\overline{A}$ texture components is characterized as a texture of strengthening, whereas the A_2*, A_1*, and C components as weakened for steels similar to the one investigated.

After 8 ECAP passes (Figure 50(e)), it can be seen a mixed microstructure. Texture after 4 ECAP passes should generally remain the same. However, in the present work, the intensity in C and the appearance of texture components of recrystallization RB, Cb, Goss, and Brass appeared to increase, besides the observation of high intensity of the component B/$\overline{B}$. The evolution of these volume fractions is shown in Figure 51. Haase et al. (2016) observed this texture for FeMnCAl as a "transition texture". These authors hypothesized that the strong presence of C would be related to dislocation sliding as the primary deformation mechanism. At the same time, the intensity increases related to the B/$\overline{B}$ components would be associated

with the twinning mechanism. They also reported the strong presence of the C component and the increase of the B/$\overline{B}$ components with ECAP passes. For the steel used in this work (FeMnCCr), the texture evolution corresponds better with the correspondence proposed by (SUWAS, 2006) and with (LEI, 2017) as C and A_1* components are reduced, and B/$\overline{B}$ increased after ECAP passes. This would mean that the importance of twinning deformation would be more significant in both cases.d A_1* components are reduced, and B/$\overline{B}$ increased after ECAP passes. This would mean that the importance of twinning deformation would be more significant in both cases.

Figure 50 — (a) Ideal components in triclinic symmetry of FCC materials deformed by simple shear (die 120°), texture components of investigated TWIP steel for φ2=0° and φ2=45°, (b) after 1 ECAP pass, (c) after 2 ECAP passes, (d) after 4 ECAP passes, and (e) after 8 ECAP passes.

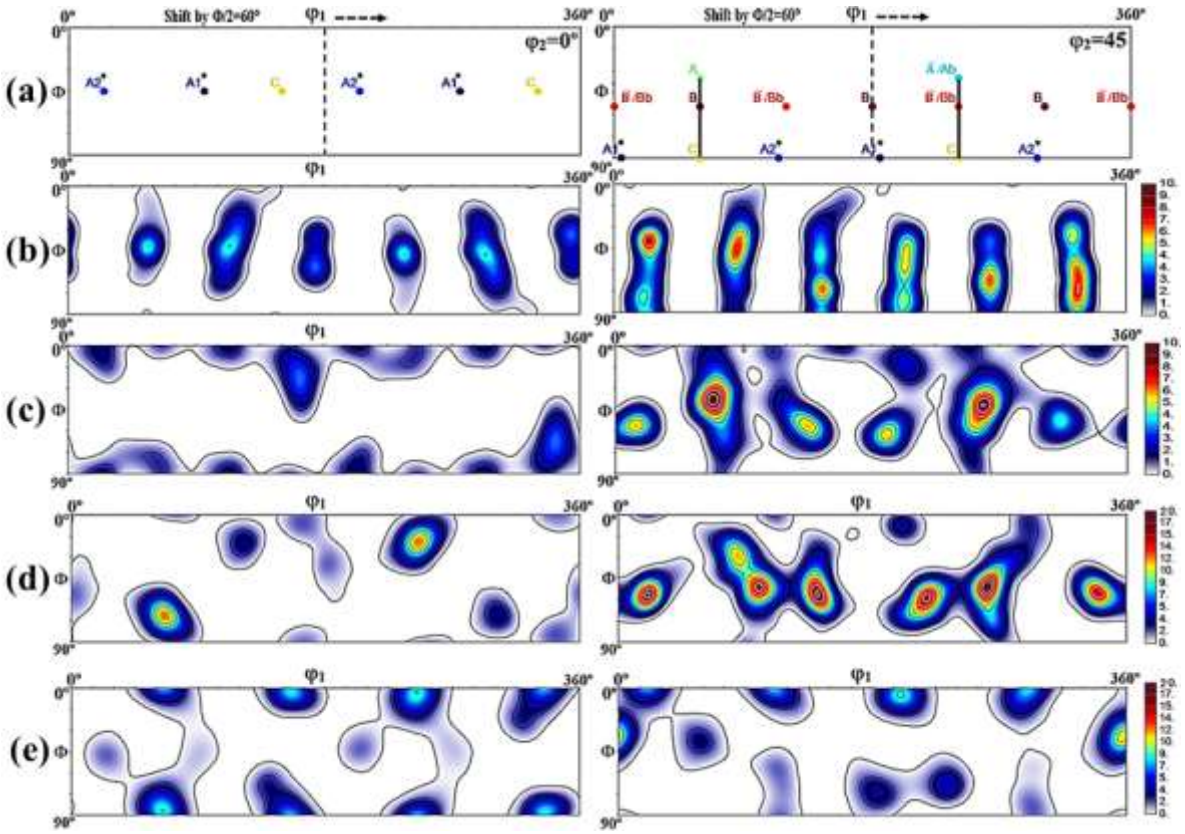

Source: Elaborated by the author.

Figure 51 — Evolution of the volume fractions of the main texture components during the ECAP process.

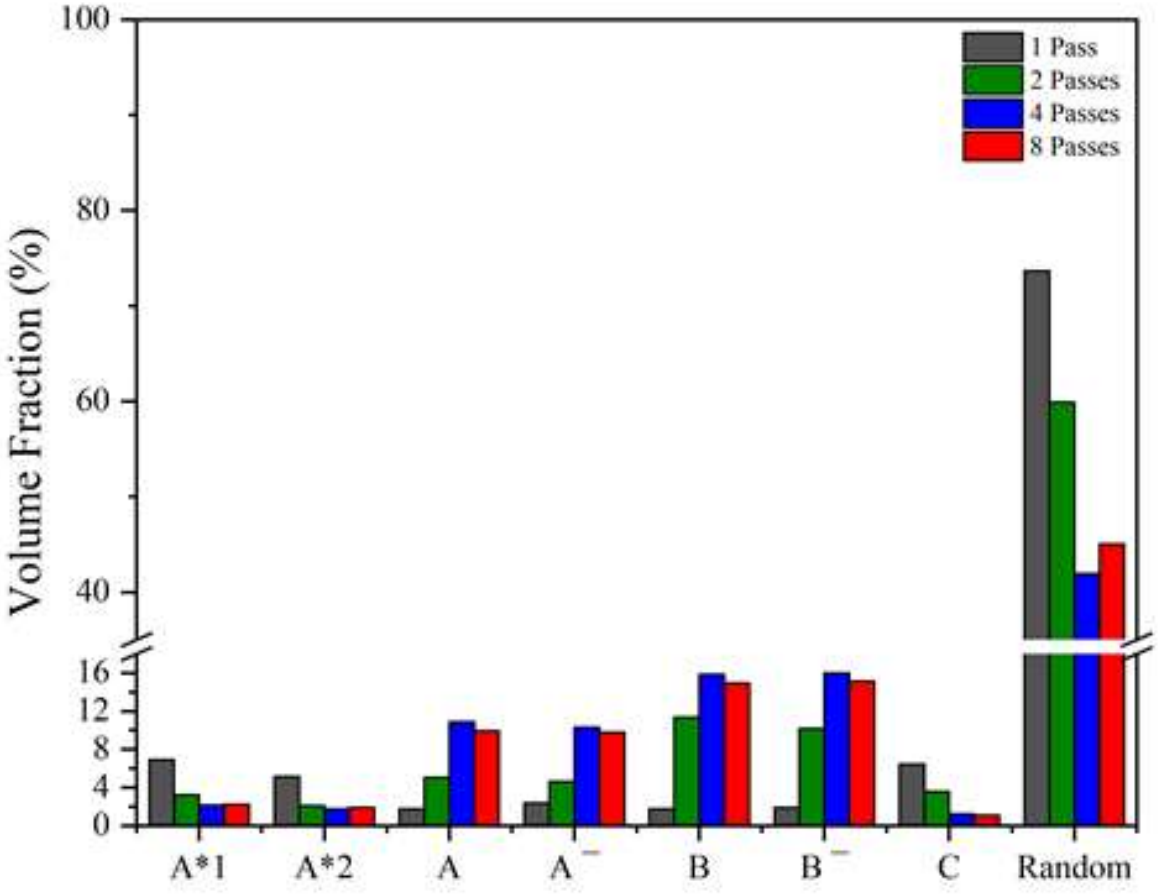

Source: Elaborated by the author.

Analyzing the anisotropy after ECAP process (Figure 52), it was observed in the TWIP steel the preference of the fiber <110>∥X (direction of extrusion), giving rise to the presence of deformation texture components such as C, B/$\overline{B}$ and A/$\bar{A}$. These are texture components characteristic of a material subjected to simple shear. However, there is also a marked influence of the fibers <110> ∥ Z and <111>∥Y. Furthermore, the parallel direction to the Z axis presented a preference for the direction <110>, which could be associated with the highest amount of grain boundaries oriented in this direction. Figure 52 suggests heterogeneity in the texture, imparted by ECAP process, especially when using ECAP matrices with Ψ>0°. Fibers <111> and <100> suggests the presence of recrystallization texture components such as Cube, Goss, Brass, Copper, Brass rotated, and twinned Cube. However, the presence of the strong fiber <111>∥Y can be also linked to the presence of special grain boundaries of the type Σ3 (60° <111>). In summary, it was possible to observe how the investigated material deforms at first following the direction of the greatest atomic density, which for FCC materials is the

<110> direction or β fiber, which is composed of the texture components C, B/$\overline{B}$, and A/$\bar{A}$ (HOSNI, 2010) (HIGUERA-COBOS, 2013).

Figure 52 — Fiber texture after ECAP process of all samples.

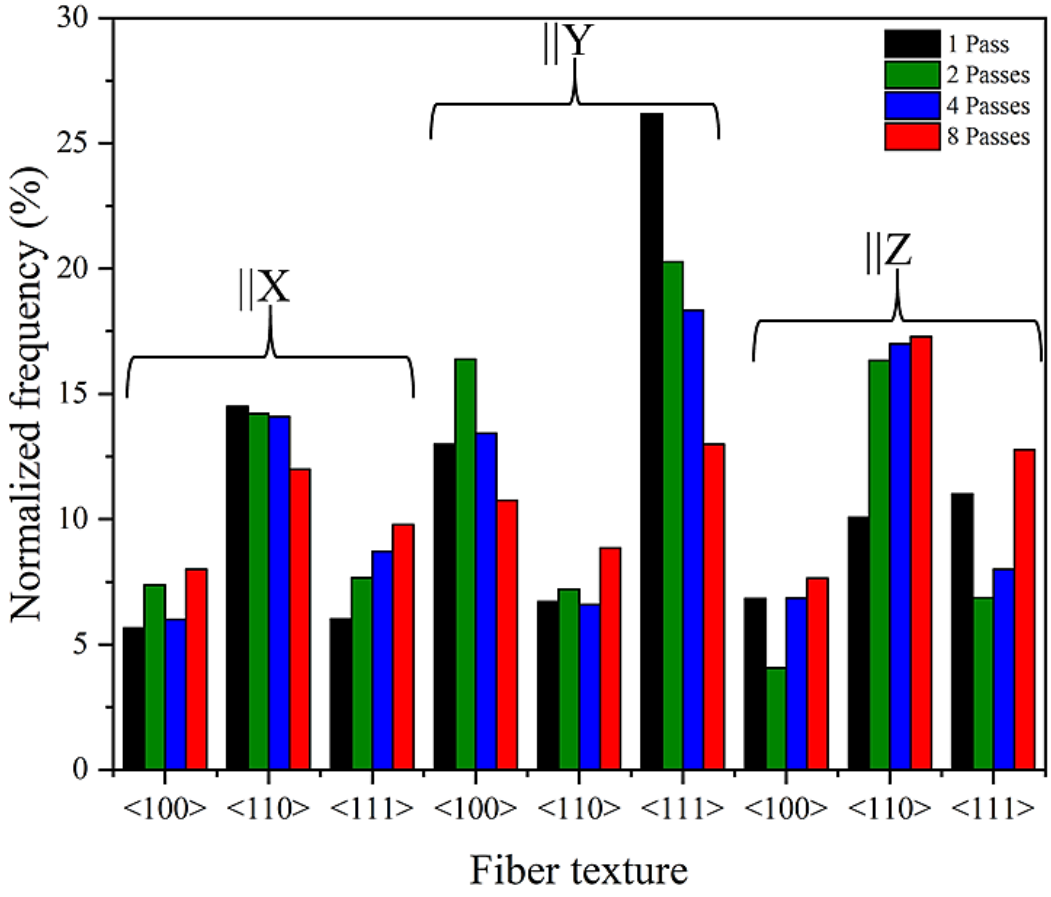

Source: Elaborated by the author.

As the deformation increases, many subgrains have been generated and block the movement of dislocations. Deformed samples of the TWIP steel showed gradual changes in their grain orientation. Some indicators of these changes include GAM, GOS, and KAM — which measure average grain misorientation, spread in grain orientation, and kernel average misorientation, respectively (TSL-OIM, 2017). Kernel Average Misorientation analysis evaluates misorientation between reference points with defined numbers of neighboring points within the grain (FUJII, 2021). The local change in orientation between 3 neighboring pixels was used to analyze the strain distribution throughout the crystal grains. KAM results are presented in Figure 53(f). The highest fraction of low KAM values (KAM < 1°) was found in the as-received sample (Figure 53(a)). The as-received (Figure 53(a)) sample with recrystallized austenite grains showed minimal intergranular misorientation in the microstructure. After

ECAP process, a significant fraction of deformed grains with medium KAM (1° < KAM < 3°) (see Figure 53(d,e)) and high (KAM > 3°) was developed. High values of KAM (see Figure 53(b,c)) could be associated with high local lattice distortion and dislocation density resulting in an increase in internal energy (BORDONE, 2022). Crystallographic defects (i.e., dislocations, shear bands and grain boundaries) that were generated during plastic deformation were absorbed and united to develop the dislocation cells, low-angle boundaries, and nano-twins. The localized stored strain energy due to lattice misfit acts as a barrier against dislocation glide, leading to the deterioration of the toughness and somehow increasing the mechanical strength. The reduction of KAM values suggests the beginning of dynamic recrystallization with subgrains developed during plastic deformation at 350 ºC (GURAO, 2012) (YIN, (2005).

Figure 53 — EBSD KAM maps: (a) as-received, (b) after 1 ECAP pass, (c) after 2 ECAP passes, (d) after 4 ECAP passes, and (e) after 8 ECAP passes, (f) Variation of kernel average misorientation distribution of all investigated specimens.

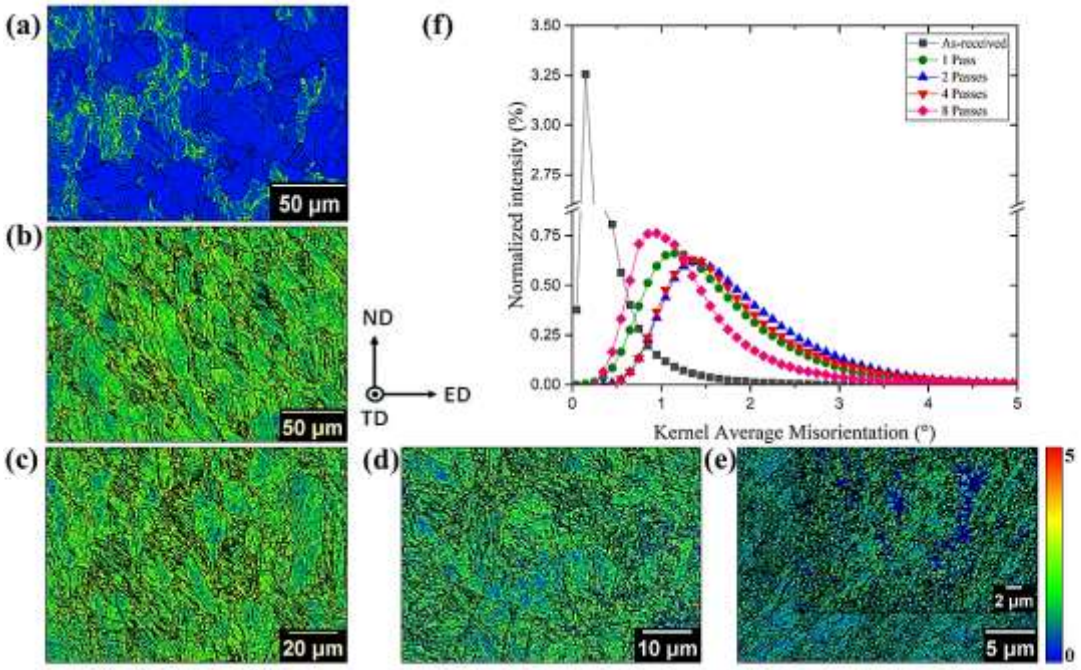

Source: Elaborated by the author.

The joint analysis of the Taylor factor and the Schmid factor was made to observe the resistance of the grains with the increase of the strain added to the qualitative growth of mechanical twins. Figure 54 shows a characteristic behavior of the two analyses. The lower the value of the Schmid factor, the higher the Taylor factor. It was observed that the grains showing mechanical twins have a high Taylor factor. This result seems to confirm the hypothesis made

by other authors (XIANFENG, 2013) (MAECEAU, 2013): a high Taylor factor implies high deformation difficulty by dislocations slip, which promotes the formation of twins. Therefore, the grain must rotate to align with the preferred planes and directions. Figure 54 shows the Taylor, Schmid factor, and CSL maps, suggesting that mechanical twins are generated within grains with a high Taylor factor value.

In Figure 54, the activated slip systems of grains associated with the extrusion direction were examined in terms of the Schmid factor. The Schmid factor measures the ease with which dislocation slip can occur on a plane. The maximum value of the Schmid factor during the ECAP process was close to 0.5. Grains with high Schmid factor values slip easily, while grains with less Schmid factor require higher shear stress to form critical slip systems necessary for deformation. Figure 54 revealed that as-received and after 1 ECAP passes, most of the grains in the sample exhibited the Schmid factor values higher than 0.4. Using the Bc route the fraction of grains with low Schmid factor values increased after 4 ECAP passes reduction, suggesting more resistance against plastic deformation reaching a complete cycle of deformation by the ECAP process. This result is in agreement with other authors (LIMA, 2022). After 8 ECAP (see Figure 54(d)) passes, an increase in the Schmid factor was observed suggesting a dynamic recrystallization process after a more significant true strain (JO, 2021).

The austenite phase (FCC crystal structure) contains 12 slip systems, and 12 twinning systems, considering 4 octahedral {111} planes with 3 close-packed <110>, <11$\bar{2}$> directions on each plane. The calculation of slip systems, twining systems and, their corresponding volume fractions in austenitic high-Mn TWIP steel according to (GUO, 2017) were carried out using the ATEX analysis software. The Table 7 show that the same active slip systems, and twinning systems, including (11$\bar{1}$)[1$\bar{1}$0], (1$\bar{1}\bar{1}$)[01$\bar{1}$], (1$\bar{1}\bar{1}$)[110], (1$\bar{1}$1)[011], (1$\bar{1}$1)[110], (111) [01$\bar{1}$], (111)[10$\bar{1}$], (111)[11$\bar{2}$], (1$\bar{1}$1)[21$\bar{1}$], (1$\bar{1}$1)[$\bar{1}$12], (11$\bar{1}$)[1$\bar{2}\bar{1}$], (11$\bar{1}$)[$\bar{2}$1$\bar{1}$], (1$\bar{1}\bar{1}$)[12$\bar{1}$], (1$\bar{1}\bar{1}$)[1$\bar{1}$2] are common in all investigated samples. The demand of at least five independent systems for plastic deformation is known as the von Mises Criterion. The present steel has more than 5 slip systems, that is, even after greater deformations (accumulating 240%) the samples did not fracture. Then, if less than 5 independent slip systems are available, the ductility is predicted to be low in the material. The point is that each grain will not be able to deform, and gaps will open up leading to the apearence of cracks (POKHAREL, 2014).

Figure 54 — EBSD (Taylor factor, Schmid factor, and CSL's) maps of samples (a) as-received, (b) after 1 ECAP pass, (c) after 4 ECAP passes, and (d) after 8 ECAP passes.

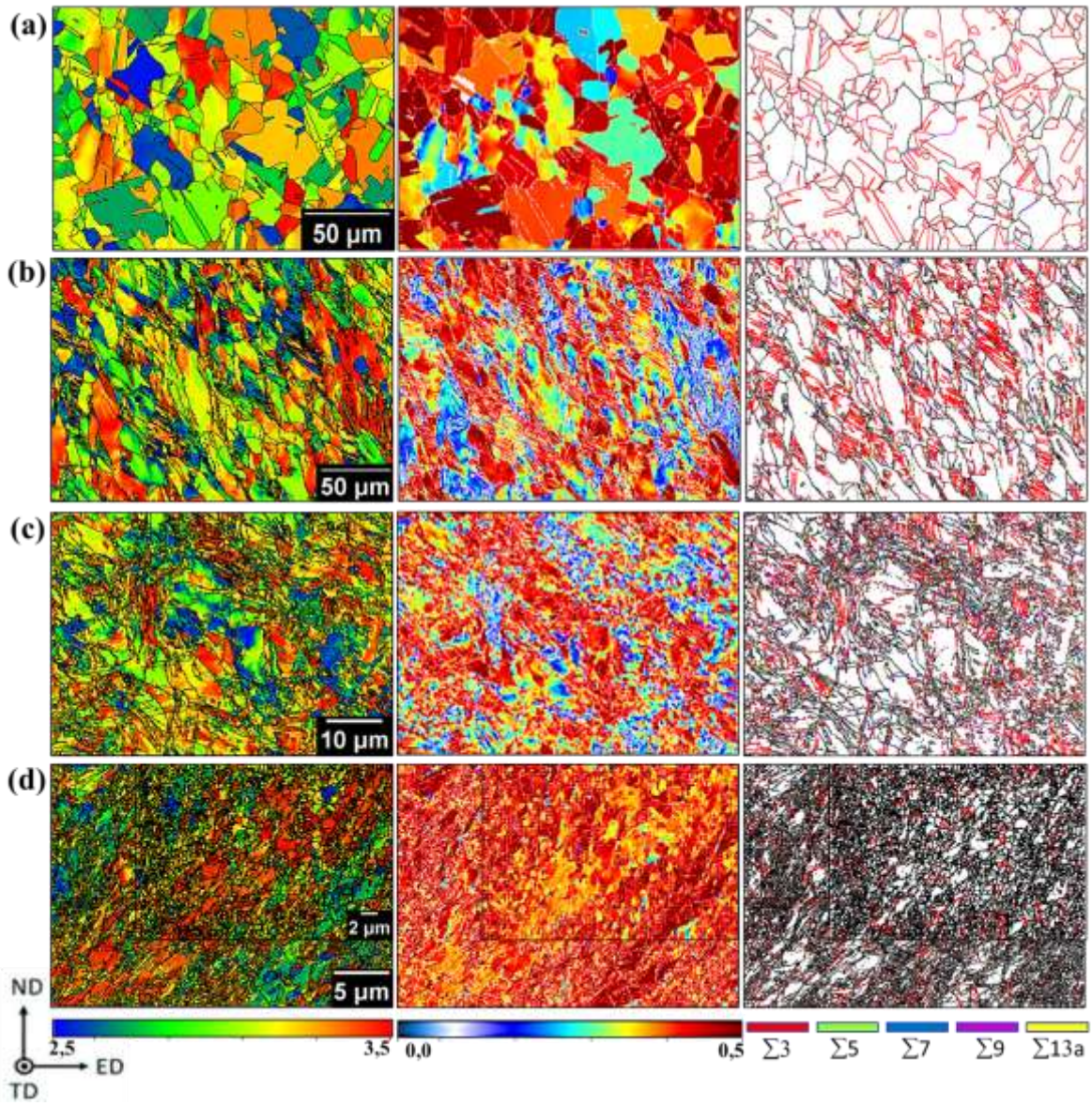

Source: Elaborated by the author.

Table 7 — Slip and Twinning systems and their corresponding volume fractions.

		As-received	1 ECAP pass	2 ECAP passes	4 ECAP passes	8 ECAP passes
Slip systems	(1 1 $\bar{1}$) [0 1 1]	0	0	0	0	0
	(1 1 $\bar{1}$) [1 0 1]	0	0	0	0	0
	(1 1 $\bar{1}$) [1 $\bar{1}$ 0]	23.411	24.321	11.325	17.136	10.153
	(1 $\bar{1}$ $\bar{1}$) [0 1 $\bar{1}$]	10.6	28.12	13.086	16.694	14.502
	(1 $\bar{1}$ $\bar{1}$) [1 0 1]	3.961	1.199	1.311	2.064	6.677
	(1 $\bar{1}$ $\bar{1}$) [1 1 0]	11.136	4.77	11.309	15.565	6.439
	(1 $\bar{1}$ 1) [0 1 1]	8.714	2.144	5.201	1.086	20.594
	(1 $\bar{1}$ 1) [1 0 $\bar{1}$]	8.6	18.221	12.451	18.58	14.844
	(1 $\bar{1}$ 1) [1 1 0]	16.941	9.662	27.16	9.564	12.18
	(1 1 1) [0 1 $\bar{1}$]	5.934	6.523	11.898	8.623	2.083
	(1 1 1) [1 0 $\bar{1}$]	10.704	5.039	6.258	10.687	12.524
	(1 1 1) [1 $\bar{1}$ 0]	0	0	0	0	0
Twinning Systems	(1 1 1) [1 1 $\bar{2}$]	14.011	10.396	13.088	16.338	10.057
	(1 1 1) [1 $\bar{2}$ 1]	0	0	0	0	0
	(1 1 1) [$\bar{2}$ 1 1]	0	0	0	0	0
	(1 $\bar{1}$ 1) [1 2 1]	8.505	11.033	7.226	5.683	7.832
	(1 $\bar{1}$ 1) [2 1 $\bar{1}$]	13.918	19.216	35.444	16.312	12.051
	(1 $\bar{1}$ 1) [$\bar{1}$ 1 2]	9.491	5.309	2.574	7.554	32.455
	(1 1 $\bar{1}$) [1 1 2]	0	0	0	0	0
	(1 1 $\bar{1}$) [1 $\bar{2}$ $\bar{1}$]	12.843	10.88	11.785	8.272	6.823
	(1 1 $\bar{1}$) [$\bar{2}$ 1 $\bar{1}$]	9.443	6.144	7.73	8.657	9.698
	(1 $\bar{1}$ $\bar{1}$) [2 1 1]	7.717	12.19	2.446	9.476	1.28
	(1 $\bar{1}$ $\bar{1}$) [1 2 $\bar{1}$]	15.948	7.423	12.418	21.837	6.926
	(1 $\bar{1}$ $\bar{1}$) [1 $\bar{1}$ 2]	8.123	17.409	7.288	5.869	12.877

Source: Elaborated by the author.

6.3.4 Mechanical Tensile tests

The microtensile test results of as received TWIP steels samples, as well as the samples processed by ECAP, are shown in Figure 55 and Table 8. Yield strength (YS) and ultimate tensile strength (UTS) increase with the number of ECAP passes. It can be seen that the YS increment is more evident than the corresponding UTS increment. Similar behaviors were found in the literature (HAASE, 2016) (TIMOKHINA, 2014) (UEJI, 2008). Serrated flows are present on the tensile test curves. They are caused by dynamic aging from stress-induced interactions between C-Mn clusters and partial dislocations (LIMA, 2022) (JO, 2021). The total elongation and ductility of the samples are drastically reduced after each ECAP pass; despite the reduction, the values obtained for elongation and toughness can be considered satisfactory. Elongation values are greater than those reported for some conventional deep drawing steels, such as high strength IF(HS) and other high Mn TWIP steels (LEI, 2017)

(HAASE, 2016) (FROMMEYER, 2000).

In the FeMnCCr-based TWIP steel, after the first ECAP pass at 350 °C, there is a significant increase in the yield strength as a result of the increase in dislocation movement activity forming many subgrains and interacting with mechanical twinning (BRACKE, 2009). This behavior was also described in previous studies on severe plastic deformation (SPD) by ECAP at similar temperatures for TWIP steels based on FeMnC (TIMOKHINA, 2014) and TWIP steels based on FeMnCAl (HAASE, 2016). There are no examples in the literature of SPD in TWIP steels based on FeMnCCr. Even with the increase in SFE values at 350 °C (BOUAZIZ, 2001), mechanical twinning was observed in the austenite grains for the current TWIP steel and in other TWIP steels processed by ECAP and cited in the literature (TIMOKHINA, 2014). The FeMnCAl TWIP steel deformed at 300 °C by Haase et. al. (2016) also shows uniform elongation similar to the steel investigated in this work. This fact can be explained by taking into account some aspects: the initial microstructure of the current TWIP steel and after 1 ECAP pass, the presence of chromium in the chemical composition of the current steel and the deformation mechanisms of the TWIP steel in tensile tests at room temperature.

In the as-received sample, the high plasticity can be explained by a high slip and free path available for dislocations to move in the austenitic matrix. As the test progresses at room temperature, the accumulation of dislocations favors the TWIP effect during the microtensile test (LIMA, 2022). Many subgrains are formed restricting the movement of dislocations. Due to this restriction of movement of dislocations, the steel starts to deform by secondary sliding systems. There is dissociation of dislocations into partial Schockley dislocations. This result is in line with what was presented by (BARBIER, 2012) when they compared the microstructural evolution of a FeMnC TWIP steel after tensile and shear tests. After the shear test, the number of twinned grains was only 70%, while in the tensile test, 90% of the grains had at least one active twining system. Here, a significant number of elongated grains with a high density of mechanical twins and subgrains can be observed, as well as some regions of the microstructure that presented a smaller number of defects. The mixed microstructure favors the maintenance of satisfactory elongation. Chromium is a powerful alloying element in steel.

The SFE of the TWIP steel used is again low, which increases the twinning activity. Tensile deformation favors the activation of secondary twins at very low deformations (BARBIER, 2012). The union of two factors: the low grain deformation and the greater ease of twinning in tensile tests at room temperature can explain the great elongation for 1-pass ECAP

samples. It can be suggested that mechanical twining was the main deformation mechanism (LEI, 2017). Mechanical twins were detected even after 4 ECAP passes, which suggests a high work hardening capacity of the investigated TWIP steel (HAASE, 2016).

After 2 ECAP passes at 350°C, the same behavior as at room temperature was observed. There is an increase in resistance while the total elongation decreases. Both effects may be related to the evolution of the microstructure. The EBSD analysis shown in Figures 46 and 47 shows a significant reduction in the size of grains and subgrains as a consequence of the high accumulated strain. It should be noted that nano-twins were found within the primary twins due to secondary twinning in a similar TWIP steel after 2 ECAP passes (LEI, 2017). Mechanical twins drastically reduce the mean free path of dislocations, which results in a significant increase in mechanical strength. The steel under study has higher values of (YS, UTS, toughness, elongation and resilience) compared to similar steels processed by ECAP.

After 8 ECAP passes the TWIP steel showed a maximum strength of 1.8 GPa with an even greater reduction in elongation. It matches well with the EBSD and SEM analysis which shows a great refinement of the microstructure. Subgrains formed in previous ECAP passes led to new fine grains with equiaxed morphology. The evolution of the dislocation density in Figure 45 shows that the dislocation density increased at a very low rate between the 4th and 8th passes. Analyzing the values of EBSD, KAM and texture intensity, the TWIP steel probably started a recrystallization process. New ultrafine grains were observed. Resilience values significantly increased after each pass. Toughness and elongation were reduced after each pass. The TWIP austenitic steel presented distortion of the crystalline network after each pass, confirmed by the XRD analysis, Figure 44 (SKILBRED, 2020) (CHENG, 2021).

Figure 55 — True stress-strain curves.

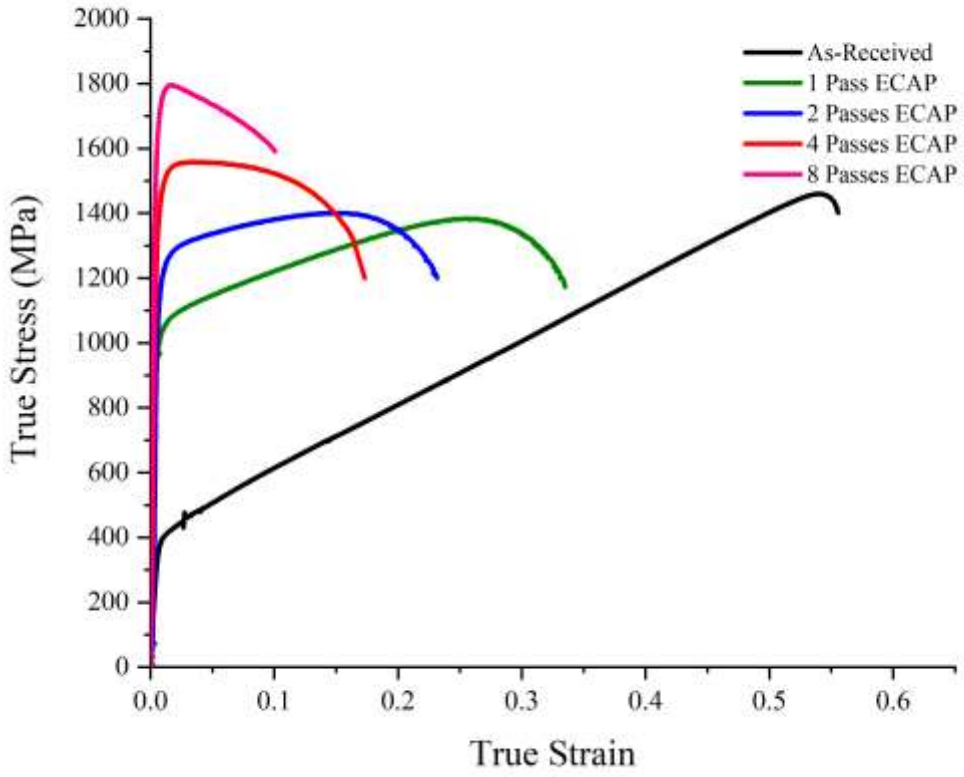

Source: Elaborated by the author.

Table 8 — Mechanical properties (defined from the true stress–true strain curves) of the studied TWIP steel in different conditions.

ECAP schedules	Yield Strength (MPa)	Ultimate tensile Strength (MPa)	Resilience ($MJ.m^{-3}$)	Elongation (%)	Toughness ($MJ.m^{-3}$)
As-received	377 ± 2	1460 ± 5	1.71	57 ± 5	593.81
1 pass	1035 ± 5	1385 ± 3	6.88	34 ± 2	421.20
2 passes	1210 ± 3	1402 ± 2	7.46	23 ± 1	307.00
4 passes	1495 ±2	1560 ± 2	10.25	17 ± 2	243.70
8 passes	1727 ± 3	1800 ± 3	11.18	10 ± 1	173.12

Source: Elaborated by the author.

Figure 56 illustrates true tensile stress (σ) and strain hardening rate curves (dσ/dε) versus true strain plots for all samples. It was observed that all samples obeyed the Considère criterion. The criterion establishes that the maximum load is the starting point of the formation

of the "neck" in the specimen (concentration of the reduction in a cross-sectional area). The stages may be related to different mechanisms: the point of transition from stage A to stage B corresponds to the beginning of twinning; the constant B-stage level may be an effect of introducing deformation twins into the deformed grains. Stage C is attributed to a decrease in twinning reaching plastic instability (XIA et al., 2017) (RENARD, 2012) (KUSAKIN, 2016) (HUGHES, 1996) (JIN, 2009). Similar behavior was found for other FeMnCAl TWIP steels, with no increase in hardening rate in stage B and with little or no increase in stage C. There are TWIP steels with different stages. Many factors can modify the stages, such as chemical composition, SFE, initial microstructure, ECAP process temperature, and ECAP matrix, among others (BARBIER, 2009) (JIN, 2009).

It is interesting to note that work hardening follows the same pattern for all samples. Although the material retains work hardening capability, no intermediate stages were detected in which the work hardening rate increased. In stage A, a drastic decrease in strain rate from 0 to 0.028 can be observed (stage A - See Figure 56(a)), which corresponds to the elastic-plastic transition. In stage B, up to 0.18 deformation (stage B-See Figure 56(b)), is associated with plastic deformation governed by the gliding of dislocations and production of mechanical twining. Finally, above 0.13 strain, an increase in strain hardening is observed (stage C- See Figure 56(c)). It stops the linear decline in work hardening rate observed in stage B and reaches steady state until fracture. This behavior is similar to that found for TWIP steels (LIMA, 2022). However, unlike what was reported by (LEI, 2017), the hardening rate is not positive. The super generation of mechanical twins caused a significant increase in mechanical strength, reducing toughness and decreasing the free path of dislocations. At the end of stage C the steel reached saturation of crystalline defects and fractured more quickly after each ECAP pass. The decrease in hardening rate is even more pronounced during secondary twinning, as secondary twinning systems are less active. Secondary twinning promotes lower hardening rates during stages B and C (JAE, 2012) (GUTIERREZ-URRUTIA, 2011). Figures 56(d) and 56(e) do not show stage A, only stages B and C for samples after 4 and 8 ECAP passes, as reported by (LEI, 2017).

Figure 56 — Strain hardening rate ($d\sigma/d\varepsilon$)-true strain curve.

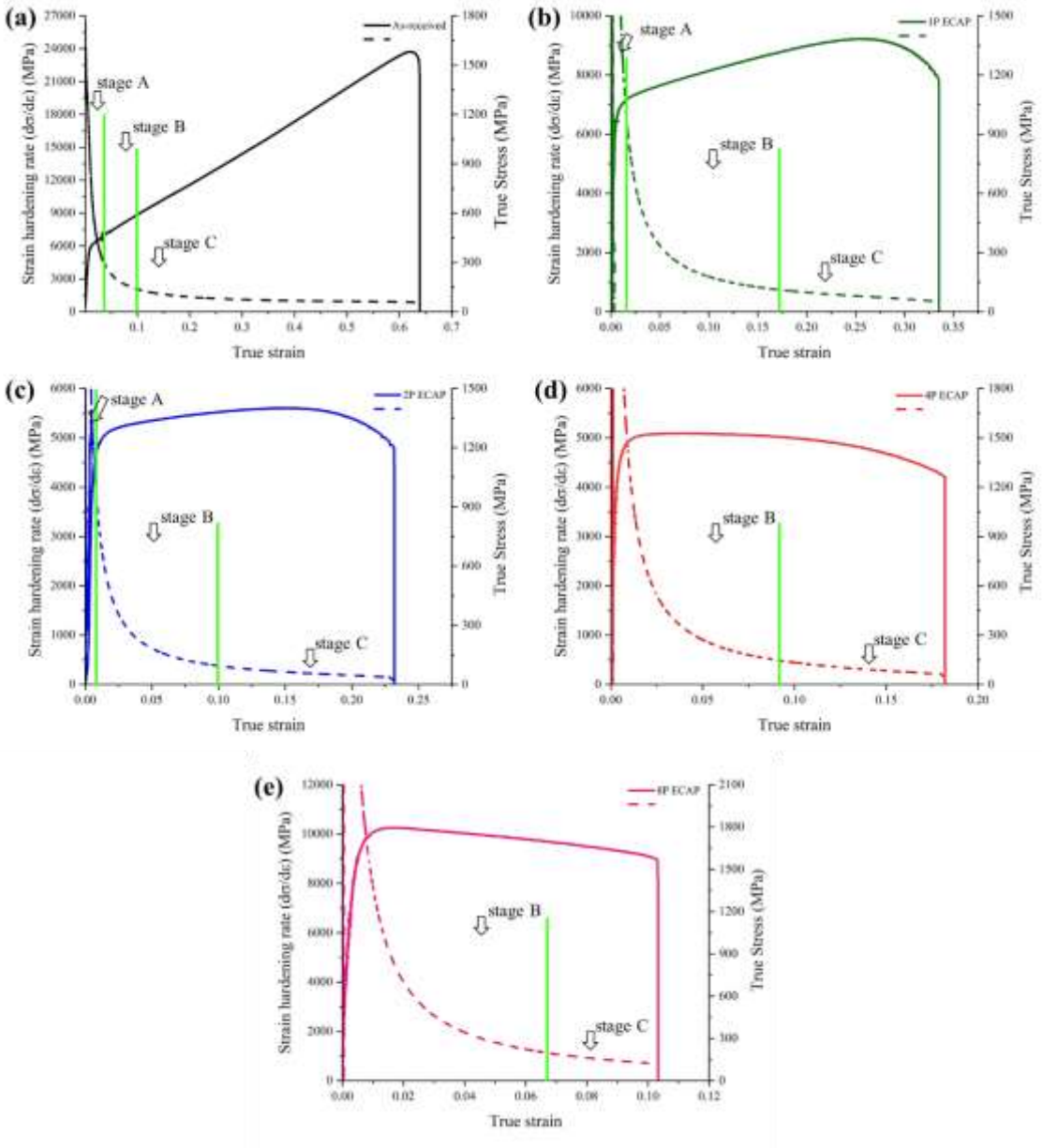

Source: Elaborated by the author.

6.3.5 Fracture analysis

Analysis of the fracture surface was carried out and are presented in Figure 57. The fractography of the as-received sample mainly contains many dimples of different sizes and depths. The images obtained correlate well with the results of elongation and toughness reported. The fracture surface changes from a typical ductile appearance for the annealed material to very small voids showing no coalescence, characterizing a fragile material surface, for 4 and 8 passes ECAP samples. Some authors (REN, 2021) reported that the greater and deeper the dimple better will be the plastic deformation capacity of the material, increasing the elongation during

tensile test. The sample after 1 ECAP pass in Figure 57b displays a behavior between the high ductility of the as-received sample (Figure 57a) and the limited ductility of the 4 passes ECAP sample (Figure 57d). Samples processed by ECAP do display some cleavage, suggesting that ductility mechanisms are still present, despite the strain hardening underwent by the material after ECAP processing. Even with limited displacement movement due to microstructural refinement, the twinning mechanism appeared to be promoting some toughness, as observed by the very small size of voids and ripples in the samples after ECAP process, especially after 2 and 4 ECAP passes. It may be suggested that mechanical twinning is an effect of tensile test temperature (room temperature). It can be concluded that the presence of strain hardening is in agreement with the analysis of the fracture surface for the samples with 8 ECAP passes that shows still some dimples (Figure 57e). In addition, the induced misfit strains revealed by the Schmid factor analysis facilitate crack propagation by providing a low-energy transgranular crack trajectory consistent with the low tensile toughness presented in Figure 57e.

Figure 57 — Fracture surfaces of the fractured tensile test specimens (a) as-received, (b) after 1 pass, (c) after 2 passes, (d) after 4 passes and (e) after 8 passes.

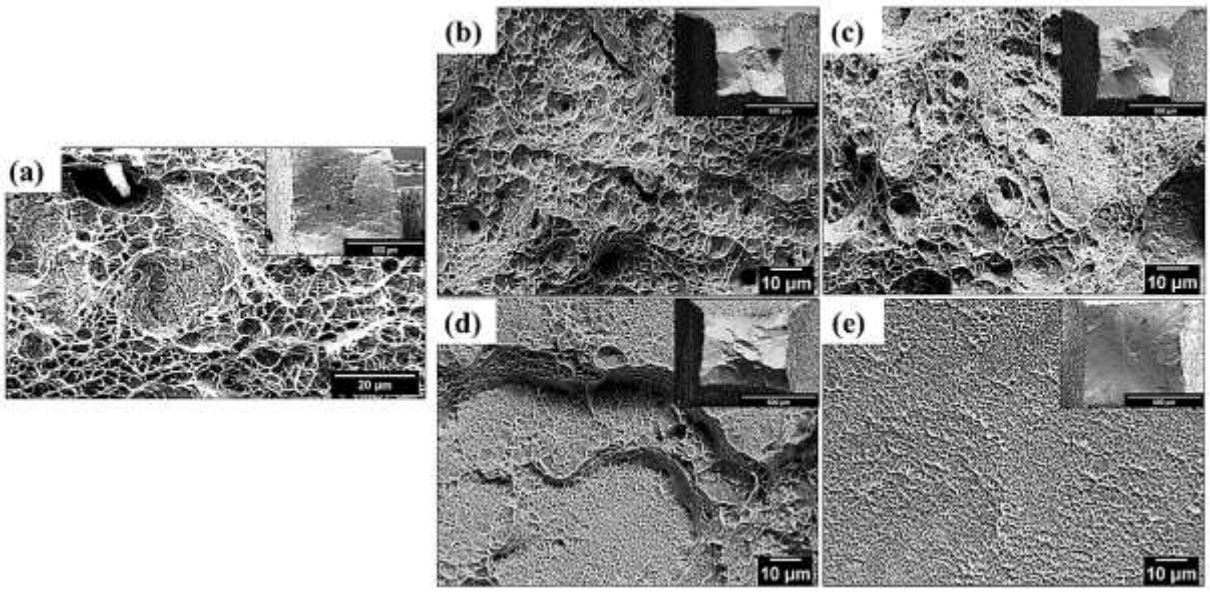

Source: Elaborated by the author.

EFFECT OF ECAP PROCESSING TEMPERATURE ON AN AUSTENITIC TWIP

STEEL'S MICROSTRUCTURE, TEXTURE AND MECHANICAL PROPERTIES.

All this chapter was published on March/16/2023 with DOI: https://doi.org/10.1016/j.jmrt.2023.03.116.

Cylindrical specimens were submitted to the different schedules of ECAP passes as given in Table 9. In a previous study of a TWIP steel similar to that investigated (TIMOKHINA, 2014), it was noticed that TWIP steel processed by ECAP at temperatures lower than 300 °C causes fracture of the punch due to high hardening rate of the material. So, the temperature of the first ECAP test was 350 ºC. Thereafter, ECAP was performed at 250 ºC.

Table 9 — ECAP schedules.

Number of ECAP passes	**1**	**2**	**4**
ECAP processing temperature	250 °C	250 °C	250 °C
	350 °C	350 °C	350 °C

Source: Elaborated by the author.

The equivalent strain ε_n (n = number of ECAP passes) introduced by ECAP was calculated following the equation in Ref. (VALIEV, 2006) and resulted in values of ε_1= 0.66 after 1 ECAP pass, ε_2 = 1.32 after 2 ECAP passes and ε_4 = 2.64 after 4 ECAP passes.

6.4 Results and discussion

6.4.1 Microscopy analysis

The OM, SEM images were made to the initial condition, i.e., as-received and after 1, 2, and 4 ECAP passes. In Figure 58(a), shows a refined microstructure, with mostly equiaxed austenitic grains containing abundant thermal twins from the hot rolling process and few mechanical twins. This condition presented a microhardness value of 202±5 HV. Consistent with reported by (LIMA 2018) (LIMA, 2022). Figure 58 images the microstructure after 1 pass (at 350 ºC-Figure 58b and 250 ºC-Figure 58d, 58e), and 4 ECAP passes ((at 350 ºC-Figure 58c and 250 ºC-Figure 58f)). Mechanical twins (white arrow) and shear bands (orange circle and lines) gradually increased with the increase in ECAP passes. After ECAP passes, elongated plastically deformed grains longitudinal along of the shear directions were observed in Figure

58(b, d). The appearance of mechanical twins is associated with low Stacking Fault Energy (SFE) of this alloy system. Despite the increased SFE of the material due to the deformation temperature of 350 °C, there has been an increase in mechanical twins, as exemplified by the inset in Figure 58d. SEM revealed that twinning and microband formation were the representative microstructural feature in the microstructure after one pass at 250 ºC. Other authors have already reported nano-twins presence within the microbands and micro-twins (TIMOKHINA, 2014). After 2 and 4 passes, plastic deformation on grains along the shear direction was also observed. After sample rotation between each pass, a complex microstructure of continuous shearing in the planes was formed (Figure 58c, 58e). These observations agree with previously published works (LEI, 2017) (ABRAMOVA, 2021) (HAASE, 2016).

The values of micro-hardness increased to 441±8 HV (Figure 59) by applying 1 ECAP pass. In samples subjected to 4 ECAP passes, the mechanical induced-twinning occurred on deformation micro shear bands, resulting in an increase of the micro-hardness to about 566±11 HV and 613±7 HV for temperatures of 350 ºC and 250 ºC, respectively. Figure 59 illustrates the development curve of the micro-hardness of the high Mn TWIP steel after ECAP passes. Austenitic grains showed a heterogeneous morphology structure due to the formation of the different defects resulting from the shear process. Note that the nano-twins did not cross the microband boundary causing a high density of twinning. This explains the excellent hardening and nucleation of ultrafine grains coupled with dislocation tangles structure as reported by previous research (LEI, 2017) (TIMOKHINA, 2014).

Figure 58 — FEGSEM secondary electron micrographs of specimens (a) as-received, (b) after

1 ECAP pass, (c) after 4 ECAP passes at 350 ºC, (d, e) after 1 ECAP pass, and (f) after 4 ECAP passes at 250 ºC. (Deformation twins are depicted with white color and annealing twins with green color).

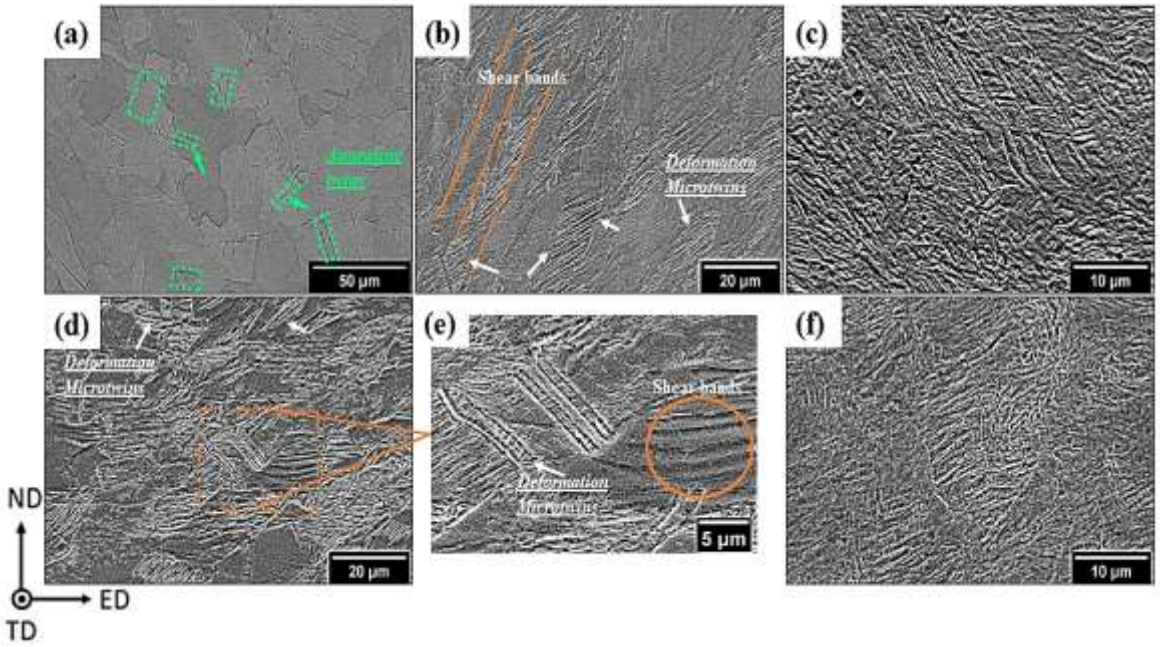

Source: Elaborated by the author.

Figure 59 — Microhardness of all samples.

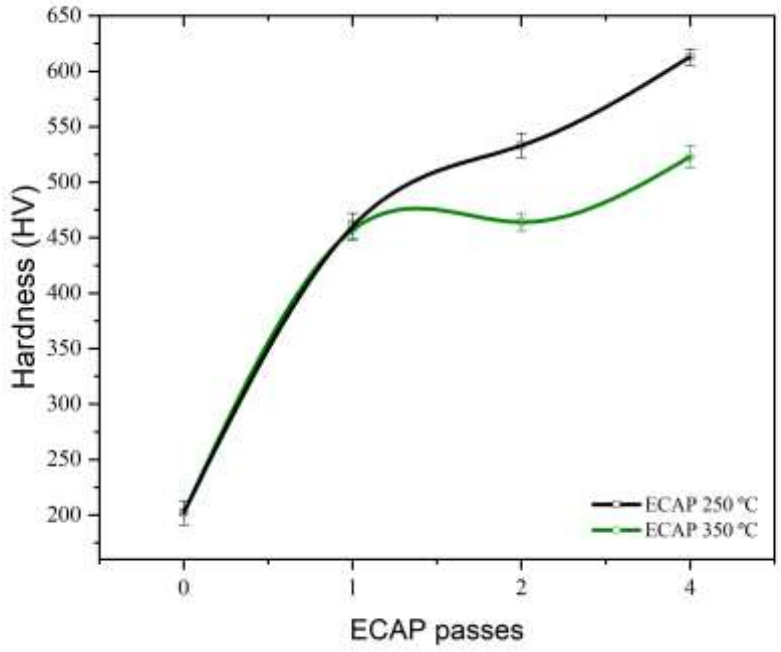

Source: Elaborated by the author.

6.4.2 XRD investigation

XRD patterns of all investigated samples are shows Figure 60. The XRD patterns after ECAP process confirmed the absence of any other phases (including α' and/or ε martensite). The dislocation densities of investigated as-received and after ECAP samples were estimated by the method proposed by (UNGAR, 1996) and the modified Williamson-Hall method and they were determined to be 6.4×10^{15} m^{-2} (after 4 ECAP passes at 350 ºC), and $8{,}3\times10^{15}$ m^{-2} (after 4 ECAP passes at 250 ºC). The evolution in dislocation density for all samples is illustrated in Figure 61. Notably, the high dislocation density due to ECAP process causes a localized lattice distortion that altered the peak shape of diffracted peak patterns' shape. A large increment in the dislocation density is also noticed after the first pass, and this coincides well with the microstructures in Figure 58 and 62, in which a large refinement was observed. A further refining of the microstructure is produced after four passes, but at a slower rate when comparing the two processing. It can be suggested that the reduction of 100 ºC favored the formation of defects and a more significant increase in the density of dislocations. As a consequence, we have an elongation of the grains, formation of shear bands and twin contours more pronounced, which agrees with hardness results reported before.

Figure 60 — XRD patterns of all samples, (a) ECAP at 250 ºC, and (b) ECAP at 350 ºC.

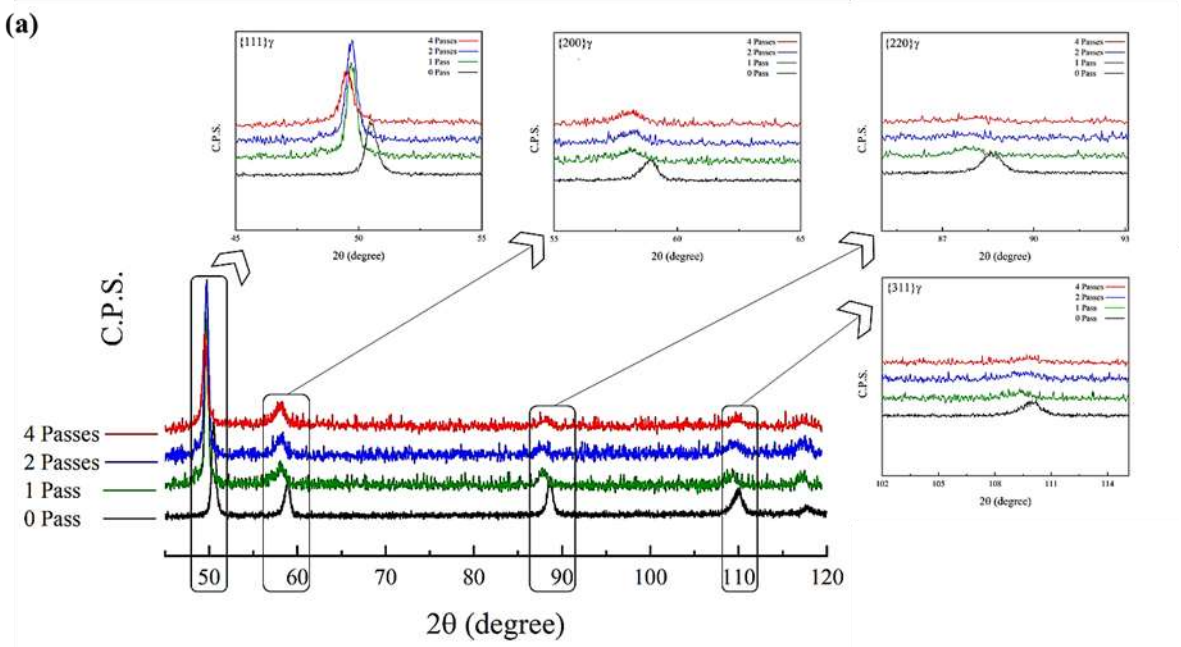

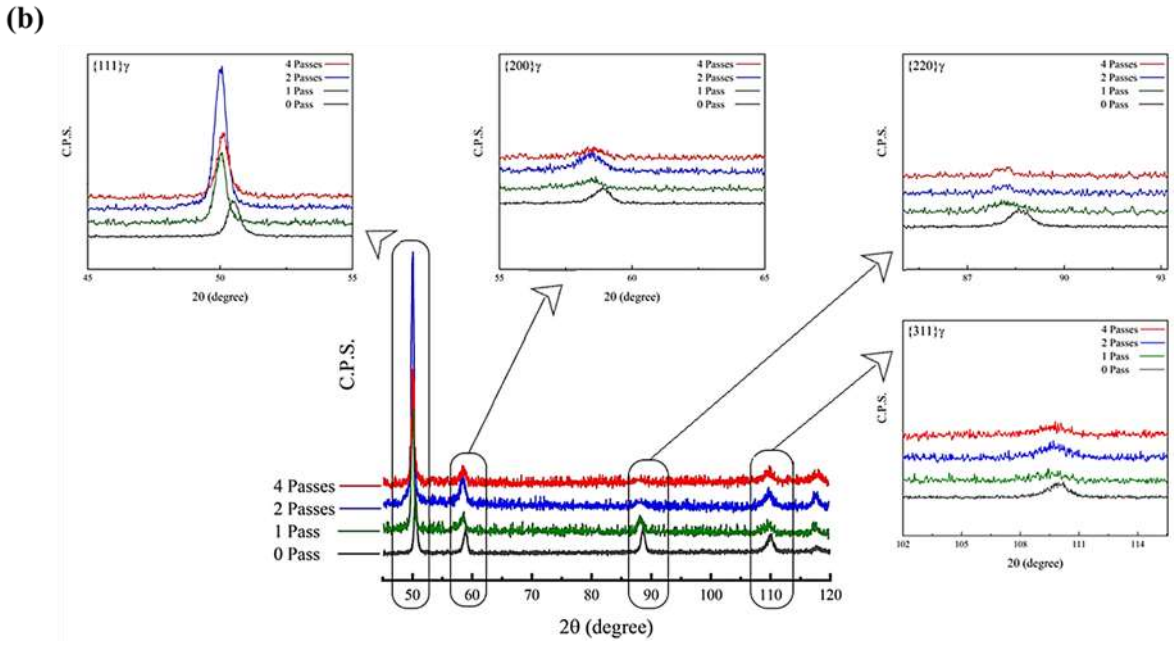

Source: Elaborated by the author.

Figure 61 — Dislocation density of all samples.

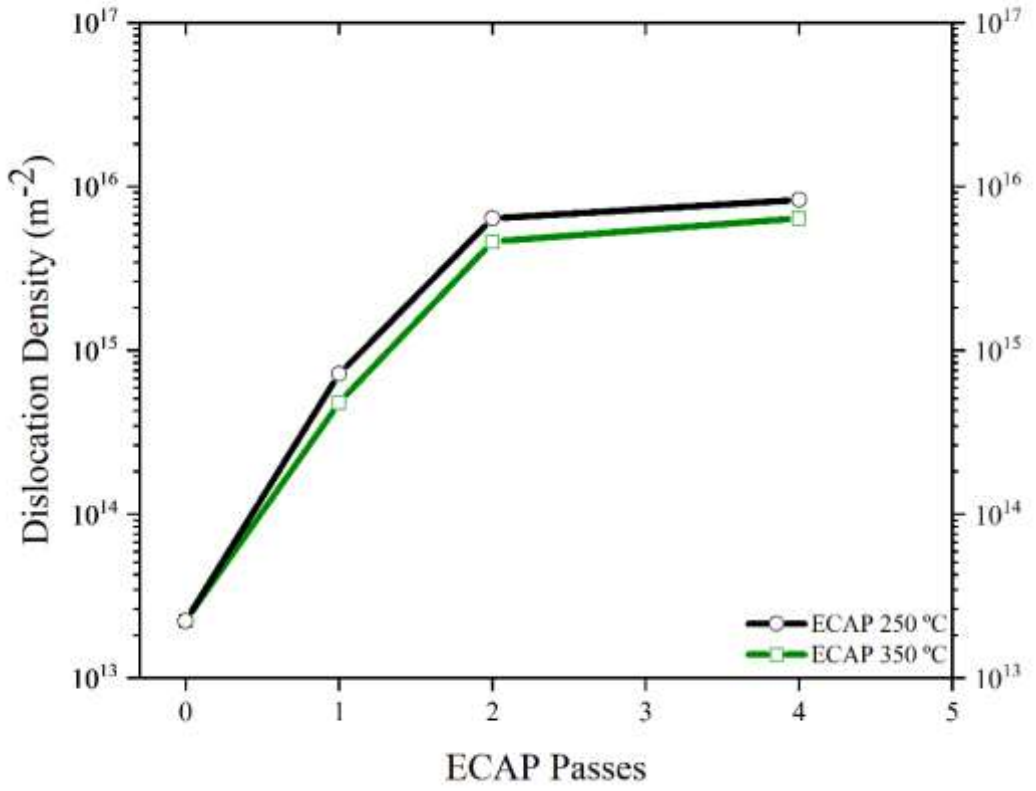

Source: Elaborated by the author.

6.4.3 Electron backscatter diffraction (EBSD) and Orientation distribution function (ODF) analysis

Orientation image maps (OIMs) and grain boundary map of the samples deformed by ECAP under different conditions obtained by EBSD are depicted in Figure 62.

The grains appear elongated in the shear direction and in some areas very fine equiaxed grains are noticed. After one pass, in addition to the elongated grains (see Figure 62b), a large quantity of low-angle grain boundaries has been generated, and concurrently in other regions, mechanical twins are observed (Figure 62a) during the ECAP process. The grain size of the new grains formed after 1 ECAP pass at 350 °C is ≅ 1μm. The average grain size is further reduced after 1 ECAP pass at 250 °C (≅ 0.6μm) (Figure 62g, 62h). The presence of large elongated grains vanishes bit by bit in a refined microstructure. Figure (62e, 62f, 62k, 62l) summarizes observations on the microstructure of the TWIP steel subjected to 4 ECAP passes.

The microstructure is composed of deformation bands inhabited by thin twins (white lines) indicating a progressive refinement. The reduction of the process temperature intensified the refinement associated to deformation bands, forming misaligned structures (ABRAMOVA, 2021). After 4 passes at 250 °C, the microstructure was more refined and it is very difficult to detect areas without a high concentration of defects, mainly subgrain contours (illustrated in green). The average grain size after 4 passes is 0.20 μm ± 0.05 μm. Values after 2 and 4 passes were similar to those found at 350 °C. The effect of temperature was more significant after 1 ECAP pass (see Figure 63).

The dependence of the average grain size (misorientation >15º) with the number of ECAP passes is displayed in Figure 63. After 4 passes, a still not stable grain size was observed. A very similar distribution is observed at both processing temperatures. This is an indication that a steady state has not yet been reached and the material would withstand more deformation without fracturing (HIGUERA-COBOS, 2013). Deformation twins are noted at all stages of deformation by ECAP. One should take into account the step sizes used in the EBSD analysis and a lower indexing rate in the more deformed samples. The microstructure of TWIP steel after multipass ECAP at 350 °C and 250 °C up to four passes is in agreement with the literature for processing in similar dies and temperatures (LEI, 2017) (ABRAMOVA, 2021) (HAASE, 2016) (TIMOKHINA, 2014).

Figure 62 — EBSD grain map, grain boundary map, IQ mapping, and IPF mapping of the samples: 1 pass (a, b), 2 passes (c, d), 4 passes (e, f) at 350 °C, 1 pass (g, h), 2 passes (i, j), and 4 passes (k, l) at 250 °C (grains boundary map: black line ─ high-angle grain boundary, green line ─ low angle grain boundary, and white line ─ twin boundary).

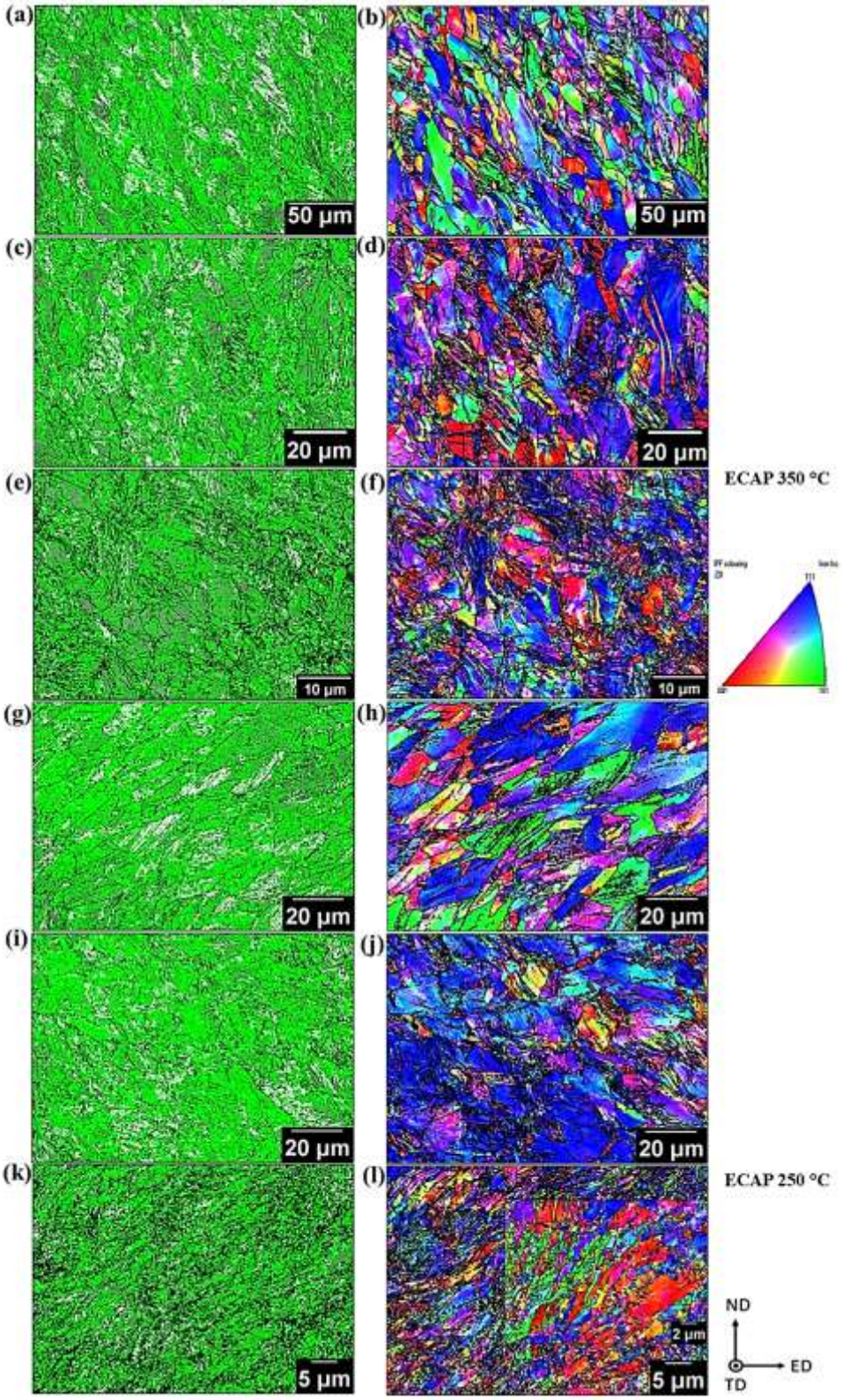

Source: Elaborated by the author.

Figure 63 — Average grain size with the number of ECAP passes.

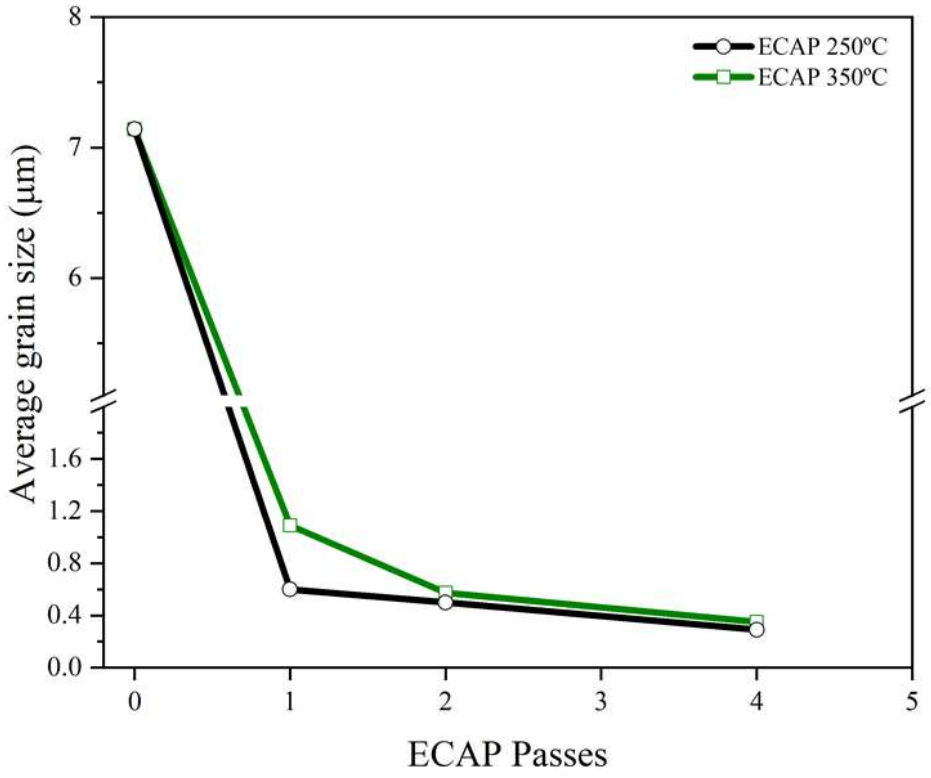

Source: Elaborated by the author.

Regarding the nature of the grain boundaries, Figure 64 provides the fraction of low angle grain boundaries (LAGBs, $2° < \Theta < 5°$), high angle grain boundaries (HAGBs, $15 ° < \Theta$), and coincidence site lattice (CSL) boundaries. New grains originate mainly within the shear bands, at grain boundaries and as a consequence of dislocation rearrangement. Accumulation of dislocations form subgrains and gradually lead to refinement of the microstructure (DESPRÉS, 2020). The as received sample was found to have the lowest fraction of low angle misorientation due to recovery during hot rolling (manufacturing process). The initial material contains approximately 30% of the total CSL. After ECAP passes, one can show a large number of subgrains generated in the first pass, which decreases progressively with increasing passes (Figure 63). Greater refinement was noted after 1 ECAP pass at 250 °C.

With decreasing temperature and SFE, a high amount of dislocations and crystallographic defects are generated during ECAP passes, suggesting a greater refinement in the samples processed at 250 °C (see Figure 64). Twinning is usually not hoped-for coarse-grained material for these temperatures. The decrease in the grain size normally suppresses

twinning (ALLAIN, 2004). The major reduction in the grain size after 4 ECAP passes should make twinning more difficult (TIMOKHINA, 2014) (see Figure 64).

The results suggest that a gradual increase in grain disorientation led to grain fragmentation and reoriented texture components. It is commonly observed in austenitic steels the development of low energy CSL boundaries (BELADI, 2013) (HIGUERA-COBOS, 2013). The results suggest that the largest portion of CSLs is due to the formation of slip bands and deformation twins. As proposed by (YE, 2021), the authors suggested that the planar slip dislocation contains many Shockley partial dislocations which produce deformation twins massively acquiring the planar slip dislocations. It can be seen that the fraction of CSL boundaries decreases with the progressive amount of strain (see Figure 64). However, this is only partially true. What happens is a limitation of the EBSD technique in detecting very thin mechanical twins. The results of HAGB and LAGB fractions are similar to those reported by Cabrera et al. (2017) in TWIP steel processed by ECAP. Anyway, and based on other investigations (LEI, 2017) (HIGUERA-COBOS, 2014) (MURR, 2004), there is evidence of a saturation in the proportions of HAGB and LAGB with the increase in the number of ECAP passes.

Figure 64 — Misorientation grade of the grain boundaries with the number ECAP passes.

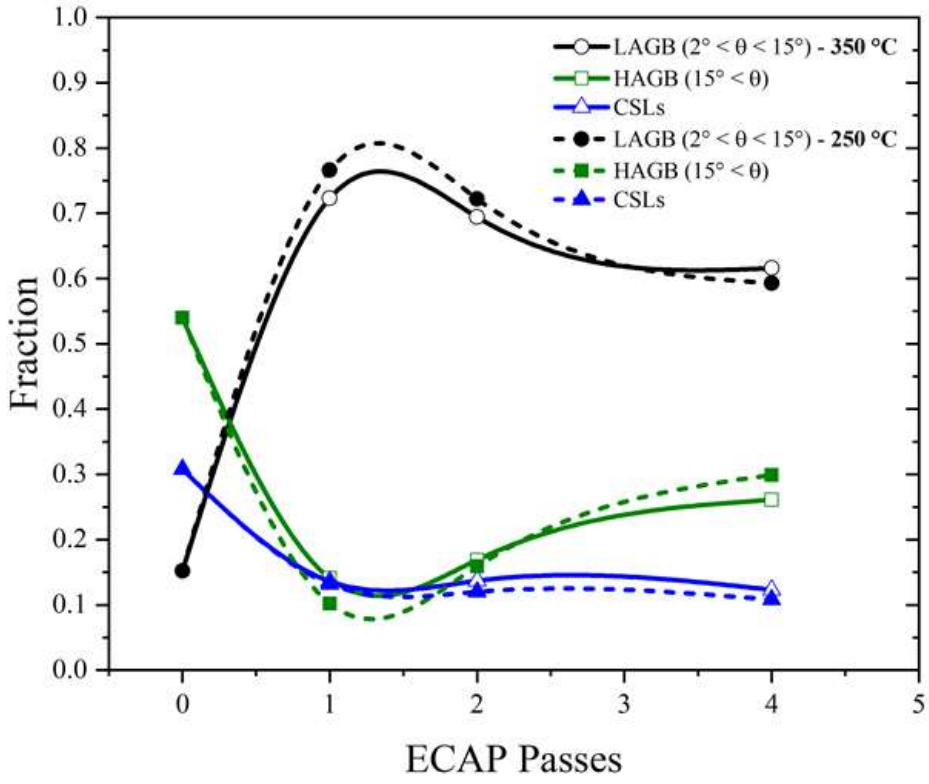

Source: Elaborated by the author.

The texture of the material deformed after ECAP passes (at two temperatures) and the ideal position for texture components for FCC materials deformed by simple shear are presented in Figure 65, Figure 66 and defined in Table 6. Monoclinic symmetry can be observed in some cases since the components are symmetrical every 180º. Figure 65 and 66 shows the texture after 1 ECAP pass, all shear texture components, as listed in Table 10, were immediately formed and developed a complete fiber at (0-360°, 45°, 0°). Variances in Euler space from ideal orientations is usual in ECAP processes, which are related to different processing factors (HAASE, 2016) (BEYERLEIN, 2009) (HIGUERA-COBOS, 2014). After one ECAP pass, the presence of A_1* and A_2*, part of α fiber, can be noticed in the TWIP steels. The components showed more intensity at 250 °C. Which suggests a more pronounced texture with the reduction of temperature. This effect indicates twinning, which is consistent with the observations in Figures 58 and 62. The components showed similar intensities to the FeMnCAl TWIP steel studied by (HAASE, 2016) (LEI, 2017). The evolution in fiber B is related to the increase of component B (MURR, 2004), mainly due to the replacement of orientations of component C

by orientations B ({112}\<110>) (HIGUERA-COBOS, 2014).

The texture became more pronounced after 4 ECAP passes, as indicated by an increased texture index and a decreased volume fraction of randomly oriented grains (See Figure 67). Some authors report texture embrittlement or saturation between 2 and 4 ECAP passes following route Bc (SANDIP, 2011) (MOLODOVA, 2007) (SAIYI, 2005) (GAZDER, 2006) (FERRASSE, 2004). Haase et al. (2016) hypothesized that the strong presence of C would be related to dislocation sliding. At the same time, the increase in B/$\overline{B}$ components would be associated with the twinning mechanism. Authors also reported the strong presence of the C component and the increase of the B/$\overline{B}$ components with ECAP passes. For the TWIP steel used in this work, at both processing temperatures, the texture evolution corresponds better with the proposed by (LEI, 2017) (SUWAS, 2003) as C and A_1* components are reduced, and B/$\overline{B}$ increased after ECAP passes. These results suggest that the importance of twinning deformation would be more significant in both cases.

Figure 65 — (a) Ideal components in triclinic symmetry of FCC materials deformed by simple shear (die 120°), texture components of investigated TWIP steel for φ2=0° and φ2=45°, (b) after 1 ECAP pass, (c) after 2 ECAP passes, and (d) after 4 ECAP passes at 350 °C.

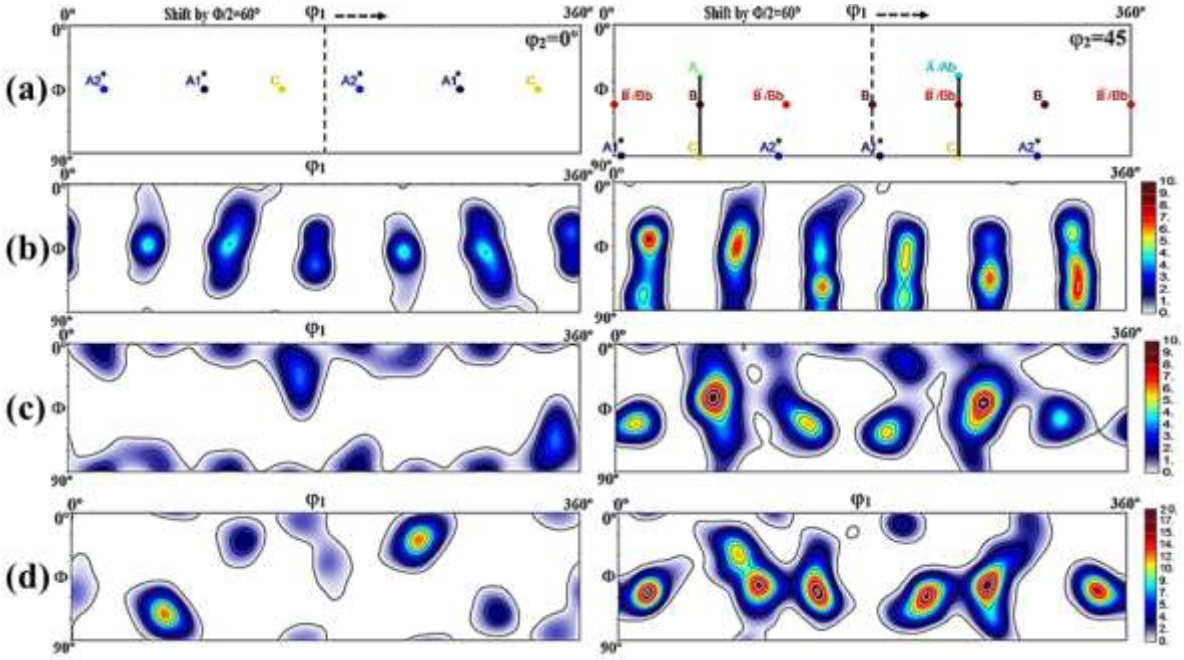

Source: Elaborated by the author.

Figure 66 — (a) Ideal components in triclinic symmetry of FCC materials deformed by simple shear (die 120°), texture components of investigated TWIP steel for φ2=0° and φ2=45°, (b)

after 1 ECAP pass, (c) after 2 ECAP passes, and (d) after 4 ECAP passes at 250 °C.

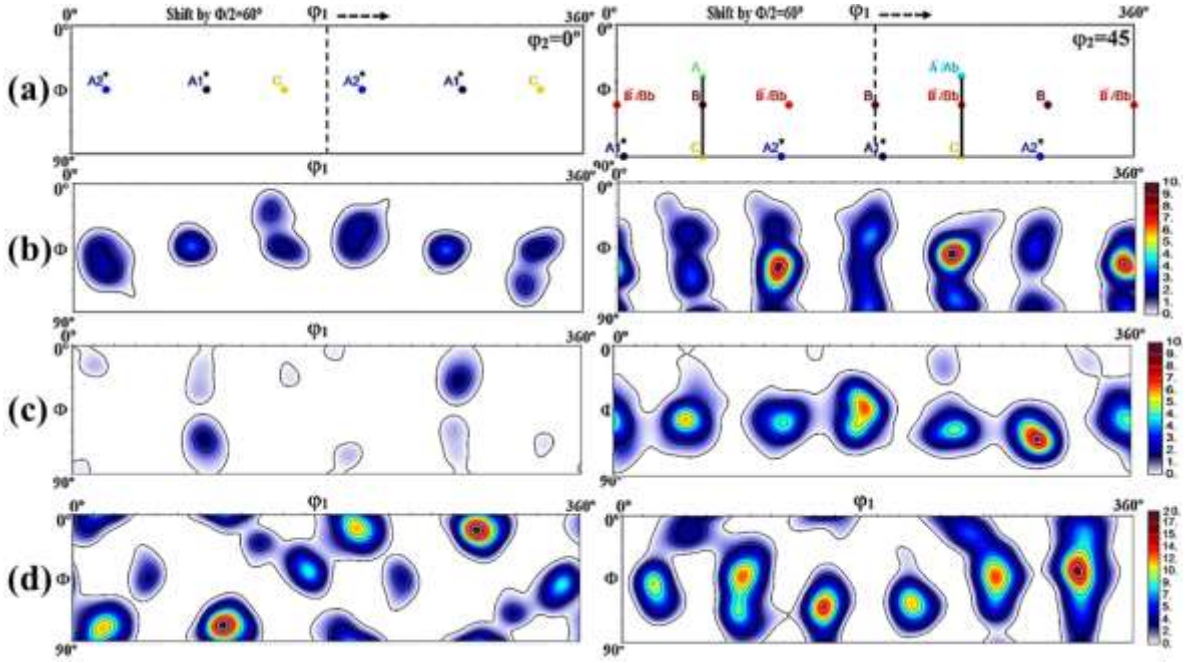

Source: Elaborated by the author.

Figure 67 — Evolution of the volume fractions of the main texture components during ECAP process. (a) after 1, 2, 4 ECAP passes at 350 °C, and (b) after 1, 2, 4 ECAP passes at 250 °C.

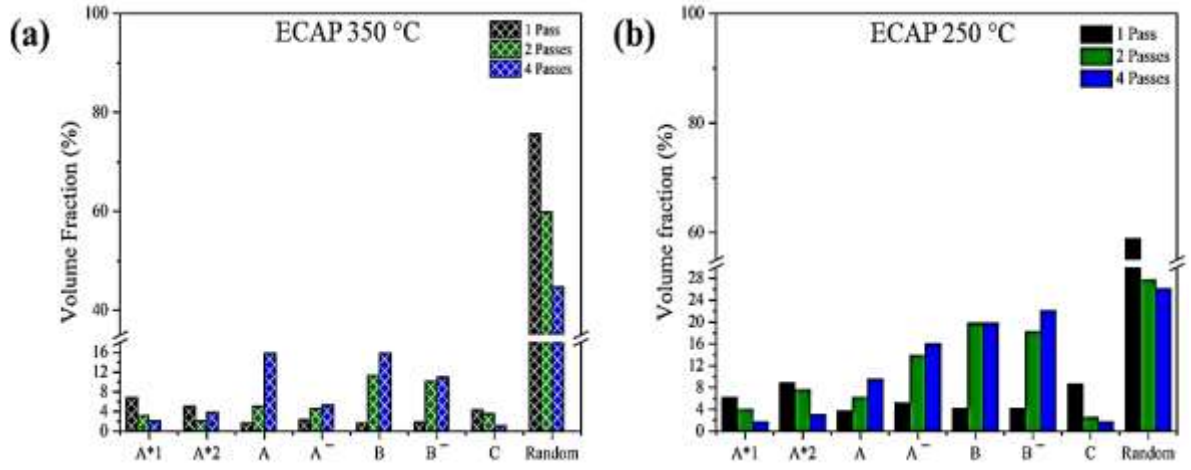

Source: Elaborated by the author.

It was observed in TWIP steel a preference for fiber <110> ‖ X (direction of extrusion), giving rise to the presence of deformation texture components such as C, B/B̄ y A/Ā (see Figure 68). Texture components usually found in materials subjected to simple shear (LEI, 2017). A marked presence of <110> ‖ Z y <111> ‖ Y fibers was also reported. Figure 68 suggests the strong heterogeneity in the texture imparted by ECAP process, mainly when using ECAP matrices with configuration of Ψ>0° . However, the presence of the strong fiber

<111> ‖ Y also can be linked to the presence of special grain boundaries of the type Σ3 (60° <111>). The fiber <111> ‖ Y enlargement is not reported in Figure 68. Therefore, it can be suggested that the EBSD technique is limited to identify very thin mechanical twins. It can be concluded that the steel under study deforms following the <110> direction and plane (111) of higher atomic density for the FCC materials, or β fiber, which is composed of texture components B/$\bar{B}$, and A/ $\bar{A}$ (HIGUERA-COBOS, 2013) (HIGUERA-COBOS, 2014) (HOSNI, 2010). Figure 68 shows a similar behavior for both test temperatures. The significant difference noted was texture intensity. At a temperature of 250 °C, the TWIP steel was more textured with less randomly oriented grains.

Figure 68 — Fiber texture after ECAP process, (a) after 1, 2, 4 ECAP passes at 350 °C, and (b) after 1, 2, 4 ECAP passes at 250 °C.

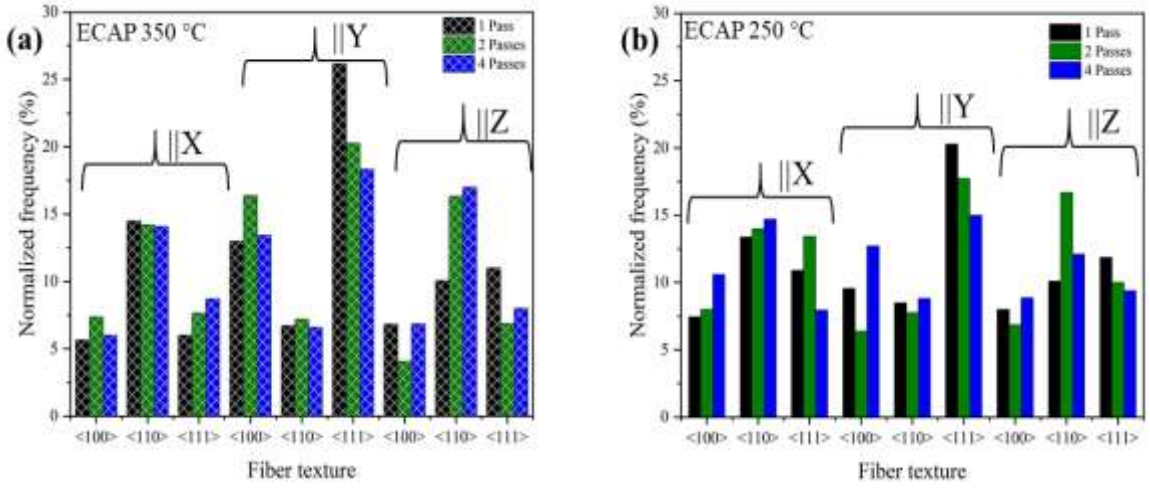

Source: Elaborated by the author.

Increasing ECAP-passes, many subgrains are generated blocking dislocation movement. KAM results obtained are showed in Figure 69(h). KAM became stronger with increasing strain. The highest fraction of low KAM values (KAM < 1°) was found in the as-received sample (Figure 69(a)). The as-received sample with recrystallized austenite grains showed minimal intergranular misorientation in the microstructure. After ECAP process, a significant fraction of deformed grains with medium KAM (1° < KAM < 3°) (see Figure 69(b, c, d)) and high KAM (> 3°) was developed. High values of KAM (see Figure 69(f, g)) could be associated with high local lattice distortion and dislocation density resulting in an increase in internal energy (VICENTIS, 2017). Higher KAM value meant higher geometrically necessary dislocation (GND) density, resulting in higher strength during the ECAP process. It can be

suggested that the presence of two variants (see Figure 46) of deformation twins played an important role in reducing the mean free path of dislocations. As related in (HOSNI, 2010), finer and denser twins provide more interfaces between the matrix and twins to accommodate more dislocations leading to a composite effect, resulting in higher work hardening rates and KAM (HOSNI, 2010).

Figure 69 — EBSD KAM maps: (a) as-received, (b) after 1 ECAP pass, (c) after 2 ECAP passes, (d) after 4 ECAP passes at 350 °C, and (e) after 1 ECAP pass, (f) after 2 ECAP passes, (g) after 4 ECAP passes at 250 °C, (h) Variation of kernel average misorientation distribution of all investigated specimens.

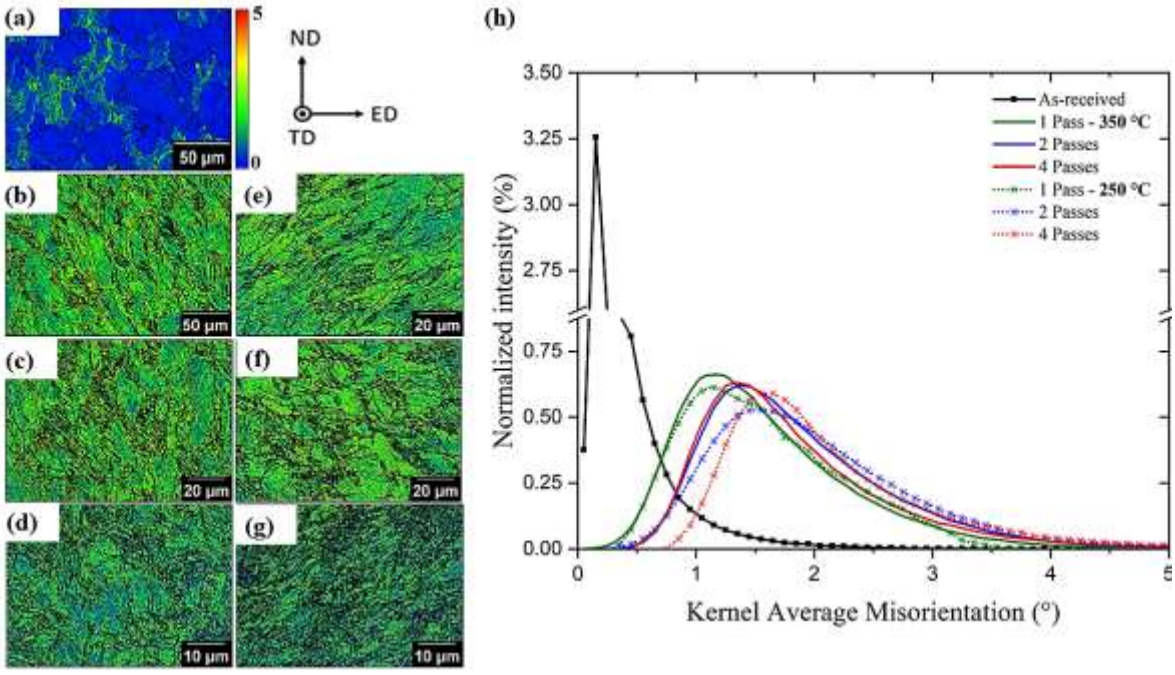

Source: Elaborated by the author.

The analysis of the Taylor factor was made to observe the resistance of the grains with the increase of the strain. It was observed that the grains showing mechanical twins have a high Taylor factor. This result seems to confirm the hypothesis made by other authors (XIANFENG, 2013): high Taylor factor implies high difficulty for deformation by displacement slip, which promotes the formation of deformation twins. According to the author (XIANFENG, 2013), Taylor's theory of plastic deformation states that grains with a higher Taylor factor will dissipate more strain energy and, therefore, deformation will be more difficult because the orientation of the grains needs to rotate to be closer to the <111>. In other words, the greater the Taylor factor, the easier it is for twins to form. Figure 70 shows the Taylor factor

and CSL's maps, indicating that mechanical twins are generated within grains with a high value of the Taylor factor. The results demonstrate that the Taylor factor can provide an important guideline to determine the deformation mode and deformation structures, that is, a high Taylor factor corresponds to deformation twinning and a low Taylor factor to slipping. For an intermediate value of the Taylor factor, it corresponds to the multislip mode. (SKILBRED, 2020) (BORDONE, 2022) (XIANFENG, 2013).

Regarding the nature of the grain boundaries (see Figure 70), the material studied here, in the as-received condition and deformed, presents particularly special limits (coincidence site lattice – CSL) such as mechanical twins. The initial condition contains approximately 30% of CSL ∑3 and 1.33% of CSL ∑9. In the deformed material, one can notice a large quantity of subgrains generated in the fourth pass, (see Figure 70 (k,n)). However, after the second pass, the deformation introduced into the material promotes a new increase in the CSL fraction, (see Figure 70) that can be partially attributed to special misorientation fractions with twin character CSL ∑3. After the first ECAP pass, TWIP steel showed a qualitative reduction in CSL grain contours. Values of ≅ 4% of CSL ∑3 were obtained. The misorientation distribution functions from the second to the fourth passes were similar. This is an indication that a steady state has not been achieved after 4 passes and further deformation would introduce significant changes in the microstructure. The total CSL fraction in the second and fourth passes were ≅ 4.8% CSL ∑3, and ≅ 5% CSL ∑3. With the temperature reduction of the ECAP process (350 °C to 250 °C), the values after 1, 2, and 4 ECAP passes were 5% CSL ∑3, 3.75% CSL ∑3, and 4.5% CSL ∑3 respectively. However, this is only partially true. What happens is a limitation of the EBSD technique in detecting grains boundary CSL. This behavior of CSL ∑3 fractions are similar to those reported by (LEI, 2017).

Figure 70 — EBSD Taylor factor, maps of (a) as-received, (b) after one pass, (c) after two passes, (d) after four passes at 350 ºC while (e) after one pass, (f) after two passes, (g) after four passes at 250 ºC. EBSD CSL' maps of maps of (h) as-received, (i) after one pass, (j) after two passes, (k) after four passes at 350 ºC while (l) after one pass, (m) after two passes, (n) after four passes at 250 ºC.

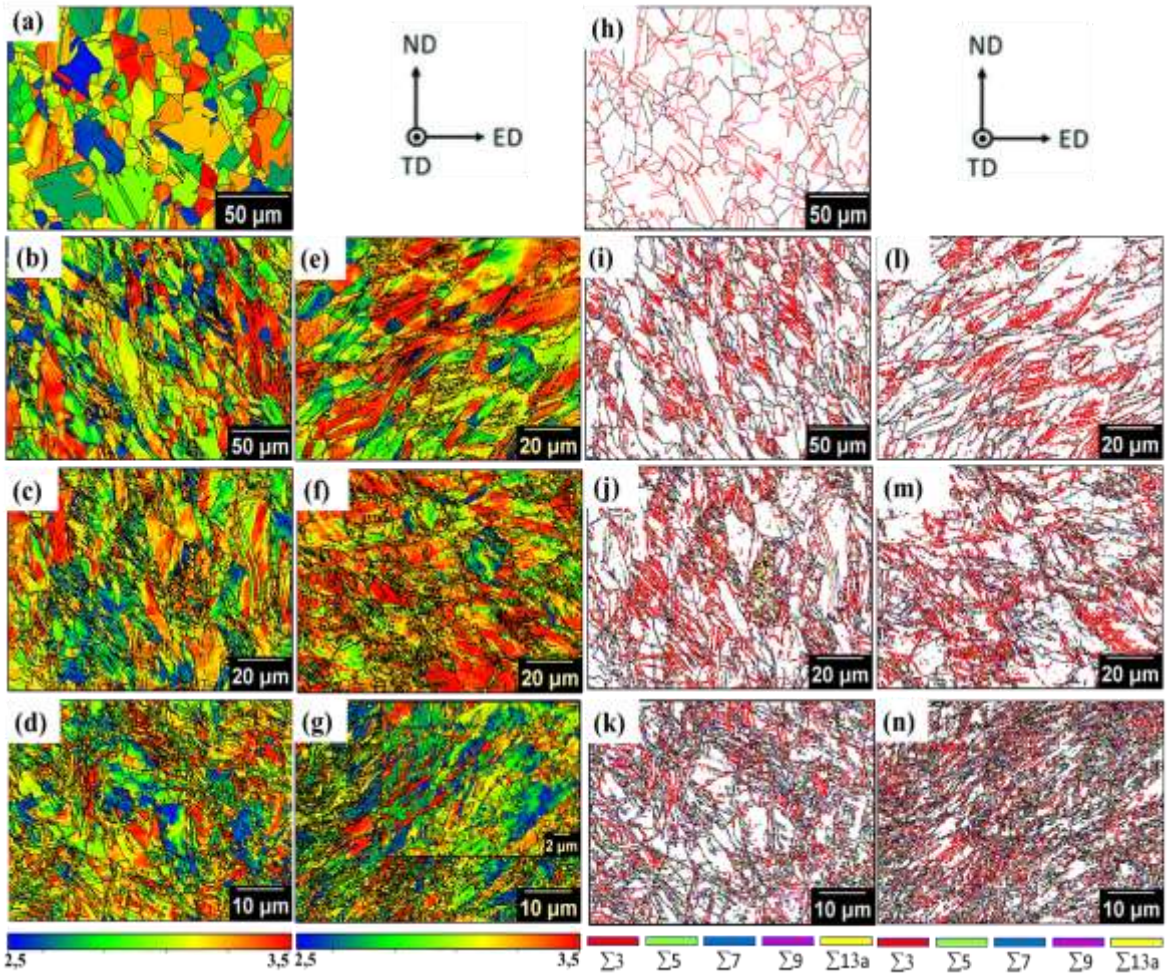

Source: Elaborated by the author.

6.4.4 Mechanical Tensile tests

The true stress-strain curves of the as-received TWIP steel and after ECAP process (both ECAPed at 350 °C and at 250 °C temperature) are shown in Figure 71. The corresponding data are summarized in Table 10. The as-received material shows good mechanical properties, combining high ultimate tensile strength (UTS) above 1460 MPa and large ductility (total true strain close to 0.57) with a moderate yield strength (YS) of 377 MPa. The high plasticity can

be explained by a high slip and free path available for dislocations to move in the austenitic matrix. As the test progresses at room temperature, the accumulation of dislocations favors the TWIP effect during the tensile test (LIMA, 2022). Yield strength (YS) and ultimate tensile strength (UTS) increase with the strain passes. Similar mechanical behaviors were found in the literature (LEE, 2018) (TIMOKHINA, 2014). Serrated flows were observed on the tensile test curves. They are caused by dynamic aging from stress-induced interactions between C-Mn clusters and partial displacements (SUWAS, 2006) (SEUNG-JOONN, 2018). The toughness of the samples is drastically reduced after each ECAP pass. Despite the reduction, the values obtained for total elongation are considered satisfactory. Elongation results are greater than those reported for some conventional deep drawing steels, such as high strength IF(HS) and other high Mn TWIP steels (GRÄSSEL, 2000) (LEI, 2017) (ABRAMOVA, 2021) (HAASE, 2016).

After the first ECAP pass at 350 °C, there is a significant increase in the yield strength (1035 MPa at 350 °C and 1190 MPa at 250 °C) as a result of the increase in dislocation movement activity forming many subgrains and interacting with mechanical twinning (BRACKE, 2009). Even with the increase in SFE (ALLAIN, 2004), mechanical twinning was observed in the austenite grains for the current TWIP steel at both test temperatures. The TWIP steel deformed at 300 °C by (HAASE, 2016) also showed a behavior similar to steel investigated in this work.

Changes in tensile properties with temperature actually reflect SFE's dependence on temperature. The SFE in metallic materials with FCC structure decreases with decreasing temperature, leading to an increase in the critical resolved shear stress (CRSS) for sliding and a decrease (CRSS) for twinning. Therefore, when stress and temperature decrease, sliding becomes difficult while twinning tends to be easy. In this case, although the CRSS for twinning is higher, favoring slip deformation in most cases, twinning is still preferred when stress concentration arises in the material, mainly at low temperatures. Mechanical twins drastically reduce the mean free path of dislocations, which results in a significant increase in mechanical strength (SKILBRED, 2020) (XIANFENG, 2013).

The restriction of movement of dislocations caused by the formation of many subgrains restricts movement of dislocations. Thus, the steel begins to deform by secondary sliding systems, causing the dissociation of dislocations with a Burgers vector into partial Schockley dislocations. Chromium is an excellent alloying element of steel. It is mainly added to increase steel's hardenability and corrosion resistance, as well as the yield strength of steel. Chromium, when present in the steel, reduces the stacking fault energy, favoring the TWIP

effect (SKILBRED, 2020) (TIMOKHINA, 2014) (CHENG, 2021) (CHENG, 2021). After two ECAP passes, the same behavior at both temperatures was observed. There is an increase in resistance while the total elongation decreases. Both effects may be related to the evolution of the microstructure. After 4 ECAP passes at 250 °C the TWIP steel showed a maximum strength of 1.9 GPa with an even greater reduction in elongation. But it maintained a satisfactory total elongation greater than $\varepsilon = 8\%$. It matches well with the EBSD and SEM analysis which shows a great refinement of the microstructure. Mechanical twins drastically reduce the mean free path of dislocations, which results in a significant increase in mechanical strength. The steel under study has higher values of (YS, UTS, toughness, elongation and resilience) compared to similar steels processed by ECAP. Resilience values significantly increased after each pass, consequence of the significant increase in the YS. Toughness and elongation were reduced after each pass. The TWIP austenitic steel presented distortion of the crystalline network after each pass, confirmed by the XRD analysis, Figure 60.

Comparing the present FeMnCCr TWIP steel with the FeMnCAl TWIP steel deformed by ECAP with equivalent number passes (HAASE, 2016), it must be said that the behavior is similar, with a large increase in YS and UTS together with a better ductility after hardening. The FeMnCr TWIP steel processed by ECAP at two different temperatures has a larger UTS than the FeMnCAl steel, but this can be connected with the larger twinning activity in FeMnCr TWIP steel due to the absence of aluminum that increase the SFE, in addition to the presence of chromium that decrease the SFE (LEI, 2017).

Figure 71 — True stress-strain curves.

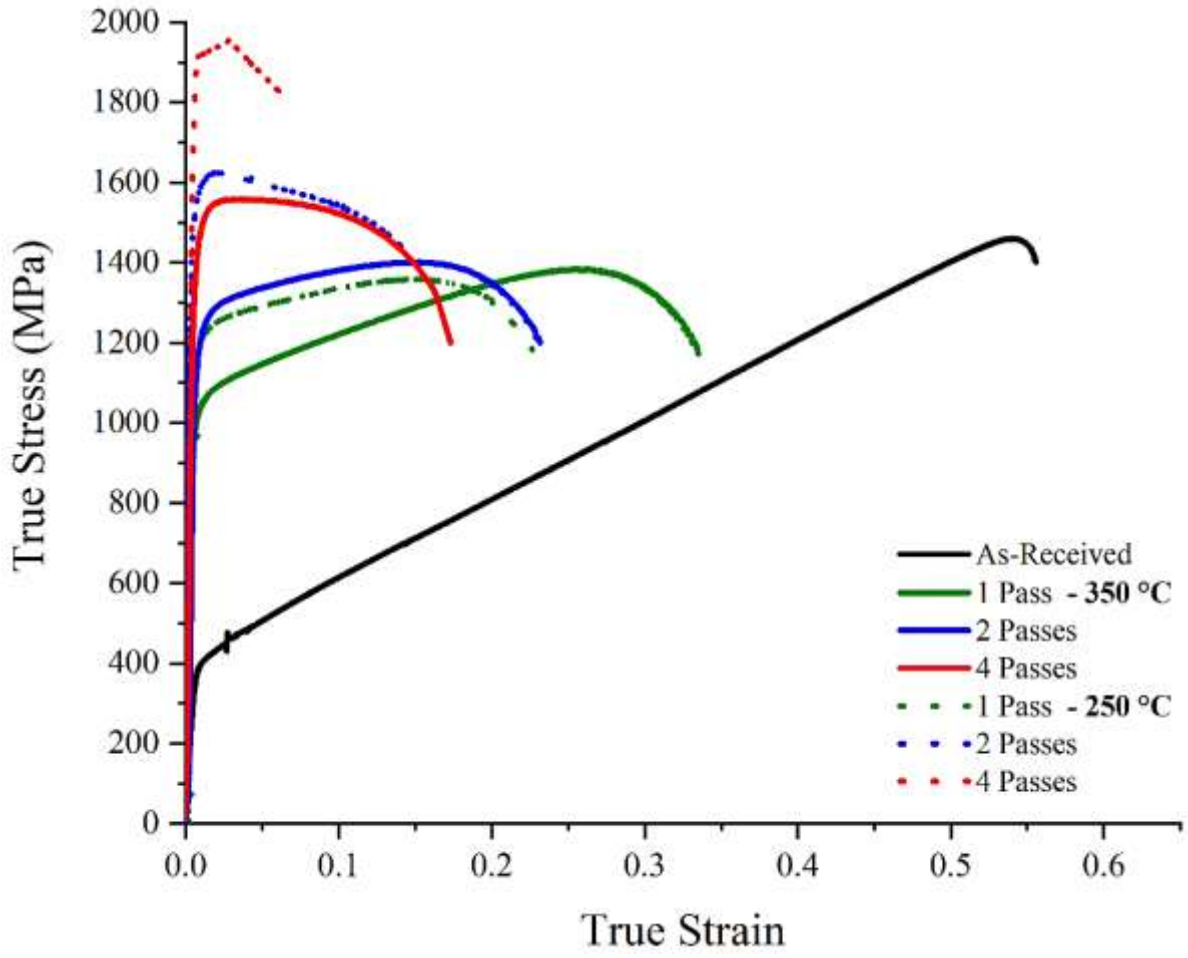

Source: Elaborated by the author.

Table 10 — The studied TWIP steel's mechanical properties (defined from the true stress–true strain curves) in different conditions.

ECAP schedules	Yield Strength (MPa)	Ultimate tensile Strength (MPa)	Resilience ($MJ.m^{-3}$)	Elongation (%)	Toughness ($MJ.m^{-3}$)
As-received	377 ± 2	1460 ± 5	1.71	57 ± 5	593.81
at 350 °C					
1 pass	1035 ± 5	1385 ± 3	6.88	34 ± 2	421.20
2 passes	1210 ± 3	1402 ± 2	7.46	23 ± 1	307.00
4 passes	1495 ±2	1560 ± 2	10.25	17 ± 2	243.70
at 250 °C					
1 pass	1205 ± 3	1360 ± 2	6.82	24 ± 2	293.86
2 passes	1590 ± 3	1625 ± 3	8.54	15 ± 1	222.09
4 passes	1915 ±2	1960 ± 2	9.34	7 ± 2	118.65

Source: Elaborated by the author.

Figure 72 illustrates the strain hardening rate curves (dσ/dε) versus true strain plots for all samples. The results suggest all samples obeyed the Considère criterion. The criterion say that the maximum load is the starting point of the formation of the "neck" in the specimen (concentration of the reduction in a cross-sectional area). The stages may be correlated with different mechanisms: the transition from stage A to stage B corresponds to the beginning of twinning; the constant B-stage level may be an effect of introducing deformation twins into the deformed grains. Already stage C is attributed to a decrease in twinning reaching plastic instability (HUGHES, 1996). Similar behavior was found for other FeMnCAl TWIP steels, with no increase in hardening rate in stage B and with little or no increase in stage C. Many factors can provoke changes in the stages, such as chemical composition, SFE, initial grain size, ECAP process temperature, ECAP matrix configuration, among others (BARBIER, 2009) (JIN, 2009).

It can be noted that work hardening follows the same pattern for all samples. Although the material retains work hardening capability, no intermediate stages were detected in which the work hardening rate increased. In stage A at 350 °C, a drastic decrease in strain rate from 0 to 0.028 can be observed (stage A in Figure 72a), which corresponds to the elastic-plastic transition. In stage B, up to 0.12 deformation (stage B in Figure 72a), is associated with plastic deformation governed by the gliding of dislocations and production of mechanical twining. Above 0.13 strain, an increase in strain hardening is observed (stage C in Figure 72a). Strain hardening stops the linear decline in work hardening rate observed in stage B and reaches steady state until fracture. This behavior is similar to that found for TWIP steels (LIMA, 2022). The stages at 250 °C repeated the same behavior. Figure 72b also shows the presence of three stages during the strain deformation rate. The main difference was the faster hardening rate reduction with smaller stages at smaller true deformations. The tensile specimens after ECAP 250 ºC brooked faster during the test at room temperature.

However, unlike what was reported by (LEI, 2017), the hardening rate is not positive. The super generation of mechanical twins caused a significant increase in mechanical strength, reducing toughness and decreasing the free path of dislocations. At the end of stage C the steel reached saturation of crystalline defects and fractured more quickly after each ECAP pass. The decrease in hardening rate is even more pronounced during secondary twinning, as secondary twinning systems are less active. Secondary twinning promotes lower hardening rates during stages B and C (JAE, (2012) (GUTIERREZ-URRUTIA, 2011). Figures 72(d) and 72(e) do not show stage A, only stages B and C for samples after 4 and 8 ECAP passes, as reported by (LEI, 2017).

Figure 72 — Strain hardening rate (dσ/dε)-true strain curve for all samples.

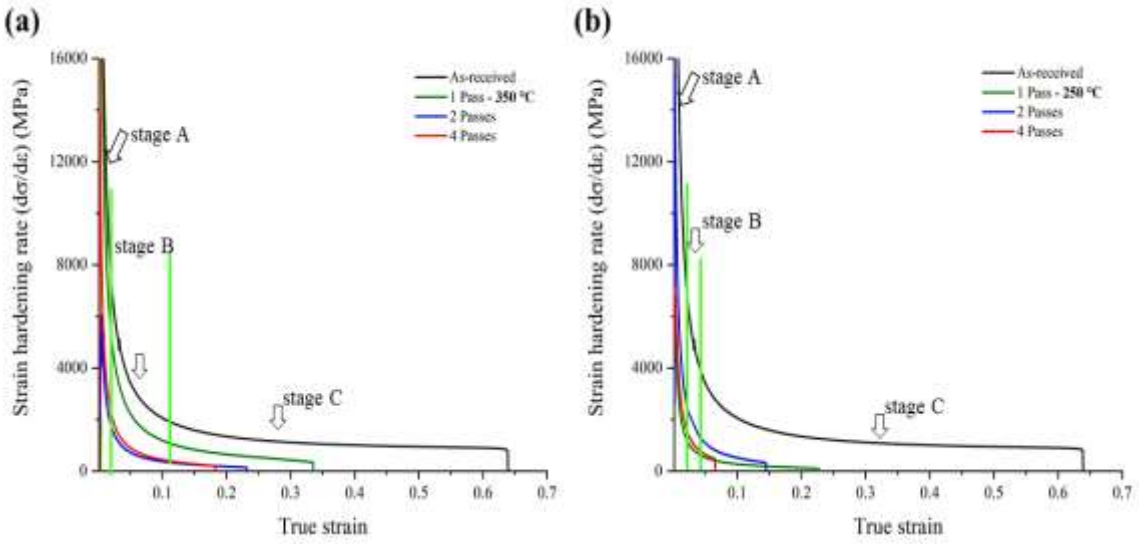

Source: Elaborated by the author.

6.4.5 Fracture analysis

The fracture surface for the all studied samples is shown in Figure 73. The as-received sample exhibits a large ductility, and fracture occurs by void coalescence and growth. Smaller amounts of voids and dimples are observed in general in the ECAPed samples, where some cleavage, as well as a subcell structure (characteristic of fine-grained materials), is apparent. The sample after 1 ECAP pass in Figure 73 displays a behavior between the high ductility of the as-received sample and the drastically limited ductility of the 4 passes ECAP sample at 250 °C (see Figure 73).

YANAGIMOTO et al. (2011) described that there are two different models of dimples for ductile fracture, these are: larger dimples formed by the decohesive mechanism in the inclusion-matrix interphase, and smaller dimples caused by the dislocation interaction mechanism (DESPRÉS, 2020). After ECAP passes, the micro-dimples are finer and more diversified, there are more small dimples in the fracture surface of ECAP-ed samples than in the as-received condition. Even with limited displacement movement due to microstructural refinement, the twinning mechanism appeared to be promoting some tenacity, as observed in Figure 73.

It may be suggested that mechanical twinning is a consequence of tensile test at room temperature. Although both samples deformed by ECAP have similar features, the sample after one pass at 350 °C shows higher ductility than the sample pressed at 250 °C, which is in

line with the tensile test results. In the samples deformed by ECAP at 250 °C, the size of its cavities is smaller and the zones of cleavage and subcell structures are larger. After 4 ECAP passes the UTS was of 1.9 GPa.

Figure 73 — Fracture surfaces of the fractured tensile test specimens (a) as-received, (b) one pass, (c) two passes, (d) four passes at 350 °C and (e) one pass, (f) two passes, (g) four passes at 250 °C.

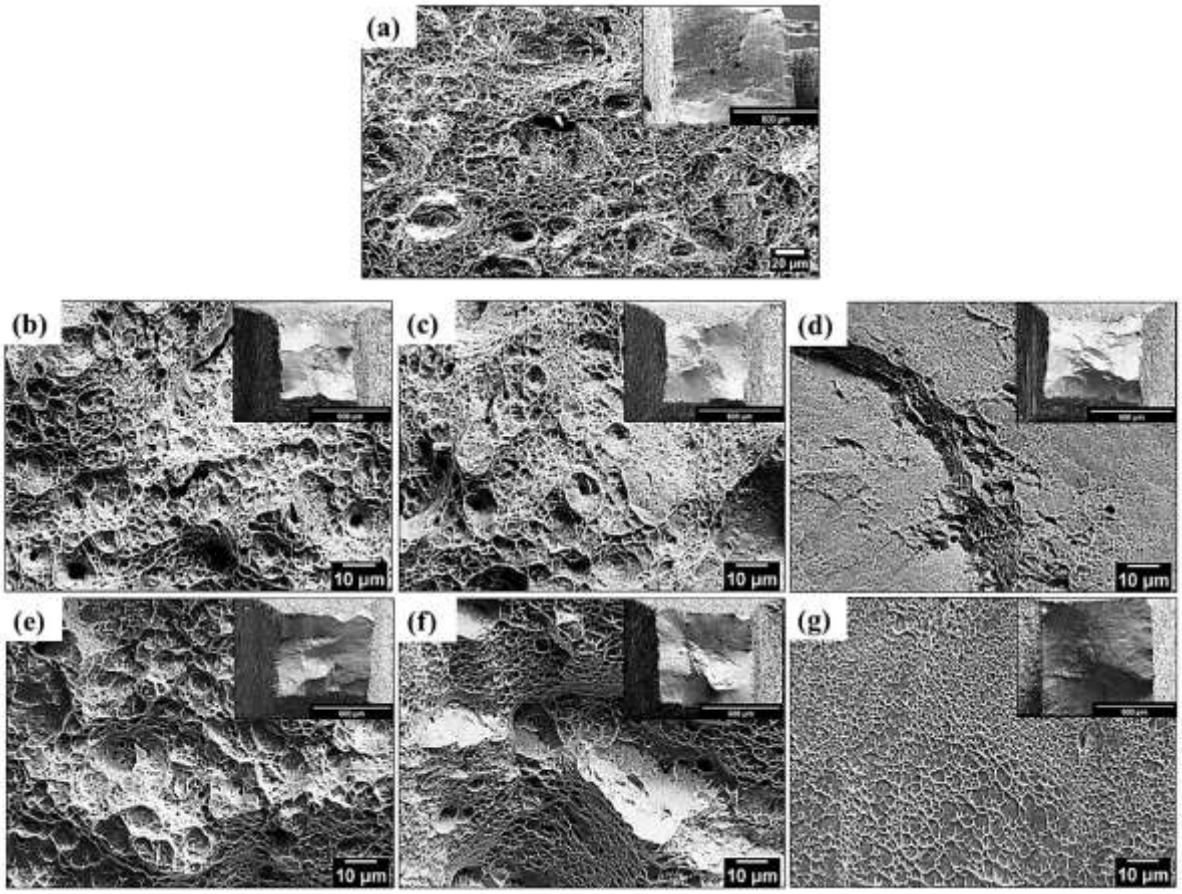

Source: Elaborated by the author.

7 RESULTS: HOT TORSION PROCESS

MICROSTRUCTURE, PROPERTIES AND CRYSTALLOGRAPHIC ORIENTATION OF NOVEL AUSTENITIC FE-26MN-0.4C STEEL UNDER HOT TORSION PROCESS

7.1 Review

The literature has reported on the hot deformation processes applied to some TWIP steels (ABRAMOVA, 2021) (LEE, 2018). Those investigations have demonstrated the effectiveness of high-temperature methodology in improving the YS, ductility and plasticity values. Among these, it is worth highlighting the dynamic softening phenomena in terms of dynamic recrystallization (DRX). This is one of the most important phenomena that can be considered to improve the mechanical properties of steel. These properties can be obtained by controlling the load over the material during strain aiming to refine the grains and acquire better stability (DONG, 2018) (ANDERSON, 2019). Therefore, the understanding of microstructural evolution and dynamic recrystallization is fundamental to control the thermomechanical variables for the improvement of hot-processed steels.

Ultra-fine grain TWIP steel (UFG TWIP) also shows discontinuous stress-strain flow curves rather than continuous ones. This typically happens in FCC metals and alloys, and this discontinuous behavior also occurs in other UFG materials despite the crystalline structure and their chemical composition. However, research about the mechanisms regarding discontinuous flow followed by yield drop in UFG alloys, mainly for interstitial free metals and alloys, are under investigation (HUNG, 2021). For instance, Bai et al. (2021) proposed that discontinuous yielding in UFG Fe-31Mn-3Al-3Si TWIP steel is a consequence of the lack of displacements inside the recrystallized ultrafine grain, which may be compatible with strain-induced twinning. In contrast to the improvement in yield strength, it is known that a finer grain size makes cross deformations in FCC materials less frequent.

In this work, for the first time this specific experimental austenitic TWIP steel with a high content of manganese and chromium was deformed under hot torsion experiments at different amount of strain. The present investigation's importance and novelty are the results that will help in the decision-making of the parameters to improve the microstructure and achieve a high YS. Due to strain mechanisms, subsequent tensile tests were employed to quantify the mechanical properties, and these were complemented by detailed microstructure

characterization techniques (XRD, EBSD, KAM). It was observed that while dislocations contribute to maximize the yield stress of the investigated steel, the TWIP effect was the most important mechanism at larger strains. So, the main point is that mechanical twins help to maintain the large plasticity of TWIP steels and the detailed scientific investigations are described below. All this chapter was published on May/26/2023 with DOI: https://doi.org/10.1016/j.msea.2023.145206.

7.2 Methodology

Torsion specimens with a length of 12 mm and a diameter of 8.0 mm were machined, see Figure 74. Mechanical tests were performed on a computerized hot torsion machine. The specimens were heated in an infrared radiation furnace coupled to the machine. A proposed experimental austenitic steel with high Mn content was investigated in the present study. Its chemical composition is shown in Table 1. The calculated SFE value was approximately 21 mJ/m^2 at room temperature and 162 mJ/m^2 at 900 °C (ALLAIN, 2004) (ALLAIN, 2004).

Two deformation routes were used. Route A triplicates of the specimen were tested with strain application up to 2.5. Route B triplicates of the specimen were tested with strain application up to 3.0. The tests were carried out at 900 °C with a strain rate of 0.05 s^{-1}. Strain of 0.6, 0.75, 2.2 and 2.6 were considered from calculated regions inside (radius from center to the surface) of the strained specimens. The axes of the cylindrical samples were parallel to those of the rolling direction of the plates. Only isothermal conditions were employed. Specimens were heated to 900 °C at a rate of 30 °C/s and held for 10 minutes. After the strains, the specimens were rapidly cooled to room temperature. The thermomechanical scheme used is shown in Figure 74 and Figure 75.

Figure 74 — Torsion testing schedule for the thermomechanical simulations of the TWIP steel. The deformations were applied at 900°C. The specimen configuration used for the hot torsion simulation and parameters information is also shown.

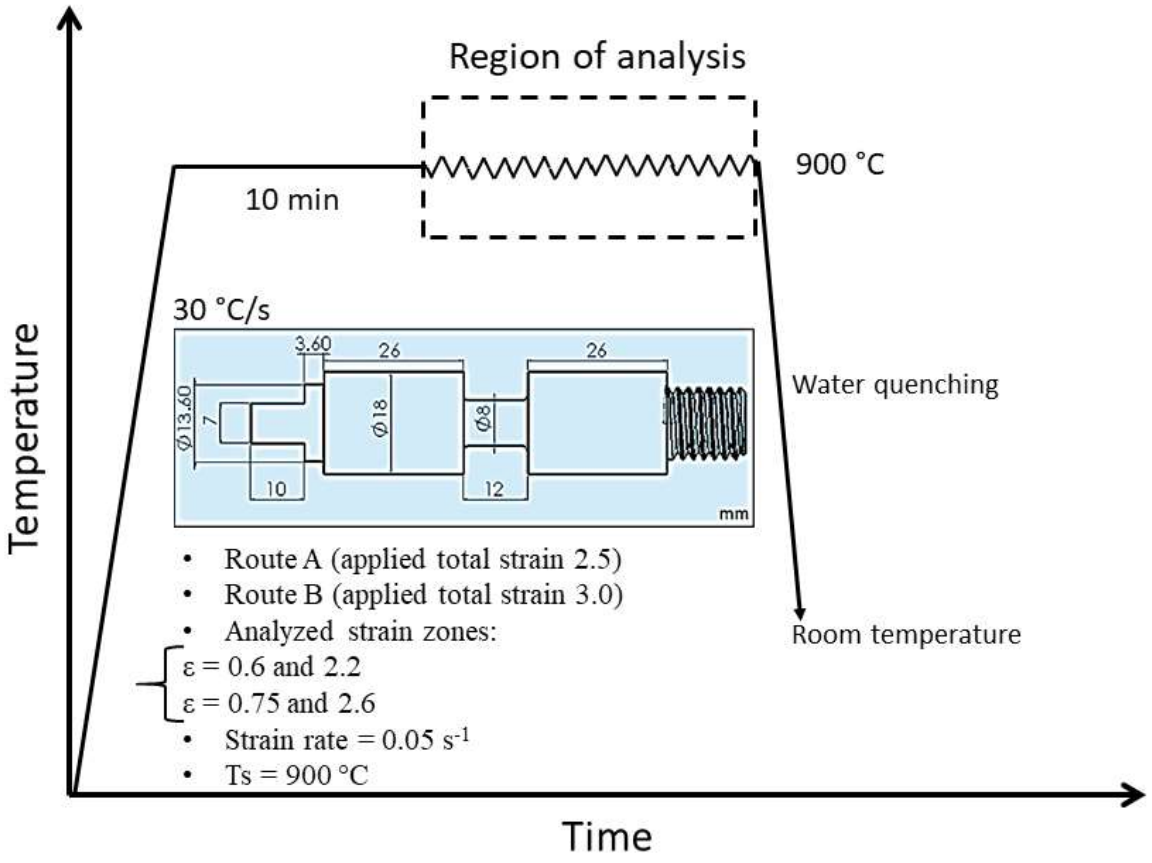

Source: Elaborated by the author.

The torsion specimens were sectioned longitudinally in order to provide cross sections for microstructure analysis, as displayed in Figure 75. Shear direction (SD, parallel to 'x'), normal direction (ND, parallel to 'y') and transverse direction (TD, parallel to 'z'), respectively, were cut from the deformed specimen. Cross-section supplies the microstructures related to the increasing deformations since there is no deformation in the center of the specimens and presents its maximum value at the surface. The microstructure of the deformed specimens was examined in tangential sections from the surface of the specimen to near the center. It is known that the strain varies from zero at the centers to a maximum at the surface in torsion experiments. Further information regarding this method is given in the results section.

Figure 75 — (a) Specimen extraction zone for further tensile tests, (b) longitudinal cross-sections schematic diagram of torsion sample, and (c) sample analysis zones.

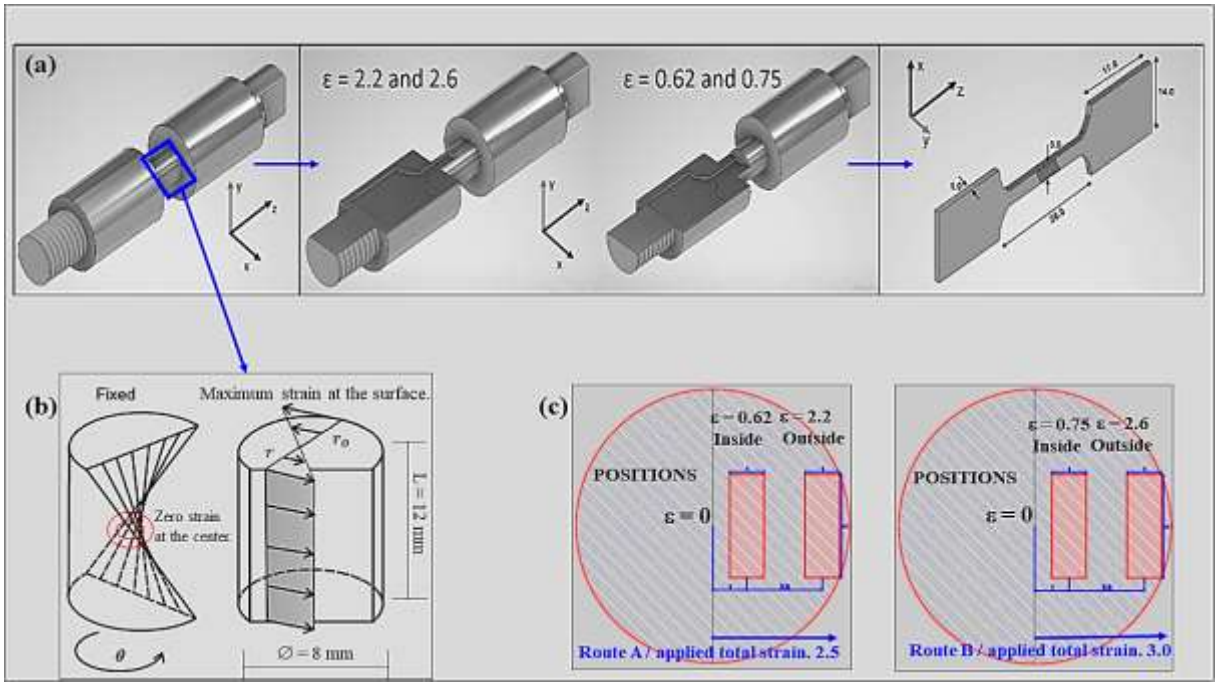

Source: Elaborated by the author.

Sample preparation was similar to that used in previous proesses. Electron backscatter diffraction (EBSD) analysis were carried out in one SEM FEI Quanta FEG 450, operated at 20 kV, using a working distance of 13 mm and with a tilted angle of 70°. Different scan step sizes were used: 0.3 μm for the as received condition, 0.2/0.08 μm for the samples with strain of 2.6 and 0.2 μm for the samples with 2.2 of strain. The indexing rate was above 90% for all samples. Uniaxial tensile tests were performed at room temperature. The specimens were machined along the torsion direction (see Figure 75). These experiments were performed using a universal testing machine (MTS 370) at a speed of 2 x 10^{-2} s^{-1}. ASTM E8 standard recommendation for reduced size specimens was followed. High resolution fracture graphs were obtained for discussion under a scanning electron microscope (FEI Quanta FEG 450) operated at 20 kV.

7.3 Results and discussion

7.3.1 Microscopy analysis

Images were taken for the initial condition, i.e., as received and after the application of hot torsion simulations. Microstructure with mostly equiaxed austenitic grains containing thermal twins from the hot rolling process and few mechanical twins are depicted in Figure 76(a, b). This observation agrees with other researchers who have found similar trends (BAI, 2021) (ARANAS, 2015) . Figure 76 also shows the microstructure after application of strains under torsional deformation as identified in the image. Twins (yellow lines) and shear bands (circle and green lines) were observed. One can observe plastically deformed grains along the shear directions (see Figure 76c, d, e, and f).

The high manganese content caused the increase and stabilization of the austenitic field. The appearance of twins is associated with the low stacking fault energy (SFE) of the present material. Despite the high temperature of deformation, there was clearly a grain refinement, as exemplified in Figure 76g, 76i. A complex continuous shear microstructure in the planes after sample rotation between each different strain was formed. Pure shear strain lines can be seen in Figure 76k. The austenitic grains showed a heterogeneous morphological structure due to the formation of different crystalline defects resulting from the shear process of the structure. Figure 76g, 76h, 76i, and 76j, suggest the presence of ultrafine grains coupled in a tangled structure of dislocation as reported in the literature (LEI, 2017) (HAASE, 2016) (TIMOKHINA, 2014) (ARANAS, 2015) (TAEKYUNG, 2012).

Figure 76 — FEG-SEM secondary electron micrographs of samples before and after deformation using torsion. (a, b) as-received, (c, d) after deformed to a strain of ε= 0.62 (route A – inside), (e, f) after deformed to a strain of ε= 2.2 (route A – outside), (g, h) after deformed to a strain of ε= 0.75 (route B – inside), (i, j) after deformed to a strain of ε= 2.6 (route B – outside), (k) shear lines and (l) optical micrography of a torsion sample deformed to a strain of ε= 2.6 at the outer radius at 900 °C at a rate 0.05 s^{-1}. (Twins are depicted with yellow and shear bands at green)

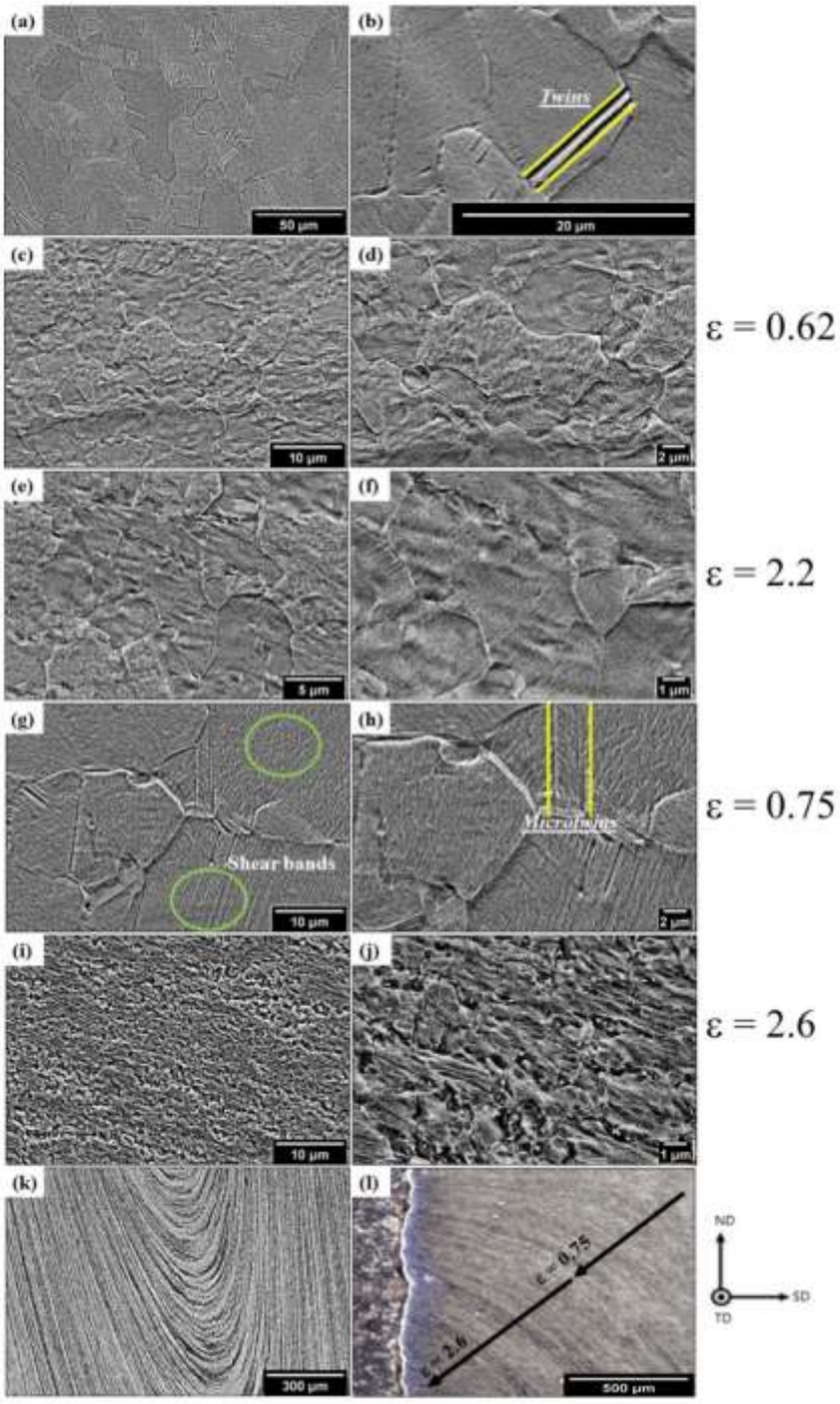

Source: Elaborated by the author.

7.3.2 XRD investigation

XRD of all investigated samples are shown in Figure 77. XRD patterns after the hot torsion process confirmed the absence of any other phases like α' and/or ε martensite. It can be suggested that these effects are correlated with the increase of the dislocation density, and additionally the lattice distortion induced by plastic strain due to pure shear applied over the metal (VAN, 1996) (YE, 2021).

Figure 77 — XRD patterns for samples. Shifts of the diffraction peaks and broadening are observed.

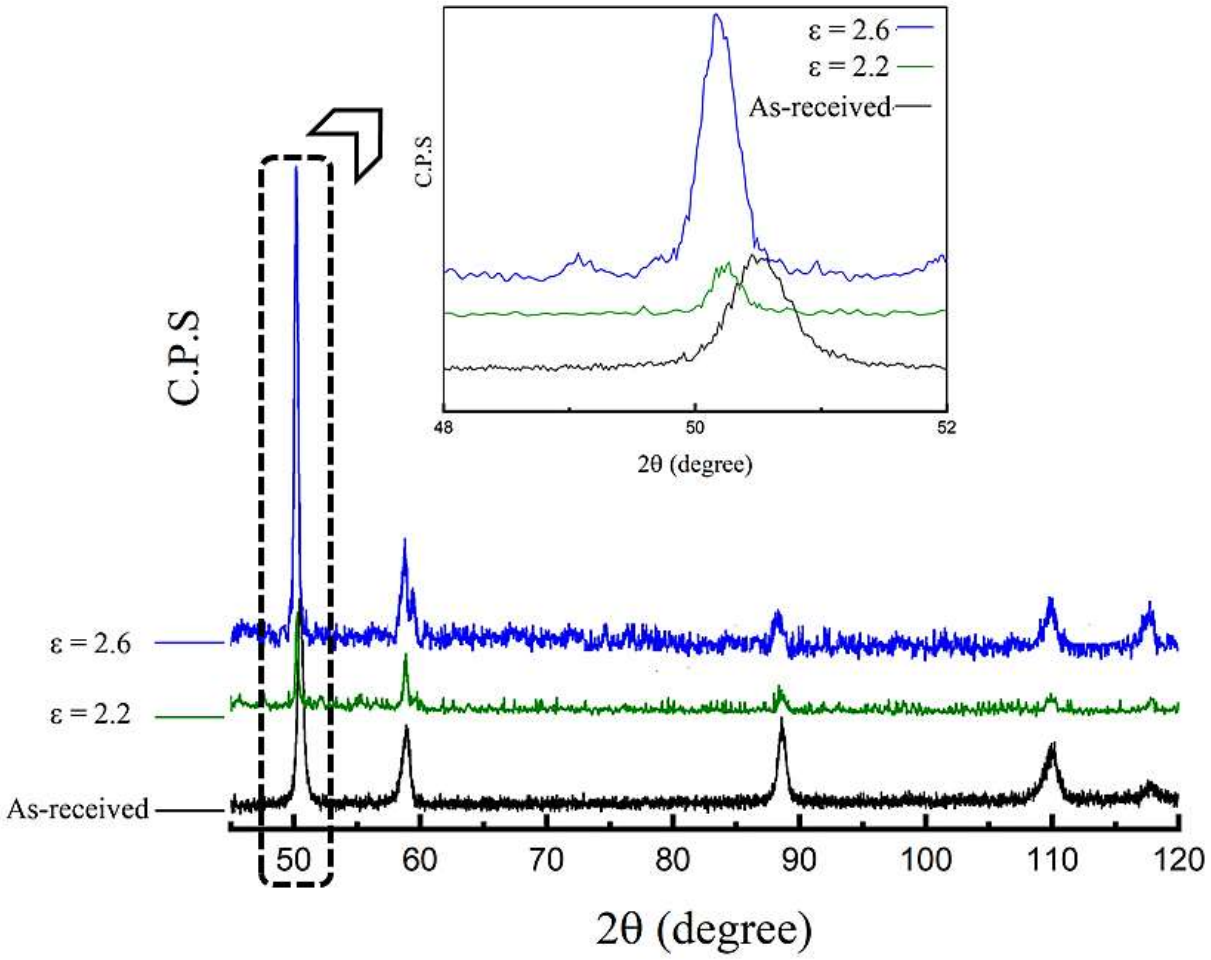

Source: Elaborated by the author.

The dislocation densities of the investigated samples were calculated by using the method proposed by (UNGAR, 1996) and modified Williamson-Hall methodology. The values

were determined to be 2.23 × 10^{13} m^{-2} for the as received sample, 1.8 × 10^{14} m^{-2} and 3.2 × 10^{14} m^{-2} after ε = 2.2 of strain, near to the center and at the surface, respectively, and 2.9×10^{14} m^{-2} and 3.5 × 10^{14} m^{-2} after ε = 2.6 of strain, near to the center and at the surface of the specimen, respectively. The evolution of the dislocation density for all samples is illustrated in Figure 78. Notably, the high dislocation density due to the torsion process caused a localized lattice distortion that changed the peak shape of the diffracted peak patterns.

Figure 78 — Dislocation density evolution for all samples.

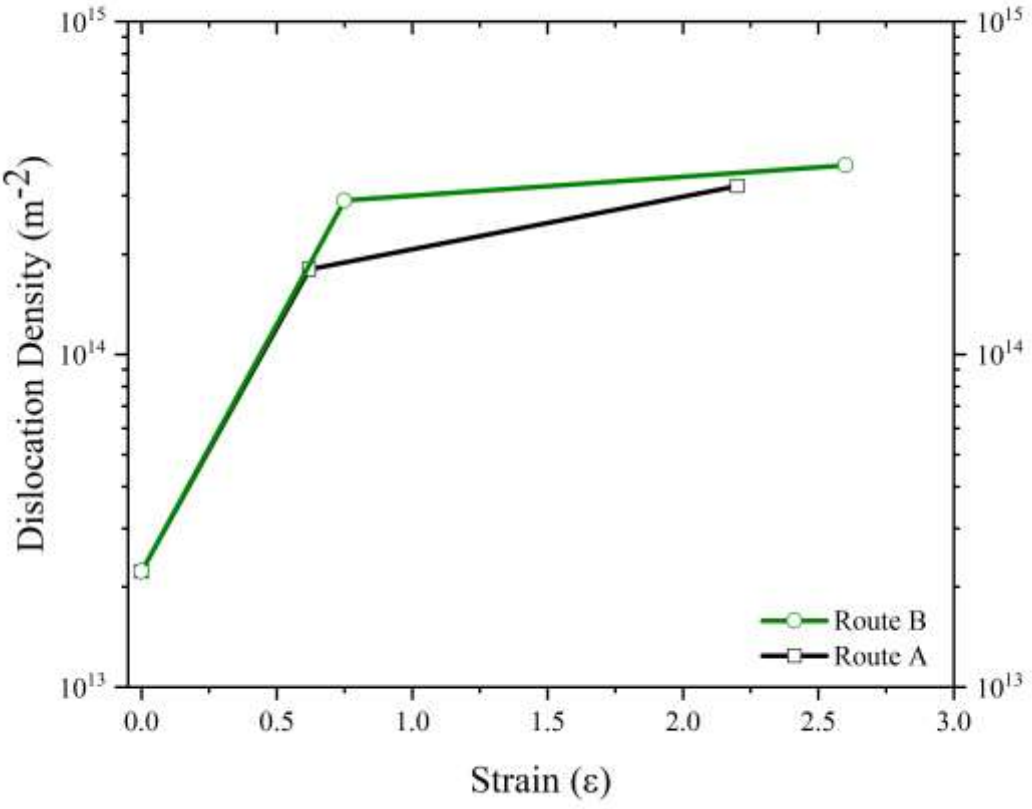

Source: Elaborated by the author.

7.3.3 Electron backscatter diffraction (EBSD) and Orientation distribution function (ODF) analysis

To analyze the texture and misorientation of the investigated steel, orientation image maps (OIMs), ODFs and grain contour maps of the samples were obtained by the EBSD technique. The results are represented in Figures 79 and 80, for the as received and strained samples, respectively. The images revealed that, with increasing amount of deformation, a

gradual misorientation gradient develops in the microstructure. In the as received, the material presented a homogeneous microstructure formed by equiaxed grains with an average grain size of 7 μm ± 1 μm (twins not considered). Figure 79a suggests that few subgrains (illustrated in red) and several annealing twins (CSL-Σ3 mostly) are present in the as-received sample. The as-received sample showed (001)[100] and (001)[120] as preferred crystallographic orientations, see Figure 79b, 79d and 79e. Previous research (ZINOVIEVA, 2020) has suggested that the appearance of the (001)[100] component may result from the fine columnar grains developed during solidification in the direction of maximum heat conduction accompanied by dynamic recrystallization. Other research (ZHANG, 2016) suggested that the {001}<120> components originate during recrystallization of {001} columnar grains which may lead to low yield strength. Figure 79c shows a predominance of high angle boundaries. ODFs plotted for the as-received sample were performed using orthorhombic symmetry, see Figure 79d and 79e. Similar ODFs were reported for a similar TWIP steel (ALLAIN, 2004).

Figure 79 — EBSD grain map, grain boundary of the as-received sample, (a) CSL mapping, (b) and (c) IPF mapping (grains boundary map: blue line ─ high-angle grain boundary, red line ─ low angle grain boundary), and corresponding ODFs at constant (d) φ_2=0° and (e) φ2=45° sections.

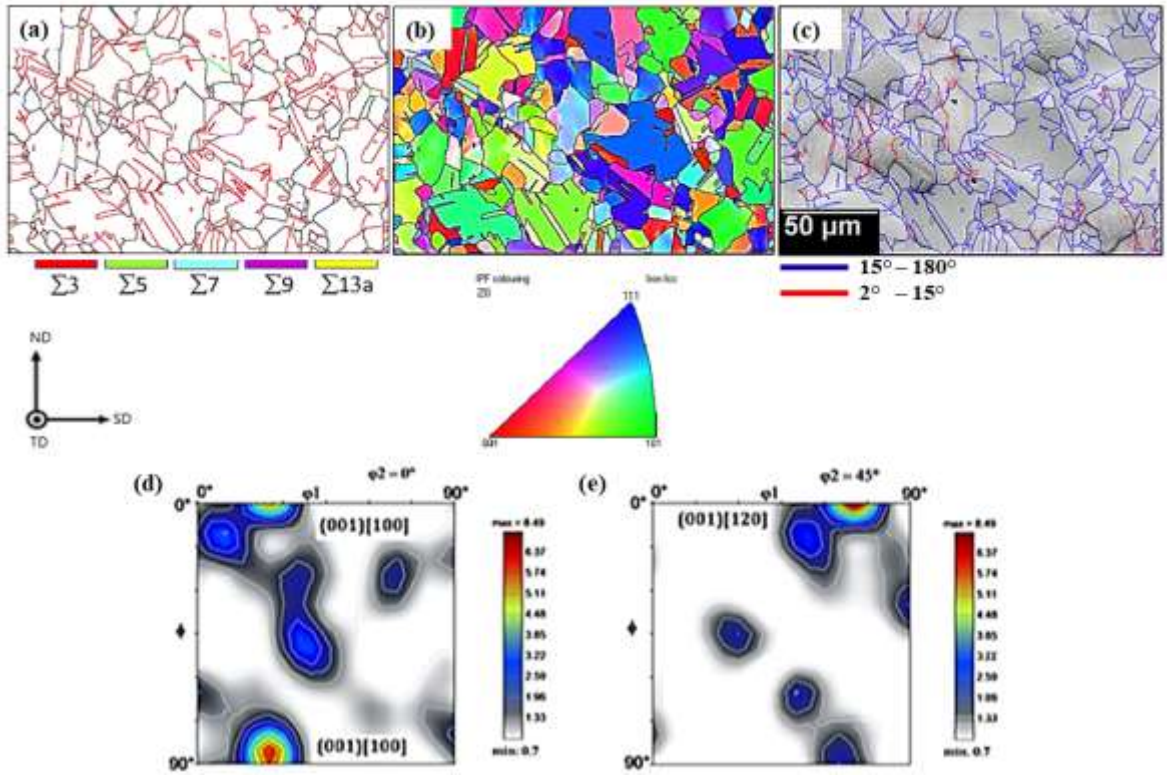

Source: Elaborated by the author.

The characteristics of the microstructure after the hot torsion process can be observed in Figure 80. The grains appear elongated according to the shear direction and in some regions ultra-fine grains (UFG) are perceived. After the first deformation, in addition to the elongated grains, see Figure 80a-h, a large amount of low angle grain boundaries was generated and, simultaneously, in other regions, annealing twins are observed (Figure 80e). The innermost region (inside), close to the center (radius, r_0), showed a mixed microstructure between new subgrains between larger grains, see Figure 80a-d. Comparing with the outermost zone (outside), at the surface of the sample (radius, r=4 mm), a slightly more intense refinement can be observed (see Figure 80e, 80h). A small difference was also noticed in the recrystallized fraction map, which suggests a greater effect of temperature in the outer zone of the specimens. The average grain size after route A of deformation was determined as ≅ 2.5 μm. When the total deformation was increased to route B, the grain size reduced drastically to ≅ 0.8 μm, see Figure 80i-p. The presence of ultrafine grains (UFG) can be observed. The presence of large and elongated grains disappears into a refined microstructure as the strain is increased. Figure 80 summarizes the observations on the microstructure of TWIP-FeMnCCr steel subjected to simple shear shear by torsion.

Figure 80 — EBSD grain map, CSL grain boundary map, Recrystallized fraction map, IPF, and grain mapping of the samples: strain of ε=2.5 (route A) (a - h), strain of ε=3.0 (route B) (l - p) ((grains boundary map: blue line ─ high-angle grain boundary, red line ─ low angle grain boundary).

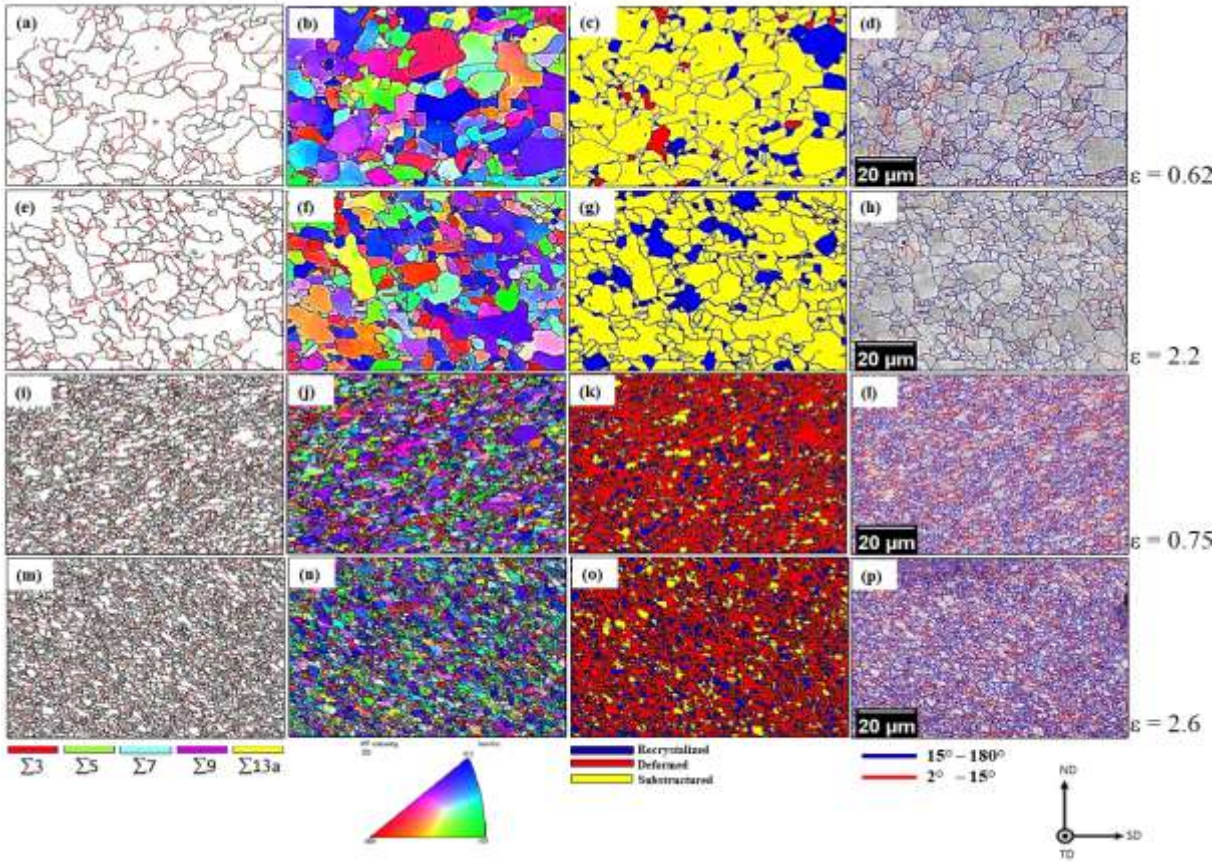

Source: Elaborated by the author.

The evolution profile of the average grain size after the hot torsion process is depicted in Figure 81. According to the literature (HAMADA, 2007), steels deformed by means of low strain rate, pass through softening due to dynamic recrystallization (DRX), although it is stated that Mn delays the onset of DRX which suggests that the presence of Mn in metallic alloys also retards grain boundary migration.

Figure 81 — Evolution of the average grain size for different degrees of deformation.

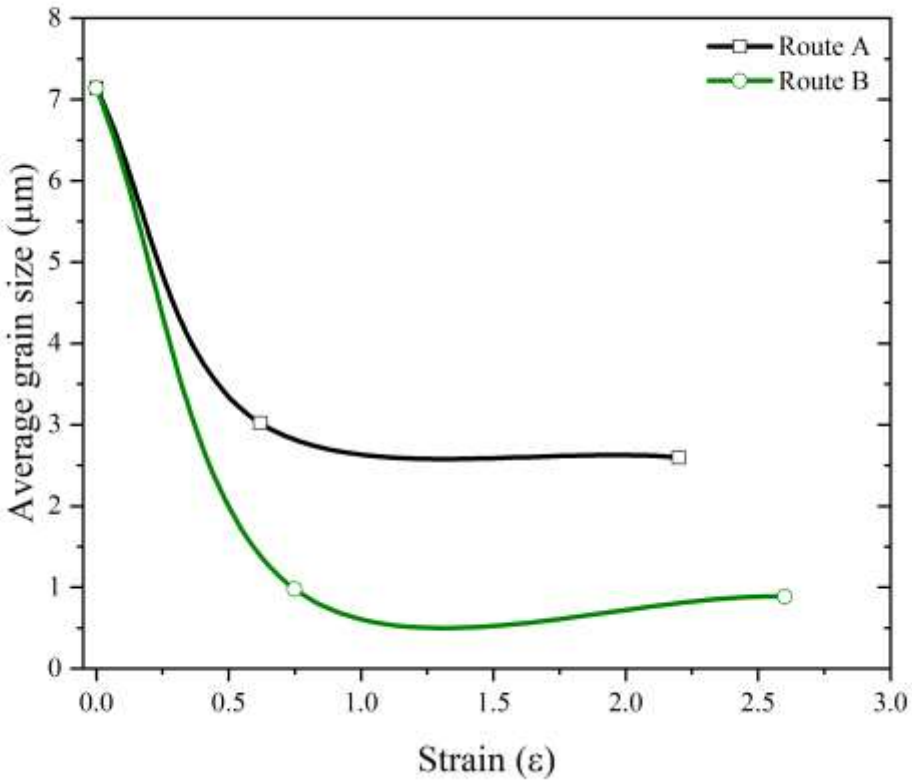

Source: Elaborated by the author.

Hung et. al. (2021) executed a detailed study of a high-Mn austenitic steel with ultrafine grains (UFG), approximately 1 μm and smaller, subjected to various strain levels. In their research, the reported deformation twinning behavior was divided into three categories based on grain size. The dominant plastic deformation mechanism of UFG TWIP steel is: (a) by slipping in grains greater than 1 μm, (b) by a mixture of slip and strain induced twinning into grains of about 1 μm and (c) by twinning in grains smaller than 1 μm. It seems that the sources of dislocation have shifted from the interior of the grain to the grain boundaries when the grain size approaches 1 μm. This caused the appearance of partial dislocations, i.e. change of deformation mode from sliding in the grain to stacking faults and deformation twin nucleation. The results shown in Figure 82 suggested a small increase of 0.4 in the strain (2.2 to 2.6 strain) was much more effective in refining the microstructure of the present TWIP-FeMnCCr steel.

The misorientation of the grain boundaries (see Figure 82), gives the fraction of low

angle boundaries (LAGBs, 2° < Θ < 5°), high angle boundaries (HAGBs, 15 ° < Θ) and Coincidence Site Lattice (CSL) limits. New grains originate mainly within shear bands, twins, and at grain boundaries because of dislocation slip. The accumulation of dislocations forms subgrains and gradually leads to the refinement of the microstructure (DESPRÉS, 2020). The as-received sample was found to have the lowest fraction of low angle deviations due to recovery during hot rolling (manufacturing process). The starting material contains approximately 30% of the total CSL. After the torsion process, many fine grains generated in the first pass can be observed, see Figure 81.

Figure 82 — Misorientation grade of the grain boundaries of all samples.

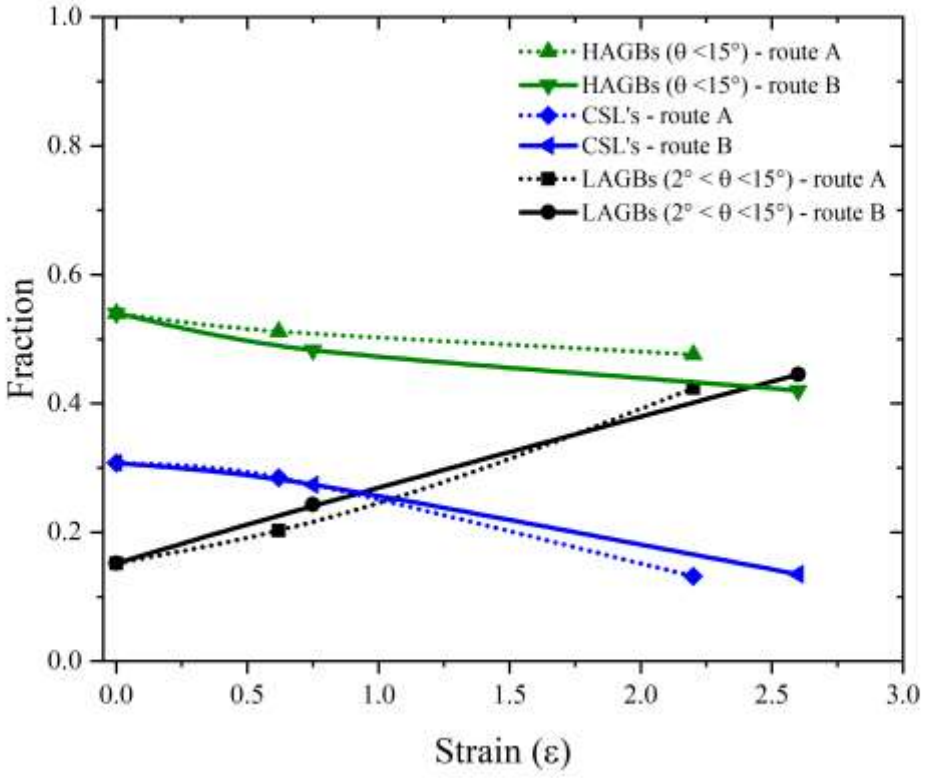

Source: Elaborated by the author.

The increase of the strain over the material promotes a decrease in the fraction of HAGBs, as well as the misorientation fractions with CSLs of twins. The results also showed a continuous increase in the LAGBs fractions with a consequent decrease in the high misorientation fractions. Decreasing grain size normally suppresses twinning (ALLAIN, 2004). The large reduction in grain size after high strain (ε = 3.0) should prevent twinning

(TIMOKHINA, 2014), see Figure 81. It is commonly observed in austenitic steels the development of low energy CSL boundaries (BELADI, 2013) (HIGUERA-COBOS, 2013) (HIGUERA-COBOS, 2014). As proposed by (YE, 2021), the planar slip dislocations contain many Shockley partial dislocations that produce deformation twins massively acquiring the planar slip dislocations. In Figure 82, it can be seen that the fraction of the CSL limits decreases with the progressive amount of strain.

The results presented until here agree with research performed by (HAMADA, 2007). They reported an average grain size during partial dynamic recrystallization of ≅ 4 μm after rolling process test at 900 °C at strain rate of 0.005 s^{-1} in a TWIP steel with high Mn content with addiction of Aluminum, similar the one studied in the present article. It was also reported by the authors that the relative high content of Mn significantly retards the rate of SRX- static recrystallization kinetics. Somani et al. (2012) investigated the SRX of many C-Mn and microalloyed steels and found that the Mn has a great influence on this softening mechanism. Cho and co-workers (CHO, (2002) also observed that the addition of Mn considerably slows the recrystallization kinetics.

Beyerlein and Toth (2009) defined the ideal orientations of pure shear strain. In this work, the texture of the current TWIP-FeMnCCr steel was analyzed in triclinic symmetry (0° - 360°). The texture of the investigated material deformed by torsion and the ideal position of the texture components for FCC materials deformed by simple shear are shown in Figure 83, Figure 84 and defined in Table 11. It can be suggested that monoclinic symmetry is present in some cases as the components are symmetrical every 180°. Monoclinic symmetry was also observed in research elsewhere (SUWAS, 2006) (HIGUERA-COBOS, 2014).

As listed in Table 11, all pure shear texture components were immediately formed at (0-360°, 45°, 0°). Small variations in Euler space from ideal orientations are common and are related to different material processing factors (HAASE, 2016) (BEYERLEIN, 2009) (SUWAS, 2006). Strengthening of the fiber-B orientations with increasing stress in low-SFE metals has been observed. The evolution of the fiber-B is related to the increase of the B component mainly due to the replacement of the C component orientations by the B orientations ({112}\<110>) (HIGUERA-COBOS, 2014).

Table 11 — Definition of the ideal texture components for simple shear strain.

Crystal Structure	Texture components	{hkl}<uvw>	φ1(°)	Φ(°)	φ2 (°)
FCC	A_1*	$(111)[\bar{1}\bar{1}2]$	35.26/215.26	45	0
			305.26/125.26	90	45
	A_2*	$(111)[11\bar{2}]$	324.74/144.74	45	0
			54.74/234.74	90	45
	A	$(1\bar{1}1)[110]$	0	36.26	45
	$\bar{A}$	$(\bar{1}1\bar{1})[\bar{1}\bar{1}0]$	180	35.26	45
	B	$(1\bar{1}2)[110]$	0/120/240	54.74	45
	$\bar{B}$	$(\bar{1}1\bar{2})[\bar{1}\bar{1}0]$	60/180/240	54.74	45
	C	{001}<110>	90/270	45	0
			0/180	90	45
	{111}-/A-fiber	{111}<uvw>			
	<111>-/B-fiber	{hkl}<110>			

Source: BEYERLEIN, (2009).

Figure 83 — (a) Ideal components in triclinic symmetry of FCC materials deformed by simple shear and texture components of the investigated TWIP steel for ϕ_2=0° and ϕ_2=45°, (b) deformed at 0.6 strain (inside zone of the sample – route A), c) deformed at 0.75 strain (inside zone of the sample – route B).

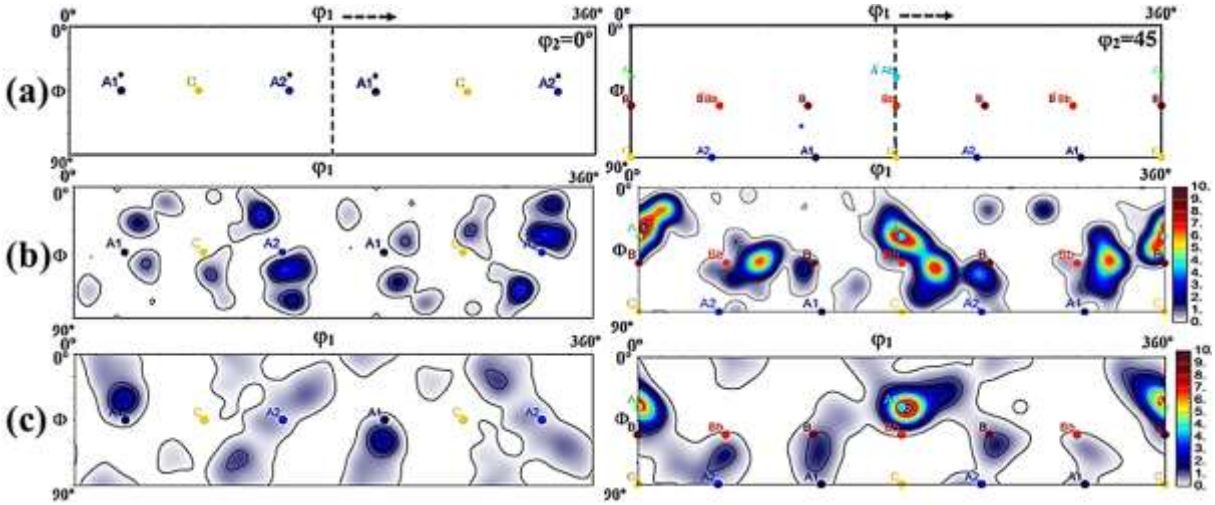

Source: Elaborated by the author.

Figure 84 — (a) Ideal components in triclinic symmetry of FCC materials deformed by simple shear and texture components of the investigated TWIP steel for ϕ2=0° and ϕ2=45°, (b) deformed at 2.2 strain (outside the zone of the sample – route A), c) deformed at 2.6 strain (outside the zone of the sample – route B).

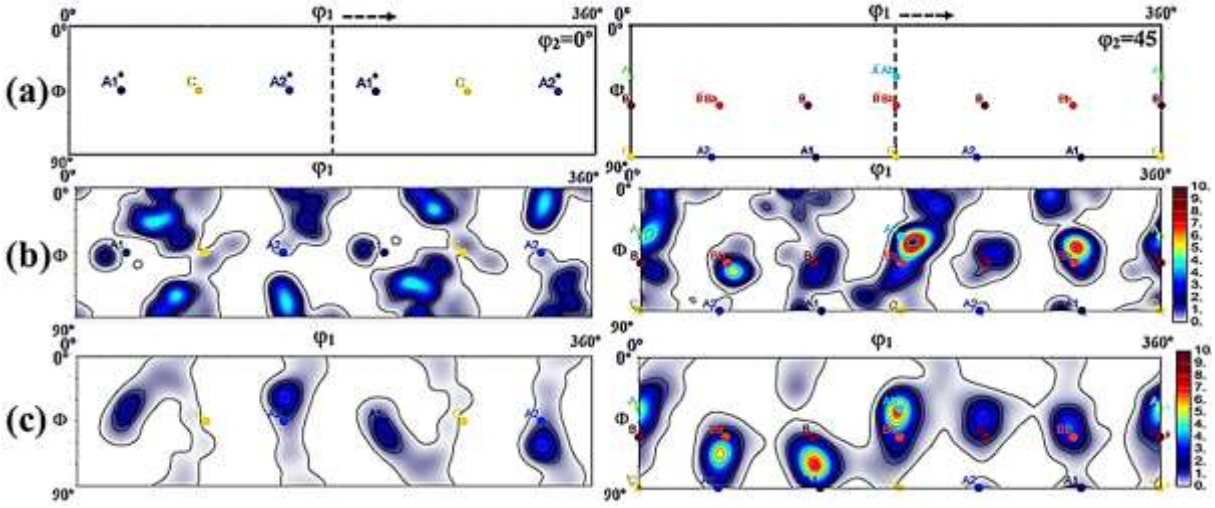

Source: Elaborated by the author.

Some researchers have suggested changes in the texture component from C over A_1* to B as the SFE decreases (SKROTZKI, 2003) (BEYERLEIN, 2007). Other authors (SAEED-AKBARI, 2012) (SUWAS, 2003) (SANDIP, 2011), have suggested that the effect of SFE on texture evolution during pure shear deformation is similar to that of texture development during cold rolling. They suggested the following conditions: S => A_1*, Cu => C, Brass => B/$\overline{B}$. In the cold rolling texture, the texture components {112}<111> Cu and {123}<634> S decrease with decreasing SFE, while the texture component {110}<112> Brass increases. The texture component C is expected to decrease, while the texture components $(1\bar{1}1)[110]$, $(\bar{1}1\bar{1})[\bar{1}\bar{1}0]$, $(1\bar{1}2)[110]$, $(\bar{1}1\bar{2})[\bar{1}\bar{1}0]$ strengthen as the SFE decreases. The texture component C was weakened after deformation, see Figures 83, 84 and 85. A decrease in A_2* and A_1* components has been reported in other materials with low SFE (HAASE, 2016) (LEI, 2017). These trends partially coincide with the evolution in the texture of the current investigated material, as there was a decrease in the C component in the present TWIP-FeMnCCr steel.

The texture after the hot torsion deformation presented some modifications between the two analyzed regions in the samples. Internal and external zone, with lower and higher applied strains respectively. Texture results suggest a decrease in A_1*, A_2* and C texture components and an increase in A/$\overline{A}$, B/$\overline{B}$ components. Texture in the outer zone became more

pronounced as indicated by an increased texture index and a decreased volume fraction of randomly oriented grains. The evolution of these volume fractions is shown in Figure 85. The texture evolution agrees with the ones proposed by (SUWAS, 2006), and with by (LEI, 2017) since C, A_2* and A_1* are reduced and A/$\overline{A}$, B/$\overline{B}$ increased after the deformation process.

Figure 85 — Evolution of the volume fractions of the main texture components during torsion process.

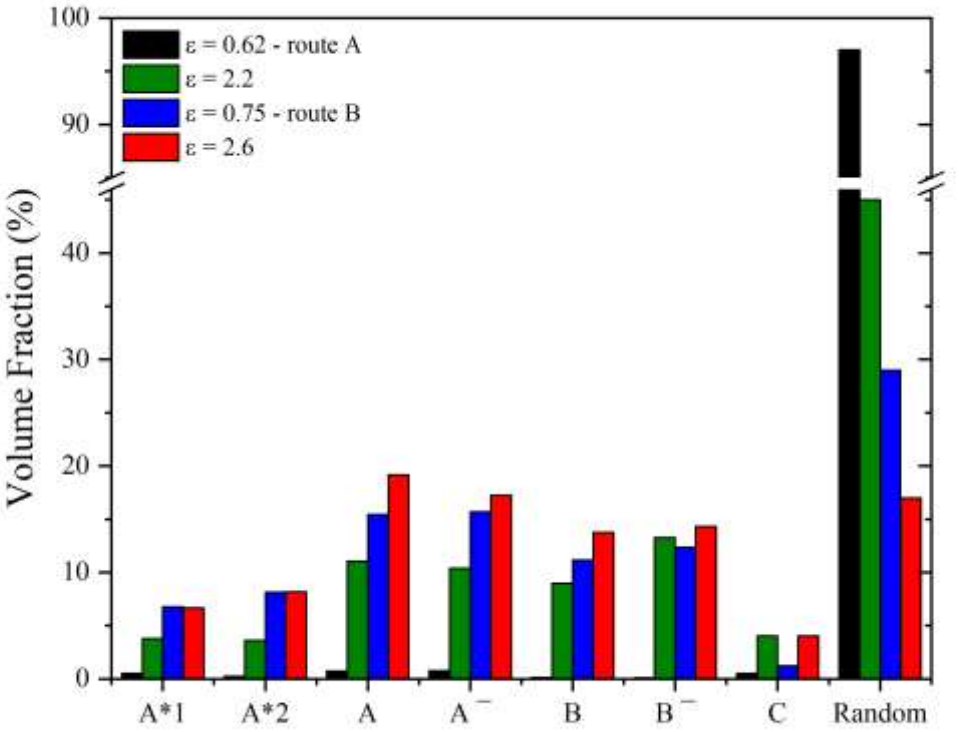

Source: Elaborated by the author.

Regarding the anisotropy of the samples with greater deformation after the torsion process, a preference for the <110>∥X fiber is observed. This favors the presence of deformation components such as $(1\,\bar{1}\,1)[110]$, $(\bar{1}\,1\,\bar{1})[\bar{1}\bar{1}\,0]$, $(1\,\bar{1}\,2)[110]$, $(\bar{1}\,1\,\bar{2})[\bar{1}\bar{1}\,0]$, characteristics of a material subjected to pure shear (LEI, 2017), see Figure 86. However, the marked influence of the <110> ∥ Z and <111> ∥Y fibers is also observed. The material showed a preference for the β fiber or the <110> fiber. Fibers <111> and <100> indicate the presence of recrystallization components such as cube, goss, brass, copper, brass, rotated cube and twinned. However, the presence of the strong <111>∥Y fiber can also be linked to the presence

of special grain boundaries of the Σ3 type (60°<111>). In conclusion, it can be suggested that TWIP-FeMnCCr steel deforms following the direction of the highest atomic density which for FCC materials is the <110> direction and (111) plane or β-fiber. With increasing strain, many subgrains are generated that block the movement of dislocations (HIGUERA-COBOS, 2014) (HOSNI, 2010).

Figure 86 — Fiber texture after torsion simulation for samples with maximum strains of ε=2.5 (route A) and ε=3.0(route B) (outside zone).

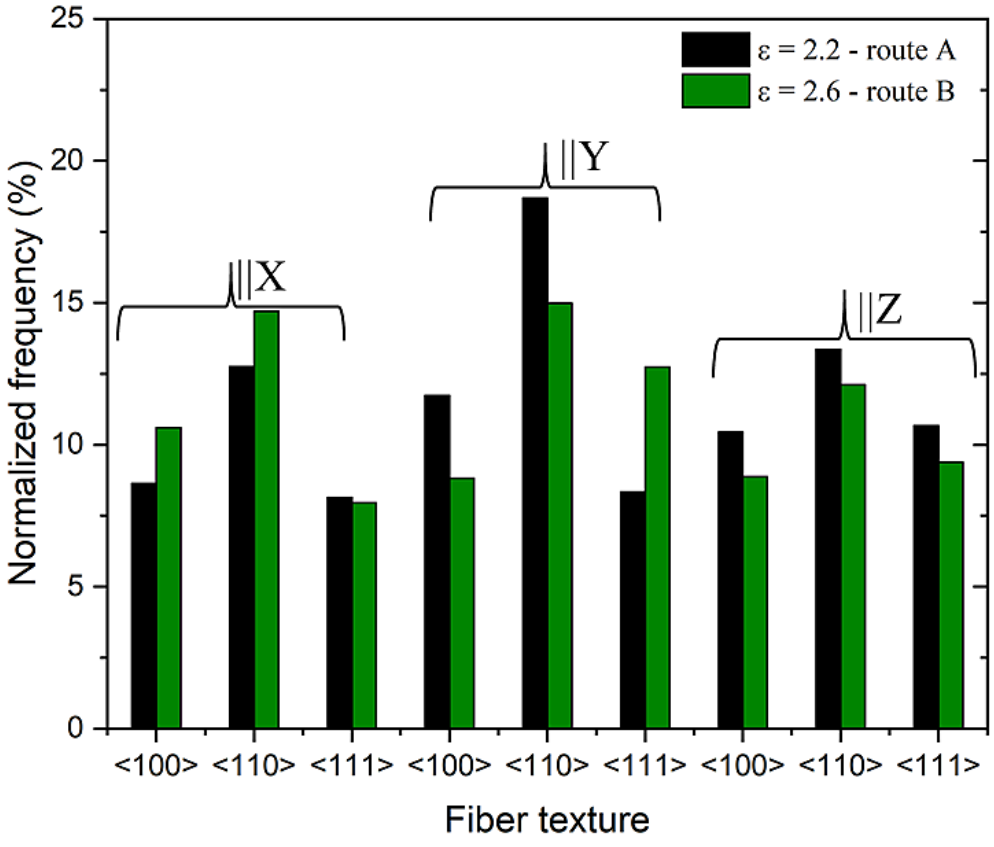

Source: Elaborated by the author.

The local change in orientation between 3 neighboring pixels was used to show the stress distribution along the grains. The largest amount of low KAM values (KAM < 1°) was found in the as-received sample (Figure 87(a). After the torsion process, a significant fraction of deformed grains with medium KAM (1° < KAM < 3°) (see Figure 87(b, c)) and high KAM (> 3°) values were evidenced. Average KAM values can be observed in the samples which passed through lower deformation. In this case, it is worth mentioning that the temperature and low strain rate (0.05 s^{-1}) were not efficient to refine the microstructure of the TWIP-FeMnCCr

steel. High KAM values (see Figure 87(d,e)) may be associated with high local lattice distortion and dislocation density which led to an increase in internal energy (VICENTIS, 2017).

Figure 87 — EBSD KAM maps: (a) as received, (b) after deformation of ε=0.62 (route A - inside zone), (c) after deformation of ε=2.2 (route A - outside zone), (d) after deformation of ε=0.75 (route B - inside zone), and (e) after deformation of ε=2.6 (route B - outside zone), (f) Variation of kernel average misorientation distribution of the samples.

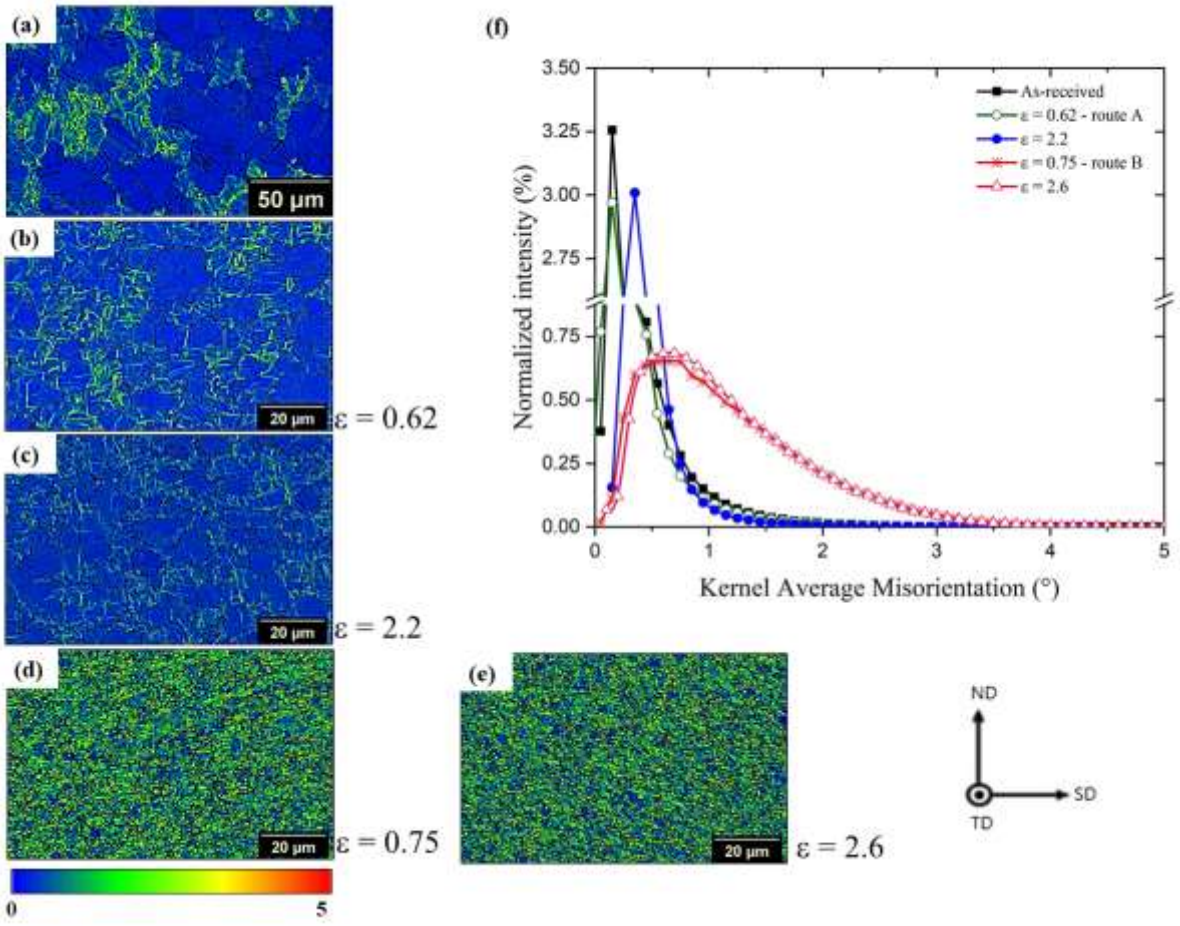

Source: Elaborated by the author.

Crystallographic defects such as dislocations, twins, shear bands and grain boundaries generated during the deformation process can be absorbed and joined together to develop dislocation cells and low angle boundaries. The ultrafine generated grains act as a barrier against dislocation slip, leading to toughness deterioration and increasing tensile strength. The sample with the highest deformation at a rate of 0.05 s^{-1} showed effective grain refinement and significant change of the KAM values.

A simultaneous investigation of Taylor and Schmid factor were carried out to observe the resistance of the grains in response of to the application of strain. Figure 88 shows a similar behavior for the two analysis. Through the results it can be suggested that the smaller

Schmid factor of the grains correspond to the greater Taylor factor. According to Taylor's theory of plastic deformation (XIANFENG, 2013), grains with a higher Taylor factor will dissipate more strain energy and thus deformation will be more difficult because the grain orientation needs to rotate to be closer to the <111> pole. In other words, the greater Taylor factor facilitates the formation of twins. These results suggest that the Taylor factor can provide an important guideline for determining the deformation mode. That is, a high Taylor factor corresponds to deformation by twinning (twin) and a low Taylor factor corresponds to deformation by sliding (slip), while an intermediate value of the Taylor factor corresponds to the multislip mode (XIANFENG, 2013) (MAECEAU, 2013).

Grain activated slip systems associated with the strain direction were examined in terms of the Schmid factor, see Figure 88. The Schmid factor can provide an indication on how which dislocation slip can occur in a plane. The maximum value of the Schmid factor during the torsion process was approximately 0.5. Grains with high Schmid factor values slip easily, while grains with lower Schmid factor values require higher shear stress to form critical slip systems necessary for deformation to occur. Figure 88 revealed that, as received, the samples presented relative low values while after lower strains of $\varepsilon = 0.6$ and $\varepsilon = 0.75$, the highest percentage of grains exhibited Schmid factor values greater than 0.4. After larger deformations, in the region closest to the maximum torsion sample radius, the fraction of grains with low Schmid factor values increased, suggesting that the grains have a greater resistance to plastic deformation.

According to previous research (XIANFENG, 2013) (MAECEAU, 2013) when stress and temperature decrease, sliding becomes difficult while strain twinning tends to be favored. Although the critical resolved shear stress (CRSS) for twinning is greater than that for sliding in most cases, the twinning mode is still preferred when stress concentration arises, particularly at relatively low temperatures. Therefore, when the temperature decreases, a greater stress is needed to overcome the CRSS and thus promote the formation of twins. The observed reduction in Schmid factor, see Figure 88i and 88j, suggests a more significant true strain at 900 °C (SITDIKOV, 2013). This result seems to agree with other investigated TWIP steels (LIMA, 2022).

Austenitic steels with FCC structure contain 12 sliding systems and 12 twinning systems, considering 4 octahedral planes {111} with 3 compressed directions <110>, in each plane. Calculation of slip systems and their corresponding volume fractions in high Mn TWIP steel according to (LIMA, 2022). was performed using ATEX analysis software. Table 12 shows that the same active slip systems, including $(11\bar{1})[1\bar{1}0]$, $(1\bar{1}\bar{1})[01\bar{1}]$, $(1\bar{1}\bar{1})[110]$, $(1\bar{1}1)[011]$,

$(1\bar{1}1)[110]$, $(111)\ [01\bar{1}]$, $(111)[10\bar{1}]$ are common in all investigated samples. The requirement of at least five independent plastic deformation systems is known as the von Mises Criterion. So, if less than 5 independent sliding systems are available, ductility is predicted to be low in the material. The issue is that each grain will not be able to deform, and cracks will open up leading to the appearance of failures (MAECEAU, 2013). The investigated steel has more than 5 sliding systems, that is, even after greater deformations (accumulating almost 3.0 of strain) the samples did not fracture.

Figure 88 — EBSD (Taylor factor and Schmid factor) maps of specimens (a, b) as-received, (c, d) after deformation of ε=0.62 (route A - inside zone), (e, f) after deformation of ε=2.2 (route A - outside zone), (g, h) after deformation of ε=0.75 (route B - inside zone), and (i, j) after deformation of ε=2.6 (route B - outside zone).

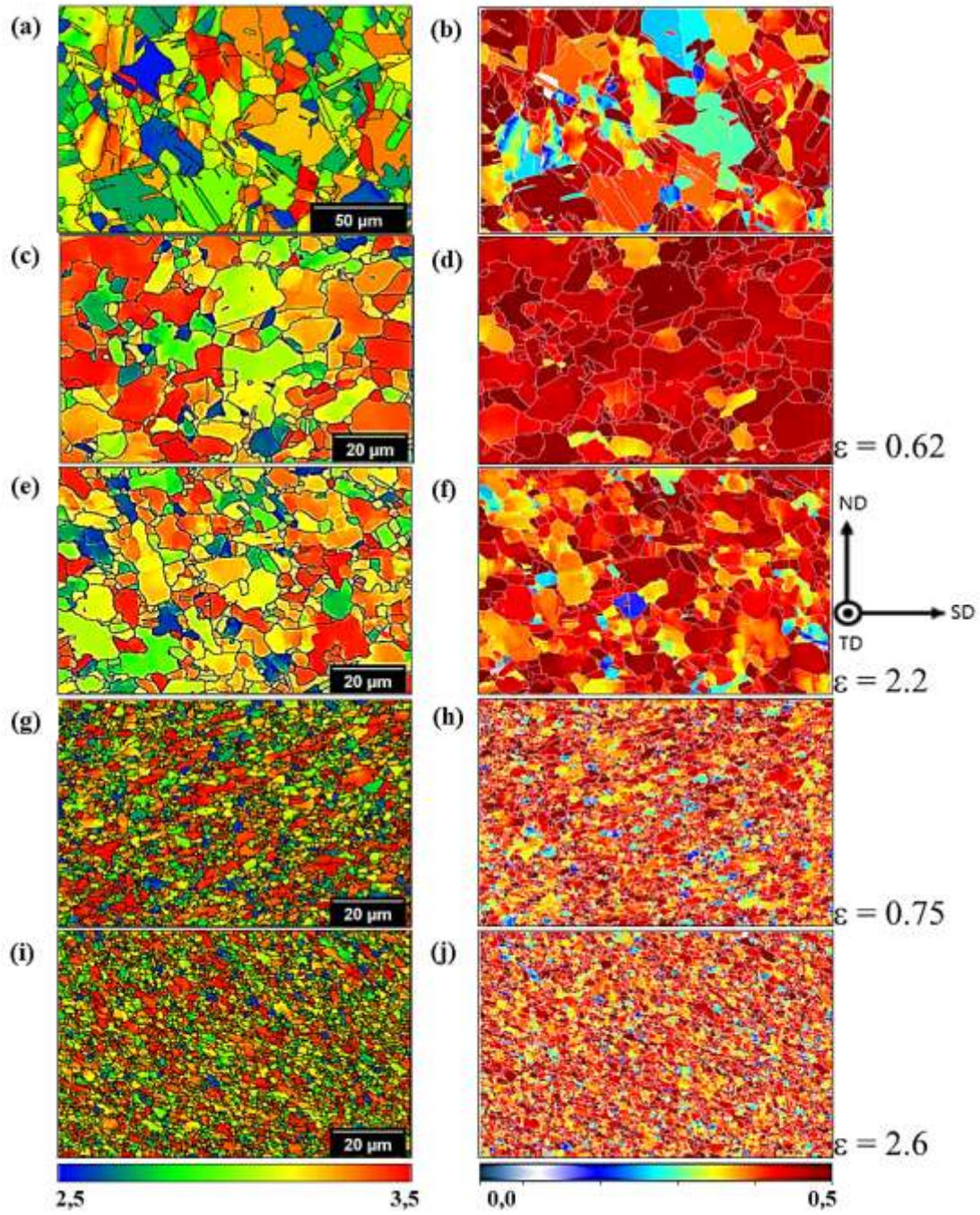

Source: Elaborated by the author.

Table 12 — Slip systems components and their volume fractions according to the quantity of deformation.

		As-received	ε=0.62 route A inside	ε=2.2 route A outside	ε=0.75 route B inside	ε=2.6 route B outside
Slip systems	(1 1 $\bar{1}$) [0 1 1]	0	0	0	0	0
	(1 1 $\bar{1}$) [1 0 1]	0	0	0	0	0
	(1 1 $\bar{1}$) [1 $\bar{1}$ 0]	23.411	13.714	15.101	11.935	10.992
	(1 $\bar{1}$ $\bar{1}$) [0 1 $\bar{1}$]	10.6	21.844	27.022	21.079	15.067
	(1 $\bar{1}$ $\bar{1}$) [1 0 1]	3.961	9.087	6.498	16.528	15.542
	(1 $\bar{1}$ $\bar{1}$) [1 1 0]	11.136	1.337	13.21	4.72	11.843
	(1 $\bar{1}$ 1) [0 1 1]	8.714	14.109	10.9	14.105	15.154
	(1 $\bar{1}$ 1) [1 0 $\bar{1}$]	8.6	22.811	5.879	17.052	9.569
	(1 $\bar{1}$ 1) [1 1 0]	16.941	7.906	8.113	5.804	12.592
	(1 1 1) [0 1 $\bar{1}$]	5.934	4.032	2.541	5.18	2.677
	(1 1 1) [1 0 $\bar{1}$]	10.704	5.161	10.738	3.597	6.565
	(1 1 1) [1 $\bar{1}$ 0]	0	0	0	0	0

Source: Elaborated by the author.

7.3.4 Mechanical Tensile tests

The stress-strain curves of the TWIP-FeMnCCr steel in Figure 89 demonstrate that the yield stress (YS) and ultimate tensile stress (UTS) improved as the strain imposed on the samples increased. The YS increment is more evident than the corresponding UTS increment. Similar behaviors were found in the literature (TIMOKHINA, 2014) (TIMOKHINA, 2014) (JO, 2021). The YS values increased from 377 MPa in the as received sample to 463 MPa, 729 MPa, after ε = 2.2 and ε = 2.6, respectively. The yield strength of the samples after application of route A has increased and after application of route B, the value has become almost twice as compared to the received one. With regard to elongation, the initial specimen fractured at the engineering strain of 89% and the elongation values decreased to approximate values of 34% and 6% in the samples which experienced strain of ε = 2.2 and ε = 2.6, respectively. The results obtained from the tensile tests are summarized in Table 13.

The as-received sample showed large plasticity, which can be explained by the high slip and free path available for dislocations to move in the austenitic matrix. One can notice the presence of “serrated points” along the line of the stress versus strain graph. The serrations are due to dynamic stress aging (DSA) or Portevin-LeChatelier effect arising from interactions between solute atoms and/or movement of dislocations. The serrations from the tests carried

out at room temperatures are characterized as type C. They are yield losses that occur below the general level of the stress-strain curve are considered to be due to the unlocking of dislocation (RODRIGUEZ, 1984) (SCHOECK, 1984).

It has already been mentioned that deformed samples produce many subgrains which restrict the movement of the dislocations. Due to this dislocation movement restriction, the TWIP steel starts to deform by secondary sliding systems. Therefore, there is dissociation of dislocations with a Burgers vector into partial Schockley dislocations. This result seems to be in agreement with previous research (BARBIER, 2012) where the authors compared the microstructural evolution of a FeMnC TWIP steel after tensile and shear tests. The result of the shear test showed that the number of twinned grains was only 70%, while in the tensile test, 90% of the grains had at least one active sliding system.

Figure 89 — Engineering stress-strain curves.

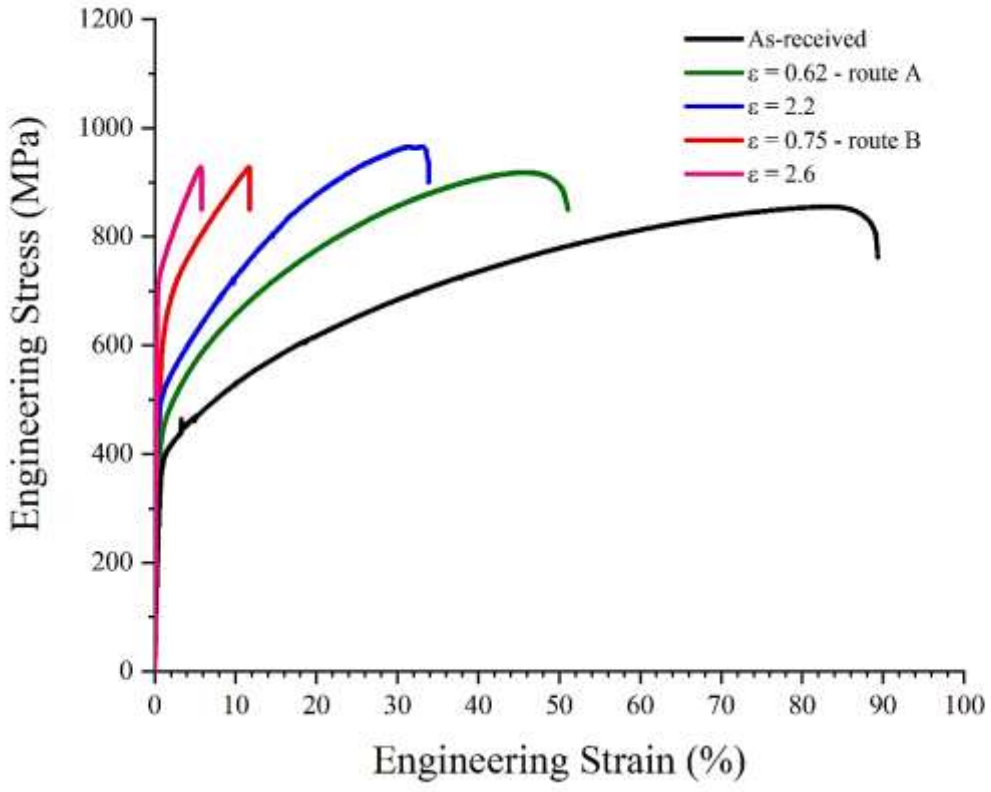

Source: Elaborated by the author.

In the sample with 2.2 strain, a significant number of subgrains can be observed, as well as some regions of the microstructure that presented a smaller number of defects, see

Figure 80. The mixed microstructure favored the maintenance of a significant elongation and a satisfactory yield strength.

In terms of chemical composition, chromium is present in small amounts in certain structural steels used in the oil and gas industry. It is mainly used to increase the hardenability and corrosion resistance of steel, as well as increase the yield strength. Additionally, when this chemical element is added to steel, it reduces the stacking fault energy and favors the TWIP effect (SKILBRED, 2020) (CHENG, 2021) (SEOK, 2019). During tensile tests at room temperature, the SFE of the TWIP steel used in this investigation was low, which increases the twinning activity. Changes in tensile properties with temperature reflect SFE's dependence on temperature. The SFE in austenitic steels decreases with decreasing temperature, leading to an increase in the resolved critical shear stress (CRSS) for sliding and decreasing it for twinning. In other words, when stress is applied at lower temperature, sliding becomes difficult while strain induced twinning tends to be easy. Although the CRSS required for twinning is greater than that for sliding in most cases, the twinning mode is still preferred when stress concentration arises, particularly when deformation occurs at relatively low temperatures (SEOK, 2019) (MAECEAU, 2013).

The union of two factors: the high refinement of the grain and the greater facility of twinning during the tensile tests at room temperature, can explain the small elongation for the sample which suffered higher strain. It can be suggested that mechanical sliding was the main deformation mechanism (LEI, 2017) (HAASE, 2016) (ABRAMOVA, 2016). The overall mechanical properties (i.e. strength and ductility) from all conditions can be more effectively compared by analyzing the ECO index (see Table 13), a product of ultimate tensile strength (UTS) and fracture elongation (%) (KANG, 2016). Before deformation, the material had an ECO index of approximately 76 GPa%. As deformation progressed, the ECO index of the TWIP-FeMnCCr steel sharply decreased. The sample after after application of route A reached less than half of the initial value. It can be suggested that the reason for this significant decrease in ECO despite the increase in UTS is due to the severe loss of elongation of the TWIP-FeMnCCr steel with higher strain.

Analyzing the values of EBSD, KAM and texture intensity, the TWIP-FeMnCCr steel started a recrystallization process with the nucleation of new ultrafine grains. The expected values for UTS were not obtained. A possible explanation for low values would be through two factors: torsion test temperature and the microstructure with very refined grains. Therefore, the dislocations had no room to move, accumulating stress and reducing the hardening capacity of the steel leading to early fracture of the tensile specimen. The resilience values were initially

reduced and with the advancement of deformation they increased which may indicate the more pronounced effect of YS.

Table 13 — Mechanical properties (defined from the engineering stress-strain curves) of the investigated TWIP-FeMnCCr steel in different conditions.

Hot Torsion schedules	Yield Strength (MPa)	Ultimate tensile Strength (MPa)	Resilience ($MJ.m^{-3}$)	Elongation (%)	Toughness ($MJ.m^{-3}$)	ECO index (GPa %)
As-received	370 ± 20	855 ± 25	2.02	89 ± 2	702.31	76
ε = 0.62 route-A Inside	445 ± 4	918 ± 10	3.12	51 ± 2	401.83	46
ε = 2.2 route-A Outside	460 ± 3	945 ± 10	1.52	34 ± 2	270.00	32
ε = 0.75 route-B Inside	626 ± 4	925 ± 10	4.17	12 ± 2	90.21	11
ε = 2.6 route-B Outside	729 ± 3	930 ± 10	3.18	6 ± 2	46.74	5

Source: Elaborated by the author.

Work hardening rate curves ($d\sigma/d\varepsilon$) versus true strain of all samples are displayed in Figure 90. In terms of strain hardening behavior, samples processed with lower strains showed a fair amount of work hardening. However, as the torsion process exceeded ε = 2.2, softening occurred and later the ductility steadily decreased. The stages may be related to different mechanisms, namely: the transition point from stage A to B corresponds to the beginning of twinning; the constant level of stage B can be caused by the introduction of strain induced twins into the microstructure. Stage C is attributed to a decrease in twinning reaching plastic instability (HUGHES, 1996) (JIN, 2009). Similar behavior was found for other FeMnCAl TWIP steels, with no increase in strain rate in stage B and with little or no increase in stage C (BARBIER, 2009). There are TWIP steels with different stages. Many factors can modify the stages, such as chemical composition, SFE, initial microstructure, temperature of the applied deformation process, amount of applied deformation, among others (BARBIER, 2009).

Figure 90 — Strain hardening rate (dσ/dε) - true strain curve for all samples.

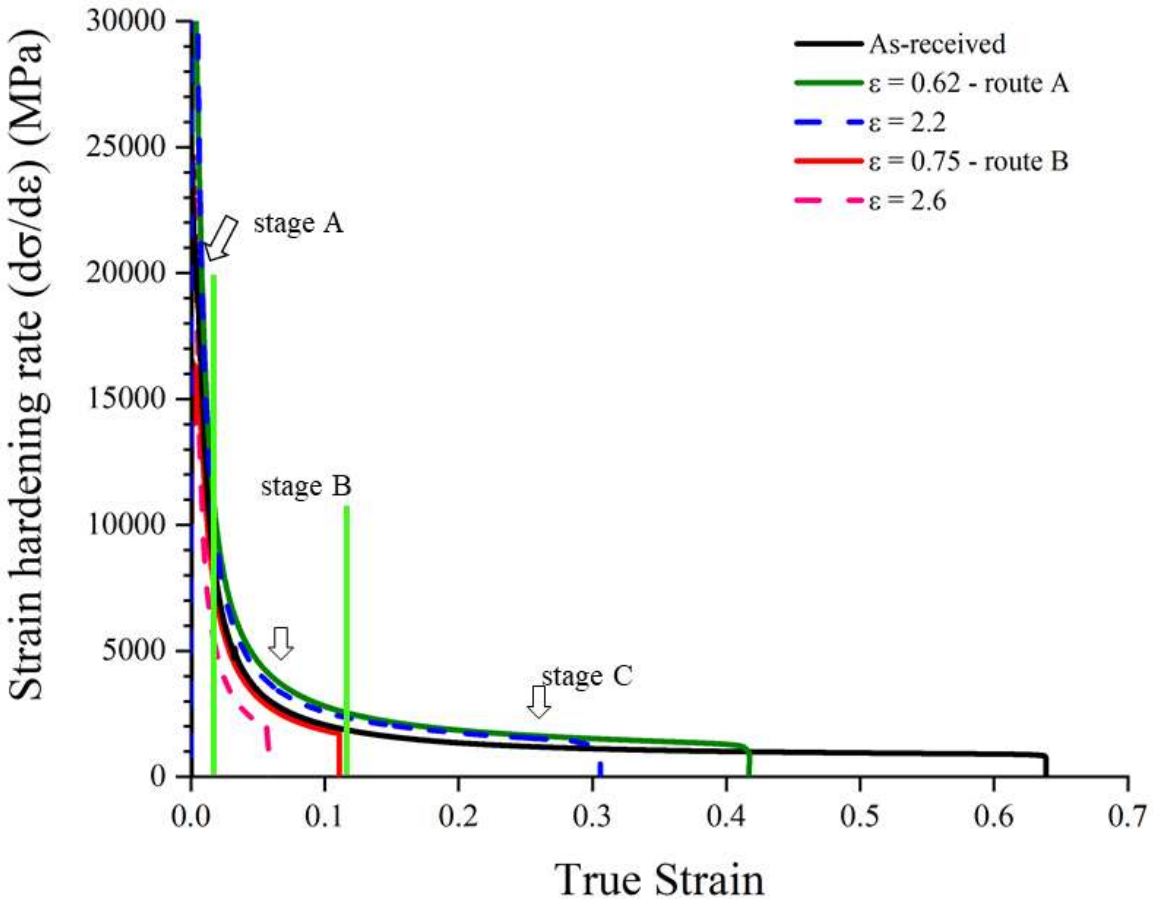

Source: Elaborated by the author.

In stage A, there is a drastic drop in the strain rate (0 to 0.04 of strain), which corresponds to the elastic-plastic transition. In stage B, up to 0.15 strain, is associated with plastic deformation governed by the sliding of dislocations and the production of mechanical twining. Finally, above 0.16 strain, an approximate constancy of work hardening rate is observed. It stops the linear decrease in work hardening rate observed in stage B and reaches steady state until fracture of the specimens. This behavior is similar to that found for TWIP steels (LIMA 2018) (BEYERLEIN, 2007). The super generation of mechanical twins caused an increase in mechanical strength, reducing toughness and decreasing the free path of dislocations. The samples with the greatest deformation (ε = 2.2) showed a suppression of stage C. Due to the refinement of the microstructure, the steel reached saturation of crystalline defects and fractured more quickly. The results obtained confirm the hypothesis raised by other authors (ZHI, 2020), who suggested that substructure gradients remained during tensile deformation.

This may lead to strain mismatch and strain partitioning between the surface and center of the tested sample.

7.3.5 Fracture analysis

To understand the fracture mechanism, fractographic analysis was performed on tensile samples using SEM. Fracture surfaces of tensile specimens are shown in Figure 91. Each condition of strain which the samples passed through is informed in the Figure. There are two types of ductile fracture dimples: large cavities, formed by mechanisms of interaction between the matrix and inclusions, and smaller cavities, which are probably formed by some mechanism related to dislocations (HIGUERA-COBOS, 2014). The surface of the as-received sample mainly contains deep dimples. Ductile materials have a cup-cone fracture surface. The obtained images correlate well with this type of structure and with the elongation and toughness results found for this sample.

After torsional straining for the sample with $\varepsilon = 2.2$, the images indicate changes in the fracture surface. The surfaces indicate a quasi-cleavage feature containing step-like ridges that is due to twin-twin or twin-slip interactions (MOHAMMADI, 2020). According to the literature (REN, (2021), the greater the diameter and the deeper the corrugation, the better the energy absorption capacity of the material during deformation, increasing elongation and hardening during the tensile test.

For samples with greater deformation, the ductile appearance changes to very small voids in diameter and without depth, characteristics of a brittle material surface. Although previous studies have reported a positive effect of twins in obtaining high strength and high plasticity (MOHAMMADI, 2020), the current study suggests that grain refinement and the preexistence of micro-twins in the microstructure suppress the formation of strain-induced twins and decrease the induced plasticity by twinning (MOHAMMADI, 2020). This indicates that the micro-twins in TWIP steel contribute to high strength and not high ductility when in a pre-refined microstructure. Some studies have suggested that grain and twin boundaries are favorable sites for crack initiation (MOHAMMADI, (2020). In other words, crack propagation occurs faster than dislocation accumulation at grain and twin boundaries.

Figure 91 — Fracture surfaces of the fractured tensile test specimens (a, b) as-received, (c, d) after deformation of ε= 0.62 (route A - inside zone), (e, f) after deformation of ε= 2.2 (route A - outside zone), (g, h) after deformation of ε= 0.75 (route B - inside zone), and (i, j) after s deformation of ε= 2.6 (route B – outside zone).

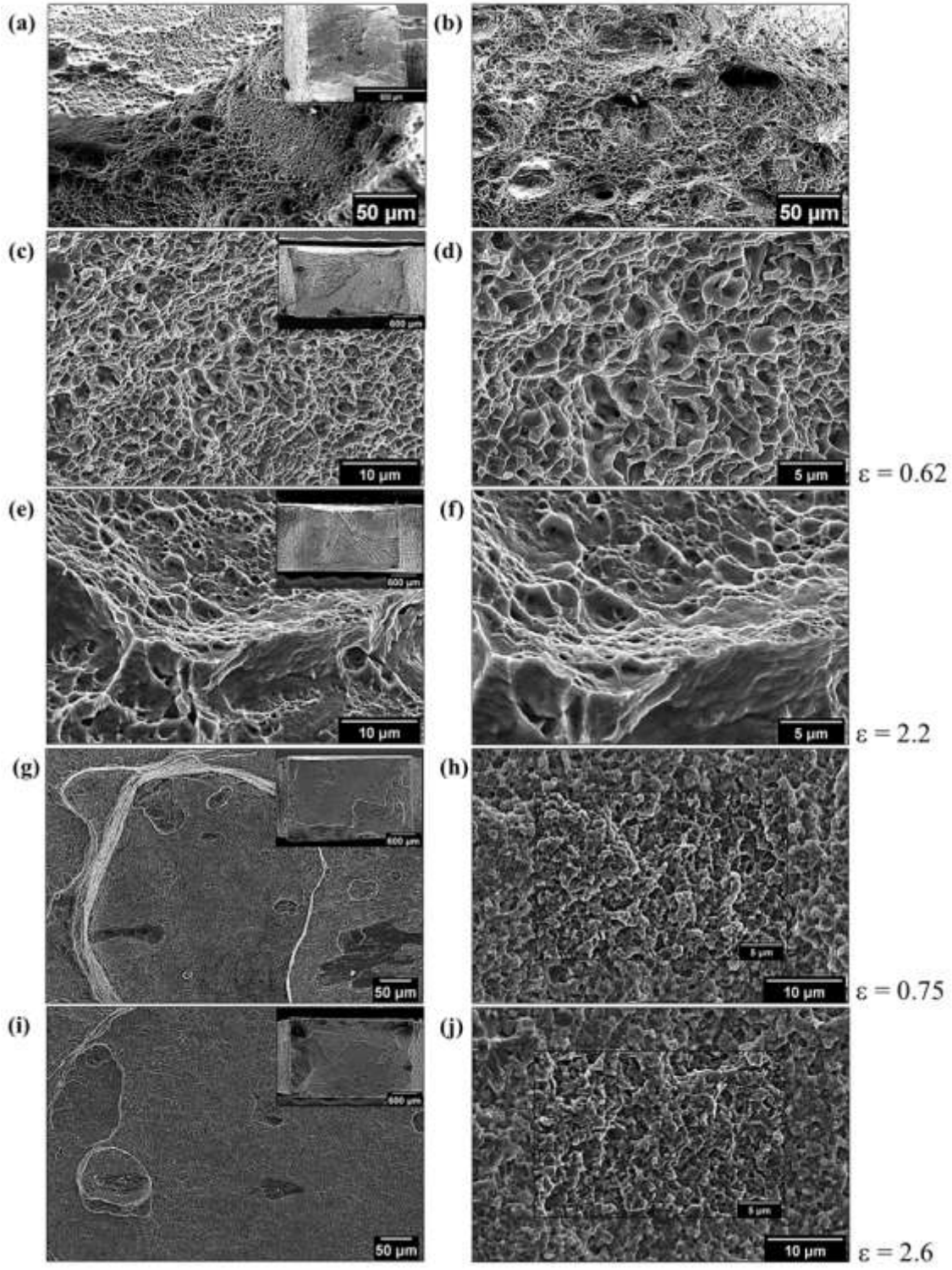

Source: Elaborated by the author.

8 RESULTS: ANALYSIS OF DEFORMATION PROCESSES AND MECHANICAL PROPERTIES.

This work studied the influence of the strain type and process temperature on the mechanical behavior of a TWIP steel with high manganese content. It was confirmed that the combination of pure shear deformation at a low temperature significantly increases the mechanical properties of TWIP steel. Taking into account the peculiarities and costs of each process, they can be analyzed only based on the results presented in this work. These results made it possible to assess which of the processes presented the best results after processing TWIP steel with high manganese content.

Cold rolling produced excellent properties with a well-deformed microstructure. Because it is a simple process and widely used in the industrial sector, cold rolling can be a good processing option for this steel. The material has good plasticity; however, its high manganese content makes machining and processing at room temperature difficult. The microstructure showed a high degree of deformation despite having low yield strength values after tensile tests.

The ideal deformation mechanism for an application requiring a higher yield strength is simple shear. Two techniques presented in this work showed the powerful deformation power of this mechanism. After a hot torsion test (900 ºC), the material showed an ultrafine microstructure and can be used in some applications that do not require high maximum resistance values. The hot torsion process is beneficial in that regardless of the degree of deformation applied, the material can be processed by another deformation mechanism afterward, if necessary. It is noteworthy that after the hot torsion process, the yield strength values presented were higher than those obtained by the same material after cold rolling.

Already after processing by ECAP (350º and 250º), the material showed very high values of mechanical properties. The presented microstructure confirms this behavior. The presence of a mixed microstructure with crystallographic defects, twins, and subgrains after deformation by simple shear provided the necessary texture to reach mechanical strength values greater than 1.9 GPa. Remembering that in the ECAP process, the great advantage is the maintenance of the material dimensions after processing. After being submitted to ECAP, the samples showed the highest dislocation density (see Figure 92) values compared to the other processes investigated. In the Figure 93 below, a significant increase in the yield strength can

be seen, for example, after ECAP passes. The yield strength of the as-received material increased from 377 MPa to 1495 MPa and 1915 MPa when deformed by ECAP at 350 °C and 250 °C temperature, and the tensile strength reached 1960 MPa.

Figure 92 — Dislocation density for different process of deformation investigated.

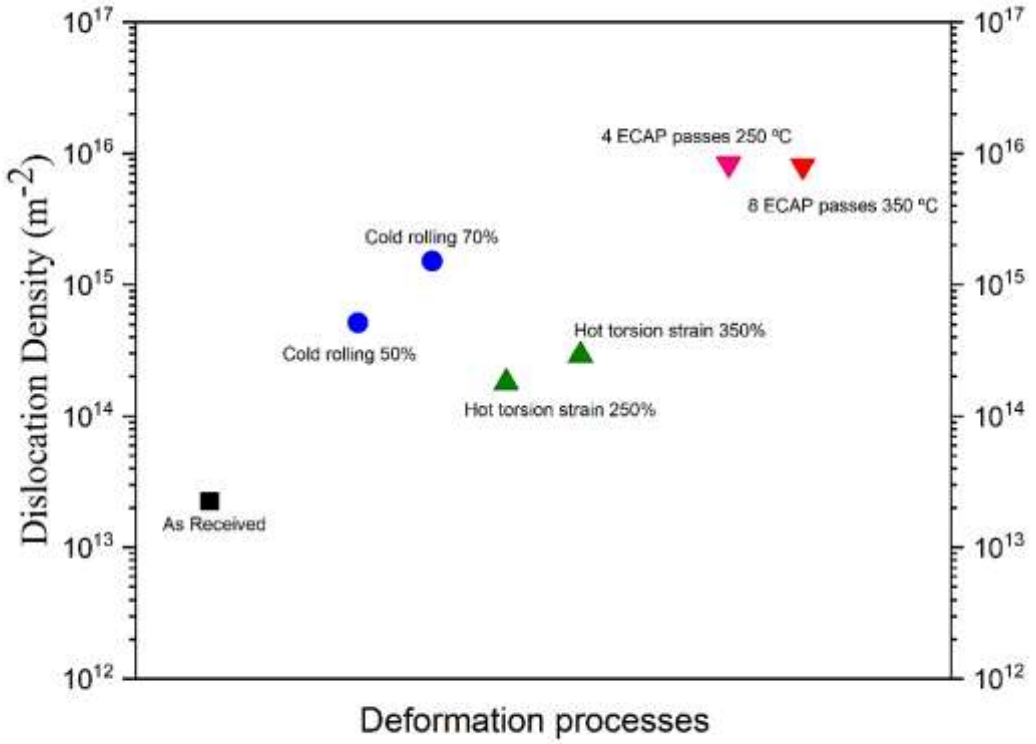

Source: Elaborated by the author.

Figure 93 — Engineering stress-strain curves for different process of deformation investigated.

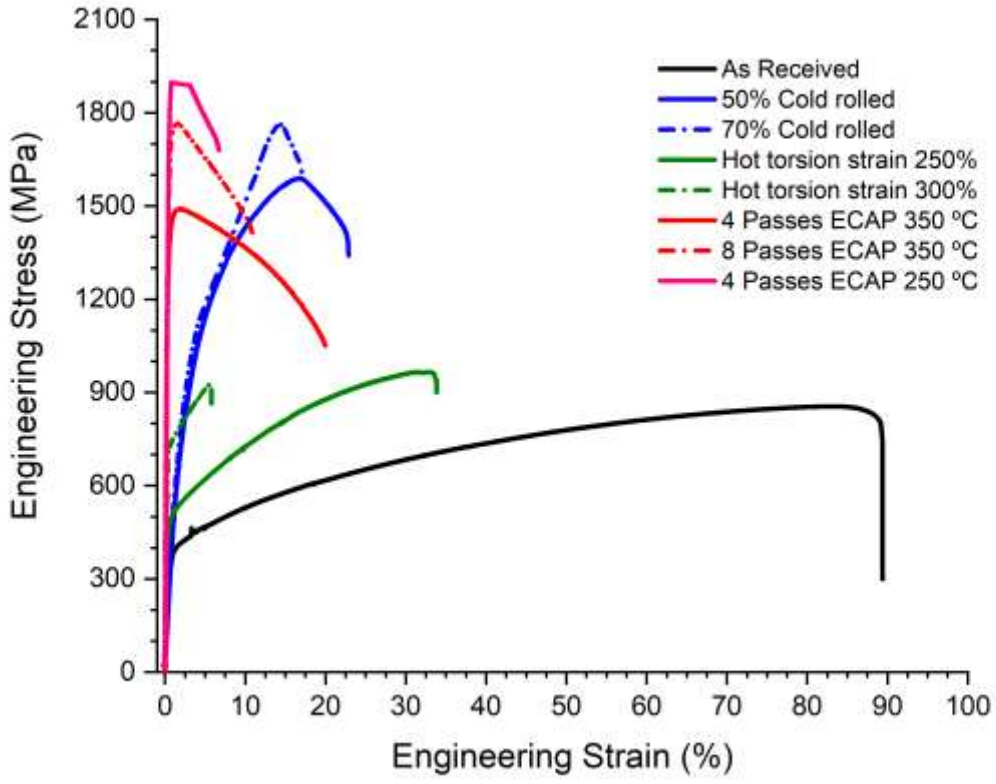

Source: Elaborated by the author.

9 CONCLUDING REMARKS

9.1 COLD ROLLING

This chapter the effect of cold rolling on the microstructure, texture evolution and mechanical properties of an advanced high-Mn austenitic TWIP steel was studied. The main results can be summarized as follows.

(1) With increasing the rolling reduction applied, {110}<110> and {111}<110> components were predominant. This can be attributed to the formation of subgrains and substructures in the austenite. Characteristic components of deformation in FCC materials at low temperatures.

(2) The gradual development of the shear bands and a rise in dislocation density by increased degree of deformation promotes dislocation glide and twin-induced plasticity.

(3) Grain refinement coupled with increased fraction of low-energy Σ3 twin boundaries; i) increased local lattice distortion ii) reduced the cleavage (001) planes, thereby resulting in an acceptable balance between strength and elongation.

(4) Cold rolling resulted in significant increase in the ultimate strength up to 1760 MPa after rolling to a total strain of 17%. The strengthening of the present steel during cold rolling was attributed to an increase in the dislocation density and reduction of the free path for dislocation motion.Ultra-high strength austenitic TWIP steels can be considered as potential materials to be employed in the petroleum industry.

9.2 EQUAL CHANNEL ANGULAR PRESSING

The isothermal equal channel angular pressing of a TWIP steel with the presence of Chromium was successfully performed in this chapter. The corresponding microstructure evolution texture and mechanical behavior were investigated. The main findings were:

(1) The evolution of the microstructure after one and two ECAP passes showed that the grains were elongated in the shear direction and that a large number of subgrains were introduced. At the same time, mechanical twins were created with smaller thickness as deformation proceeded. During ECAP passes, dislocation and twinning activity led to a further refinement of the microstructure, hindering further deformation and resulting in the low hardening rate obtained

during the tensile test of the eight ECAP passes sample.

(2) After deformation by ECAP, simple shear textures were identified. One ECAP pass samples showed preference toward A_1*, A_2* and C component, while the two and four ECAP passes samples showed a preference toward the b fiber, represented by its $B/\overline{B}$ components. This increase in $B/\overline{B}$ components together with the decrease in C shear texture component may indicate a large effect of deformation twinning in the processing of TWIP steel by ECAP at 350 °C.

(3) Yield strength and Ultimate tensile strength increased significantly after ECAP process. On the other hand, ductility and toughness decreased with the increase in the number of passes. The fracture surface analysis showed that the number and size of dimples decreased dramatically with the increase in the number of ECAP passes, up to eight ECAP passes, for which the sample showed limited ductile fracture. The present FeMnCCr-based steel showed hardening evolution with strain with periods of constant strain hardening rate. This behavior could be related to the ability of the material to deform by twinning, activating primary and secondary twin systems. The strain hardening rate decreased constantly with strain with uniform elongation.

(4) The gradual development of the shear bands and a rise in dislocation density by an increased degree of deformation promotes dislocation glide and twin-induced plasticity, resulting in a satisfactory balance between strength and elongation. The mechanical behavior of TWIP steel with high manganese content suggests it is a potential material to be employed in the petroleum industry.

(5) In this chapter, the influence of temperature on the ECAP process of TWIP steel was also studied. The performance of an ECAP die with an inner angle of $\Phi = 120$ ° and an outer angle of $\psi = 30$° has enabled to severely deform a FeMnCCr TWIP steel by ECAP at two different temperatures until fourth pass. Further deformation was not achieved due to fractures. After ECAP pass at 250 °C temperature, there is a strong reduction in the grain size together with a high increase in mechanical twins and subgrains caused by dislocation glide rendering a homogeneous and dense microstructure. On the contrary, the material after passes at 350 °C shows also an important reduction in grains size but lower than the process at 250 °C temperature.

(6) The results presented that there is the competition between the effect of the deformation temperature, SFE, grain size and accumulated strain on the mechanism of deformation. The wide amount of the dislocation substructure such as parallel microbands, dislocation cells, sub-

grains, stacking faults etc. was formed as a function of ECAP schedule. The formation of micro-twins within twins was also found.

(7) The direct relationship between the dislocation sub-structure development after different ECAP schedules and strain hardening behavior were studied. The yield strength of the as-received material is increased from 377 MPa to 1495 MPa and 1915 MPa when deformed by ECAP at 350 °C and 250 °C, respectively, and the ultimate tensile strength arrived to 1960 MPa. The ductility is greatly reduced due to increase in crystalline defects.

9.3 HOT TORSION

In the present study, torsional deformation was used to generate structural gradients in order to improve the yield strength and maintain the ductility of the present TWIP-FeMnCCr steel. The main conclusions can be seen as follows:

(1) Gradient structures with sub-grain generation and dislocation displacement structures were applied to TWIP-FeMnCCr steel. A significant refinement was shown along the radial direction from the center to the surface of the TWIP-FeMnCCr steel samples due to shear. The sub-threshold reinforcement and gradient structure result in exceptional properties, Yield Strength of 730 MPa, Ultimate tensile Strength of 930 MPa, and reasonable Toughness of 46 $MJ.m^{-3}$, as a result of the activation of multiple strengthening mechanisms.

(2) Microstructural observations revealed that the gradient substructures caused a distortion in the crystal lattice, as evidenced by peak shifts in XRD analyses. Dislocation density was increased from 2.23 x 10^{13} to 3.5 x 10^{14} m^{-2}, as a consequence of crystal lattice distortion. The increase in KAM angle values showed a large amount of energy stored in the microstructure which modified the misorientation leading to the creation of sub-grains. Taylor and Schmidt Factor analysis indicated the effect of applied deformation during torsion which led to an increase in the strain resistance of the grains, even at high temperatures.

(3) Tensile tests over the TWIP-FeMnCrC steel samples promoted the reinforcement of fiber-B due to the increase of the B component orientations $A/\bar{A}$, $B/\bar{B}$ which replaced the C component orientations. The texture of the outer zone of the torsion-strained specimens became stronger and influenced the decrease of randomly oriented grains volume fraction. Greater strains because of simple shear favored the <110> ∥ X fiber in terms of anisotropy.

(4) The presented results show that application of simple shear on the investigated material can be used in a thermomechanical processing control in order to enhance the softening mechanisms which can lead to an excellent combination of mechanical properties and activating mechanisms

resulting in heterogeneous microstructures. This can preferably be economical and viable ways to be used from the point of view of industrial applications.

10 SUGGESTIONS FOR FUTURE WORKS

An innovative study involving severe plastic deformation (SPD) is suggested as future work, specifically, processing TWIP steel with processes such as: Repetitive corrugation and straightening (RCS) (SAITO, 1999) (VALIEV, 1997), constrained groove pressing (CGP) (BENJAMIN, 1970). This study would help us understand better the superplasticity of the present TWIP steel even after different types of deformation. One can also suggest the application of different amounts of deformation by cold rolling. Because in the present work, only two reduction measures were possible (50% and 70%).

It is also important to observe the behavior of the present TWIP steel in electrochemical tests (open potential circuit, linear polarization and electrochemical impedance spectroscopy) to evaluate the resistance to corrosion in saline environment under. As positive points, steel has high levels of chromium and copper, elements that increase the corrosion resistance of these types of steel. Unlike most TWIP steels on the market that only have aluminum and silicon in their compositions.

REFERENCES

ABRAMOVA, M. M. et al. Structural and phase transformation in a TWIP steel subjected to high pressure torsion. **Materials Letters**, v. 166, p. 321–324, 1 mar. 2016. DOI: https://doi.org/10.1016/j.matlet.2015.12.095.

ABRAMOVA, M. M. et al. Tailoring Extra-Strength of a TWIP Steel by Combination of Multi-Pass Equal-Channel Angular Pressing and Warm Rolling. **Metals**, v. 11, n. 3, p. 518–518, 22 mars. 2021. DOI: https://doi.org/10.3390/met11030518.

ALLAIN, S. et al. Correlations between the calculated stacking fault energy and the plasticity mechanisms in Fe–Mn–C alloys. **Materials Science and Engineering A-structural Materials Properties Microstructure and Processing**, v. 387-389, p. 158–162, 15 dez. 2004. DOI: https://doi.org/10.1016/j.msea.2004.01.059.

ANDERSON, F. et al. Thermomechanical Behavior of Biocompatible Austenitic Stainless Steels during Simulated Torsion Tests. **Journal of Materials Engineering and Performance**, v. 28, n. 9, p. 5890–5901, 1 set. 2019. DOI: https://doi.org/10.1007/s11665-019-04324-4.

ARANAS, C. et al. Ferrite Formation above the Ae_3 Temperature during the Torsion Simulation of Strip Rolling. **Isij International**, v. 55, n. 11, p. 2426–2434, 1 jan. 2015. DOI: https://doi.org/10.2355/isijinternational.ISIJINT-2015-320.

BAGHERPOUR, E.; REIHANIAN, M.; EBRAHIMI, R. On the capability of severe plastic deformation of twining induced plasticity (TWIP) steel. **Materials & Design (1980-2015)**, v. 36, p. 391–395, abr. 2012. DOI: https://doi.org/10.1016/j.matdes.2011.11.055.

BAI, Y. et al. Unique transition of yielding mechanism and unexpected activation of deformation twinning in ultrafine grained Fe-31Mn-3Al-3Si alloy. **Scientific Reports**, v. 11, n. 1, 5 ago. 2021. DOI: https://doi.org/10.1038/s41598-021-94800-6.

BALUCH, N.; UDIN, Z. M.; ABDULLAH, C. S. Advanced High Strength Steel in Auto Industry: an Overview. **Engineering, Technology & Applied Science Research**, v. 4, n. 4, p. 686–689, 18 ago. 2014. DOI: https://doi.org/10.48084/etasr.444.

BARBIER, D. et al. Analysis of the tensile behavior of a TWIP steel based on the texture and microstructure evolutions. **Materials Science and Engineering: A**, v. 500, n. 1-2, p. 196–206, jan. 2009. DOI: http://dx.doi.org/10.1016/j.msea.2008.09.031.

BARBIER, D.; FAVIER, V.; BOLLE, B. Modeling the deformation textures and microstructural evolutions of a Fe–Mn–C TWIP steel during tensile and shear testing. **Materials Science and Engineering A-structural Materials Properties Microstructure and Processing**, v. 540, p. 212–225, 1 abr. 2012. DOI: https://doi.org/10.1016/j.msea.2012.01.128.

BELADI, H.; ROHRER, G. S. The Distribution of Grain Boundary Planes in Interstitial Free

Steel. **Metallurgical and Materials Transactions A**, v. 44, n. 1, p. 115–124, 8 set. 2012. DOI: https://doi.org/10.1007/s11661-012-1393-0.

BELTRÃO, R.L.C., SOMBRA, C.L., LAGE, A.C.V.M., FAGUNDES NETTO, J.R. and HENRIQUES C.C.D – **Challenges and new technologies for the development of the presalt cluster**. In: OFFSHORE TECHNOLOGY CONFERENCE, Houston, Santos Basin, Brazil. 2009. p. May 4-7, 2009, Working Paper OTC 19880. Available at: <https://onepetro.org/OTCONF/proceedings-abstract/09OTC/All-09OTC/OTC-19880-MS/35954>. Access in: 24/08/2023. DOI: https://doi.org/10.4043/19880-MS.

BELYAKOV, A.; KAIBYSHEV, R.; TORGANCHUK, V. Microstructure and Mechanical Properties of 18%Mn TWIP/TRIP Steels Processed by Warm or Hot Rolling. **steel research international**, v. 88, n. 2, p. 1600123, 8 jun. 2016. DOI: https://doi.org/10.1002/srin.201600123.

BENJAMIN, J. S. Dispersion strengthened superalloys by mechanical alloying. **Metallurgical and Materials Transactions B**, v. 1, n. 10, p. 2943–2951, out. 1970.DOI: https://doi.org/10.1007/BF03037835.

BERBON, P. B. et al. Influence of pressing speed on microstructural development in equal-channel angular pressing. **Metallurgical and Materials Transactions A**, v. 30, n. 8, p. 1989–1997, ago. 1999. DOI: https://doi.org/10.1007/s11661-999-0009-9.

BERKUM, VAN et al. Diffraction-Line Broadening due to Strain Fields in Materials; Fundamental Aspects and Methods of Analysis. **Acta Crystallographica Section A**, v. 52, n. 5, p. 730–747, 1 set. 1996. DOI: https://doi.org/10.1107/S0108767396005727.

BEYERLEIN, I. J. et al. Role of twinning on texture evolution of silver during equal channel angular extrusion. **Philosophical Magazine**, v. 87, n. 6, p. 885–906, 11 jan. 2007. DOI: https://doi.org/10.1080/14786430601003866.

BEYERLEIN, I. J.; TÓTH, L. S. Texture evolution in equal-channel angular extrusion. **Progress in Materials Science**, v. 54, n. 4, p. 427–510, jun. 2009. DOI: https://doi.org/10.1016/j.pmatsci.2009.01.001.

BHARGAVA, M.; TEWARI, A.; MISHRA, S. K. Forming limit diagram of Advanced High Strength Steels (AHSS) based on strain-path diagram. **Materials & Design**, v. 85, p. 149–155, nov. 2015. DOI: https://doi.org/10.1016/j.matdes.2015.06.147.

BORDONE, M.; MONSALVE, A.; PEREZ IPIÑA, J. Fracture toughness of High-Manganese steels with TWIP/TRIP effects. **Engineering Fracture Mechanics**, v. 275, p. 108837, nov. 2022. DOI: https://doi.org/10.1016/j.engfracmech.2022.108837.

BOUAZIZ, O.; ALLAIN, S.; SCOTT, C. Effect of grain and twin boundaries on the hardening mechanisms of twinning-induced plasticity steels. **Scripta Materialia**, v. 58, n. 6, p. 484–487, mar. 2008. DOI: https://doi.org/10.1016/j.scriptamat.2007.10.050.

BOUAZIZ, O.; GUELTON, N. Modelling of TWIP effect on work-hardening. **Materials Science and Engineering: A**, v. 319-321, p. 246–249, dez. 2001. DOI:

https://doi.org/10.1016/S0921-5093(00)02019-0.

BOUAZIZ, O. et al. High manganese austenitic twinning induced plasticity steels: A review of the microstructure properties relationships. **Current Opinion in Solid State and Materials Science**, v. 15, n. 4, p. 141–168, ago. 2011. DOI: https://doi.org/10.1016/j.cossms.2011.04.002.

BRACKE, L. et al. Microstructure and texture evolution during cold rolling and annealing of a high Mn TWIP steel. **Acta Materialia**, v. 57, n. 5, p. 1512–1524, mar. 2009. DOI: https://doi.org/10.1016/j.actamat.2008.11.036.

BRUNA, R. Effects of hot and warm rolling on microstructure, texture and properties of low carbon steel. **REM. Revista Escola de Minas**, v. 64, n. 1, p. 57–62, 1 mar. 2011. DOI: https://doi.org/10.1590/S0370-44672011000100007.

CALLISTER, W. D.; RETHWISCH, D. G. **Ciência e Engenharia de Materiais - Uma Introdução**. [s.l: s.n.]. 5, ed.; 2008.

CEES T. B. Future Steel Vehicle: leading edge innovation for steel body structures. **Ironmaking & Steelmaking**, v. 39, n. 7, p. 477–492, 1 out. 2012. DOI: https://doi.org/10.1179/0301923312Z.000000000123.

CHANG, J.; YOON, J. W.; KIM, G.-H. Development of submicron sized grain during cyclic equal channel angular pressing. **Scripta Materialia**, v. 45, n. 3, p. 347–354, 1 ago. 2001. DOI: https://doi.org/10.1016/S1359-6462(01)01040-5.

CHEN, J. et al. Grain size dependence of twinning behaviors and resultant cryogenic impact toughness in high manganese austenitic steel. **Journal of Materials Research and Technology**, v. 10, p. 175–187, jan. 2021. DOI: https://doi.org/10.1016/j.jmrt.2020.12.030.

CHENG, M. et al. Comparative studies on microstructure evolution and corrosion resistance of 304 and a newly developed high Mn and N austenitic stainless-steel welded joints. **Corrosion Science**, v. 183, p. 109338–109338, 1 maio 2021. DOI: https://doi.org/10.1016/j.corsci.2021.109338.

CHO, S.-H.; KI BONG KANG; JONAS, J. J. Effect of manganese on recrystallisation kinetics of niobium microalloyed steel. **Materials Science and Technology**, v. 18, n. 4, p. 389–395, 1 abr. 2002. DOI: https://doi.org/10.1179/026708302225001859.

CHOI, J. K. et al. **High Manganese Austenitic Steel for Cryogenic Applications**. In: THE TWENTY-SECOND INTERNATIONAL OFFSHORE AND POLAR ENGINEERING CONFERENCE. Rhodes, Greece Available at: <https://onepetro.org/ISOPEIOPEC/proceedings-abstract/ISOPE12/All-ISOPE12/ISOPE-I-12-599/13027>. Access in: 24 aug. 2023.

COELHO, Paloma Pereira da Silva. **Estudo da susceptibilidade à corrosão sob tensão em atmosfera de H2S das armaduras de tração de dutos flexíveis**. 2013. Dissertação (Mestrado em Engenharia Mecânica e Tecnologia de Materiais) - Centro Federal de Educação Tecnológica Celso Suckow da Fonseca, Rio de Janeiro, setembro de 2013. Available at: <chrome-extension://efaidnbmnnnibpcajpcglclefindmkaj/https://dippg.cefet-

rj.br/ppemm/attachments/article/81/25_Paloma%20Pereira%20da%20Silva%20Coelho.pdf>. Access in: 24 aug. 2023.

COSTA E SILVA, A. L.; MEI, P. R. **Aços e ligas especiais**. 3ª ed. São Paulo: Edgard Blücher, 2011.

DE COOMAN, B. C.; CHIN, K.-G.; KIM, J.-K. High Mn TWIP Steels for Automotive Applications. **InTech e Books**, 8 jan. 2011. DOI: https://doi.org/10.5772/14086.

DE COOMAN, B. C.; ESTRIN, Y.; KIM, S. K. Twinning-induced plasticity (TWIP) steels. **Acta Materialia**, v. 142, p. 283–362, jan. 2018. DOI: https://doi.org/dx.doi.org/10.1016/j.actamat.2017.06.046.

DESPRÉS, A. et al. Contribution of intragranular misorientations to the cold rolling textures of ferritic stainless steels. **Acta Materialia**, v. 182, p. 184–196, 1 jan. 2020. DOI: https://doi.org/doi.org/10.1016/j.actamat.2019.10.023.

DNPM, DEPARTAMENTO NACIONAL DE PRODUÇÃO MINERAL. **Sumário Mineral, 2015.** (Brasil). Available at: < http://www.dnpm.gov.br/dnpm/sumarios/manganes-sumario-mineral-2015/view# >. Access in May/2021.

DONG, H. S. et al. Effect of pressing temperature on microstructure and tensile behavior of low carbon steels processed by equal channel angular pressing. **Materials Science and Engineering A-structural Materials Properties Microstructure and Processing**, v. 323, n. 1-2, p. 409–415, 1 jan. 2002. DOI: https://doi.org/10.1016/S0921-5093(01)01395-8.

DUAN, X. et al. Twinning behaviour of TWIP steel studied by Taylor factor analysis. **Philosophical Magazine Letters**, v. 93, n. 5, p. 316–321, 1 maio 2013. DOI: https://doi.org/10.1080/09500839.2013.776185.

DUMAY A et al. Influence of addition elements on the stacking-fault energy and mechanical properties of an austenitic Fe–Mn–C steel. **Materials Science and Engineering A-structural Materials Properties Microstructure and Processing**, v. 483-484, p. 184–187, 15 jun. 2008. DOI: https://doi.org/10.1016/j.msea.2006.12.170.

EDAX. **TSL-OIM v 5.2: users manual**. Mahwahm NJ, 2017.

EIVANI, A.R.; TAHERI A. K. An upper bound solution of ECAE process with outer curved corner. **Journal of Materials Processing Technology**, v. 182, n. 1-3, p. 555–563, 1 fev. 2007. DOI: https://doi.org/10.1016/j.jmatprotec.2006.09.021.

ETOU, M. et al. Super Short Interval Multi-Pass Rolling Process for Ultrafine-grained Hot Strip. **ISIJ International**, v. 48, n. 8, p. 1142–1147, 2008. DOI: https://doi.org/10.2355/isijinternational.48.1142.

FENG, Z.; ZECEVIC, M.; KNEZEVIC, M. Stress-assisted (γ→α′) and strain-induced (γ→ε→α′) phase transformation kinetics laws implemented in a crystal plasticity model for predicting strain path sensitive deformation of austenitic steels. **International Journal of Plasticity**, v. 136, p. 102807, jan. 2021. DOI: https://doi.org/doi.org/10.1016/j.ijplas.2020.102807.

FERRASSE, S. et al. Development of a submicrometer-grained microstructure in aluminum 6061 using equal channel angular extrusion. **Journal of Materials Research**, v. 12, n. 5, p. 1253–1261, 1 May 1997. DOI: https://doi.org/10.1557/JMR.1997.0173.

FERRASSE, S. et al. Texture evolution during equal channel angular extrusion. **Materials Science and Engineering: A**, v. 368, n. 1-2, p. 28–40, mar. 2004. DOI: https://doi.org/10.1016/j.msea.2003.09.077.

FLOREZ, M. A. C., M. N. S Lima, W. S. Araujo, M. J. G. Silva. Characterization and Comparative Analysis of Corrosion Resistance of 4 High Manganese Steels Models in Aqueous Solution of NaCl. **Mater Res-Ibero-AM J**. v. 22 (suppl 1) 2019. DOI: https://doi.org/10.1590/1980-5373-MR-2019-0283.

FLOREZ, M. A.; et al. Comparative study of corrosion resistance between four non-commercial high manganese steel models and 9% nickel steel in aqueous solution of H_2SO_4. **International Journal of Materials Research**, v. 111, n. 8, p. 661–667, 1 ago. 2020. DOI: https://doi.org/10.3139/146.111925.

FROMMEYER, G.; DREWES, E. J.; ENGL, B. Physical and mechanical properties of iron-aluminium-(Mn, Si) lightweight steels. **Revue de Métallurgie**, v. 97, n. 10, p. 1245–1253, out. 2000. DOI: https://doi.org/10.1051/metal:2000110.

FROMMEYER, G.; BRÜX, U.; NEUMANN, P. Supra-Ductile and High-Strength Manganese-TRIP/TWIP Steels for High Energy Absorption Purposes. **ISIJ International**, v. 43, n. 3, p. 438–446, 2003. DOI: https://doi.org/10.2355/isijinternational.43.438.

FUJII, T. et al. Analysis of the early stage of stress corrosion cracking in austenitic stainless steel by EBSD and XRD. **Materials Characterization**, v. 172, p. 110882–110882, 1 fev. 2021. DOI: https://doi.org/10.1016/j.matchar.2021.110882.

GAZDER, A. A. et al. Microstructure and texture evolution of bcc and fcc metals subjected to equal channel angular extrusion. **Materials Science and Engineering A-structural Materials Properties Microstructure and Processing**, v. 415, n. 1-2, p. 126–139, 15 jan. 2006. DOI: https://doi.org/10.1016/j.msea.2005.09.065.

GIRARD, G. et al. Cyclic response of electrodeposited copper films. Experiments and elastic–viscoplastic mean-field modeling. **Mechanics of Materials**, v. 153, p. 103685–103685, 1 fev. 2021. DOI: https://doi.org/doi.org/10.1016/j.mechmat.2020.103685.

GRÄSSEL, O. et al. High strength Fe–Mn–(Al, Si) TRIP/TWIP steels development — properties — application. **International Journal of Plasticity**, v. 16, n. 10-11, p. 1391–1409, jan. 2000. DOI: https://doi.org/10.1016/S0749-6419(00)00015-2.

GUAN, X. et al. Grain boundary engineering of AL6XN super-austenitic stainless steel: Distinctive effects of planar-slip dislocations and deformation twins. **Materials Characterization**, v. 170, p. 110689–110689, 1 dez. 2020. DOI: https://doi.org/10.1016/j.matchar.2020.110689.

GUO, N. et al. Misorientation-Dependent Twinning Induced Hardening and Texture Evolution

of TWIP Steel Sheet in Plastic Deformation Process. **Metals**, v. 7, n. 9, p. 348, 5 set. 2017. DOI: https://doi.org/10.3390/met7090348.

GURAO, N.P. et al. Evolution of Crystallographic Texture and Microstructure During Cold Rolling of Twinning-Induced Plasticity (TWIP) Steel: Experiments and Simulations. **Metallurgical and Materials Transactions**, v. 43, n. 13, p. 5193–5201, 5 set. 2012. DOI: https://doi.org/10.1007/s11661-012-1346-7.

GUTIERREZ-URRUTIA, I.; RAABE, D. Dislocation and twin substructure evolution during strain hardening of an Fe–22wt.% Mn–0.6wt.% C TWIP steel observed by electron channeling contrast imaging. **Acta Materialia**, v. 59, n. 16, p. 6449–6462, set. 2011. DOI: https://doi.org/10.1016/j.actamat.2011.07.009.

HAASE, C. et al. Equal-channel angular pressing and annealing of a twinning-induced plasticity steel: Microstructure, texture, and mechanical properties. **Acta Materialia**, v. 107, p. 239–253, 1 abr. 2016. DOI: https://doi.org/10.1016/j.actamat.2016.01.056.

HALDAR, A.; SUWAS, S.; BHATTACHARJEE, D. Microstructure and texture in steels: and other materials. 1. ed. London: **Springer**, 2009. 488 p. ISBN 978-1-84882-454-6. DOI: https://doi.org/10.1007/978-1-84882-454-6.

HAMADA, A.; LEO PENTTI KARJALAINEN; SOMANI, M. C. The influence of aluminum on hot deformation behavior and tensile properties of high-Mn TWIP steels. **Materials Science & Engineering A,** v. 467, n. 1-2, p. 114–124, 1 out. 2007. DOI: https://doi.org/10.1016/j.msea.2007.02.074.

HAUPT et al. The Influence of Warm Rolling on Microstructure and Deformation Behavior of High Manganese Steels. **Metals**, v. 9, n. 7, p. 797, 18 jul. 2019. DOI: https://doi.org/10.3390/met9070797.

HIGUERA-COBOS, O. F.; CABRERA, J. M. Mechanical, microstructural and electrical evolution of commercially pure copper processed by equal channel angular extrusion. **Materials Science and Engineering: A**, v. 571, p. 103–114, jun. 2013. DOI: https://doi.org/10.1016/j.msea.2013.01.076.

HIGUERA-COBOS, O. F.; BERRÍOS-ORTIZ, J. A.; CABRERA, J. M. Texture and fatigue behavior of ultrafine grained copper produced by ECAP. **Materials Science and Engineering: A**, v. 609, p. 273–282, jul. 2014. DOI: https://doi.org/10.1016/j.msea.2014.05.011.

HIRSCH, J.; LÜCKE, K. Mechanism of deformation and development of rolling textures in polycrystalline fcc metals-II. Simulation and interpretation of experiments on the basis of Taylor-type theories. **Acta Metallurgica.** Overview no. 76. , v. 36, n. 11, p. 2883–2904, nov. 1988. DOI: https://doi.org/10.1016/0001-6160(88)90173-3.

HOHENWARTER, A.; PIPPAN, R. Fracture of ECAP-deformed iron and the role of extrinsic toughening mechanisms. **Acta Materialia**, v. 61, n. 8, p. 2973–2983, maio 2013. DOI: https://doi.org/10.1016/j.actamat.2013.01.057.

HORITA, Z.; FUJINAMI, T.; LANGDON, T. G. The potential for scaling ECAP: effect of

sample size on grain refinement and mechanical properties. **Materials Science and Engineering: A**, v. 318, n. 1-2, p. 34–41, nov. 2001. DOI: https://doi.org/10.1016/S0921-5093(01)01339-9.

HUANG, J. Y. et al. Microstructures and dislocation configurations in nanostructured Cu processed by repetitive corrugation and straightening. **Acta Materialia**, v. 49, n. 9, p. 1497–1505, maio 2001. DOI: https://doi.org/10.1016/S1359-6454(01)00069-6.

HUGHES, D. A. et al. Stacking Fault Energy and Microstructure Effects on Torsion Texture Evolution. **Proceedings: Mathematical, Physical and Engineering Sciences**, v. 456, n. 1996, p. 921–953, 2000. DOI: http://www.jstor.org/stable/2665470.

HULL, D.; BACON, D. J. **Introduction to dislocations**. Amsterdam; London: Butterworth-Heinemann, 2011.

HUMPHREYS, J.; ROHRER, G. S.; ROLLETT, A. D. **Recrystallization and related annealing phenomena**. Amsterdam ; Oxford ; Cambridge (Ma): Elsevier, Cop, 2017.

HUNG, C.-Y. et al. Grain size altering yielding mechanisms in ultrafine grained high-Mn austenitic steel: Advanced TEM investigations. **Journal of Materials Science & Technology**, v. 86, p. 192–203, 1 set. 2021. DOI: https://doi.org/10.1016/j.jmst.2021.01.031.

HOSNI, I. et al. On the mechanism of twin formation in Fe–Mn–C TWIP steels. **Acta Materialia**, v. 58, n. 7, p. 2464–2476, 1 abr. 2010. DOI: https://doi.org/10.1016/j.actamat.2009.12.032.

IWAHASHI, Y. et al. Principle of equal-channel angular pressing for the processing of ultra-fine grained materials. **Scripta Materialia**, v. 35, n. 2, p. 143–146, jul. 1996. DOI: https://doi.org/10.1016/1359-6462(96)00107-8.

IWAHASHI, Y. et al. An investigation of microstructural evolution during equal-channel angular pressing. **Acta Materialia**, v. 45, n. 11, p. 4733–4741, nov. 1997. DOI: https://doi.org/10.1016/S1359-6454(97)00100-6.

JAE, E. J.; YOUNG, K. L. Effects of Al on microstructure and tensile properties of C-bearing high Mn TWIP steel. **Acta Materialia**. v. 60, n. 4, p. 1680–1688, 1 fev. 2012. DOI: https://doi.org/10.1016/j.actamat.2011.12.004.

JIANG, H. et al. Microstructural evolution, microhardness and thermal stability of HPT-processed Cu. **Materials Science and Engineering: A**, v. 290, n. 1-2, p. 128–138, 15 out. 2000.

JIN, J.-E.; LEE, Y.-K. Strain hardening behavior of a Fe–18Mn–0.6C–1.5Al TWIP steel. **Materials Science and Engineering: A**, v. 527, n. 1-2, p. 157–161, dez. 2009. DOI: http://dx.doi.org/10.1016/j.msea.2009.08.028.

JO, M. C. et al. Effects of Al addition on tensile properties of partially recrystallized austenitic TRIP/TWIP steels. **Materials Science and Engineering A-structural Materials Properties Microstructure and Processing**, v. 806, p. 140823–140823, 1 mar. 2021. DOI:

https://doi.org/10.1016/j.msea.2021.140823.

KAMACHI, M. et al. A model investigation of the shearing characteristics in equal-channel angular pressing. **Materials Science and Engineering A-structural Materials Properties Microstructure and Processing**, v. 347, n. 1-2, p. 223–230, 1 abr. 2003. DOI: https://doi.org/10.1016/S0921-5093(02)00589-0.

KAMALI, H. et al. Deformation mechanism and texture evolution of a low-Ni Cr–Mn–N austenitic stainless steel under bending deformation. **Materials Science and Engineering A-structural Materials Properties Microstructure and Processing**, v. 804, p. 140724–140724, 1 fev. 2021. DOI: https://doi.org/10.1016/j.msea.2020.140724.

KANG, J. Y. et al. Outstanding mechanical properties of high-pressure torsion processed multiscale TWIP-cored three layer steel sheet. **Scripta Materialia**, v. 123, p. 122–125, 1 out. 2016. DOI: https://doi.org/10.1016/j.scriptamat.2016.06.009.

KESTENS, L. A. I.; PIRGAZI, H. Texture formation in metal alloys with cubic crystal structures. **Materials Science and Technology**, v. 32, n. 13, p. 1303–1315, set. 2016. DOI: https://doi.org/10.1080/02670836.2016.1231746.

KHODDAM, S.; HODGSON, P. Conversion of the hot torsion test results into flow curve with multiple regimes of hardening. **Journal of Materials Processing Technology**, v. 153-154, p. 839–845, 1 nov. 2004. DOI: https://doi.org/10.1016/j.jmatprotec.2004.04.171.

KHODDAM, S.; HODGSON, P. D. A heuristic model selection scheme for representing hot flow data using the hot torsion test results. **Materials & Design**, v. 31, n. 4, p. 2011–2017, abr. 2010. DOI: https://doi.org/10.1016/j.matdes.2009.10.027.

KHODDAM, S. et al. Surface wrinkling of the twinning induced plasticity steel during the tensile and torsion tests. **Materials in engineering**, v. 60, p. 146–152, 1 ago. 2014. DOI: https://doi.org/10.1016/j.matdes.2014.03.063.

KIM, I. et al. Effects of equal channel angular pressing temperature on deformation structures of pure Ti. **Materials Science and Engineering A-structural Materials Properties Microstructure and Processing**, v. 342, n. 1-2, p. 302–310, 1 fev. 2003. DOI: https://doi.org/10.1016/S0921-5093(02)00318-0.

KOCH, C. C.; WHITTENBERGER, J. D. Mechanical milling/alloying of intermetallics. **Intermetallics**, v. 4, n. 5, p. 339–355, jan. 1996. DOI: https://doi.org/10.1016/0966-9795(96)00001-5.

KOWALSKA, J.; KOWALSKI, M. Development of Microstructure and Texture After Cold-Rolling Fe-24Mn-3Al-3Si High-Manganese Steel. **Journal of Materials Engineering and Performance**, v. 29, n. 3, p. 1495–1501, 16 dez. 2019. DOI: https://doi.org/10.1007/s11665-019-04516-y.

KRÜGER, L. et al. Stress-deformation behaviour of high manganese (AI, Si) TRIP and TWIP steels. **Journal de Physique IV (Proceedings)**, v. 110, p. 189–194, set. 2003. DOI: https://doi.org/10.1051/jp4:20020692.

KUSAKIN, P. S.; KAIBYSHEV, R. O. High-Mn twinning-induced plasticity steels:Microstructure and mechanical properties. **Reviews on Advanced Materials Science**, v. 44, n. 4, p. 326–360, 2016. Available at: https://www.scopus.com/inward/record.uri?eid=2-s2.0-84979581686&partnerID=40&md5=eb563570a076b0753b766b8f069bee0e Access in: 25 aug. 2023.

LEE, Y. K.; CHOI, C.-J. Driving force for γ→ε martensitic transformation and stacking fault energy of γ in Fe-Mn binary system. **Metallurgical and Materials Transactions**, v. 31, n. 2, p. 355–360, 1 fev. 2000. DOI: https://doi.org/10.1007/s11661-000-0271-3.

LEE, J. C.; SEOK, H.-K.; SUH, J.-Y. Microstructural evolutions of the Al strip prepared by cold rolling and continuous equal channel angular pressing. **Acta Materialia**, v. 50, n. 16, p. 4005–4019, 1 set. 2002. DOI: https://doi.org/10.1016/S1359-6454(02)00200-8.

LEE, J. U. et al. Grain-Refined AZ92 Alloy with Superior Strength and Ductility. **Metals and Materials International**, v. 24, n. 4, p. 730–737, 14 mar. 2018. DOI: https://doi.org/10.1007/s12540-018-0097-4.

LEE, W. et al. Equal channel angular pressing of a TWIP steel: microstructure and mechanical response. **Journal of Materials Science**, v. 52, n. 11, p. 6291–6309, 6 fev. 2017. DOI: https://doi.org/10.1007/s10853-017-0862-7.

LI, S.; BEYERLEIN, I. J.; BOURKE, M. A. M. Texture formation during equal channel angular extrusion of fcc and bcc materials: comparison with simple shear. **Materials Science and Engineering A-structural Materials Properties Microstructure and Processing**, v. 394, n. 1-2, p. 66–77, 1 mar. 2005. DOI: http://dx.doi.org/10.1016/j.msea.2004.11.032.

LI, X. et al. Wear and corrosion resistant Mn-doped austenitic cast iron prepared by powder metallurgy method. **Journal of Materials Research and Technology**, v. 9, n. 3, p. 6376–6385, maio 2020. DOI: https://doi.org/10.1016/j.jmrt.2020.03.099.

LIMA, M. N. DA S. **Microestrutura, corrosão e propriedades mecânicas de um aço com alto teor de manganês (27%p) para aplicações criogênicas**. 2018. Dissertação (Mestrado em Engenharia e Ciência de Materiais) - Centro de Tecnologia, Universidade Federal do Ceará, Fortaleza, 2018. Available at: <http://www.repositorio.ufc.br/handle/riufc/30474>. Accessed on Jan/2021.

LIMA, M. N. da S.; LOUREIRO, R. de C. P.; BÉREŠ, M.; MASOUMI, M.; MUÑOZ, J. C.; RODRIGUES, S. F.; ABREU, H. F. G.; Marreiro, J. M. C. Influence of cold deformation on microstructure, crystallographic orientation and tensile properties of an experimental austenitic Fe–26Mn-0.4C steel. **Journal of materials research and technology**, v. 19, p. 7–19, 1 jul. 2022. DOI: https://doi.org/10.1016/j.jmrt.2022.05.020.

LIN, T. H.; ITO, M. Theoretical plastic distortion of a polycrystalline aggregate under combined and reversed stresses. **Journal of the Mechanics and Physics of Solids**, v. 13, n. 2, p. 103–115, abr. 1965. DOI: https://doi.org/10.1016/0022-5096(65)90024-4.

MARCEAU, R. K. W. et al. Multi-Scale Correlative Microscopy Investigation of Both Structure and Chemistry of Deformation Twin Bundles in Fe–Mn–C Steel. **Microscopy and Microanalysis**, v. 19, n. 6, p. 1581–1585, 8 out. 2013. DOI:

https://doi.org/10.1017/S1431927613013494.

MASOUMI, M. et al. Texture evolution and phase transformation of 25Cr-6Mo-5Ni experimental duplex stainless steel during hot and cold rolling. **Journal of Materials Research and Technology**, v. 6, n. 3, p. 232–240, 1 jul. 2017. DOI: https://doi.org/10.1016/j.jmrt.2017.01.001.

MATOSO, M. S. et al. Processing a twinning-induced plasticity steel by high-pressure torsion. **Scripta Materialia**, v. 67, n. 7-8, p. 649–652, 1 out. 2012. DOI: https://doi.org/10.1016/j.scriptamat.2012.07.019.

MEDEIROS, L. M. F. **Análise das propriedades mecânicas e da energia de falha de empilhamento em aços alto manganês**. 2017. Monografia (Graduação em Engenharia Metalúrgica) - Universidade Federal do Ceará, Fortaleza, 2017. Available in: <https://repositorio.ufc.br/bitstream/riufc/29492/1/2017_tcc_lmfmedeiros.pdf.> Accessed on March/2020.

MENDONÇA, R. R. **Soldagem por fricção e mistura mecânica de aço austenítico alto manganês com efeito TRIP**. 2014. Dissertação. (Metrado em Ciência) - Engenharia de Materiais da Escola de Engenharia de São Carlos, p. 29-31. São Carlos. São Paulo. 2014. Available at: < https://teses.usp.br/teses/disponiveis/18/18158/tde-14102014-082116/pt-br.php.>. Accessed on March/2020.

MEYERS, M. A.; MISHRA, A.; BENSON, D. J. Mechanical properties of nanocrystalline materials. **Progress in Materials Science**, v. 51, n. 4, p. 427–556, maio 2006. DOI: https://doi.org/10.1016/j.pmatsci.2005.08.003.

MIN, J. et al. Constitutive modeling of deformation behavior of high-entropy alloys with face-centered cubic crystal structure. **Materials research letters**, v. 5, n. 5, p. 350–356, 21 fev. 2017. DOI: https://doi.org/10.1080/21663831.2017.1292325.

MOHAMMADI, A. et al. Influence of nanotwins on hydrogen embrittlement of TWIP (twinning-induced plasticity) steel processed by high-pressure torsion. **Materials Science and Engineering A-structural Materials Properties Microstructure and Processing**, v. 783, p. 139273–139273, 1 maio 2020. DOI: https://doi.org/10.1016/j.msea.2020.139273.

MOLODOVA, X. et al. Texture and microstructure evolution of ECAP processed AlMg1Mn0.14 alloy. **International Journal of Materials Research**, v. 98, n. 3, p. 158–166, 1 mar. 2007. DOI: https://doi.org/10.3139/146.101446.

MOLODOVA, X. et al. Thermal stability of ECAP processed pure copper. **Materials Science and Engineering A-structural Materials Properties Microstructure and Processing**, v. 460-461, p. 204–213, 1 jul. 2007. DOI: https://doi.org/10.1016/j.msea.2007.01.042.

NEVES, A. et al. Effect of cold rolling reduction on texture, recrystallization and mechanical properties of UNS S32304 Lean Duplex stainless steel. **Materials Science and Engineering A-structural Materials Properties Microstructure and Processing**, v. 802, p. 140577–140577, 1 jan. 2021. DOI: https://doi.org/10.1016/j.msea.2020.140577.

MURR, L. E.; ESQUIVEL, E. V. Observations of common microstructural issues associated

with dynamic deformation phenomena: Twins, microbands, grain size effects, shear bands, and dynamic recrystallization. **Journal of Materials Science**, v. 39, n. 4, p. 1153–1168, fev. 2004. DOI: https://doi.org/10.1023/B:JMSC.0000013870.09241.c0.

NAKASHIMA, K. et al. Influence of channel angle on the development of ultrafine grains in equal-channel angular pressing. **Acta Materialia**, v. 46, n. 5, p. 1589–1599, mar. 1998. DOI: https://doi.org/10.1016/S1359-6454(97)00355-8.

NAKASHIMA, K. et al. Development of a multi-pass facility for equal-channel angular pressing to high total strains. **Materials Science and Engineering: A**, v. 281, n. 1-2, p. 82–87, abr. 2000. DOI: https://doi.org/10.1016/S0921-5093(99)00744-3.

NETO. J.R. B. **Microestrutura, textura cristalográfica e propriedades de ligas de magnésio processadas por extrusão em canal iguais angular**. 2020. PhD thesis (PhD in Engineering and Materials Science) – Centro de Tecnologia, Universidade Federal do Ceará, Fortaleza, 2020. Available at: <https://repositorio.ufc.br/bitstream/riufc/53490/1/2020_tese_jrbarrosneto.pdf.>. Accessed on March/2021.

PETROV. Y. N. **On the electron structure of Mn–, Ni– and Cr–Ni–Mn austenite with different stacking fault energy. Scripta Materialia**, vol. 53, pp. 1201–1206, 2005. https://doi.org/10.1016/j.scriptamat.2005.07.002.

POKHAREL, R. et al. Polycrystal Plasticity: Comparison Between Grain - Scale Observations of Deformation and Simulations. **Annual Review of Condensed Matter Physics**, v. 5, n. 1, p. 317–346, mar. 2014. DOI: https://doi.org/10.1146/annurev-conmatphys-031113-133846.

QIN, B.; H. K. D. H. BHADESHIA. Plastic strain due to twinning in austenitic TWIP steels. **Materials Science and Technology**, v. 24, n. 8, p. 969–973, 1 ago. 2008. DOI: https://doi.org/10.1179/174328408X263688.

RAAB, G. I. et al. The formation of a high-strength state in martensitic Ti Grade 4 by ECAP. **Journal of Alloys and Compounds**, v. 922, p. 166205–166205, 1 nov. 2022. DOI: https://doi.org/10.1016/j.jallcom.2022.166205.

RANDALL, M. G.; SEONG, J. P.. **Mathematical relations in particulate materials processing: ceramics, powder metals, cermets, carbides, hard materials, and minerals**. Hoboken, Nova Jersey: Wiley, 2008.

REN, J.; CHEN, Q.; CHEN, J. Role of vanadium additions on tensile and cryogenic-temperature charpy impact properties in hot-rolled high-Mn austenitic steels. **Materials Science and Engineering A-structural Materials Properties Microstructure and Processing**, v. 811, p. 141063–141063, 1 abr. 2021. DOI: https://doi.org/10.1016/j.msea.2021.141063.

RENARD, K.; JACQUES, P. On the relationship between work hardening and twinning rate in TWIP steels. **Materials Science and Engineering A-structural Materials Properties Microstructure and Processing**, v. 542, p. 8–14, 1 abr. 2012. DOI: http://dx.doi.org/10.1016/j.msea.2012.01.123.

RICHERT, M.; MCQUEEN, H. J.; RICHERT, J. Micrbband Formation in Cyclic Extrusion Compression of Aluminum. **Canadian Metallurgical Quarterly**, v. 37, n. 5, p. 449–457, dez. 1998. DOI: https://doi.org/10.1179/cmq.1998.37.5.449.

RICHERT, J. R. A New Method for Unlimited Deformation of Metals and Alloys. **Aliminum**, v. 62, p. 604–607, 1986. DOI: https://cir.nii.ac.jp/crid/1570009750478759552.

RIZZO, Nicolau Antonio Dos Santos. **Avaliação dos efeitos da pressão parcial de CO2 no processo de corrosão -fadiga em armaduras e tração de dutos flexíveis**. Master's thesis. (Master in Mechanical Engineering and Materials Technology) Centro Federal de Educação Tecnologia – Celso Suckow da Fonseca CEFETRJ. Rio de Janeiro. RJ. 2011. Available at: <chrome-extension://efaidnbmnnnibpcajpcglclefindmkaj/https://dippg.cefet-rj.br/ppemm/attachments/article/81/11_Fabio%20Pinheiro%20dos%20Santos.pdf>. Accessed on May/2021.

RODRIGUEZ, P. Serrated plastic flow. **Bulletin of Materials Science**, v. 6, n. 4, p. 653–663, 1 set. 1984. DOI: https://doi.org/10.1007/BF02743993.

SAEED, A. A. et al. Characterization and Prediction of Flow Behavior in High-Manganese Twinning Induced Plasticity Steels: Part I. Mechanism Maps and Work-Hardening Behavior. **Metall Mater Trans A.** v. 43, n. 5, p. 1688–1704, 1 maio 2012. DOI: https://doi.org/10.1007/s11661-011-0993-4.

SAITO, Y. et al. Ultra-fine grained bulk aluminum produced by accumulative roll-bonding (ARB) process. **Scripta Materialia**, v. 39, n. 9, p. 1221–1227, 5 out. 1998. DOI: https://doi.org/10.1016/S1359-6462(98)00302-9.

SAITO, Y. et al. Novel ultra-high straining process for bulk materials—development of the accumulative roll-bonding (ARB) process. **Acta Materialia**, v. 47, n. 2, p. 579–583, jan. 1999. DOI: https://doi.org/10.1016/S1359-6454(98)00365-6.

SAIYI, L. et al. Texture evolution during multi-pass equal channel angular extrusion of copper: Neutron diffraction characterization and polycrystal modeling. **Acta Materialia**, v. 53, n. 7, p. 2111–2125, 1 abr. 2005. DOI: https://doi.org/10.1016/j.actamat.2005.01.023.

SAIYI, L. et al. Texture evolution during equal channel angular extrusion: Effect of initial texture from experiment and simulation. **Scripta Materialia**, v. 52, n. 11, p. 1099–1104, jun. 2005. DOI: https://doi.org/10.1016/j.scriptamat.2005.02.008.

SANDIP GHOSH CHOWDHURY et al. Texture evolution during room temperature ageing of silver processed by equal-channel angular pressing. **Scripta Materialia**, v. 64, n. 11, p. 1007–1010, 1 jun. 2011. DOI: https://doi.org/10.1016/j.scriptamat.2011.02.005.

SANGWON, L. W. et al. Effect of Cu addition on the mechanical behavior of austenitic twinning-induced plasticity steel. **Scripta Materialia**, v. 65, n. 12, p. 1073–1076, 1 dez. 2011. https://doi.org/10.1016/j.scriptamat.2011.09.019.

SANTOS, R. G. D. **Transformações de fases em materiais metálicos**. [s.l.] Campinas. São Paulo: Fundação de Desenvolvimento da Unicamp - Funcamp (editora Unicamp), ed. 1. ISBN

8526807145. 2006.

SCHOECK, G. The portevin-le chatelier effect. A kinetic theory. **Acta Metallurgica**, v. 32, n. 8, p. 1229–1234, ago. 1984. DOI: https://doi.org/10.1016/0001-6160(84)90129-9.

SCHUMANN, V. H. **Martensitische Umwandlung in austenitischen**. Neue Hütte, v. 17, p. 605-609. 1972.

SCHWARTZ, A. J.. KUMAR, M.; ADAMS, B. L.; FIELD, David P. (ed.). **Electron backscatter diffraction in materials science**. New York: Spring, 2000. DOI: https://doi.org/10.1007/978-1-4757-3205-4.

SEGAL, V. M.; REZNIKOV, V. I.; DROBYSHEVSKIY, A. E.; and KOPYLOV, V. I.. Plastic Working of Metals by Simple Shear. **Russian Metallurgy**, 1, 99-105., 1981.

SEGAL, V. M.. **The Method of Material Preparation for Subsequent Working**. Patent of the USSR, number: 575892, p. 330. Russia. 1977.

SEGAL, V. M.. Materials processing by simple shear. **Materials Science and Engineering A**, volume 197, issue 2, 1 July 1995, pages 157-164, 1995. https://doi.org/10.1016/0921-5093(95)09705-8.

SEOK, G. L. et al. Effects of Cr addition on Charpy impact energy in austenitic 0.45C-24Mn-(0,3,6)Cr steels. **Journal of Materials Science & Technology**, v. 50, p. 21–30, 1 ago. 2020. DOI: https://doi.org/10.1016/j.jmst.2019.12.032.

SEUNG-JOON, Lee,; FUJII, H.; KOHSAKU, U. Thermodynamic calculation of the stacking fault energy in Fe-Cr-Mn-C-N steels. **Journal of Alloys and Compounds**, v. 749, p. 776–782, 1 jun. 2018. DOI: https://doi.org/10.1016/j.jallcom.2018.03.296.

SEVILLANO, J. G.; J.; VAN HOUTTE, P.; AERNOUDT, E. Large strain work hardening and textures. **Progress in Materials Science**, v. 25, n. 2-4, p. 69–134, jan. 1980. DOI: https://doi.org/10.1016/0079-6425(80)90001-8.

SHAMANIAN, M. et al. Interface microstructure across cladding of super duplex stainless steel with austenitic stainless steel buffer layer. **Surface and Coatings Technology**, v. 259, p. 532–542, nov. 2014. DOI: https://doi.org/10.1016/j.surfcoat.2014.10.034.

SHIEKHELSOUK, M. et al. Modelling the behaviour of polycrystalline austenitic steel with twinning-induced plasticity effect. **International Journal of Plasticity**, v. 25, n. 1, p. 105–133, jan. 2009. DOI: https://doi.org/10.1016/j.ijplas.2007.11.004.

SHIH, M. H. et al. Microstructure and flow stress of copper deformed to large plastic strains. **Scripta Materialia**, v. 45, n. 7, p. 793–799, out. 2001. DOI: https://doi.org/10.1016/S1359-6462(01)01098-3.

SHIMADA, M. et al. Optimization of grain boundary character distribution for intergranular corrosion resistant 304 stainless steel by twin-induced grain boundary engineering. **Acta Materialia**, v. 50, n. 9, p. 2331–2341, 24 maio 2002. DOI: https://doi.org/10.1016/S1359-6454(02)00064-2.

SITDIKOV, O. S.; RUSTAM KAIBYSHEV; SAKAI, T. Dynamic Recrystallization Based on Twinning in Coarse-Grained Mg. **Materials Science Forum**, v. 419-422, p. 521–526, 1 mar. 2003. DOI: https://doi.org/10.4028/www.scientific.net%2FMSF.419-422.521.

SKILBRED, E. S.; LOOTZ, S. A.; JOHNSEN, R. **Hydrogen Embrittlement Susceptibility of Steel Armor Wires for Flexible Pipes**. Nace International. C 2020-14489. Available at: <https://onepetro.org/NACECORR/proceedings-abstract/CORR20/All-CORR20/NACE-2020-14489/445983>. Access in: 25 ago. 2023.

SKROTZKI, W. et al. Torsion Texture Measurements With High-Energy Synchrotron Radiation on NiAl. **Textures and Microstructures**, v. 35, n. 3-4, p. 163–173, 1 jan. 2003. DOI: https://doi.org/10.1080/07303300310001628733.

SMALLMAN, R. E.; BISHOP, R. J. **Modern physical metallurgy and materials engineering: science, process, applications.** Oxford; Boston: Butterworth Heinemann, 1999.

SOMANI, M. C.; L.P. KARJALAINEN. A Rationale for SRX Regression Model of Hot-Deformed Austenite Using an Orthogonal Taguchi L8 Matrix Steels. **Materials Science Forum**, v. 715-716, p. 751–757, 1 abr. 2012. DOI: https://doi.org/10.4028/www.scientific.net/msf.715-716.751.

STOLYAROV, V. V. et al. Influence of ECAP routes on the microstructure and properties of pure Ti. **Materials Science and Engineering: A**, v. 299, n. 1-2, p. 59–67, fev. 2001. DOI: https://doi.org/10.1016/S0921-5093(00)01411-8.

SUO, T. et al. Tensile ductility of ultra-fine grained copper at high strain rate. **Advanced Materials Research**, v. 160-162, p. 260–266, nov. 2010. DOI: https://doi.org/10.4028/www.scientific.net/amr.160-162.260.

SUTTON, B.J. **Solidification behavior and hot cracking susceptibility of high manganese steel weld metals**. 2013. THESIS. Graduate Program in Welding Engineering. The Ohio State University. Ohio. 2013. Available at: <https://api.semanticscholar.org/CorpusID:136159857.>. Accessed in: 25/08/2023.

SUWAS, S. et al. Evolution of crystallographic texture during equal channel angular extrusion of copper: The role of material variables. **Metallurgical and Materials Transactions**, v. 37, n. 3, p. 739–753, 1 mar. 2006. DOI: https://doi.org/10.1007/s11661-006-0046-6.

TAEKYUNG, L. et al. Tensile deformation behavior of Fe–Mn–C TWIP steel with ultrafine elongated grain structure. **Materials Letters**, v. 75, p. 169–171, 1 maio 2012. DOI: https://doi.org/10.1016/j.matlet.2012.02.012.

TAMARELLI, C. M. **AHSS 101: the evolving use of advanced high-strength steels for automotive applications. Steel Market Development Institute**. Michigan: AISI, 2011. 45p. Steel Market Development Institute. Available at: <https://www.autosteel.org>. Access in: 13 ago. 2021.

TIMOKHINA, I.; MEDVEDEV, A. E.; RIMMA LAPOVOK. Severe plastic deformation of a TWIP steel. **Materials Science and Engineering A-structural Materials Properties**

Microstructure and Processing, v. 593, p. 163–169, 1 jan. 2014. DOI: https://doi.org/10.1016/j.msea.2013.11.013.

TOKITA, S. et al. In situ EBSD observation of grain boundary character distribution evolution during thermomechanical process used for grain boundary engineering of 304 austenitic stainless steel. **Materials Characterization**, v. 131, p. 31–38, set. 2017. DOI: https://doi.org/10.1016/j.matchar.2017.06.032.

UEJI R. et al. Tensile properties and twinning behavior of high manganese austenitic steel with fine-grained structure. **Scripta Materialia**, v. 59, n. 9, p. 963–966, 1 nov. 2008. DOI: https://doi.org/10.1016/j.scriptamat.2008.06.050.

UMANTSEV, A. **Thermal effects in kinetics of phase transforations**. *In*: UMANTSEV, Alexander. Field theoretic metrhod in phase transformations. [New Jersey]: Springer, 2012. p. 201-244. ISBN 1461414865.

UNGAR T.; BORBÉLY, A.. The effect of dislocation contrast on x-ray line broadening: A new approach to line profile analysis. **Applied Physics Letters**, v. 69, n. 21, p. 3173–3175, 18 nov. 1996. DOI: https://doi.org/10.1063/1.117951.

VALIEV, R. Z.; KRASIL'NIKOV, N. A.; TSENEV, N. K. Plastic deformation of alloys with submicron-grained structure. **Materials Science and Engineering A-structural Materials Properties Microstructure and Processing**, v. 137, p. 35–40, 1 maio 1991. DOI: https://doi.org/10.1016/0921-5093(91)90316-F.

VALIEV, R. Z.; KORZNIKOV, A. V.; MULYUKOV, R. R. Structure and properties of ultrafine-grained materials produced by severe plastic deformation. **Materials Science and Engineering: A**, v. 168, n. 2, p. 141–148, ago. 1993. DOI: https://doi.org/10.1016/0921-5093(93)90717-S.

VALIEV, R. Z. Structure and mechanical properties of ultrafine-grained metals. **Materials Science and Engineering: A**, v. 234-236, p. 59–66, ago. 1997. DOI: https://doi.org/10.1016/S0921-5093(97)00183-4.

VALIEV, R. Z.; ALEXANDROV, I. V. Nanostructured materials from severe plastic deformation. **Nanostructured Materials**, v. 12, n. 1-4, p. 35–40, jan. 1999. DOI: https://doi.org/10.1016/S0965-9773(99)00061-6.

VALIEV, R. Z.; ISLAMGALIEV, R. K.; ALEXANDROV, I. V. Bulk nanostructured materials from severe plastic deformation. **Progress in Materials Science**, v. 45, n. 2, p. 103–189, mar. 2000. DOI: https://doi.org/10.1016/S0079-6425(99)00007-9.

VALIEV, R. Nanostructuring of metals by severe plastic deformation for advanced properties. **Nature Materials**, v. 3, n. 8, p. 511–516, ago. 2004. DOI: https://doi.org/10.1038/nmat1180.

VALIEV, R. Z.; LANGDON, T. G. Principles of equal-channel angular pressing as a processing tool for grain refinement. **Progress in Materials Science**, v. 51, n. 7, p. 881–981, set. 2006. DOI: https://doi.org/10.1016/j.pmatsci.2006.02.003.

VALIEV, R.Z.; Zhilyaev, A.P.; Langdon, T.G. **Bulk nanostructured materials: fundamentals and applications**. John Wiley & Sons: Hoboken. New Jersey. USA, pp. 1–456. 2013.

VAN, B. et al. Diffraction-Line Broadening due to Strain Fields in Materials; Fundamental Aspects and Methods of Analysis. **Acta Crystallographica Section A**, v. 52, n. 5, p. 730–747, 1 set. 1996. DOI: https://doi.org/10.1107/S0108767396005727.

VERCAMMEN. **Processing and Tensile Behaviour of TWIP steels Microstructural and Texture Analysis**. 2004. Ph.D. thesis. Katholieke Universiteit Leuven, Belgium. 2004.

VINCENTIS N.S. et al. XRD and EBSD analysis of anisotropic microstructure development in cold rolled F138 stainless steel. **Materials Characterization**, v. 123, p. 137–152, 1 jan. 2017. DOI: https://doi.org/10.1016/j.matchar.2016.11.018.

WANG, Y. M.; MA, E.; CHEN, M. W. Enhanced tensile ductility and toughness in nanostructured Cu. **Applied Physics Letters**, v. 80, n. 13, p. 2395–2397, abr. 2002. DOI: https://doi.org/10.1063/1.1465528.

WANG, H. et al. Corrosion behaviour of Al-added high Mn austenitic steels in molten lead bismuth eutectic with saturated and low oxygen concentrations at 450 °C. **Corrosion Science**, v. 175, p. 108864–108864, 1 out. 2020. DOI: https://doi.org/10.1016/j.corsci.2020.108864.

WEON, S. et al. Enhancing high-cycle fatigue properties of cold-drawn Fe–Mn–C TWIP steels. **International Journal of Fatigue**, v. 85, p. 57–64, abr. 2016. DOI: https://doi.org/10.1016/j.ijfatigue.2015.12.007.

XIA, Y. et al. Effect of Cr on mechanical properties and corrosion behaviors of Fe-Mn-C-Al-Cr-N TWIP steels. **Journal of Materials Science & Technology**, v. 33, n. 12, p. 1555–1560, 1 dez. 2017. DOI: https://doi.org/10.1016/j.jmst.2017.08.004.

YAMASHITA, A. et al. Influence of pressing temperature on microstructural development in equal-channel angular pressing. **Materials Science and Engineering: A**, v. 287, n. 1, p. 100–106, jul. 2000. DOI: https://doi.org/10.1016/S0921-5093(00)00836-4.

YAN, S. Z. et al. Compositional dependence of the Néel transition, structural stability, magnetic properties and electrical resistivity in Fe–Mn–Al–Cr–Si alloys. **Materials Science and Engineering A-structural Materials Properties Microstructure and Processing**, v. 334, n. 1-2, p. 19–27, 1 set. 2002. DOI: https://doi.org/10.1016/S0921-5093(01)01781-6.

YANG, G.; KIM, J.-K. An Overview of High Yield Strength Twinning-Induced Plasticity Steels. **Metals**, v. 11, n. 1, p. 124, 10 jan. 2021. DOI: https://doi.org/10.3390/met11010124.

YANAGIMOTO, J. et al. Continuous bending-drawing process to manufacture the ultrafine copper wire with excellent electrical and mechanical properties. **CIRP Annals**, v. 60, n. 1, p. 279–282, 2011. DOI: https://doi.org/10.1016/j.cirp.2011.03.148.

YE, F. et al. Effects of dislocations and hydrogen concentration on hydrogen embrittlement of austenitic 316 stainless steels. **Journal of Alloys and Compounds**, v. 876, p. 160134–160134, 1 set. 2021. DOI: https://doi.org/10.1016/j.jallcom.2021.160134.

YIN, F. et al. The Damping Behavior of Ni Added Mn-Cu Damping Alloys. **MATERIALS TRANSACTIONS**, v. 44, n. 9, p. 1671–1674, 2003. DOI: https://doi.org/10.2320/matertrans.44.1671.

ZHANG, N.; YANG, P.; MAO, W. {001}〈120〉−{113}〈361〉 recrystallization textures induced by initial {001} grains and related microstructure evolution in heavily rolled electrical steel. **Materials Characterization**, v. 119, p. 225–232, set. 2016. DOI: https://doi.org/10.1016/j.matchar.2016.08.009.

ZHI, H. et al. Outstanding Tensile Properties and Their Origins in Twinning-Induced Plasticity (TWIP) Steels with Gradient Substructures. **Materials**, v. 13, n. 5, p. 1184, 6 mar. 2020. DOI: https://doi.org/10.3390/ma13051184.

ZINOVIEVA, O. et al. Three-dimensional analysis of grain structure and texture of additively manufactured 316L austenitic stainless steel. **Additive Manufacturing**, v. 36, p. 101521, dez. 2020. DOI: https://doi.org/doi.org/10.1016/j.addma.2020.101521.

ZUGHAER, H. J.; NUTTING, J. Deformation of sintered copper and 50Cu–50Fe mixture to large strains by cyclic extrusion and compression. **Materials Science and Technology**, v. 8, n. 12, p. 1104–1107, 1 dez. 1992. DOI: https://doi.org/10.1179/mst.1992.8.12.1104.

ZUOGUI, Z. et al. Grain refining performance for Al and Al–Si alloy casts by addition of equal-channel angular pressed Al–5 mass% Ti alloy. **Materials Science and Engineering A-structural Materials Properties Microstructure and Processing**, v. 425, n. 1-2, p. 55–63, 1 jun. 2006. DOI: https://doi.org/10.1016/j.msea.2006.03.018.